Elucidation of reaction mechanism at the anode/electrolyte interface and cathode material for rechargeable magnesium battery

Tuerxun Feilure

Elucidation of reaction mechanism at the anode/electrolyte interface and cathode material for rechargeable magnesium battery

Tuerxun Feilure

Graduate School of Human and Environmental Studies

Kyoto University

Supervised by

Prof. Dr. Yoshiharu Uchimoto

Outline

Chapter 1. General Introduction

1-1. Background

With the increasing depletion of fossil energy and environmental pollution, the development of clean, efficient, and sustainable new energy technologies has become a matter of urgency.[1] Renewable energy sources such as solar, geothermal, and wind have been mentioned as candidates for new energy sources.[2, 3] However, the output of renewable energies are influenced by weather and time, and have obvious unforgettable stability, discontinuity and uncontrollability. To achieve a stable energy supply, energy-storage media, such as rechargeable batteries, have gained attention.

Rechargeable batteries are considered to be one of the most effective energy storage technologies and play an important role in balancing the output power and storing the remaining power efficiently. Among rechargeable batteries, lithium-ion batteries are considered to be the most promising because of their high energy density and high power density. Today, lithium-ion batteries are used not only as a power storage medium, but also in electric vehicles that emit no exhaust gas and hybrid vehicles with reduced exhaust gas emissions. However, although lithium-ion batteries have high performance compared to other rechargeable batteries, they are insufficient for use as a power source for electric vehicles or as a large-scale power storage medium.[4-6] Therefore, post lithium ion rechargeable batteries are needed to achieve higher capacity, higher output, and better safety.

1-2. Lithium-Ion Batteries

Rechargeable batteries continue to attract increasing interest in applications ranging from microchips to grid-scale energy storage. A range of rechargeable batteries such as lead-acid, nickel-cadmium, nickel-metal hydride and lithium-ion batteries (LIBs) have been commercialized.[2]

Compared to conventional lead-acid batteries, Ni-Cd batteries, and nickel-metal hydride batteries, lithium-ion batteries have various advantages such as high energy density, relatively high output, and low self-discharge, making them the most powerful rechargeable batteries available today. Lithium-ion batteries were first commercialized by SONY in the 1990s and were originally produced by combining transition metal oxide cathodes, graphite anodes and $LiPF_6$ in carbonate electrolytes in a battery cell.[7] Over the past decades, the revolution in electronics and the desire for emission-free transportation and renewable energy sources have continued to drive battery technology toward higher energy density, lower cost, and greater sustainability. [8-12] Lithium-ion batteries are already widely used as a power source for portable devices. In addition, the application to electric vehicles and industrial batteries has been studied recently.

In a typical lithium-ion battery, as show in Figure 1-1, composite oxide of Li and transition metals such as $LiCoO_2$ is used as the positive electrode, and graphite is used as the negative electrode. Lithium salt such as $LiClO_4$ and $LiPF_6$ dissolved in organic solvents can be used as the electrolyte.[13-15] The reaction equations for a battery using $LiCoO_2$ as the positive electrode material and carbon as the negative electrode material show on below:

Anode	$Li_xC_6 \rightarrow C_6 + xLi^+ + xe^-$
Cathode	$Li_{1-x}CoO_2 + xLi^+ + xe^- \rightarrow LiCoO_2$
Total	$Li_xC_6 + Li_{1-x}CoO_2 \rightarrow C_6 + LiCoO_2$

During charging process, lithium ions in the crystal structure of $LiCoO_2$ are extracted from the cathode material and dissolved into the electrolyte. At this time, charge compensation is performed by the Co. The lithium ions dissolved in the electrolyte move through the electrolyte and are inserted into the graphite of the anode material. [16, 17] In this process, carbon is reduced.

As a result of these reactions, electrons are transferred from the cathode to the anode via an external circuit. [13, 14, 18-20] During discharge process, the opposite reaction occurs, resulting in the transfer of lithium ions and electrons from the anode to the cathode. In this case, the skeleton of the crystal structure of the host compound is not changed by the insertion and removal of lithium ions.

Currently, lithium-ion secondary batteries, which have features such as high energy density, are being considered for power storage applications combined with renewable energy and as a power source for electric vehicles and other applications. However, lithium-ion secondary batteries have problems with energy density, material cost, and safety.[21, 22] In addition, when considering full-scale use in electric vehicles, for example, it is estimated that an extremely high energy density of about 500 $Whkg^{-1}$ is required to achieve a cruising range comparable to that of current gasoline vehicles, and the performance of current lithium-ion batteries is insufficient. Therefore, the development of innovative secondary batteries is required.

1-3. Multivalent Cation Batteries

With the increase in global energy consumption, the need to expand the use of renewable energy, and its use in electric vehicles, rechargeable batteries will require even higher performance in the future. Li metal as an anode has not been realized because Li has a unique characteristic of easily causing needle-like precipitation (called dendrite precipitation) on the Li metal anode during charging, and this needle-like Li can break through the separator and reach the cathode, causing a short circuit, which is a fatal safety problem. The use of Li metal as an anode has not been realized because of this fatal safety problem. Graphite is basically used as the anode of current Li-ion batteries, but its capacity density is very small compared to the weight capacity of Li metal. Figure 2-2 clearly shows the large penalty upon moving from Li

metal to LIBs.[23] The potential for developing next-generation batteries is also clear. In order to achieve even higher energy densities, secondary batteries using multivalent cation metals as anodes, are expected to be candidates for next-generation secondary batteries. On the other hand, multivalent intercalation batteries using aqueous electrolytes are attracting attention due to their affordability, ease of manufacturing, and safety.

By using metals such as Ca, Mg, and Al, which do not cause dendrite precipitation, as the anode and utilizing their precipitation and dissolution, it will be possible to dramatically increase the capacity of the anode compared to the current graphite. Metal anode secondary batteries with multivalent ion carriers, such as Ca^{2+} ,[24-27] Zn^{2+} and Y^{3+} as carriers,[28, 29] aluminum secondary battery with Al^{3+} as carriers, and using Mg^{2+} as carriers for magnesium rechargeable batteries[24,30-32] have been reported. Among them, magnesium secondary batteries have received the most attention for the reasons described hereinafter. Table 1-1 shows a comparison of the properties of various anode metals.[33] In determining the theoretical weight capacity and volume capacity, the following reactions are assumed to occur:

$$M^{x+} + xe^{-} \Leftrightarrow M$$

Since Mg metal has a high theoretical weight and volume capacity and a relatively low redox potential, secondary batteries using Mg metal as the anode are expected to have a high energy density. In particular, with regard to the theoretical volume capacity, it is about twice that of lithium, which is an advantage because it can be packed in a large amount in a limited space, such as a secondary battery for electric vehicles. As mentioned in the previous section, graphite is basically used as the anode of current Li-ion batteries, but its capacity density is 372 mAg^{-1}, which is very small compared to the weight capacity of Li metal (3862 $mAhg^{-1}$). The characteristics of magnesium when compared with lithium and other metals are can be summarized with reference to Table 1-1. Because dendrite precipitation does not occur, Mg metal can be used as the anode, enabling a dramatic increase in the capacity of the anode. The

crustal abundance is more than 300 times greater than Li, which means that the cost can be reduced and it is suitable for large scale production. Because of its high melting point and low reactivity, unlike Li and Na, it is a metal that can be handled relatively safely in air and water, enabling the construction of highly safe secondary batteries. Overall, it can be said that magnesium is a material that can realize high capacity, high energy density, high safety, and low cost, which cannot be achieved by the extension of the current lithium-ion battery. The research on the electrochemistry of elements such as Zn, Ca, and Al, which are also polyvalent metals, is becoming more and more popular every year, and research on Mg is the metallic element that attracts the most attention.

1-4. Magnesium-ion Batteries

Lithium-ion secondary batteries, which have the highest energy density of all commercialized secondary batteries, are now used in a wide range of applications, from small electronic devices such as computers and smartphones to large ones such as electric vehicles, and have become indispensable in our daily lives. However, lithium-ion batteries have problems in terms of safety and cost due to lithium resources, and their theoretical capacity has reached its limit, so it is necessary to develop next-generation secondary batteries with high energy density, high safety, and low cost. It is estimated that an energy density of 500 Wh kg^{-1} is required for an electric vehicle to have the same cruising range as a current gasoline vehicle. However, the current lithium-ion battery does not meet the energy density shown by the green line. In order to achieve higher energy density, rechargeable batteries using multivalent cation metals as the anode are expected to be a candidate for next-generation rechargeable batteries.[34]

Magnesium rechargeable batteries are attracting attention as a large-scale energy storage application other than lithium ions battery because of their many advantages such as high capacity, low cost, environmental friendliness, and abundance of magnesium.[34-36] However, divalent magnesium ions interact more strongly than monovalent lithium ions, and are difficult

to diffuse in the solid phase, resulting in extremely slow electrode reactions. Furthermore, there is no known magnesium electrolyte that can charge and discharge stably and safely through repeated dissolution and precipitation of magnesium metal. In other words, the problems related to the cathode and electrolyte need to be solved in order to create a magnesium secondary battery. Thus, the very important factors for the practical application of RMB is that development of stable and highly efficient electrode materials and the optimization of electrolytes.[35-38]

1-4-1. Electrolytes

The role of electrolyte in the battery system is that transferring the ions between the cathode and anode. As show in Figure 1-3, the following properties are required for the electrolyte of Mg rechargeable battery:

(1) Reversible deposition/dissolution reactions of magnesium metal.

(2) High ionic conductivity.

(3) High electrochemical stability (electrochemical window).

(4) High safety.

In addition, safety is also important for electrolytes for Mg batteries, such as low volatility, low flammability, and low toxicity. One of the challenges in developing electrolytes capable of reversible magnesium precipitation is to achieve reduction resistance to prevent the formation of impermeable solid electrolyte interface (SEI). SEI formation is a polarity that readily forms a reductive passivation layer at positive potentials higher than the reduction potential of magnesium metal. Preventing the use of commercially available magnesium analogs of lithium salts in aprotic solvents.[39] In the absence of a protective SEI, the electrode must be inert in the battery electrolyte to prevent degradation.[40, 41]

1-4-2. Anode Materials

Most of the materials used for the negative electrode of rechargeable magnesium

batteries are currently magnesium metal or its alloys, while others are less well reported. However, the surface of magnesium metal can easily form a passivation film which cannot conduct magnesium ions, thus making the reversible dissolution and deposition of magnesium metal in organic electrolytes very difficult.

Research into alloyed or inserted anodes has been driven in part by the high impedance of magnesium metal anodes in existing electrolytes (several orders of magnitude higher than that of commercial lithium-ion batteries).[41] Recently, it has been found that Bi, Sb as well as BiSb alloys are compatible with conventional electrolytes and can achieve reversible deposition and dissolution of magnesium in acetonitrile solution of conventional electrolyte $Mg(TFSI)_2$, which can be used as the negative electrode of rechargeable magnesium batteries, and provides a new idea for the research development of rechargeable magnesium batteries.[42-45] When using the nanometer size material as an active material , better cycle life can be obtained due to better control of bulk changes. Currently, the cycle life of the anode exceeds 100 stable cycles, which is much better than the cathode cycle life.

1-4-3. Cathode Materials

The cathode material plays an important role in the whole rechargeable magnesium battery system, and the requirements for the cathode material are mainly:

(1) High working voltage and specific capacity.

(2) Fast Mg^{2+} migration rate and reversible kinetics.

(3) Good cycling stability.

Magnesium metal anode secondary batteries have major challenges that need to be addressed before the batteries can be commercialized, one of which is the development of a cathode material that can reversibly insert and extract divalent magnesium ions. Magnesium ions have the same ionic radius as lithium ions, but their valence is twice that of lithium ions,

resulting in a higher charge density.[46] Therefore, it is difficult to diffuse them within the cathode. There are few matrix materials that can reversibly embed magnesium ions, making the development of appropriate cathode materials one of the challenges in the development of rechargeable batteries

1-5. Current Rechargeable Magnesium Battery Electrolytes

1-5-1. Grignard-Based Electrolytes

It has been reported by various groups that Mg deposition/dissolution reactions proceed reversibly in an electrolyte containing Grignard's reagent (RMgX, R: ethyl, butyl X: Cl, Br) dissolved in THF. In 2000, Aurbach et al. reported first prototype of RMBs, using $Mg(AlCl_2R)_2$/tetrahydrofuran (THF) as an electrolyte.[47] The main drawback of the first prototype electrolyte is its low electrochemical stability window due to the relatively weak Al-C bond that is easily broken by the elimination reaction, which limits the choice of high-voltage cathode materials. Subsequently, the another type of magnesium battery electrolyte consisting of PhMgCl and $AlCl_3$ in ether solution was developed.[48] The THF solution of all-phenyl magnesium halide aluminum salt complex was synthesized by using PhMgCl and $AlCl_3$ in the molar ratio of 1:2 as reaction materials, which is called "APC" electrolyte, and its electrochemical window can reach more than 3 V (vs. Mg RE) at Pt electrode, which is about 1 V higher than the first generation electrolyte. The obtained APC electrolyte had a 100% cycle efficiency of reversible Mg deposition-dissolution, higher conductivity and faster Mg electrochemical deposition-dissolution kinetic process.[49] It also has been reported that the electrochemical stability window of the "APC" electrolyte is closely related to the different metals used as working electrodes, and the electrolyte does have a stable electrochemical window of more than 3 V at Pt electrodes, but on Cu, Ni, Al stainless steel (SS), etc. the electrochemical stability window is around 2.0 V.[50] The reason for this is presumed to be most

likely due to the presence of halogen ions in the organomagnesium halide aluminum complex electrolyte, thus causing corrosion of common metals and resulting in a lower electrochemical window on common metals.[51, 52] Moreover, the second generation electrolyte has a stronger volatility, which seriously weakens the advantage of rechargeable magnesium batteries in terms of safety performance.[53] It also has been evaluated that the mechanism by which the performance of Grignard reagents is improved after adding ionic liquids.[54] They pointed out that the Grignard reagent selectively extracts acidic protons from the ionic liquid, yielding a series of Mg complexes with high chemical stability derived from their resonant structures.

Furthermore, the reaction mechanism of the magnesium deposition dissolution reaction has been analyzed by many researchers. From further analysis by nuclear magnetic resonance spectroscopy (NMR)[55], X-ray absorption spectroscopy (XAS),[56] and Raman spectroscopy[57], it is known that in the THF electrolyte system of organic Mg-Al complexes, the electrochemical reaction effective cation ions are $MgCl^+$, $Mg_2Cl_3^+$, while the anions are $AlCl_{4-n}R_n^-$ ($n \leq 4$), which are coordinated certain THF molecules to a stable state. The R group in the anion is extremely important for the reversibility of magnesium deposition, and the anodic stability of the system is determined by the stability of the R-Al bond formed by adsorption.

XAS technique employed during the magnesium deposition process is a powerful tool for analyzing the dynamic change in the local structure of magnesium ions. X-rays of the energy E, which passes through a homogeneous sample of the thickness x, is attenuated. In analogy to the Lambert-Beer law. Once the X-ray comes into contact with the sample, the x-ray photon may be absorbed by the atom and excite one of its electrons into the continuum leaving an electron hole in the initial core shell. This process is known as photoelectric absorption. When an electron fills the core hole, it can simultaneously emit a fluorescent photon or another electron (Auger electron) from the other core shell, and these processes are called fluorescence emission and Auger emission, respectively.

Nakayama et al. further analyzed the complex electrolyte components of the "first generation electrolyte" using X-ray absorption fine structure (XAFS) spectroscopy combined with nuclear magnetic resonance spectroscopy (NMR) techniques and found that the main components of the $Mg(AlCl_2EtBu_2)$/THF electrolyte were $(Mg_2Cl_2THF_4)^{2+}$, $(R_2AlCl_2)^-$, $(RAlCl_3)^-$, $R_2AlClTHF$ and R_3AlTHF (R = Et or Bu).[57] Mg^{2+} is adsorbed on the electrode and further gains electrons to be deposited on the electrode surface. Among them, the neutral group $R_2AlClTHF$ plays a key role in the reversibility of deposition-dissolution

1-5-2. Boron-Containing Electrolytes

Boron-containing anion-based electrolytes are promising as non-corrosive Mg electrolyte systems because they can promote the reversible deposition and dissolution of Mg without the involvement of chlorine. In the 1990s, Gregory et al. demonstrated that Mg organoboronates $(Mg(BPh_2Bu_2)_2$ or $Mg(BPhBu_3)_2)$ was compatible with the Mg anodes.[58] However, batteries using this electrolyte need to be operated below 2 V due to low anode stability. Subsequently, the inorganic salt $Mg(BH_4)_2$ ether-based electrolyte was firstly proposed by Mohtadi.[59] This electrolyte system does not contain any halogen element and is the latest breakthrough point of inorganic magnesium salt in the field of rechargeable magnesium batteries. In their research, they firstly prepared a ligated electrolyte system by dissolving $Mg(BH_4)_2$ in ether solvents such as DME and THF respectively as shown in Figure 1-5. Electrochemical tests on this electrolyte system showed that the reversible deposition and dissolution of magnesium metal in the electrolyte indicated that the electrolyte was active. They also added a halogen-free additive ($LiBH_4$) to the electrolyte. The addition of $LiBH_4$ increased the current density of the electrolyte by several orders of magnitude and increased the Coulomb efficiency to 94%. (Figure 1-6).

Although a low electrochemical stability was obtained, this pioneering work laid the

basic for further improving the performance of $Mg(BH_4)_2$ -based electrolyte systems.[60, 61] The electrochemical stability window has been extended by dissolving $Mg(BH_4)_2$ and $LiBH_4$ in a mixture of TG, DME, and PP14TFSI solvents.[62] The ionic conductivity of the $Mg(BH_4)_2$/diglyme electrolyte has been improved, with high Coulombic efficiency and high electrochemical window (2.8 V vs. Mg, Figures 1-7 and 1-8), when *tris*(2H-hexafluoroisopropyl) borate) (THFPB) was used as an additive.[63] Overall, the reducing nature of BH_4^- decreases the stability of the anode, so it is very important to select the functional solvent and additives to improve the electrochemical stability of $Mg(BH_4)_2$-based electrolytes.

Because of the potential to improve the electrochemical stability of electrolyte solutions, magnesium salts based on carba-chloroso-borate anions have attracted the attention of many researchers. Recently, Tutusaus et al. reported the boron-containing anion-based electrolyte $Mg(CB_{11}H_{12})_2$/tetraglyme [64] with non-corrosive to the cell, and had excellent compatibility with the Mg anode, and also showed high anodic stability (Figure 1-9). Subsequently, carborane anions (such as $CB_{11}H_{11}F^-$ and $HCB_9H_9^-$) electrolytes which exhibit high Coulombic efficiency and high anodic stability (Figure 1-10) have been reported.[65, 66] $Mg[B(hfip)_4]_2$-based electrolyte reported by Karger et al. which shows the excellent ionic conductivity, good anodic stability and high Coulombic efficiency for Mg deposition (Figure 1-11).[67] The several boron-containing electrolytes by combining THFPB with different common magnesium salts ($Mg(BH_4)_2$,[63] MgF_2,[68] MgO,[69] $MgCl_2$[70]) for a Mg/S battery have been developed by Cui's group.

1-5-3. Other Novel Magnesium Electrolytes

The organometallic magnesium complexes have been contained in many of the previously reported electrolytes, which may be undesirable for the safe use of rechargeable magnesium battery. Magnesium aluminum chloride complex called as MACC electrolyte is the one of the typical inorganic electrolyte which has been widely studied. The reversibility of

magnesium deposition/stripping in $MgCl_2$-$AlCl_3$ electrolyte solutions have been confirmed in 2014. In DME solvent, $MgCl_2$-$AlCl_3$ electrolyte exhibited excellent electrochemical performance such as low overpotential for the magnesium deposition and wide electrochemical windows.[71, 72] However, this kind of electrolytes require electrochemical conditioning to achieve reversible Mg plating/stripping.[73] Conditioning-free MACC electrolyte have been developed with the Mg powers,[74] $Mg(HMDS)_2$ (HMDS = hexamethyldisilazide),[75] and $Mg(TFSI)_2$[76] as the additives. In addition, the coulombic efficiency in the first cycle reach to the 100% by dissolving metallic Mg in $AlCl_3$/THF with the help of $CrCl_3$.[77]

In order to develop a non-nucleophilic electrolyte compatible with the electrophilic sulfur cathode, Kim et al. reported an HMDSMgCl-$AlCl_3$/THF electrolyte of Mg/S secondary batteries as a first prototype.[78] However, the rapidly decreasing of the capacity is the one of the problem of this system. Subsequently, the neutral product [(HMDS) $AlCl_2$] was changed to the complex [Mg_2Cl_3] [(HMDS)$AlCl_3$] which electrochemically active by adding $MgCl_2$ to the electrolytes.[79] Furthermore, by using a mixture of glyme and ionic liquid as $(HMDS)_2Mg$-$AlCl_3$ electrolyte, a discharge potential has been largely increase for the first time in an Mg/S battery.[80]

Recently, the reversible magnesium deposition dissolution reaction reported in $Mg(TFSI)_2$-based electrolytes which also show the excellent ionic conductivity, high electrochemical stability and good solubility in ethers.[76, 81]However, due to the decomposition of the $TFSI^-$,the passivation reaction occur on the anode and electrolyte interface which impeded the Mg plating/stripping process, resulting a large overpotential.[82] Simple salt $Mg(TFSA)_2$ dissolved in triglyme also show the reversible magnesium deposition/dissolution reaction as show in Figure 1-12.[72, 83] Furthermore, the chain length of glyme and the type of anion affected the solvation structure have been reported.[84,85, 86] The electrochemical performance of $Mg(TFSI)_2$-based electrolytes have been improved by introducing the additives like $MgCl_2$ (Figure 1-13).[87] Similarly, the $Mg[TFSI]_2$/tetraglyme electrolyte with $Mg(BH_4)_2$ as

an additive, exhibits stable cyclic efficiency.[88]

To summarize, different electrolytes contain their own unique properties. Grignard-based electrolytes, the earliest electrolytes used in RMB, have high Coulombic efficiency and low deposition overpotential, but their development is limited by the low anode stability and high chemical reactivity. Among boron-containing electrolytes, $Mg(BH_4)_2$ in ether solvents show limited solubility and low electrochemical window. Carbaborate anionic electrolytes have a wide electrochemical range, but the high raw material prices limit the research and application of these materials. The $(HMDS)_2Mg$-based electrolyte also presents the disadvantage in price, although it exhibits excellent electrochemical performance. MACC-based electrolytes have significant cost advantages, but limited in practical application due to corrosion problems and long-term electrochemical conditioning. Although, high electrochemical window and high ionic conductivity have been exhibited in the $Mg(TFSI)_2$-based electrolyte, the overpotential of the magnesium deposition is too high because of the surface passivation layer, and the decomposition reaction of TFSI anions on the Mg anode interface requires further research and discussion.

1-6. Current Rechargeable Magnesium Battery Cathodes

1-6-1. Chevrel Phase Materials

The main structure of the Chevrel phase compound $Mg_xMo_3X_4$ (X = S, Se, Te) contains Mo_6S_8 blocks. Each block contains an octahedral cluster of the molybde-num atoms inside a cube of sulphur atoms. Aurbach et al. showed that Mg^{2+} can be inserted reversibly and with a relatively fast reaction rate in this compound, making it an excellent cathode material for Mg^{2+} storage.[89] The process of Mg^{2+} ions insertion into this cathode material takes place in two different stages, which relates to the occupation of the inner sites and the outer sites. (Figure 1-14).[47] The Chevrel phase Mo_6S_8 which synthesized from $Cu_2Mo_6S_8$ by acid leaching of copper,

shows good electrochemical performance, including long cycle life, good rate capability, and high discharge capacity.[90] However, only 60-80% of the Mg^{2+} ions are extracted from the Mo_6S_8 cathode during the initial charge stage because of the partial charge entrapment. Two approaches have been proposed by Kim's group for improving the Mg storage performance of Mo_6S_8.[91] As shown in Figure 1-15, by adding a composite of Cu nanoparticles and graphene, Cu reacts electrochemically with Mo_6S_8 to form $Cu_xMo_6S_8$. The higher rate capability leaded by the nano particles, as the smaller particles can provide shorter Mg^{2+} diffusion length, therefore, sub-micro size Chevrel phase shows higher discharge capability than micro size Chevrel phase materials. The increase in the discharge capacity of Mo_6S_8 and excellent cycling performance helped by the presence of nano-scale Cu crystallites. On the other hand, the particle size of the Chevrel phase Mo_6S_8 samples have been reduced by the mechanical milling.[92] Subsequently, the effects of interstitial vacancies and Mg ordering on the activity of Mo_6S_8 cathode have been reported from a thermodynamic point of view.[93]

1-6-2. Transition Metal Oxides

For high energy density lithium-ion batteries, oxides are widely used cathode material. The strong oxygen-metal bonding in oxides allows transition metal oxides to have high ionic properties, resulting in compounds with high anodic oxidation potentials. Compare with transition metal sulfides, oxides have many advantages such as, easy to prepare, relatively low cost and higher chemical stability. Transition metal oxides are widely studied as a cathode material in lithium-ion batteries, but only a small fraction of them are suitable to be used as cathode materials for rechargeable magnesium batteries. Because of the relative abundance and low cost of Manganese, the manganese dioxide become a particularly attractive candidate for cathode material. Although, many reports of experimental results on the intercalation of Mg^{2+} into MnO_2 have been reported, but the capacity fade still is the problem.[41] The phase behavior of the magnesium ions intercalation and de-intercalation in potassium-stabilized α-MnO_2 has

been investigated and found that during cycling ,a core-shell structure with MgO and an unreacted K-αMnO_2 core were formed together with the reduced of the manganese oxides on the surface.[94] Various MnO_2 samples synthesized with different physical parameters by Zhang et al, at the same time electrochemical performance have been stabilized in cells with APC electrolytes and magnesium metal as a anode.[95]

Spinel structural materials with the general formula AB_2O_4 are widely used as cathode materials. In the spinel structure, for cation, there are two different sites (tetrahedral and octahedral) to occupy, and the other octahedral sites are vacant. Recently, experimental and computational investigations of the Mg^{2+} intercalation/de-intercalation reaction in different spinel oxides such as $MgMn_2O_4$, $MgCo_2O_4$, and Co_3O_4 have been developed by Okamoto et al.[96] In order to facilitate the demagnesiation reaction, $Mg(TFSA)_2$/CsTFSA ionic liquid electrolytes have been utilized at150 ℃. The intercalation of Mg^{2+} was found to occur mainly through a process that the authors call "intercalation and pushout" where the Mg^{2+} inserted into vacant sites in the spinel structure, the cations at tetrahedral sites were pushed out to other octahedral vacant sites, resulting in a rocksalt structure (Figure 1-16). Although this process is reversible, it was found that as the amount of Mg^{2+} insertion increases, the entire structure changes to rock salt.

Vanadium oxides continue to attract significant attention as a potential intercalation cathode for Mg batteries, based on prior promising results, mainly with V_2O_5, especially when molecules of water are contained into the V_2O_5 structure and/or the hydrous electrolyte.[29, 32, 58, 97] Although V_2O_5 have high theoretical capacity and large spaces in the crystal structure, but the reversibility of this material is poor. The reversibility of the electrochemical cycling of V_2O_5 in Mg^{2+} containing electrolytes have been demonstrated by Novak et al.[98] The amount of water in the electrolyte correlate to the obtained capacity which contained water. Imamura et al. developed complex comprising V_2O_5 in xerogel state with acetylene black in acetone to obtain

V_2O_5/C complex and coated it onto nickel foam and indium tin oxide coated glass collectors. Those materials produced excellent cycling performance and discharge capacity.[99] The crystal structure of the V_2O_5 xerogel can be found in Figure 1-17.[100] There is a large space between the layer structure, in the different insertion sites for magnesium ions (site a and site b), two-step electrochemical reaction will occur.[101] V_2O_5 xerogel has shown high performance as a cathode material for magnesium secondary batteries, but it is not applicable to actual magnesium storage systems because of the tendency of passivation films to form on Mg metal surface due to the presence of water.[102] Subsequently, materials such as hollandite-type MnO_2 with large spacing also have been studied.[103]

1-6-3. Other Novel Magnesium Cathodes

Nanostructured materials may also be used as another approach to realize high-capacity cathode materials.[104-107] During the charge–discharge reactions, the guest cations undergo adsorption/desorption in nanosheet structures.

Polyanionic compounds with a three-dimensional network structure are composed of polyanions that have strong covalent bonds with transition metals.[108, 109] Polyanionic compounds have been the focus of attention in cathode research for lithium-ion batteries for the past 20 years because of their excellent cation diffusion, structural stability, and safety.[110] Among them, $LiFePO_4$ with olivine structure is the most widely used as a cathode for lithium-ion batteries. Such compounds have also been investigated as intercalation cathodes for magnesium-ion batteries. Olivine-type $MgMSiO_4$ (M = transition metal) has a considerable redox potential and theoretical capacity.[111, 112] The multivalent transition metals have a potential to reduce the structural damage during de-intercalation of the Mg^{2+} ions. Considering the advantages which we mentioned before, several nanoparticles with the short solid phase diffusion distance such as $MgMnSiO_4$,[113] $Mg_{1.03}Mn_{0.97}SiO_4$,[114] $MgFeSiO_4$,[83, 115] and 3D

heterogeneous porous $MgCoSiO_4$[116] were studied as potential Mg storage cathode materials in recent years. In particular, the silicate $MgFeSiO_4$ may facilitate the diffusion of Mg^{2+} in addition to its high safety and low cost. Its high theoretical capacity (~362.4 $mAhg^{-1}$) and relatively high intercalation voltage (~2.4 V vs Mg) result in a high theoretical energy density (~869 Wh kg^{-1}, ~2.549 Wh cm^{-3}). Compared to other intercalation cathodes (~77 Wh kg^{-1} and ~0.400 Wh cm^{-3} for Chevrel Mo_6S_8 and ~325 Wh kg^{-1} and ~1.188 Wh cm^{-3} for V_2O_5), the values are very high.[114, 117] Recently, Orikasa et al. found that a meta-stable phase of $MgFeSiO_4$, synthesized from the electrochemical ion exchange of Li_2FeSiO_4, exhibited improved electrode kinetics. In other words, $2Li^+$ extraction from Li_2FeSiO_4 followed by Mg^{2+} insertion generated $MgFeSiO_4$, demonstrated a high reversible capacity of over 300 $mAhg^{-1}$ at a voltage of about 2.4 V vs Mg, with good retention upon cycling (Figure 1-18).[83] In terms of capacity, voltage, and cycling characteristics, it can be said that the performance exceeds that of oxide cathodes, but these results were obtained at a slow rate of 1/50 C, and there are still issues in terms of rate characteristics.

1-7. Objective

Since a clear understanding of the reaction mechanism will provide useful information for the design of new electrolytes and cathode materials for the practical application of magnesium secondary batteries, therefore, the purpose of this study was to develop design guidelines for electrolytes and cathode materials for the practical application of magnesium secondary batteries. In recent years, high-performance electrolytes and cathode materials for magnesium secondary batteries have been developed, but the behavior of magnesium ions in the anode reaction process and phase transition behavior of magnesium ions in cathode materials have not been clarified. Therefore, for the electrolyte system, the coordination relationship between magnesium ions, anions and solvents in electrolytes was investigated

using Raman spectroscopy, operando soft X-ray absorption spectroscopy, DFT calculations and XPS. The electronic and local structures around magnesium ions and the reduction resistance of anions were analyzed to elucidate the reaction mechanism of the anode in magnesium secondary batteries. For the development of the next generation cathode materials, we focused on spinel-type structural oxides and investigated the phase transition mechanism associated with Mg insertion in the cathode materials by electrochemical measurements, X-ray absorption spectroscopy, and synchrotron X-ray diffraction.

1-8. Outline of the Present Thesis

The present thesis consists of seven chapters, which report the reaction mechanism at the anode/electrolyte interface and cathode materials for rechargeable magnesium batteries and provides new insight into the design of electrolytes and cathode materials in anticipation of practical application of rechargeable magnesium batteries.

In Chapter 1, the necessity of further improving the performance of secondary batteries from the viewpoint of energy and environmental issues have been discussed. As a background of the research, an overview of rechargeable batteries, magnesium-ion batteries, electrolytes and cathode materials was given. Finally, the purpose of this research which is to obtain design guidelines for electrolytes and cathode materials was summarized.

In Chapter 2, the determining factors and the polarization behavior of Mg^{2+} during Mg deposition process in $Mg(TFSA)_2$ and $Mg(BH_4)_2$ based electrolytes were analyzed. Firstly, the coordination structure of the magnesium ions in the bulk solution of each electrolyte analyzed by Raman spectroscopy. Subsequently, the dynamic change in the electronic and local structures of the magnesium ions near the anode surface in each electrolyte were examined using the *operando* SXAS technique. The reductive stability of each anion in these electrolytes was determined by DFT calculation. XPS measurements were conducted to clarify the decomposition action of these anions.

In Chapter 3, $Mg[B(HFIP)_4]_2$, having a weakly coordinating anion, was chosen as a model magnesium salt to demonstrate the potential for expanding the choice of the electrolyte solvent, and was compared with $Mg(TFSA)_2$. The electrochemical deposition of magnesium in $Mg[B(HFIP)_4]_2$-based and $Mg(TFSA)_2$-based electrolyte systems employing both triglyme and 2-MeTHF as solvents was comparatively evaluated. Focus was placed on the interactions among the magnesium ions, anions, and solvent during magnesium deposition, and the factors determining the polarization behavior were discussed.

In Chapter 4, the interaction between Mg^{2+} and anions was investigated in boron based electrolytes with different anion sizes to clarify the effect of anion species on Coulombic efficiency and polarization. The coordination structure of the magnesium ions in the bulk solution of each electrolyte was analyzed by Raman spectroscopy. The reductive stability and decomposition reaction of each anion was determined by DFT calculations and EIS.

In Chapter 5, detailed crystal structure analysis of magnesium insertion into spinel oxides was presented, and the details of the mechanism of the transition from the spinel layer to rock-salt layer were clarified. The crystal and valance changes in $MgMn_2O_4$ during Mg^{2+} insertion were investigated using XRD and XAS in order to elucidate the mechanism of the phase transition from spinel to rock-salt.

In Chapter 6, we focused on $ZnMn_2O_4$ and elucidated the phase transition reaction mechanism associated with Mg insertion. The suppression of the phase transition associated with large volume change in magnesium secondary battery cathode materials was found to be important for the improvement of spinel oxide electrochemical properties.

In Chapter 7, presents the conclusions from the current research and the future prospects for magnesium secondary batteries.

References

1. J. B. Goodenough and K.-S. Park, *J. Am. Chem. Soc.*, **2013**, 135, 1167-1176.
2. M. Armand and J.-M. Tarascon, *Nature*, **2008**, 451, 652-657.
3. B. Dunn, H. Kamath and J.-M. Tarascon, *Science*, **2011**, 334, 928-935.
4. K. Wang, K. Jiang, B. Chung, T. Ouchi, P. J. Burke, D. A. Boysen, D. J. Bradwell, H. Kim, U. Muecke and D. R. Sadoway, *Nature*, **2014**, 514, 348-350.
5. S. Chu, Y. Cui and N. Liu, *Nat. Mater.*, **2017**, 16, 16-22.
6. L. Nyholm, G. Nyström, A. Mihranyan and M. Strømme, *Adv. Mater.*, **2011**, 23, 3751-3769.
7. C. Grey and J. Tarascon, *Nat. Mater.*, **2017**, 16, 45-56.
8. J. Liu, M. Kunz, K. Chen, N. Tamura and T. J. Richardson, *J. Phys. Chem. Lett*, **2010**, 1, 2120-2123.
9. J. Nanda, J. Remillard, A. O'Neill, D. Bernardi, T. Ro, K. E. Nietering, J. Y. Go and T. J. Miller, *Adv. Funct. Mater.*, **2011**, 21, 3282-3290.
10. S. H. Ng, F. La Mantia and P. Novák, *Angew. Chem., Int. Ed.*, **2009**, 48, 528-532.
11. G. Ouvrard, M. Zerrouki, P. Soudan, B. Lestriez, C. Masquelier, M. Morcrette, S. Hamelet, S. Belin, A. M. Flank and F. Baudelet, *J. Power Sources*, **2013**, 229, 16-21.
12. R. Van Noorden, *Nature News*, **2014**, 507, 26.
13. Z. Gong and Y. Yang, *Energy Environ. Sci.*, **2011**, 4, 3223-3242.
14. R. Koksbang, J. Barker, H. Shi and M. Saidi, *Solid State Ionics*, **1996**, 84, 1-21.
15. G. Rousse and J. Tarascon, *Chem. Mater.*, **2014**, 26, 394-406.
16. A. K. Padhi, K. S. Nanjundaswamy and J. B. Goodenough, *J. Electrochem. Soc.*, **1997**, 144, 1188.
17. J. N. Reimers and J. Dahn, *J. Electrochem. Soc.*, **1992**, 139, 2091.
18. R. Malik, D. Burch, M. Bazant and G. Ceder, *Nano Lett.*, **2010**, 10, 4123-4127.

19. N. Meethong, H.-Y. S. Huang, W. C. Carter and Y.-M. Chiang, *ECS Solid State Lett.*, **2007**, 10, A134.

20. Y. Orikasa, T. Maeda, Y. Koyama, H. Murayama, K. Fukuda, H. Tanida, H. Arai, E. Matsubara, Y. Uchimoto and Z. Ogumi, *J. Am. Chem. Soc.*, **2013**, 135, 5497-5500.

21. Z. Ogumi, *Electrochemistry*, **2010**, 78, 319-324.

22. K. Xu and A. von Cresce, *J. Mater. Chem.*, **2011**, 21, 9849-9864.

23. A. Ponrouch, J. Bitenc, R. Dominko, N. Lindahl, P. Johansson and M. R. Palacin, *Energy Storage Mater*, **2019**, 20, 253-262.

24. G. Amatucci, F. Badway, A. Singhal, B. Beaudoin, G. Skandan, T. Bowmer, I. Plitz, N. Pereira, T. Chapman and R. Jaworski, *J. Electrochem. Soc.*, **2001**, 148, A940.

25. D. Aurbach, R. Skaletsky and Y. Gofer, *J. Electrochem. Soc.*, **1991**, 138, 3536.

26. M. Hayashi, H. Arai, H. Ohtsuka and Y. Sakurai, *ECS Solid State Lett.*, **2004**, 7, A119.

27. D. Le, S. Passerini, F. Coustier, J. Guo, T. Soderstrom, B. Owens and W. H. Smyrl, *Chem. Mater.*, **1998**, 10, 682-684.

28. R. Balasubramanian, A. Veluchamy and N. Venkatakrishnan, *J. Power Sources*, **1994**, 52, 305-308.

29. P. Bruce, F. Krok, P. Lightfoot, J. Nowinski and V. Gibson, *Solid State Ionics*, **1992**, 53, 351-355.

30. A. Brenner, *J. Electrochem. Soc.*, **1996**, 143, 3133.

31. P. Novák, W. Scheifele and O. Haas, *J. Power Sources*, **1995**, 54, 479-482.

32. J. Pereira-Ramos, R. Messina and J. Perichon, *J. Electroanal. Chem.*, **1987**, 218, 241-249.

33. J. O. Besenhard and M. Winter, *ChemPhysChem*, **2002**, 3, 155-159.

34. X. Zhao, Z. Zhao‐Karger, M. Fichtner and X. Shen, *Angew. Chem., Int. Ed.*, **2020**, 59, 5902-5949.

35. F. Liu, T. Wang, X. Liu and L. Z. Fan, *Adv. Energy Mater.*, **2020**, 2000787.

36. P. Wang and M. R. Buchmeiser, *Adv. Funct. Mater.*, **2019**, 29, 1905248.

37. J. Muldoon, C. B. Bucur and T. Gregory, *Angew. Chem., Int. Ed.*, **2017**, 56, 12064-12084.

38. N. N. Rajput, T. J. Seguin, B. M. Wood, X. Qu and K. A. Persson, in *Modeling Electrochemical Energy Storage at the Atomic Scale*, Springer, 2018, pp. 79-124.

39. Z. Lu, A. Schechter, D. Aurbach, *J Electroanal Chem*, **1999**, 466, 203-217.

40. C. B. Bucur, T. Gregory and J. Muldoon, in *Rechargeable Batteries*, Springer, 2015, pp. 611-635.

41. C. B. Bucur, T. Gregory, A. G. Oliver and J. Muldoon, *J. Phys. Chem. Lett*, **2015**, 6, 3578-3591.

42. F. Murgia, E. T. Weldekidan, L. Stievano, L. Monconduit and R. Berthelot, *Electrochem. commun*, **2015**, 60, 56-59.

43. K. Periyapperuma, T. T. Tran, M. Purcell and M. Obrovac, *Electrochim Acta*, **2015**, 165, 162-165.

44. Y. Shao, M. Gu, X. Li, Z. Nie, P. Zuo, G. Li, T. Liu, J. Xiao, Y. Cheng and C. Wang, *Nano Lett.*, **2014**, 14, 255-260.

45. N. Singh, T. S. Arthur, C. Ling, M. Matsui and F. Mizuno, *Chem. Commun.*, **2013**, 49, 149-151.

46. E. Levi, M. Levi, O. Chasid and D. Aurbach, *J. Electroceramics*, **2009**, 22, 13-19.

47. D. Aurbach, Z. Lu, A. Schechter, Y. Gofer, H. Gizbar, R. Turgeman, Y. Cohen, M. Moshkovich and E. Levi, *Nature*, **2000**, 407, 724-727.

48. D. Aurbach, G. S. Suresh, E. Levi, A. Mitelman, O. Mizrahi, O. Chusid and M. Brunelli, *Adv. Mater.*, **2007**, 19, 4260-4267.

49. N. Pour, Y. Gofer, D. T. Major and D. Aurbach, *J. Am. Chem. Soc.*, **2011**, 133, 6270-6278.

50. R. Attias, M. Salama, B. Hirsch, Y. Goffer and D. Aurbach, *Joule*, **2019**, 3, 27-52.

51. F.-f. Wang, Y.-s. Guo, J. Yang, Y. Nuli and S.-i. Hirano, *Chem. Commun.*, **2012**, 48, 10763-10765.

52. Q. S. Zhao, Y. N. NuLi, Y. S. Guo, J. Yang and J. L. Wang, *Electrochim Acta*, **2011**, 56, 6530-6535.

53. N. Yoshimoto, M. Matsumoto, M. Egashia and M. Morita, *J. Power Sources*, **2010**, 195, 2096-2098.

54. B. Lee, J.-H. Cho, H. R. Seo, S. B. Na, J. H. Kim, B. W. Cho, T. Yim and S. H. Oh, *J. Mater. Chem. A*, **2018**, 6, 3126-3133.

55. D. Aurbach, H. Gizbar, A. Schechter, O. Chusid, H. E. Gottlieb, Y. Gofer and I. Goldberg, *J. Electrochem. Soc.*, **2001**, 149, A115.

56. H. Gizbar, Y. Vestfrid, O. Chusid, Y. Gofer, H. E. Gottlieb, V. Marks and D. Aurbach, *Organometallics*, **2004**, 23, 3826-3831.

57. Y. Nakayama, Y. Kudo, H. Oki, K. Yamamoto, Y. Kitajima and K. Noda, *J. Electrochem. Soc.*, **2008**, 155, A754.

58. T. D. Gregory, R. J. Hoffman and R. C. Winterton, *J. Electrochem. Soc.*, **1990**, 137, 775.

59. R. Mohtadi, M. Matsui, T. S. Arthur and S. J. Hwang, *Angew. Chem., Int. Ed.*, **2012**, 124, 9918-9921.

60. Y. Shao, T. Liu, G. Li, M. Gu, Z. Nie, M. Engelhard, J. Xiao, D. Lv, C. Wang and J.-G. Zhang, *Sci. Rep.*, **2013**, 3, 1-7.

61. F. Tuerxun, Y. Abulizi, Y. NuLi, S. Su, J. Yang and J. Wang, *J. Power Sources*, **2015**, 276, 255-261.

62. S. Su, Y. NuLi, N. Wang, D. Yusipu, J. Yang and J. Wang, *J. Electrochem. Soc.*, **2016**, 163, D682.

63. H. Xu, Z. Zhang, J. Li, L. Qiao, C. Lu, K. Tang, S. Dong, J. Ma, Y. Liu and X. Zhou, *ACS Appl. Mater. Interfaces*, **2018**, 10, 23757-23765.

64. O. Tutusaus, R. Mohtadi, T. S. Arthur, F. Mizuno, E. G. Nelson and Y. V. Sevryugina, *Angew. Chem., Int. Ed.*, **2015**, 127, 8011-8015.

65. S. G. McArthur, R. Jay, L. Geng, J. Guo and V. Lavallo, *Chem. Commun.*, **2017**, 53, 4453-4456.

66. N. T. Hahn, T. J. Seguin, K.-C. Lau, C. Liao, B. J. Ingram, K. A. Persson and K. R. Zavadil, *J. Am. Chem. Soc.*, **2018**, 140, 11076-11084.

67. Z. Zhao-Karger, M. E. G. Bardaji, O. Fuhr and M. Fichtner, *J. Mater. Chem. A*, **2017**, 5, 10815-10820.

68. Z. Zhang, Z. Cui, L. Qiao, J. Guan, H. Xu, X. Wang, P. Hu, H. Du, S. Li and X. Zhou, *Adv. Energy Mater.*, **2017**, 7, 1602055.

69. H. Xu, Z. Zhang, Z. Cui, A. Du, C. Lu, S. Dong, J. Ma, X. Zhou and G. Cui, *Electrochem. commun*, **2017**, 83, 72-76.

70. A. Du, Z. Zhang, H. Qu, Z. Cui, L. Qiao, L. Wang, J. Chai, T. Lu, S. Dong and T. Dong, *Energy Environ. Sci.*, **2017**, 10, 2616-2625.

71. T. Liu, Y. Shao, G. Li, M. Gu, J. Hu, S. Xu, Z. Nie, X. Chen, C. Wang and J. Liu, *J. Mater. Chem. A*, **2014**, 2, 3430-3438.

72. R. E. Doe, R. Han, J. Hwang, A. J. Gmitter, I. Shterenberg, H. D. Yoo, N. Pour and D. Aurbach, *Chem. Commun.*, **2014**, 50, 243-245.

73. K. A. See, K. W. Chapman, L. Zhu, K. M. Wiaderek, O. J. Borkiewicz, C. J. Barile, P. J. Chupas and A. A. Gewirth, *J. Am. Chem. Soc.*, **2016**, 138, 328-337.

74. J. Luo, S. He and T. L. Liu, *ACS Energy Lett.*, **2017**, 2, 1197-1202.

75. S. S. Kim, S. C. Bevilacqua and K. A. See, *ACS Appl. Mater. Interfaces*, **2019**, 12, 5226-5233.

76. Y. He, Q. Li, L. Yang, C. Yang and D. Xu, *Angew. Chem., Int. Ed.*, **2019**, 131, 7697-7701.

77. J. H. Ha, B. Adams, J.-H. Cho, V. Duffort, J. H. Kim, K. Y. Chung, B. W. Cho, L. F. Nazar and S. H. Oh, *J. Mater. Chem. A*, **2016**, 4, 7160-7164.

78. H. S. Kim, T. S. Arthur, G. D. Allred, J. Zajicek, J. G. Newman, A. E. Rodnyansky, A. G. Oliver, W. C. Boggess and J. Muldoon, *Nat. Commun.*, **2011**, 2, 1-6.

79. B. Vinayan, Z. Zhao-Karger, T. Diemant, V. S. K. Chakravadhanula, N. I. Schwarzburger, M. A. Cambaz, R. J. Behm, C. Kübel and M. Fichtner, *Nanoscale*, **2016**, 8, 3296-3306.

80. Z. Zhao‐Karger, X. Zhao, D. Wang, T. Diemant, R. J. Behm and M. Fichtner, *Adv. Energy Mater.*, **2015**, 5, 1401155.

81. S.-Y. Ha, Y.-W. Lee, S. W. Woo, B. Koo, J.-S. Kim, J. Cho, K. T. Lee and N.-S. Choi, *ACS Appl. Mater. Interfaces*, **2014**, 6, 4063-4073.

82. H. Kuwata, M. Matsui and N. Imanishi, *J. Electrochem. Soc.*, **2017**, 164, A3229.

83. Y. Orikasa, T. Masese, Y. Koyama, T. Mori, M. Hattori, K. Yamamoto, T. Okado, Z.-D. Huang, T. Minato and C. Tassel, *Sci. Rep.*, **2014**, 4, 5622.

84. T. Fukutsuka, K. Asaka, A. Inoo, R. Yasui, K. Miyazaki, T. Abe, K. Nishio and Y. Uchimoto, *Chem. Lett.*, **2014**, 43, 1788-1790.

85. T. Watkins, A. Kumar and D. A. Buttry, *J. Am. Chem. Soc.*, **2016**, 138, 641-650.

86. W. A. Henderson, *J. Phys. Chem. B*, **2006**, 110, 13177-13183.

87. N. Sa, B. Pan, A. Saha-Shah, A. A. Hubaud, J. T. Vaughey, L. A. Baker, C. Liao and A. K. Burrell, *ACS Appl. Mater. Interfaces*, **2016**, 8, 16002-16008.

88. Z. Ma, M. Kar, C. Xiao, M. Forsyth and D. R. MacFarlane, *Electrochem. commun*, **2017**, 78, 29-32.

89. E. Levi, G. Gershinsky, D. Aurbach, O. Isnard and G. Ceder, *Chem. Mater.*, **2009**, 21, 1390-1399.

90. P. Saha, P. H. Jampani, M. K. Datta, C. U. Okoli, A. Manivannan and P. N. Kumta, *J. Electrochem. Soc.*, **2014**, 161, A593.

91. S.-H. Choi, J.-S. Kim, S.-G. Woo, W. Cho, S. Y. Choi, J. Choi, K.-T. Lee, M.-S. Park and Y.-J. Kim, *ACS Appl. Mater. Interfaces*, **2015**, 7, 7016-7024.

92. W. Cho, B. Moon, S. G. Woo, J. H. Kim, M. S. Park, J. S. Kim, H. Kim and Y. J. Kim, *Bull. Korean Chem. Soc.*, **2015**, 36, 1209-1214.

93. C. Ling and K. Suto, *Chem. Mater.*, **2017**, 29, 3731-3739.

94. T. S. Arthur, R. Zhang, C. Ling, P.-A. Glans, X. Fan, J. Guo and F. Mizuno, *ACS Appl. Mater. Interfaces*, **2014**, 6, 7004-7008.

95. R. Zhang, T. S. Arthur, C. Ling and F. Mizuno, *J. Power Sources*, **2015**, 282, 630-638.

96. S. Okamoto, T. Ichitsubo, T. Kawaguchi, Y. Kumagai, F. Oba, S. Yagi, K. Shimokawa, N. Goto, T. Doi and E. Matsubara, *Adv. Sci.*, **2015**, 2, 1500072.

97. P. Novák, W. Scheifele, F. Joho and O. Haas, *J. Electrochem. Soc.*, **1995**, 142, 2544.

98. E. Levi, Y. Gofer and D. Aurbach, *Chem. Mater.*, **2010**, 22, 860-868.

99. D. Imamura, M. Miyayama, M. Hibino and T. Kudo, *J. Electrochem. Soc.*, **2003**, 150, A753.

100. M. Hibino, M. Ugaji, A. Kishimoto and T. Kudo, *Solid State Ionics*, **1995**, 79, 239-244.

101. D. Imamura and M. Miyayama, *Solid State Ionics*, **2003**, 161, 173-180.

102. D. Aurbach, Y. Gofer, A. Schechter, O. Chusid, H. Gizbar, Y. Cohen, M. Moshkovich and R. Turgeman, *J. Power Sources*, **2001**, 97, 269-273.

103. R. Zhang, X. Yu, K.-W. Nam, C. Ling, T. S. Arthur, W. Song, A. M. Knapp, S. N. Ehrlich, X.-Q. Yang and M. Matsui, *Electrochem. commun*, **2012**, 23, 110-113.

104. S. Yang, D. Li, T. Zhang, Z. Tao and J. Chen, *J. Phys. Chem. C*, **2012**, 116, 1307-1312.

105. Y. Liang, H. D. Yoo, Y. Li, J. Shuai, H. A. Calderon, F. C. Robles Hernandez, L. C. Grabow and Y. Yao, *Nano Lett.*, **2015**, 15, 2194-2202.

106. Y. Liu, L. Jiao, Q. Wu, J. Du, Y. Zhao, Y. Si, Y. Wang and H. Yuan, *J. Mater. Chem. A*, **2013**, 1, 5822-5826.

107. Y. Liu, L. Jiao, Q. Wu, Y. Zhao, K. Cao, H. Liu, Y. Wang and H. Yuan, *Nanoscale*, **2013**, 5, 9562-9567.

108. M. Thackeray, L. De Picciotto, A. De Kock, P. Johnson, V. Nicholas and K. Adendorff, *J. Power Sources*, **1987**, 21, 1-8.

109. M. Thackeray and A. De Kock, *J. Solid State Chem.*, **1988**, 74, 414-418.

110. L. Sánchez and J.-P. Pereira-Ramos, *J. Mater. Chem.*, **1997**, 7, 471-473.

111. C. Kim, P. J. Phillips, B. Key, T. Yi, D. Nordlund, Y. S. Yu, R. D. Bayliss, S. D. Han, M. He and Z. Zhang, *Adv. Mater.*, **2015**, 27, 3377-3384.

112. C. Yuan, Y. Zhang, Y. Pan, X. Liu, G. Wang and D. Cao, *Electrochim Acta*, **2014**, 116, 404-412.

113. T. Mori, T. Masese, Y. Orikasa, Z.-D. Huang, T. Okado, J. Kim and Y. Uchimoto, *Phys. Chem. Chem. Phys.*, **2016**, 18, 13524-13529.

114. Z. Feng, J. Yang, Y. NuLi and J. Wang, *J. Power Sources*, **2008**, 184, 604-609.

115. J. Heath, H. Chen and M. S. Islam, *J. Mater. Chem. A*, **2017**, 5, 13161-13167.

116. Y. Zheng, Y. NuLi, Q. Chen, J. Yang and J. Wang, *Electrochim Acta*, **2012**, 66, 75-81.

117. Z. Feng, J. Yang, Y. NuLi, J. Wang, X. Wang and Z. Wang, *Electrochem. commun*, **2008**, 10, 1291-1294.

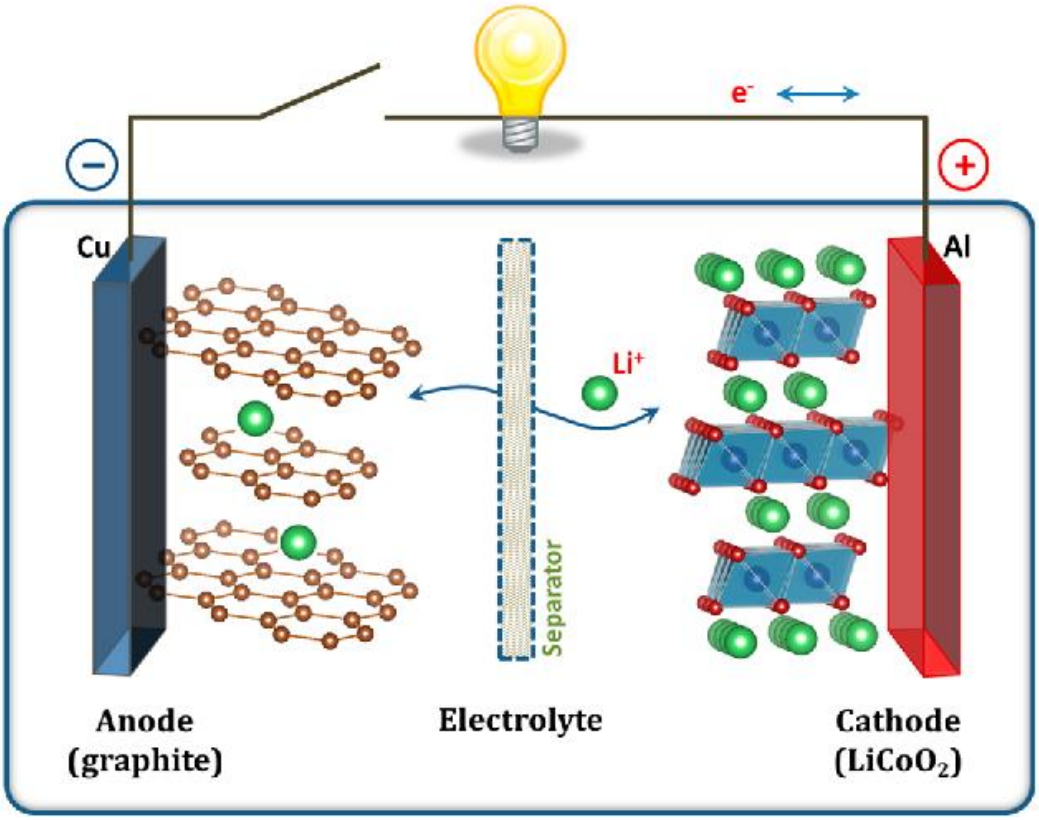

Figure. 1-1 Schematic figure of lithium-ion rechargeable battery.[1]

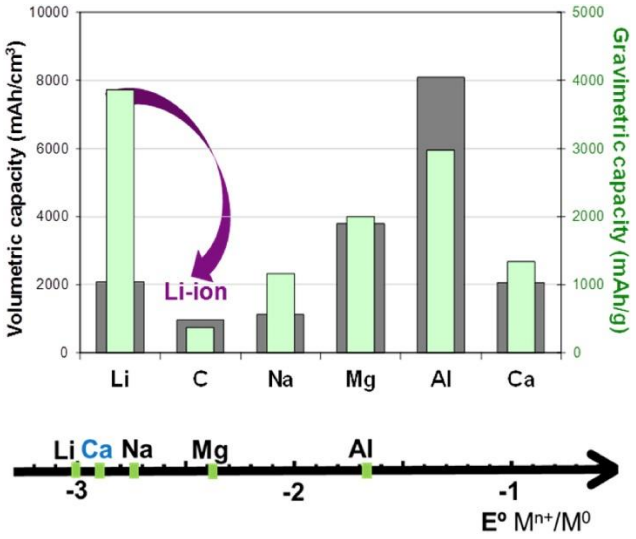

Figure. 1-2 Standard reduction potential and gravimetric/volumetric capacities of metal electrodes compared to values for graphite, typically used in the Li-ion technology.[23]

Table 1-1. The comparison of various metal negative electrodes.

Metal	Atomic weight	Valence change	Theoretical capacity [$mAhg^{-1}$, $mAhcm^{-3}$]	Electrode potential [V vs. SHE]	Terrestrial abundance	Melting Point (°C)
Li	6.94	1	3862, 2062	-3.05	0.01	180.5
K	39.09	1	685, 587	-2.93	2.40	63.7
Na	22.99	1	1166, 1132	-2.71	2.64	97.7
Ca	40.08	2	1337, 2073	-2.87	3.39	842
Mg	24.31	2	2205, 3837	-2.38	1.94	650
Al	26.98	3	2980, 8043	-1.66	7.56	660

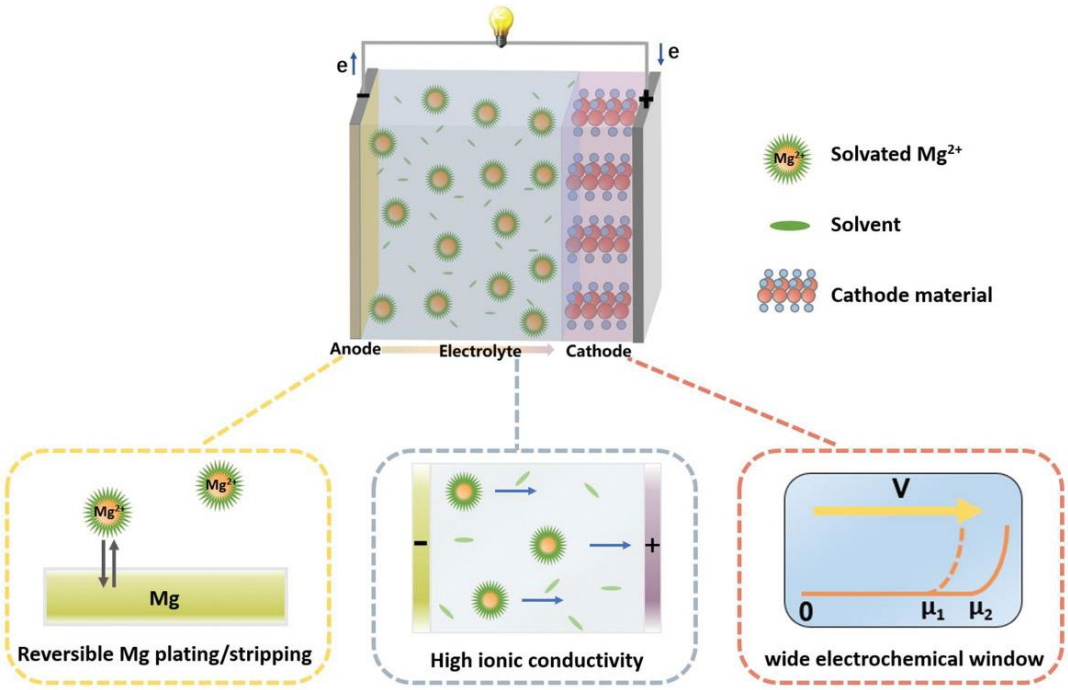

Figure. 1-3 Schematic illustration of main prerequisites for rechargeable magnesium battery electrolytes. [35]

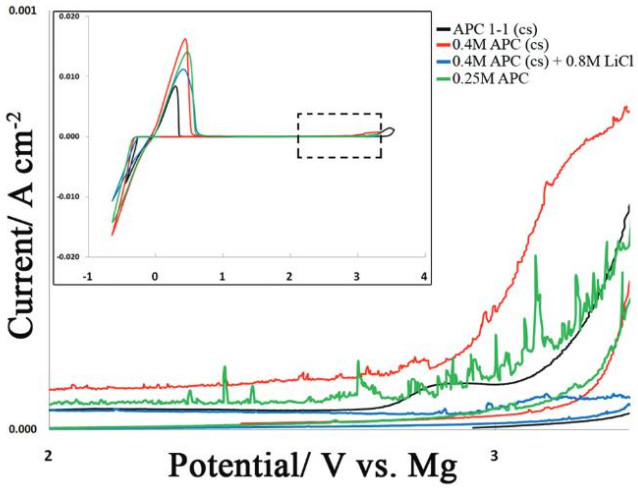

Figure. 1-4. Cyclic voltammetry of APC electrolytes.[49]

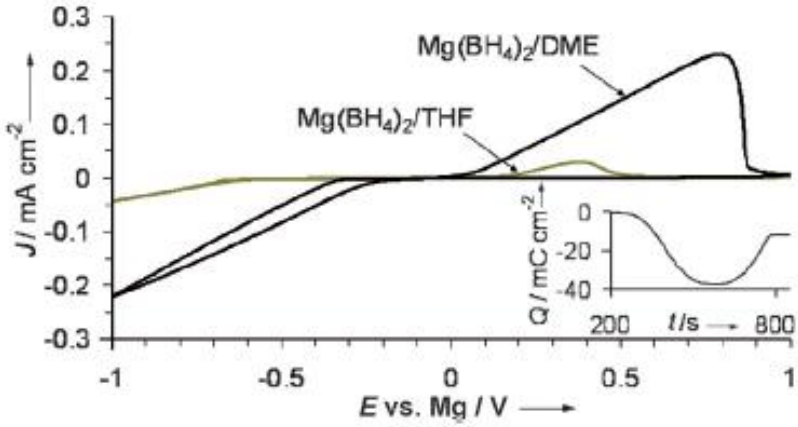

Figure. 1-5. Cyclic voltammetry of $Mg(BH_4)_2$/glyme and $Mg(BH_4)_2$/THF electrolytes.[59]

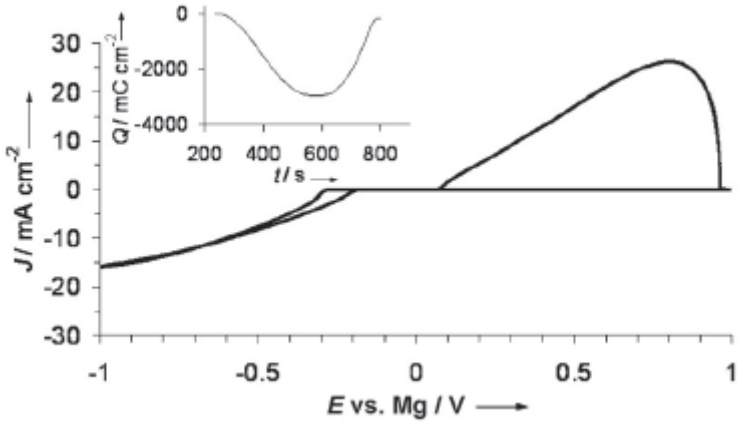

Figure. 1-6. Cyclic voltammetry of $LiBH_4/Mg(BH_4)_2$ in glyme.[60]

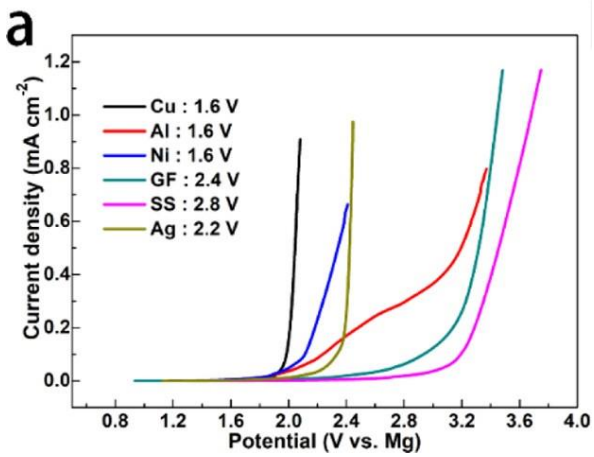

Figure. 1-7. LSV of the 0.5 M $Mg(BH_4)_2$/1.0 M THFPB-DGM electrolyte on different working electrodes.[63]

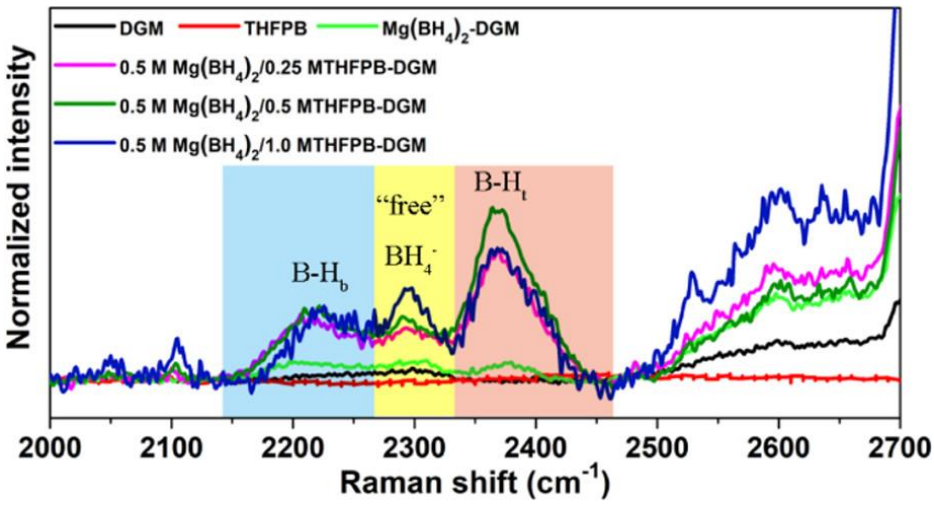

Figure. 1-8. Raman spectra in the B–H stretching region for DGM, THFPB, 0.1 M $Mg(BH_4)_2$ in DGM.[63]

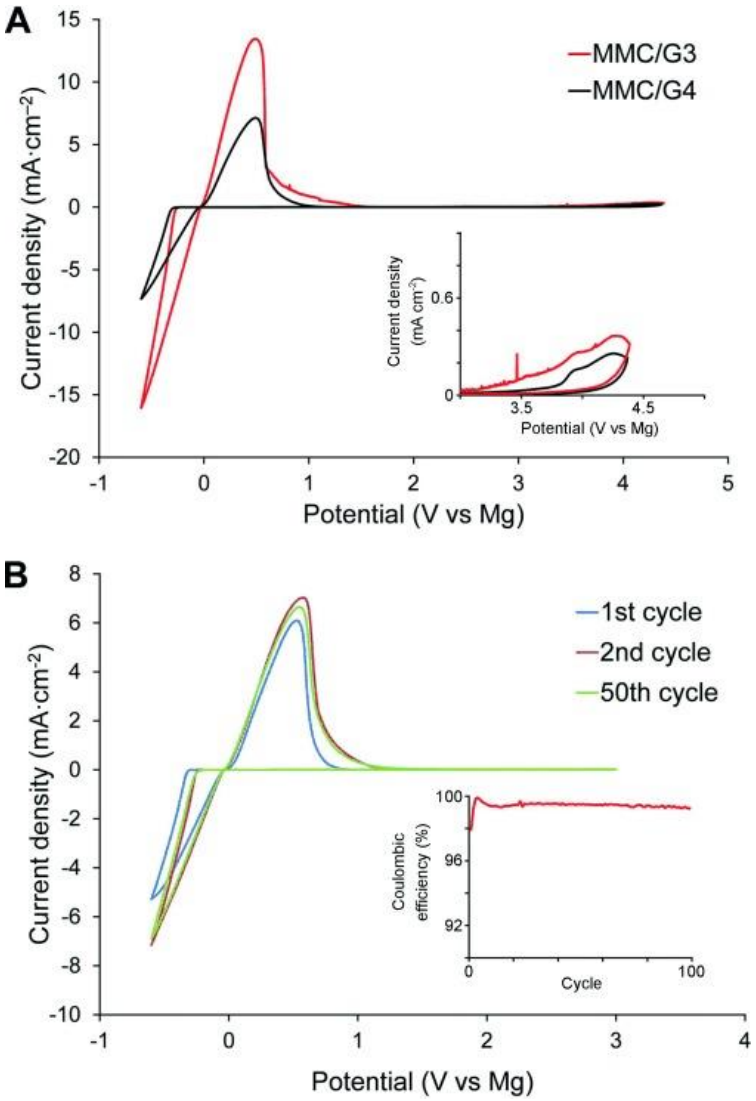

Figure. 1-9. (A) First cyclic voltammetry test of 0.75 M MMC/G3 and 0.75 M MMC/G4 on Pt electrode. (B) Selected cyclic voltammograms of 0.75 M MMC/G4 electrolyte on Pt electrode.[64]

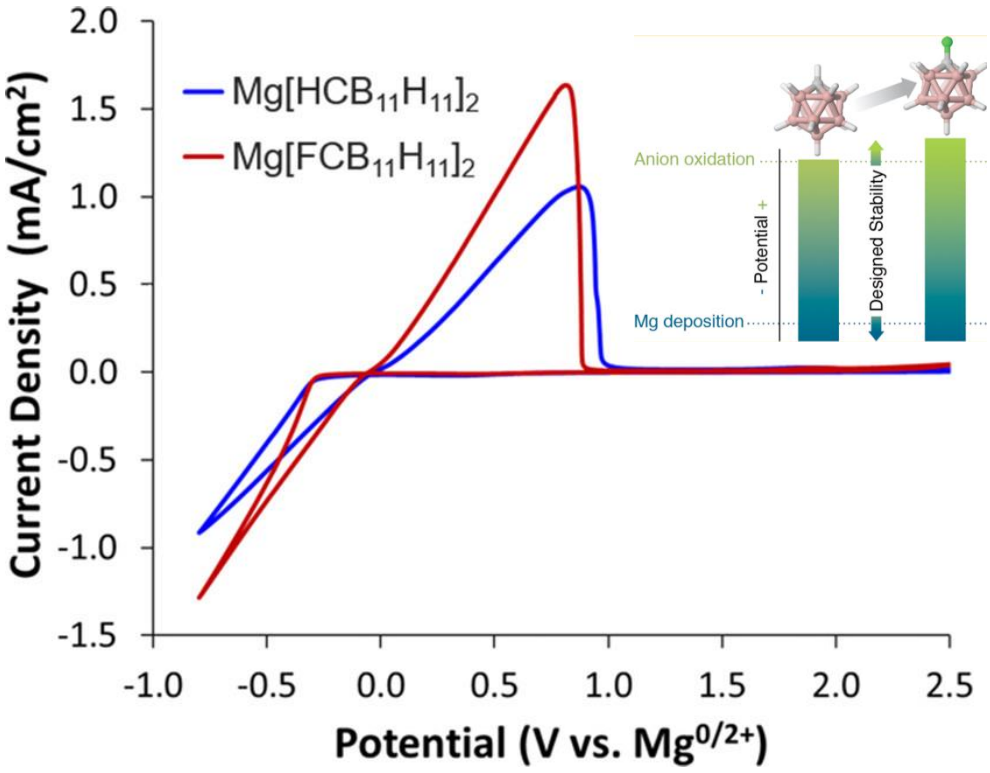

Figure. 1-10. Cyclic voltammetry of $Mg[HCB_{11}H_{11}]_2$ and $Mg[FCB_{11}H_{11}]_2$ in G3.[66]

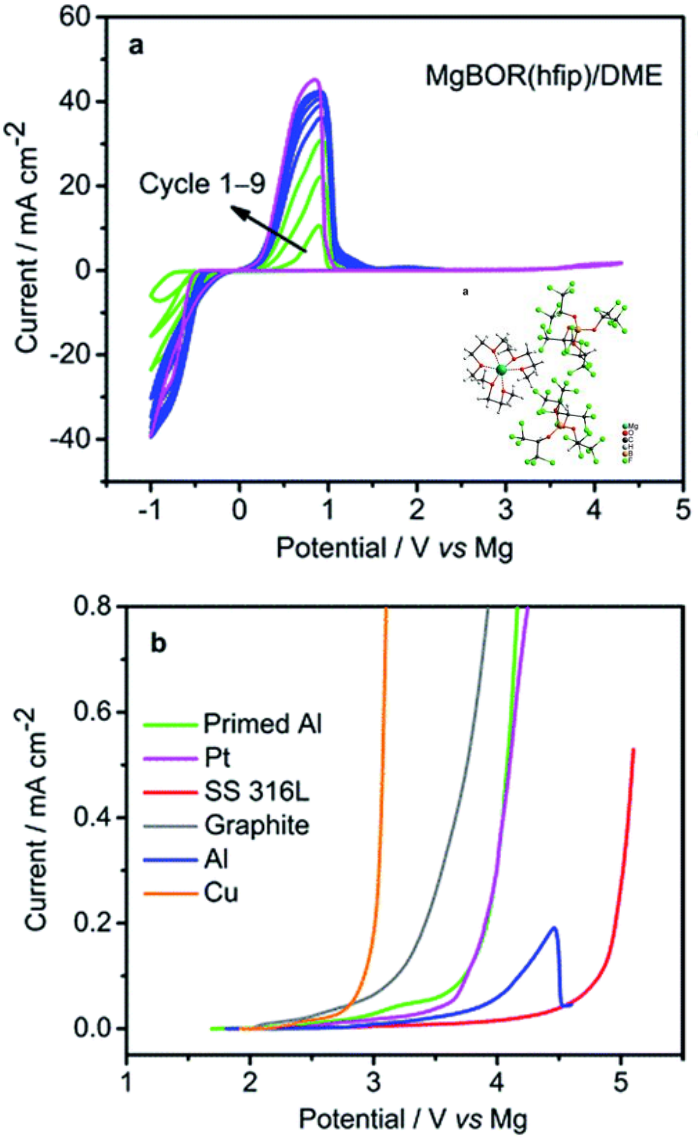

Figure. 1-11. (a) Cyclic voltammograms of MgBOR(hfip)/DME using Pt as the working electrode and Mg as the reference. (b) linear sweep voltammograms of various electrodes.[67]

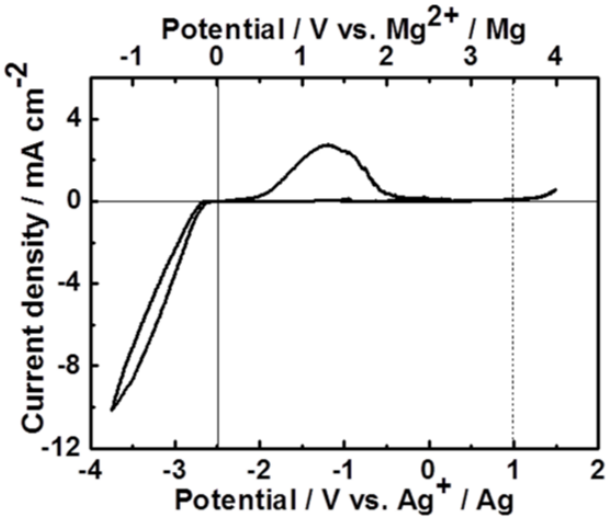

Figure. 1-12. Cyclic voltammogram for 0.5 M $Mg(TFSA)_2$ in triglyme on a Pt electrode.[83]

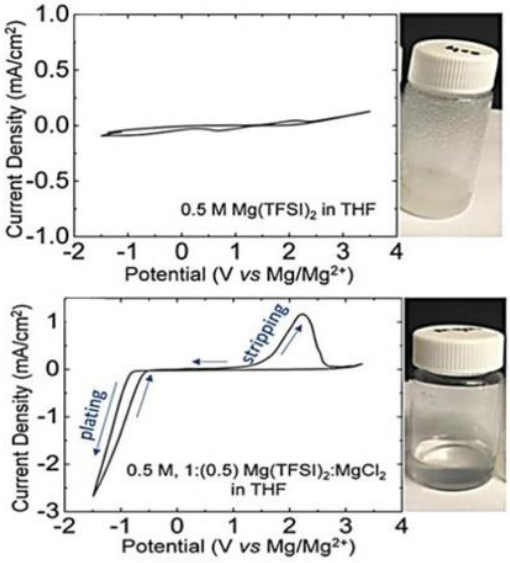

Figure. 1-13. Cyclic voltammogram and optical images of $Mg(TFSI)_2$ - based electrolyte.[87]

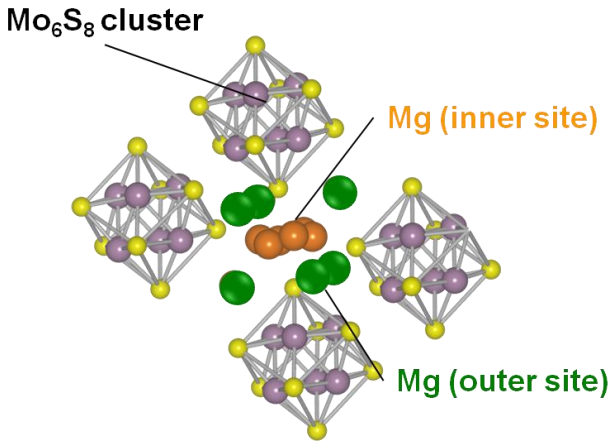

Figure. 1-14. Crystal structure of the chevrel $Mg_2Mo_6S_8$ phase. Green, orange, purple, and yellow spheres are indicated Mg (outer site), Mg (inner site), Mo, and S atoms, respectively.[47]

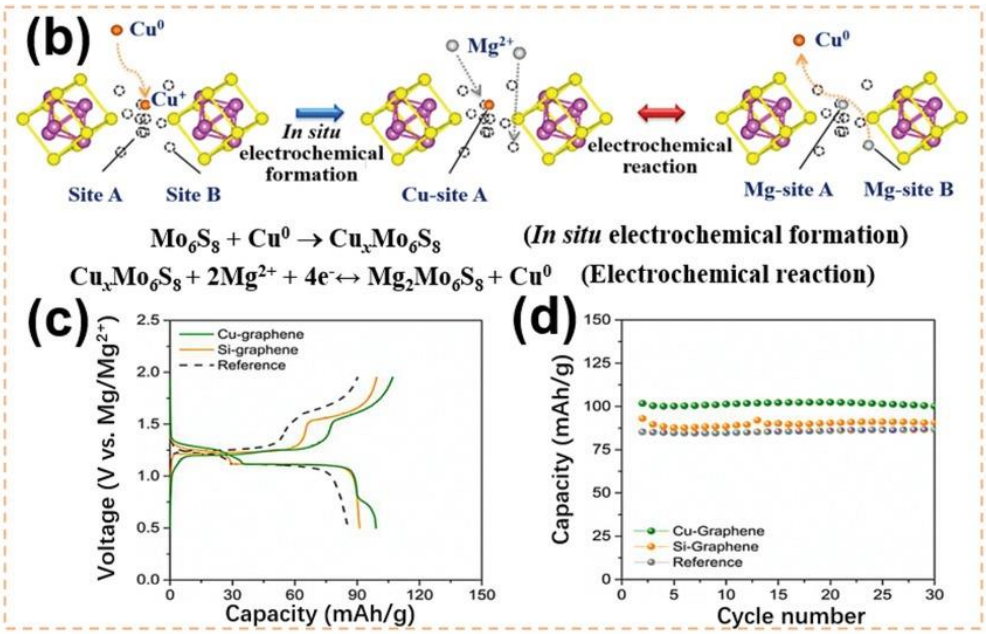

Figure. 1-15. Schematics and charge/discharge curves of Cu replacement reaction in the Mo_6S_8 during Mg^{2+} insertion and extraction. [35]

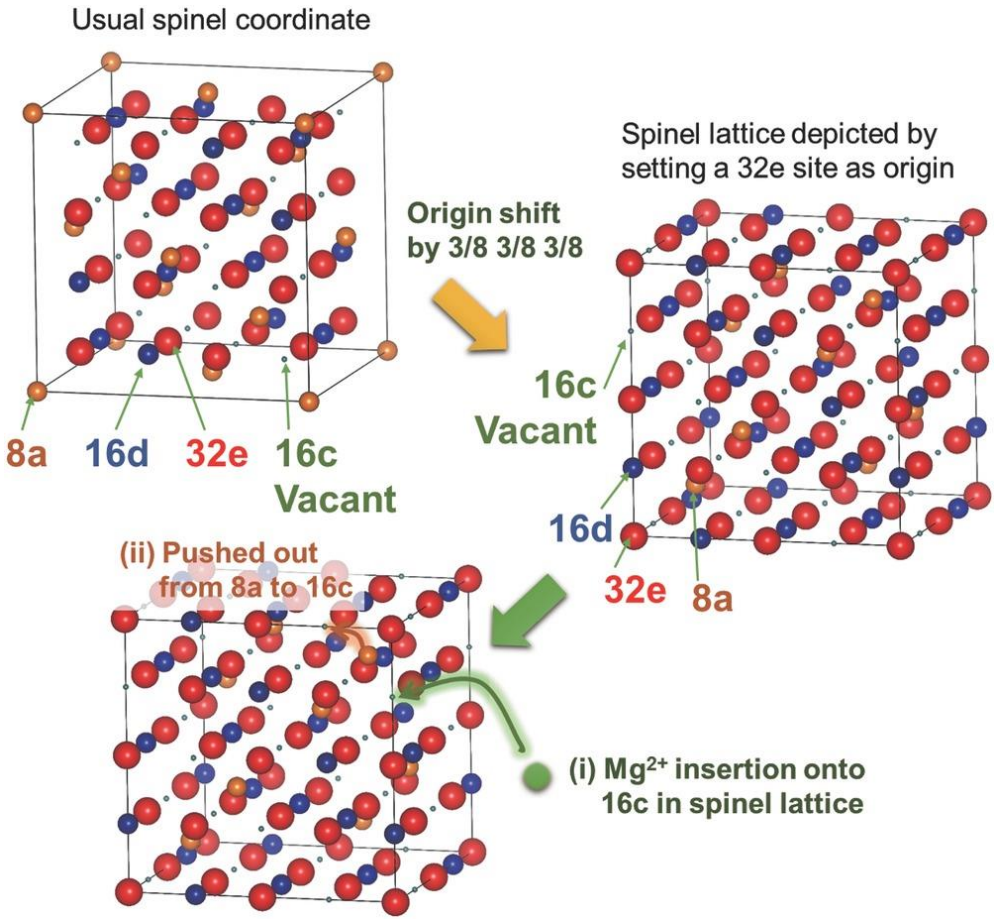

Figure. 1-16. Schematic illustration showing the cation insertion process. The upper left structure is drawn in the usual spinel coordinate, whereas the right is depicted by setting a 32e site (Wyckoff position) for oxygen in the space group No. 227 as origin. After a Mg cation is inserted into a 16c site in the spinel (left lower) structure, the original cation located in its neighboring 8a site moves to an adjacent 16c site due to the repulsion between the cations.[96]

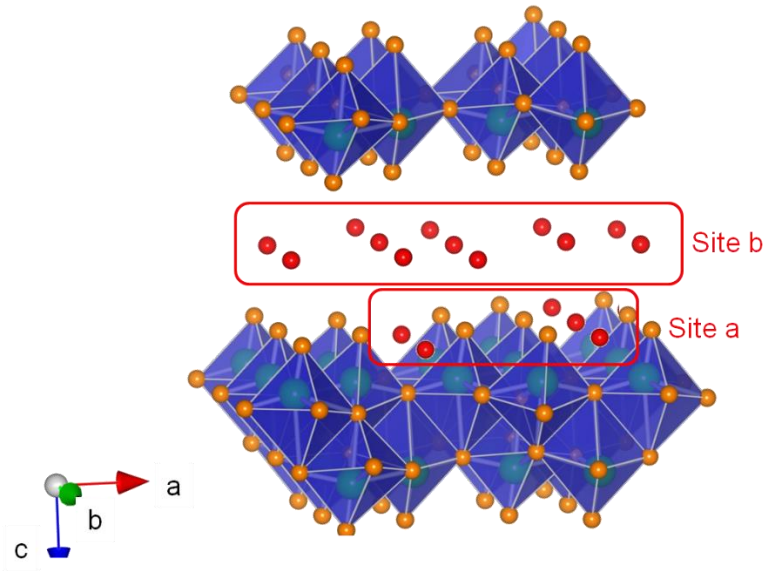

Figure. 1-17. Crystal structure of the V_2O_5 aero-gel. Green, orange, and yellow spheres are indicated V, O (1), and O (2) atoms, respectively.[100]

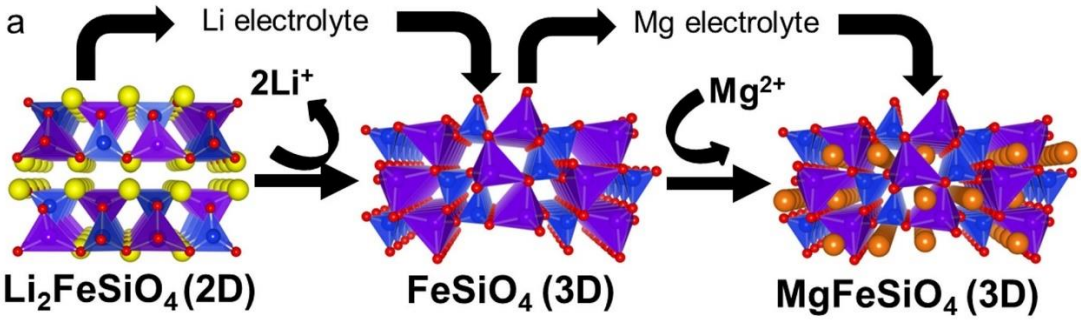

Figure.1-18. Schematic illustration of the ion-exchange methodology for the electrochemical synthesis of $MgFeSiO_4$ from Li_2FeSiO_4.[83]

Chapter 2. Determining Factor on Polarization Behavior of Magnesium Deposition for Magnesium Battery Anode

2-1. Introduction

Magnesium rechargeable batteries using magnesium as the anode are candidates for next-generation battery systems.[1-10] Magnesium has a high theoretical volumetric capacity (3832 mAh/cm^3) and a relatively low reduction potential (-2.38 V vs. SHE); thus, magnesium batteries generate a high energy density. Moreover, the safety and cost of magnesium make it superior to lithium.[4-6] These favorable properties of magnesium make magnesium rechargeable batteries attractive. However, magnesium rechargeable batteries have many challenges hindering practical applications. One major problem is the difficulty associated with reversible magnesium deposition/dissolution reactions at the anode/electrolyte interface. The electrolyte containing an inorganic salt and carbonate solvent, which is normally used in lithium-ion batteries, cannot be used for the magnesium metal deposition because the passivation film formed on the anode surface inhibits the passage of magnesium ions.[8] Therefore, many researchers have focused on highly active magnesium organohaloaluminate-based electrolytes, which support reversible magnesium deposition/dissolution reactions.[9-15] However, these electrolytes have some disadvantages, such as their low anodic stability, corrosion, and safety; thus, a breakthrough in the development of suitable electrolytes is necessary.

Recently, it was reported that reversible magnesium deposition/dissolution reactions can occur in certain electrolytes, including our group.[16-23] Among them, magnesium bis(trifluoromethanesulfonyl)amide ($Mg(TFSA)_2$)/triglyme and magnesium

borohydride ($Mg(BH_4)_2$)/tetrahydrofuran (THF) electrolytes can provide rechargeable magnesium batteries with high energy densities, without corrosion.[20,16] However, the reason for the occurrence of reversible magnesium deposition/dissolution reactions in these electrolytes has not been clearly elucidated. A clear understanding of the reaction mechanism will provide useful information to design new electrolyte materials applicable to practical magnesium rechargeable batteries.

The key factor that predominates the reaction mechanism is considered as the coordination structures of the magnesium ions at the interface between the anode. It is necessary to understand the differences between the coordination structures in the electrochemically active $Mg(TFSA)_2$/triglyme and/or $Mg(BH_4)_2$/THF electrolytes, and those of other electrolytes in which the magnesium deposition/dissolution reactions do not occur. Raman spectroscopy and X-ray absorption spectroscopy (XAS) are useful techniques for clarifying the coordination structures present in these electrolytes. Recently, a new soft XAS technique employed during the magnesium deposition process (*operando* SXAS) has been developed and applied to examine the interfacial behavior of magnesium electrolytes.[24-27] *Operando* SXAS is a powerful tool for analyzing the dynamic change in the local structure of magnesium ions. The combination of these characterization techniques, *operando* soft X-ray absorption spectroscopy, Raman spectroscopy, electrochemical impedance spectroscopy (EIS), X-ray photoelectron spectroscopy (XPS), and density functional theory (DFT) calculation, should provide a powerful method for elucidating the mechanism of Mg metal deposition. We have clarified the formation process of Mg alloy using the combination of these methods.

In this study, we elucidate the determining factor on the polarization behavior for three different electrolytes: $Mg(TFSA)_2$/triglyme, $Mg(BH_4)_2$/tetrahydrofuran (THF), and $Mg(TFSA)_2$/2-methyltetrahydrofuran (2-MeTHF), using the above-mentioned characterization methods. The former two electrolytes allow quasi-reversible magnesium deposition/dissolution, while the latter is inactive electrochemically. First, we analyzed the coordination structure of the magnesium ions in the bulk solution of each electrolyte by Raman spectroscopy. Subsequently, we examined the dynamic change in the electronic and local structures of the magnesium ions near the anode surface in each electrolyte using the *operando* SXAS technique. The reductive stability of each anion in these electrolytes was determined by DFT calculation. To clarify the decomposition action of these anions, we conducted XPS measurements.

2-2. Experimental

2.2.1. Material preparation

The 0.5 M $Mg(TFSA)_2$/triglyme and 0.5 M $Mg(TFSA)_2$/2-MeTHF electrolytes were prepared by mixing $Mg(TFSA)_2$ (KISHIDA CHEMICAL Co., Ltd., 99.9%>) with triglyme (KISHIDA CHEMICAL Co., Ltd. 99%>) or 2-MeTHF (Merck, 98%>) in an Ar-filled glove box. To decrease the water content, the $Mg(TFSA)_2$ salt was dried under vacuum at 180 °C for 48 h. The 0.5 M magnesium borohydride ($Mg(BH_4)_2$) /tetrahydrofuran (THF) electrolyte was prepared by stirring $Mg(BH_4)_2$ (Sigma-Aldrich, 95%) with THF (Wako Pure Chemical Industries, Ltd., >99.5%) in an Ar-filled glove box overnight at room temperature. The solvent was dried using 3A molecular sieves for 48 h to decrease the water content prior to use. After drying, the water content of the prepared electrolytes was less than 30 ppm, which was confirmed by Karl Fischer titration.

2.2.2. Electrochemical measurements

The magnesium deposition/dissolution reactions in each electrolyte were examined by cyclic voltammetry. A three-electrode cell, which consisted of a platinum plate as a working electrode and a magnesium rod as a counter electrode, was utilized for the measurements. Different reference electrodes were used for $Mg(TFSA)_2$/triglyme or $Mg(TFSA)_2$/2-MeTHF, and for $Mg(BH_4)_2$/THF. For the $Mg(TFSA)_2$/triglyme or $Mg(TFSA)_2$/2-MeTHF electrolytes, a double-junction reference electrode equipped with a microporous glass membrane was employed. The inner part contained lithium that was inserted into a 0.1 M solution of LiTFSA in propylene carbonate, and the outer part contained the electrolyte being analyzed. For $Mg(BH_4)_2$/THF, a magnesium rod was employed as the reference electrode. Cyclic voltammetry was performed at 25 ℃ with a potential sweep rate of 5 mV/s. The potential range was 0.2–4.2 V vs. Li^+/Li (corresponding to -0.76–3.24 V vs. Mg^{2+}/Mg) for $Mg(TFSA)_2$/triglyme, -1.04–4.2 V vs. Li^+/Li (corresponding to -2.0–3.24 V vs. Mg^{2+}/Mg) for $Mg(TFSA)_2$/2-MeTHF, and -2.0–2.0 V vs. Mg^{2+}/Mg for $Mg(BH_4)_2$/THF.

EIS was carried out to analyze the differences in the interfacial resistance using a similar cell configuration as that used in the CV measurement. The AC frequency was scanned from 1 MHz to 10 mHz with an amplitude of 50 mV. All experiments including the electrolyte preparation, cell construction, and electrochemical measurements were carried out under a dry Ar atmosphere.

2.2.3. Characterization

X-ray diffraction (XRD) was performed using an Ultima Ⅳ (Rigaku Co., Inc.) with a Cu Kα X-ray source. Scanning electron microscopy (SEM) images and energy-

dispersive X-ray spectroscopy (EDX) spectra were recorded using an S-3400 N instrument (Hitachi HighTech Co.). After the potentiostatic deposition of magnesium metal, the electrochemical cells were disassembled, and the obtained electrodes were washed with THF. Subsequently, these electrodes were dried in an Ar-filled glove box overnight. All measurements were performed without air exposure of the samples.

The Raman spectra were recorded on a MultiRAM (Bruker Optics Co., Ltd.) instrument equipped with an Nd-YAG laser (1064 nm) at room temperature. The measurement was performed between 60 and 3600 cm^{-1}. All the electrolytes were sealed in glass vessels in an Ar-filled glove box and measured without air exposure.

XPS measurements were performed to analyze the surface structure of magnesium metal. The magnesium plates, which were polished in the glove box, were immersed in the 0.5 M $Mg(TFSA)_2$/triglyme, 0.5 M $Mg(TFSA)_2$/2-MeTHF, and 0.5 M $Mg(BH)_4$/THF electrolytes for 24 h. The magnesium plates were rinsed with dimethoxyethane and dried under vacuum. The prepared samples were sealed in a transfer vessel in the glove box. The vessel was connected to the sample introduction chamber of the XPS, after which the chamber was evacuated < 1.0 Pa for 5 min. The introduction chamber was subsequently filled with dried Ar gas; thereafter, the samples were transferred into the introduction chamber. The XPS measurements were carried out with a standard XPS instrument (Shimadzu. ESCA 3400) using Mg-Kα radiation. The emission current and the acceleration voltage of the X-ray Gun were 20 mA and 10 kV, respectively. Depth profiles were obtained by Ar sputtering using an ion gun with emission currents of 20 mA and an acceleration voltage of 2 kV. The etching rate was > 40 Å min^{-1} based on SiO_2, and the etching time periods were 0, 10, 30, 60, 300, 600, 1200, 1800, and 2400 s.

The *operando* SXAS spectra for the Mg *K*-edge of the electrolytes were recorded by the partial fluorescence yield method at a beamline BL27SU in SPring-8 synchrotron radiation facility in Hyogo, Japan. A custom-made three-electrode cell, which was previously reported,[24,28] was used for the *operando* XAS measurements. Pt, with a thickness of 30 nm, was deposited as a working electrode onto a Si_3N_4 window with a 300 nm thickness (Norcada Inc.) by magnetron sputtering. The fluorescence X-ray generated from the electrolyte passing through the Si_3N_4 window was detected by a silicon drift detector (Techno X Co., Ltd.). The *operando* cell was assembled in an Ar-filled glove box and transferred into a vacuum chamber for the XAS measurements without air exposure. The *operando* XAS measurements were performed while maintaining the potential of the working electrode at several values prior to the magnesium deposition. Afterward, magnesium metal was deposited on the working electrode by applying a potential step method, and additional XAS measurements were performed. Magnesium oxide powder was used as references for X-ray energy calibration. Fourier transformed EXAFS with k^3-weight was calculated by the Athena software package.[29]

DFT calculations were carried out using the Gaussian16 Revision A.03 code[30] to investigate the coordination effect on the electronic states. For the free $TFSA^-$ and $Mg(TFSA)_2$ salt in the triglyme solvent, we calculated the optimized geometries and the corresponding HOMO and LUMO energies of the molecular systems in the triglyme solvent using the polarized continuum model (PCM) method with the parameters for the triglyme bulk solvent (dielectric constant epsilon=7.62). The solvation effect of the THF solvent was taken into account by the integral equation formalism polarizable continuum model (IEFPCM) with a dielectric constant epsilon value of 7.43, for the BH_4^- ion and

$Mg(BH_4)_2$ in the THF solvent. The M06 hybrid functional[31] for the exchange and correlation energy and the 6-311+G(d,p) basis set were used.

2-3. Results and discussion

2.3.1. Behavior of the magnesium deposition/dissolution reactions

The magnesium deposition/dissolution reactions were examined for the 0.5 M $Mg(TFSA)_2$/triglyme, 0.5 M $Mg(TFSA)_2$/2-MeTHF, and 0.5 M $Mg(BH_4)_2$/THF electrolytes by cyclic voltammetry. Figure 2-1 shows the obtained voltammograms. Figure 2-1(b) shows an enlarged figure of the current density, near the potential that the magnesium deposition occurs, during the potential sweep in the negative direction (Figure 2-1(a)). In the 0.5 M $Mg(TFSA)_2$/triglyme electrolyte, cathodic and anodic currents, which are attributed to the magnesium deposition and dissolution reactions, were observed as reported previously.[20] XRD and SEM-EDX confirmed that the deposited product, after the passage of the cathodic current in the electrolyte, was magnesium metal (Figures 2-2(a) and 2-3). Similar cathodic and anodic currents were also observed in the 0.5 M $Mg(BH_4)_2$/THF electrolyte, as reported previously,[16] and the deposited product was characterized as magnesium metal by XRD and SEM-EDX (Figures 2-2(b), and 2-4). Although the current density of the 0.5 M $Mg(BH_4)_2$/THF was exceedingly smaller than that of the 0.5 M $Mg(TFSA)_2$/triglyme, the coulombic efficiency of the 0.5 M $Mg(BH_4)_2$/THF (36%) electrolyte was similar to that of the 0.5 M $Mg(TFSA)_2$/triglyme (38%) electrolyte. In contrast to the 0.5 M $Mg(TFSA)_2$/triglyme and 0.5 M $Mg(BH_4)_2$/THF electrolytes, the cathodic and anodic currents attributed to the magnesium deposition and dissolution reactions were not observed in the 0.5 M $Mg(TFSA)_2$/2-MeTHF electrolyte.

2.3.2. Coordination structure of the magnesium ions in bulk solution

The coordination structure of the magnesium ions in the $Mg(TFSA)_2$/triglyme, $Mg(TFSA)_2$/2-MeTHF, and $Mg(BH_4)_2$/THF electrolytes is influenced by the cation-anion interactions. The magnesium ions compete with the solvents to interact with the anion; consequently, if the interaction between the magnesium ion and anion is strong, magnesium ions coordinate to the anion as well as the solvent. To examine the interactions between the anions and magnesium ions in the bulk solutions of $Mg(TFSA)_2$/triglyme, $Mg(TFSA)_2$/2-MeTHF, and $Mg(BH_4)_2$/THF, the Raman spectra of these electrolytes were collected. The Raman spectra in the region between 720 and 770 cm^{-1} for the 0.5 M $Mg(TFSA)_2$/triglyme and 0.5 M $Mg(TFSA)_2$/2-MeTHF electrolytes are shown in the Figures 2-5(a) and (b). The peaks observed in this region are attributed to the CF_3 bending vibration as well as the C-S and S-N stretching vibrations of $[TFSA]^-$,[32] and susceptibly reflect the interaction of $[TFSA]^-$ with the cation.[32-35] Notably, the peak observed at 739–742 cm^{-1} is assigned to the non-coordinated $[TFSA]^-$ anion (solvent-separated ion pairs (SSIP)), whereas the peak at 745–755 cm^{-1} signifies the $[TFSA]^-$ anion directly coordinated to the cations, which form a contact ion pair (CIP) or an aggregate (AGG). Figures 2-6 (a) and (b) show the estimated ratios of SSIP, CIP, and AGG for the $Mg(TFSA)_2$/triglyme and $Mg(TFSA)_2$/2-MeTHF electrolytes with several concentrations, determined by the Voigt function fitting. The fitting profiles are shown in Figures 2-7 and 2-8. In the $Mg(TFSA)_2$/triglyme, most of the $[TFSA]^-$ anions exist as non-coordinated free ions (SSIP), while less than 10% of the $[TFSA]^-$ anions are still intact with magnesium ions. The coordination state of $[TFSA]^-$is not dependent on the concentration of the $Mg(TFSA)_2$/triglyme electrolyte. These results are almost in agreement with a previous report.[36] In stark contrast to the case in the

$Mg(TFSA)_2$/triglyme electrolyte, all the $[TFSA]^-$ anions exist as AGGs in the $Mg(TFSA)_2$/2-MeTHF electrolyte, and the coordination state of $[TFSA]^-$ is not dependent on the concentration. The difference in the coordination states of $[TFSA]^-$ arise from the solvation ability of the solvents. The multiple oxygen atoms in triglyme can form a chelate with magnesium ions, and this strong solvation can inhibit the coordination of the magnesium ions to $[TFSA]^-$.[36] Conversely, the solvation ability of monodentate 2-MeTHF is not extremely high compared to that of triglyme; thus, magnesium ions are preferentially coordinated to $[TFSA]^-$ in $Mg(TFSA)_2$/2-MeTHF.

The Raman spectra in the region between 750 cm^{-1} and 930 cm^{-1} for the $Mg(TFSA)_2$/triglyme electrolyte with various concentrations are shown in Figure 2-9 (a). The Raman bands corresponding to the CH_2 rocking vibration and C-O-C stretching vibration of the glyme solvent appear in the region between 800 cm^{-1} and 900 cm^{-1}. [37-39] In this region, when coordination to metal ions does not occur, a band appears between 800 cm^{-1} and 865 cm^{-1}, while a characteristic band, upon complex formation with metal ions, appears between 865 cm^{-1} and 890 cm^{-1}.[38,40,41] The band intensity between 820 cm^{-1} and 860 cm^{-1} decreases with increasing $Mg(TFSA)_2$ concentration, whereas the intensity of the band around 880 cm^{-1} increases with increasing $Mg(TFSA)_2$ concentration. These results indicate that the triglyme solvent in the $Mg(TFSA)_2$/triglyme coordinates to magnesium ions; resultantly, more than 90% of the $[TFSA]^-$ anions exist as SSIP. The Raman spectra in the region between 850 cm^{-1} and 1000 cm^{-1} for the $Mg(TFSA)_2$/2-MeTHF electrolyte with various concentrations are shown in Figure 2-9 (b). The peaks assigned to the C-C stretching mode and C-O stretching mode of 2-MeTHF are observed at 920 cm^{-1} for the $Mg(TFSA)_2$/2-MeTHF electrolyte.[42-44] It has been reported that, upon coordination between THF and the cation, a peak appears at a lower wavenumber than

those indicative of the C-C stretching and C-O stretching of the non-coordinated THF by 10 cm^{-1}.[42-44] The new peak is not observed in the $Mg(TFSA)_2$/2-MeTHF electrolyte, which indicates that 2-MeTHF does not directly coordinate to magnesium ions in the $Mg(TFSA)_2$/2-MeTHF electrolyte. These results confirm that majority of the $[TFSA]^-$ anions exist as AGG in the $Mg(TFSA)_2$/2-MeTHF electrolyte.

The Raman spectra in the region between 2000 and 2500 cm^{-1} for the $Mg(BH_4)_2$/ THF electrolyte with various concentrations are shown in Figure 2-5(c). The Raman band corresponding to the B-H stretching vibration of the BH_4 coordinated to the cation appears in the region between 2100 and 2500 cm^{-1}.[45-51] The peaks were observed at 2200 and 2380 cm^{-1} in the $Mg(BH_4)_2$/THF electrolyte; additional peaks appeared at 2140 cm^{-1} and 2300 cm^{-1} with increasing concentration. The peaks observed at 2200 cm^{-1} and 2380 cm^{-1} were assigned to the bridging B-H_b vibration and B-H_t vibration, respectively. [45-51] The $Mg(BH_4)_2$ crystal that has a $P6_1$ of space group, shows a B-H_b vibration at 2300 cm^{-1}.[49] Mohtadi *et al.* proposed that the $Mg(BH_4)_2$ group in the $Mg(BH_4)_2$/THF solution is present as the contact ion pair $[Mg\{(\mu\text{-}H)_2BH_2\}]_2$, which partially dissociates into $[Mg\{(\mu\text{-}H)_2BH_2\}]^+$ and BH_4^- as in the following equation eq 1:[16]

$$[Mg\{(\mu\text{-}H)_2BH_2\}]_2 \rightleftarrows [Mg\{(\mu\text{-}H)_2BH_2\}]^+ + BH_4^- \qquad (1)$$

Based on these reports, we assigned the peak at 2300 cm^{-1} to the B-H vibration of BH_4^- in the complex of magnesium ions coordinated to multi BH_4^-. The peak at 2140 cm^{-1} may also be attributed to the B-H vibration of BH_4^- in the complex of Mg^{2+} coordinated to multi BH_4^- . We estimated the relative peak area of B-H_b and B-H_t for the $Mg(BH)_4$/THF with several concentrations by the Voigt function fitting. The fitting result and profiles are shown in Figure 2-6 (c) and Figure 2-10. The relative peak area of B-H_b increased, while the peak area of B-H_t nearly constant with increasing the concentration.

These results indicate that magnesium ions coordinate to BH_4^- in the $Mg(BH_4)_2$/THF electrolyte. It has been reported that the BH_4^- in the 0.4 M $Mg(BH_4)_2$/THF electrolyte exists as AGGs by theoretical calculation, which is in agreement with our results.[52] The Raman spectra in the region between 850 cm^{-1} and 1000 cm^{-1} for the $Mg(BH_4)_2$/THF electrolyte with various concentrations are shown in Figure 2-9(c). The peaks assigned to the C-C stretching mode and C-O stretching mode of THF were observed at 913 cm^{-1}.[42-44] The peak attributed to the coordination between THF and the cation was not observed at a wavenumber lower by 10 cm^{-1},[42-44] which indicates that the THF in the $Mg(BH_4)_2$/THF electrolyte do not directly coordinate to magnesium ions. These results confirm that the majority of the $[BH_4]^-$ exist as AGGs in the $Mg(BH_4)_2$/THF electrolyte.

2.3.3. Coordination structure of the magnesium ions at the interface between the anode and the electrolyte under an applied potential

Raman spectroscopy clearly showed that the magnesium ions had a different coordination structure in the bulk solutions of the 0.5 M $Mg(TFSA)_2$/triglyme, 0.5 M $Mg(TFSA)_2$/2-MeTHF, and 0.5 M $Mg(BH_4)_2$/THF electrolytes. To examine the coordination structure of the magnesium ions at the interface under applied potential, *operando* XAS measurements were performed for the three electrolytes. The XANES and Fourier-transformed EXAFS of each electrolyte are shown in Figures 2-11 and 2-12, respectively.

For the 0.5 M $Mg(TFSA)_2$/triglyme electrolyte, the intensity of the XANES spectrum decreased gradually from the soak state to -0.2 V, wherein the magnesium deposition did not occur (Figure 2-1(a)). Subsequently, the XANES spectrum changed considerably after the magnesium deposition. The energy at the peak top of the XANES spectrum from the soak state to -0.2 V was nearly constant, indicating that the valency of

the magnesium ions did not change. In the Fourier-transformed EXAFS (Figure 2-12(a)) of the soak state, two peaks were observed around 1.6 Å and 2.6 Å. The peak at 1.6 Å was assigned to the Mg-O bond between the magnesium ion and triglyme or between the magnesium ion and $[TFSA]^-$ because the magnesium ions in the electrolyte were coordinated to both triglyme and $[TFSA]^-$ based on the results from Raman spectroscopy. The peak at 2.6 Å was assigned to the Mg-C bond between the magnesium ion and triglyme or the Mg-S bond between the magnesium ion and $[TFSA]^-$. The Mg-O bond distance did not change from the soak state to -0.2 V, indicating that the valency of the magnesium ions did not change. These results are in agreement with the XANES results. The intensities of the two peaks in the EXAFS spectra decreased gradually from the soak state to -0.2 V, indicating that the coordination number decreased and/or the local distortion increased between the magnesium ions and triglyme. It has been reported that the coordination number of lithium-ion in a lithium glyme solvate liquid system is constant even at applied potential;[53] consequently, the decrease in the intensities of the two peaks is attributed to the increase in the local distortions. The exchange rate of the solvent, strongly enhanced by the applied potential, increased the local distortion. These tendencies were also observed during the Mg-Bi alloy formation for the 0.5 M $Mg(TFSA)_2$/acetonitrile electrolyte.[24] The EXAFS spectra changed after the magnesium deposition.

Although the spectra of the 0.5 M $Mg(TFSA)_2$/2-MeTHF electrolyte changed in a similar way to that of the 0.5 M $Mg(TFSA)_2$/triglyme electrolyte under applied potential, the change was more noticeable for the former (Figures 2-11(b) and 2-12(b)). The XANES spectrum gradually became weak and broad from the soak state to -1.2 V, indicating that the magnesium deposition did not occur (Figure 2-1(a)). The energy at the

peak top of the XANES spectrum from the soak state to -1.2 V was nearly constant, meaning that the valency of the magnesium ions did not change. In the EXAFS spectra in the soak state, two peaks were observed around 1.6 Å and 2.6 Å, corresponding to the EXAFS spectra of the 0.5 M $Mg(TFSA)_2$/triglyme. The peak at 1.6 Å was assigned to the Mg-O bond between magnesium ion and 2-MeTHF or between magnesium ion and $[TFSA]^-$ because the magnesium ions in the electrolyte were coordinated to both 2-MeTHF and $[TFSA]^-$ based on the results from Raman spectroscopy. The peak at 2.6 Å was assigned to the Mg-C bond between the magnesium ion and 2-MeTHF or the Mg-S bond between the magnesium ion and $[TFSA]^-$. The Mg-O bond distance did not change from the soak state to -1.2 V, indicating that the valency of the magnesium ions did not change. These results are well in agreement with the XANES results. The intensities of the two peaks in the EXAFS spectrum decreased from the soak state to -1.2 V. These changes for the 0.5 M $Mg(TFSA)_2$/2-MeTHF electrolyte were larger than those for the 0.5 M $Mg(TFSA)_2$/triglyme, indicating that the local coordination structure of the magnesium ions in the 0.5 M $Mg(TFSA)_2$/2-MeTHF electrolyte was distorted more largely by cathodic polarization. Majority of the $[TFSA]^-$ anions in the 0.5 M $Mg(TFSA)_2$/2-MeTHF electrolyte were coordinated to the magnesium ions; resultantly, the coulombic repulsion between the $[TFSA]^-$ anions coordinating to magnesium ion and the negatively charged electrode may become stronger than that in the case of the 0.5 M $Mg(TFSA)_2$/triglyme, resulting in a larger distortion.

For the 0.5 M $Mg(BH_4)_2$/THF electrolyte, the intensity of the XANES spectrum decreased gradually from the soak state to -0.2 V wherein the magnesium deposition did not occur (Figure 2-1(a)). Thereafter, the XANES spectrum changed considerably after magnesium metal deposition. The energy at the peak top of the XANES spectrum from

the soak state to -0.2 V was nearly constant, indicating that the valency of the magnesium ions did not change immediately before Mg metal deposition. In the EXAFS spectra (Figure 2-12(c)), a peak was observed around 1.5 Å. Although the magnesium ions coordinated with BH_4^-, according to the Raman spectroscopy results, the Mg-H bond was not detected by EXAFS analysis because the backscattering of hydrogen was considerably small. Therefore, we assigned the peak to the Mg-B bond between the magnesium ion and $[BH_4]^-$.[28] The distance of the Mg-B bond did not change from the soak state to -0.2 V, indicating that the valency of the magnesium ions did not change. These results are consistent with the XANES results. The intensity of the peak in the EXAFS spectrum decreased from the soak state to -0.2 V as in the cases of the 0.5 M $Mg(TFSA)_2$/triglyme and 0.5 M $Mg(TFSA)_2$/2-MeTHF electrolytes. These results indicate that the local coordination structure of the magnesium ions in the 0.5 M $Mg(BH_4)_2$/THF electrolyte was distorted more largely by the cathodic polarization. Moreover, the EXAFS spectra changed after the magnesium deposition reaction.

The magnesium deposition/dissolution reactions occurred in the 0.5 M $Mg(TFSA)_2$/triglyme and 0.5 M $Mg(BH_4)_2$/THF electrolytes, whereas these reactions did not occur in the 0.5 M $Mg(TFSA)_2$/2-MeTHF electrolyte. The change in the valency of the magnesium ions was not observed in the XANES spectra, and the expansion of the distance between the magnesium ion and the first nearest neighbor atom was not observed in the EXAFS spectra.

2.3.4. Reductive stability of the anion

The magnesium deposition/dissolution reactions occurred in the 0.5 M $Mg(TFSA)_2$/triglyme and 0.5 M $Mg(BH)_4$/THF electrolytes, whereas they did not occur in the 0.5 M $Mg(TFSA)_2$/2-MeTHF electrolyte. The drastic change in the valency of the

magnesium ions was not observed in the XANES spectra immediately before Mg metal deposition, and the expansion of the distance between the magnesium ion and the first nearest neighbor atom was not observed in the EXAFS spectra. These results may indicate that the intermediate states of Mg^{2+}, such as Mg^{+},[52] is not observed at potentials above the magnesium deposition potential.

These results may indicate that the difference in the behaviors of the magnesium deposition is attributed to the difference in the reductive stability of the anion in each electrolyte. For the $Mg(TFSA)_2$-base electrolytes, Raman spectroscopy revealed that all the $[TFSA]^-$ anions coordinated to the magnesium ions in the 0.5 M $Mg(TFSA)_2$/2-MeTHF electrolyte, while almost all of the $[TFSA]^-$ anions did not participate in the coordination of the magnesium ions in the 0.5 M $Mg(TFSA)_2$/triglyme electrolyte. The occurrence of the reversible magnesium deposition is dependent on the reductive stability of the $[TFSA]^-$ anion at the interface. The DFT calculation results of both coordinated and uncoordinated $[TFSA]^-$ anions to the magnesium ions in the case of $Mg(TFSA)_2$/triglyme, are shown in Table 2-1 and Figure 2-13. The LUMO energy level of the coordinated $[TFSA]^-$ anion is calculated as -1.86 eV, which corresponds to -0.19 V vs. Mg^{2+}/Mg. This energy is lower than that of the uncoordinated $[TFSA]^-$ anion (-0.35 eV), which corresponds to -1.7 V vs. Mg^{2+}/Mg, as shown in Table 2-1 and Figure 2-13(a). The DFT calculation results for the $Mg(TFSA)_2$/2-MeTHF electrolyte have been reported in Ref 24 and are listed in Table 2-1. These results indicate that the former $[TFSA]^-$ anion undergoes reduction decomposition more easily than the latter.

To confirm the decomposition of $[TFSA]^-$ on the magnesium metal surface, we analyzed the magnesium metal after immersion into the 0.5 M $Mg(TFSA)_2$/triglyme and the 0.5 M $Mg(TFSA)_2$/2-MeTHF electrolytes. The XPS analysis detected fluorine species,

which was attributed to a reduction product of the $[TFSA]^-$ anions on the surface of the magnesium metal, as shown in Figures 2-14(d) and 2-15(d) in Supporting Information. The partial reduction of $[TFSA]^-$ at the reduction potential of the magnesium ions was observed in another $Mg[TFSA]_2$-base electrolyte.[54,55]

To further examine how the passivation layer affects the interfacial resistance of the Mg anode, EIS was performed. Figure 2-16(a)(b) show the Nyquist plots of the Mg electrode immersed in different electrolytes and fitted results using equivalent electrical circuit. The EIS data were fitted with the equivalent electrical circuit as shown in Figure 2-16(c)[56,57]. The fitting parameters are summarized in Table 2-2. The solution resistance (R_s) value changes for each three-electrode cell because the position of the reference electrode cannot be correctly fixed in the cell. The Nyquist plot and bode plot showed that one semicircle appears in the $Mg(TFSA)_2$/ triglyme and $Mg(BH)_4$/THF electrolytes at high frequency (10^5 Hz), whereas that two semicircles appear in the $Mg(TFSA)_2$/2-MeTHF electrolyte at the middle (10^3 Hz) and high frequency (10^5 Hz). The semicircle at the high frequency can be attributed to the charge transfer resistance, and the semicircle at the middle frequency can be attributed to the resistance and of the passivation layer.[56-58]

The charge transfer resistance (R_{ct}) of the 0.5 M $Mg(TFSA)_2$/2-MeTHF electrolyte was comparative with that of the 0.5 M $Mg(TFSA)_2$/ triglyme electrolyte as shown in Table S1. However, the passivation layer resistance (R_{pl}) in the 0.5 M $Mg(TFSA)_2$/2-MeTHF was remarkably large, compared to the 0.5 M $Mg(TFSA)_2$/ triglyme electrolyte. The large R_{pl} of the 0.5 M $Mg(TFSA)_2$/2-MeTHF electrolyte indicates that the $[TFSA]^-$ easily decomposes to form a passivation layer and impedes the

magnesium deposition reaction, compared to the case in the 0.5 M $Mg(TFSA)_2$/triglyme electrolyte. These EIS results agree with the XPS and DFT calculation results.

For the $Mg(BH)_4$/THF electrolyte, Raman spectroscopy revealed that the majority of the $[BH_4]^-$ anions coordinate to the magnesium ions and exist as AGG. The LUMO energy levels of $[BH_4]^-$ for both coordinated and uncoordinated states to the magnesium ions were calculated, and are shown in Table 2-1 and Figure 2-13(b). The LUMO energy level of the uncoordinated $[BH_4]^-$ was reduced by coordination with the magnesium ions from 0.37 eV to -1.05 eV. However, the LUMO energy of the coordinated $[BH_4]^-$, which corresponds to -1.0 V vs. Mg^{2+}/Mg, is stable under the potential of the magnesium deposition, as shown in Table 2-1 and Figure 2-13(b). The reduction production attributed to the $[BH_4]^-$ anion was not observed on the magnesium metal surface by XPS measurements, as shown in Figure 2-17(d), which agrees with the DFT calculation result. The EIS data and fitting data of the 0.5 M $Mg(BH)_4$/THF were shown in Figure 2-16 (a)(b) and Table 2-2. The R_{ct} of the 0.5 M $Mg(BH)_4$/THF electrolyte was significantly larger than that of the 0.5 M $Mg(TFSA)_2$/triglyme electrolyte. The large R_{ct} value of the 0.5 M $Mg(BH)_4$/THF electrolyte explains the slow interfacial reaction kinetics for the deposition/dissolution reaction (Figure 2-1).

Figure 2-18 schematically illustrates the behavior of the magnesium ions at the anode/electrolyte interface. The $[TFSA]^-$ coordinated to the magnesium ions in $Mg(TFSA)_2$/2-MeTHF experience reduction decomposition, and this inhibits the magnesium deposition. Conversely, the 0.5 M $Mg(TFSA)_2$/triglyme electrolyte allows a quasi-reversible magnesium deposition. This is because most of the $[TFSA]^-$ anions do not coordinate to the magnesium ions; thus, such a $[TFSA]^-$ anion is more stable than the coordinated $[TFSA]^-$ anion, for the reduction decomposition. Noteworthily, some of the

$[TFSA]^-$ still coordinate to the magnesium ions even in highly diluted solutions. These coordinated $[TFSA]^-$ would be reduced easily. The poor Coulombic efficiency of the magnesium deposition/dissolution in $Mg(TFSA)_2$/triglyme is due to the reductive decomposition of $[TFSA]^-$ during the magnesium deposition process.

Compared to the case in the $Mg(TFSA)_2$-based electrolytes, although all of the BH_4^- coordinate with the magnesium ions in the 0.5 M $Mg(BH_4)_2$/THF electrolyte, magnesium deposition occurs. Even the LUMO energy of the BH_4^- decrease upon coordination to the magnesium ions. The BH_4^- coordinated to the magnesium ions are stable under the potential of the magnesium deposition. The magnesium deposition is not inhibited by the decomposition of the BH_4^-. However, none of the magnesium ions exist in a state separated from $[BH_4]^-$; this results in the small current density of the magnesium deposition reaction in the $Mg(BH_4)_2$/THF electrolyte (Figure 2-1).

2-4. Conclusions

The coordination structures of the magnesium ions in the bulk solution and at the anode/electrolyte interface of three magnesium electrolytes were analyzed in this study. In the 0.5 M $Mg(TFSA)_2$/triglyme electrolyte, quasi-reversible magnesium deposition/dissolution reactions occurred, whereas no magnesium deposition reaction occurred in the 0.5 M $Mg(TFSA)_2$/2-MeTHF electrolyte. In the 0.5 M $Mg(BH_4)_2$/THF electrolyte, although the current density was relatively low, reversible magnesium deposition/dissolution reactions occurred. *Operando* XAS measurements showed that the valency of the magnesium ions did not change, and the local structure distortion around the magnesium ions increased in all the electrolytes at the magnesium electrode/electrolyte interface during the cathodic polarization. We conclude that suppressing the reduction decomposition of the anion is crucial for achieving successful

magnesium deposition; furthermore, separating the magnesium ion from the anion is important for accelerating the magnesium deposition. Admittedly, the poor Coulombic efficiency associated with magnesium deposition/dissolution reactions in $Mg(TFSA)_2$/ether solutions can be remarkably improved by incorporating chloride compounds, which facilitate the dissociation of $Mg(TFSA)_2$. The findings of this study will be useful for the future design of new electrolytes for magnesium rechargeable batteries.

Refecences

1. Armand, M.; Tarascon. *Nature* **2008**, 451, 652–657.
2. Dunn, B.; Kamath, H.; Tarascon, J.-M. *Science* **2011**, 334, 928–935.
3. Yoo, H. D.; Shterenberg, I.; Gofer, Y.; Gershinsky, G.; Pour, N.; Aurbach, D. *Energy Environ. Sci.* **2013**, 6, 2265–2279.
4. Gregory, T. D.; Hoffman, R. J.; Winterton, R. C. *J. Electrochem. Soc.* **1990**, 137, 775–780.
5. Novák, P.; Imhof, R.; Haas, O. *Electrochim. Acta* **1999**, 45, 351–367.
6. Besenhard, J. O.; Winter, M. *ChemPhysChem* **2002**, 3, 155–159.
7. Aurbach, D.; Lu, Z.; Schechter, A.; Gofer, Y.; Gizbar, H; Turgeman, R.; Cohen, Y.; Moshkovich, M.; Levi, E. *Nature* **2000**, 407, 724–727.
8. Lu, Z.; Schechter, A.; Moshkovich, M.; Aurbach, D. *J. Electroanal. Chem.* **1999**, 466, 203–217.
9. Aurbach, D.; Schechter, A.; Moshkovich, M.; Cohen, Y. *J. Electrochem. Soc.* **2001**, 148, A1004–A1014.
10. Aurbach, D.; Gizbar, H.; Schechter, A.; Chusid, O.; Gottlieb, H. E.; Gofer, Y.; Goldberg, I. *J. Electrochem. Soc.* **2002**, 149, A115–A117.
11. Mizrahi, O.; Amir, N.; Pollak, E.; Chusid, O.; Marks, V.; Gottlieb, H.; Larush, L.; Zinigrad, E.; Aurbach, D. *J. Electrochem. Soc.* **2008**, 155, A103–A107.
12. Pour, N.; Gofer, Y.; Major, D. T.; Aurbach, D. *J. Am. Chem. Soc.* **2011**, 133, 6270–6278.
13. Kim, H. S.; Arthur, T. S.; Allred, G. D.; Zajicek, J.; Newman, J. G.; Rodnyansky, A. E.; Oliver, A. G.; Boggess, W. C.; Muldoon, J. *Nat. Commun.* **2011**, 2, 1–6.

14. Barile, C. J.; Spatney, R.; Zavadil, K. R.; Gewirth, A. A. *J. Phys. Chem. C* **2014**, 118, 10694–10699.

15. Barile, C. J.; Barile, E. C.; Zavadil, K. R.; Nuzzo, R. G.; Gewirth, A. A. *J. Phys. Chem. C* **2014**, 118, 27623–27630.

16. Mohtadi, R.; Matsui, M.; Arthur, T. S.; Hwang, S.-J. *Angew. Chem. Int. Ed.* **2012**, 51, 9780–9783.

17. Doe, R. E.; Han, R.; Hwang, J.; Gmitter, A. J.; Shterenberg, I.; Yoo, H. D.; Pour, N.; Aurbach, D. *Chem. Commun.* **2013**, 50, 243–245.

18. Shao, Y.; Liu, T.; Li, G.; Gu, M.; Nie, Z.; Engelhard, M.; Xiao, J.; Lv, D.; Wang, C.; Zhang, J.-G.; Liu, J. *Sci. Rep.* **2013**, 3, 1–7.

19. Ha, S.-Y.; Lee, Y.-W.; Woo, S. W.; Koo, B.; Kim, J.-S.; Cho, J.; Lee, K. T.; Choi, N.-S. *ACS Appl. Mater. Interfaces* **2014**, 6, 4063–4073.

20. Orikasa, Y.; Masese, T.; Koyama, Y.; Mori, T.; Hattori, M.; Yamamoto, K.; Okado, T.; Huang, Z.-D.; Minato, T.; Tassel, C.; Kim, J.; Kobayashi, Y.; Abe, T.; Kageyama, H.; Uchimoto, Y. *Sci. Rep.* **2014**, 4, 5622.

21. Fukutsuka, T.; Asaka, K.; Inoo, A.; Yasui, R.; Miyazaki, K.; Abe, T.; Nishio, K.; Uchimoto, Y. *Chem. Lett.* **2014**, 43, 1788–1790.

22. Carter, T. J.; Mohtadi, R.; Arthur, T. S.; Mizuno, F.; Zhang, R.; Shirai, S.; Kampf, J. W. *Angew. Chem. Int. Ed.* **2014**, 53, 3173–3177.

23. Kim, I.-T.; Yamabuki, K.; Morita, M.; Tsutsumi, H.; Yoshimoto, N. *J. Power Sources* **2015**, 278, 340–343.

24. Hattori, M.; Yamamoto, K.; Matsui, M.; Nakanishi, K.; Mandai, T.; Choudhary, A.; Tateyama, Y.; Sodeyama, K.; Uchiyama, T.; Orikasa, Y. *J. Phys. Chem. C* **2018**, 122, 25204–25210.

25. Arthur, T. S.; Glans, P.-A.; Singh, N.; Tutusaus, O.; Nie, K.; Liu, Y.-S.; Mizuno, F.; Guo, J.; Hein Alsem, D.; Salmon, N. J. *Chem. Mater* **2017**, *29*, 7183–7188.

26. Benmayza, A.; Ramanathan, M.; Arthur, T. S.; Matsui, M.; Mizuno, F.; Guo, J.; Glans, P.; Prakash, J *J. Phys. Chem. C* **2013**, 117, 26881–26888.

27. Nakayama, Y.; Kudo, Y.; Oki, H.; Yamamoto, K.; Kitajima, Y.; Noda, K. Complex *J. Electrochem. Soc.* **2008**, 155, 754–759.

28. Nakanishi, K.; Kato, D.; Arai, H.; Tanida, H.; Mori, T.; Orikasa, Y.; Uchimoto, Y.; Ohta, T.; Ogumi, Z. *Rev. Sci. Instrum.* **2014**, 85, 084103.

29. Ravel, B.; Newville, M. *J. Synchrotron Rad.* **2005**, 12, 537-541.

30. Frisch, M. J.; Trucks, G. W.; Schlegel, H. B.; Scuseria, G. E.; Robb, M. A.; Cheeseman, J. R.; Scalmani, G.; Barone, V.; Petersson, G. A.; Nakatsuji, H.; Li, X.; Caricato, M.; Marenich, A. V.; Bloino, J.; Janesko, B. G.; Gomperts, R.; Mennucci, B.; Hratchian, H. P.; Ortiz, J. V.; Izmaylov, A. F.; Sonnenberg, J. L.; Williams-Young, D.; Ding, F.; Lipparini, F.; Egidi, F.; Goings, J.; Peng, B.; Petrone, A.; Henderson, T.; Ranasinghe, D.; Zakrzewski, V. G.; Gao, J.; Rega, N.; Zheng, G.; Liang, W.; Hada, M.; Ehara, M.; Toyota, K.; Fukuda, R.; Hasegawa, J.; Ishida, M.; Nakajima, T.; Honda, Y.; Kitao, O.; Nakai, H.; Vreven, T.; Throssell, K.; Montgomery, J. J. A.; Peralta, J. E.; Ogliaro, F.; Bearpark, M.; Heyd, J. J.; Brothers, E.; Kudin, K. N.; Staroverov, V. N.; Keith, T. A.; Kobayashi, R.; Normand, J.; Raghavachari, K.; Rendell, A.; Burant, J. C.; Iyengar, S. S.; Tomasi, J.; Cossi, M.; Millam, J. M.; Klene, M.; Adamo, C.; Cammi, R.; Ochterski, J. W.; Martin, R. L.; Morokuma, K.; Farkas, Ö.; Foresman J. B.; Fox, D. J. Gaussian Inc, Wallingford, CT, 2016.

31. Zhao, Y.; Truhlar, D. G. *Theor. Chem. Acc.* **2008**, 120, 215–241.

32. Brouillette, D.; Irish, D. E.; Taylor, N. J.; Perron, G.; Odziemkowski, M.; Desnoyers, J. E. *Phys. Chem. Chem. Phys.* **2002**, 4, 6063–6071.

33. Seo, D. M.; Borodin, O.; Han, S. D.; Boyle, P. D.; Henderson, W. A. *J. Electrochem. Soc.* **2012**, 159, A1489–A1500.

34. Zhang, C.; Ueno, K.; Yamazaki, A.; Yoshida, K.; Moon, H.; Mandai, T.; Umebayashi, Y.; Dokko, K.; Watanabe, M. *J. Phys. Chem. B* **2014**, 118, 5144–5153.

35. Yamada, Y.; Furukawa, K.; Sodeyama, K.; Kikuchi, K.; Yaegashi, M.; Tateyama, Y.; Yamada, A. *J. Am. Chem. Soc.* **2014**, 136, 5039–5046.

36. Kimura, T.; Fujii, K.; Sato, Y.; Morita, M.; Yoshimoto, N. *J. Phys. Chem. C* **2015**, 119, 18911–18917.

37. Yang, X.; Su, Z.; Wu, D.; Hsu, S. L.; Stidham, H. D. *Macromolecules* **1997**, 30, 3796–3802.

38. Brouillette, D.; Irish, D. E.; Taylor, N. J.; Perron, G.; Odziemkowski, M.; Desnoyers, J. E. *Phys. Chem. Chem. Phys.* **2002**, 4, 6063–6071.

39. Ducasse, L.; Dussauze, M.; Grondin, J.; Lassegues, J. C.; Naudin, C.; Servant, L. *Phys. Chem. Chem. Phys.* **2003**, 5, 567–574.

40. Frech, R.; Huang, W. *Macromolecules* **1995**, 28, 1246–1251.

41. Grondin, J.; Lassegues, J.-C.; Chami, M.; Servant, L.; Talaga D.; Henderson, W. *Phys. Chem. Chem. Phys.* **2004**, 6, 4260–4267.

42. Ojha, A. K.; Srivastava, S. K.; Peica, N.; Schlücker, S.; Kiefer, W.; Asthana, B. P. *J. Mol. Struct.* **2005**, 735–736.

43. Benevenuto, R. L.; Alves, W. A. *J. Raman Spectrosc.* **2008**, 39, 490–494.

44. Alves, C. C.; Campos, T. B. C.; Alves, W. A. *Spectrochim. Acta, Part A* **2012**, 97, 1085–1088.

45. Taylor, R. C.; Schultz, D. R.; Emery, A. R. *J. Am. Chem. Soc*. **1958**, 80, 27–30.

46. Emery, A. R.; Taylor, R. C. *J. Chem. Phys.* **1958**, 28, 1029–1032.

47. Shirk, A. E.; Shriver, D. F. *J. Am. Chem. Soc.* **1973**, 95, 5904–5912.

48. Marks, T. J.; Kolb, J. R. *Chem. Rev.* **1977**, 77, 263–293.

49. Cerny, R.; Filinchuk, Y.; Hagemann, H.; Yvon, K. *Angew. Chem. Int., Ed.* **2007**, 46, 5765–5767.

50. Parker, S. F. Coordin. *Chem. Rev.* **2010**, 254, 215–234.

51. Poonia, N. S.; Bajaj, A. V. *Chem. Rev.* **1979**, 79, 389–445.

52. Rajput, N. N.; Qu, X.; Sa, N.; Burrell, A. K.; Persson, K. A. *J. Am. Chem. Soc.* **2015**, *137*, 3411–3420.

53. Coles, S. W.; Mishin, M.; Perkin, S.; Fedorov, M. V; Ivaništšev, V. B. *Phys. Chem. Chem. Phys.* **2017**, *19*, 11004–11010.

54. Kuwata, H.; Matsui, M.; Imanishi, N. *J. Electrochem. Soc.* **2017**, 13, A3229–A3236.

55. Jay, R.; Tomich, A. W.; Zhang, J.; Zhao, Y. F*ACS Appl Mater Inter* **2019**, 11, 11414-11420.

56. Tutusaus, O.; Mohtadi, R.; Singh, N.; Arthur, T. S.; Mizuno, F., *ACS Energy Lett.* **2017**, 2, 224-229.

57. Kang, S. J.; Kim, H.; Hwang, S.; Jo, M.; Jang, M.; Park, C.; Hong, S. T.; Lee, H., *ACS Appl Mater Inter*.**2019**, 11, 517-524.

58. Yamada, Y.; Iriyama, Y.; Abe, T.; Ogumi, Z., *Langmuir* **2009**, *25*, 12766-1277.

(a)

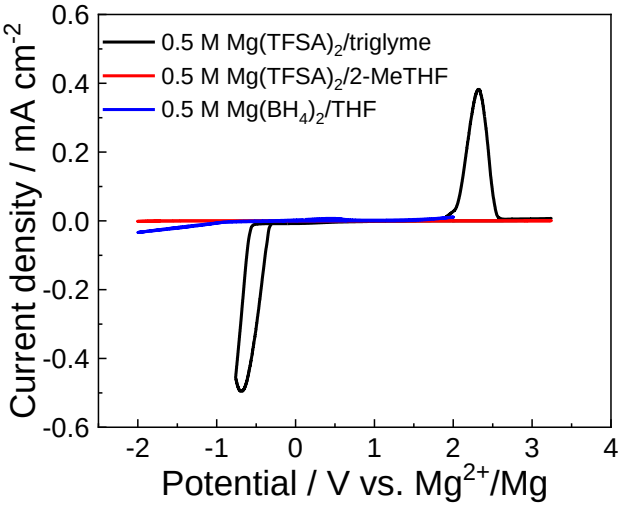

(b)

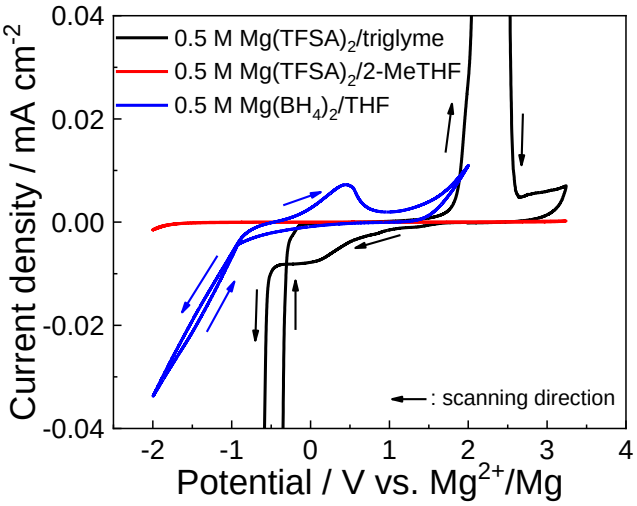

Figure 2-1. (a) Cyclic voltammograms of the 0.5 M $Mg(TFSA)_2$/triglyme, 0.5 M $Mg(TFSA)_2$/2-MeTHF, and 0.5 M $Mg(BH_4)_2$/THF at a sweeping rate of 5 mV/s. (b) Enlarged figure of (a) between -2.5 and 2.5 V (vs. Mg^{2+}/Mg)

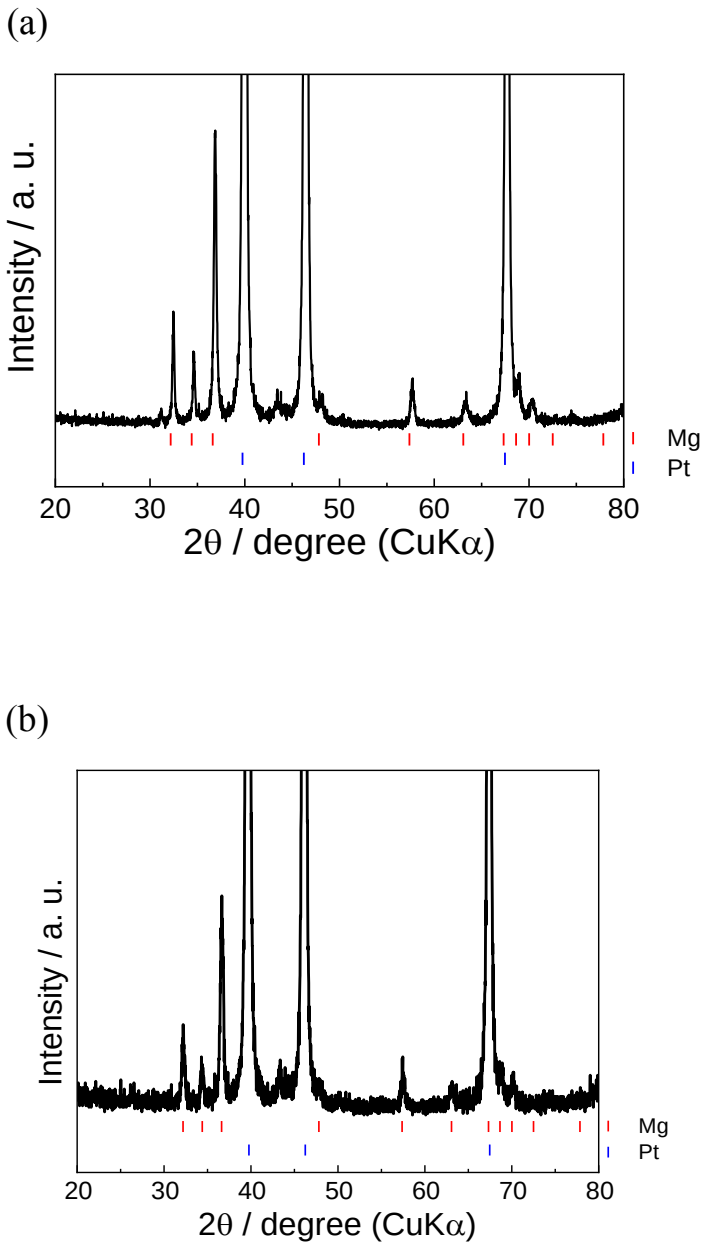

Figure 2-2. XRD patterns of electrodeposited of (a) 0.5 M $Mg(TFSA)_2$/triglyme and (b) 0.5 M $Mg(BH_4)_2$/THF on Pt substrate.

(a)

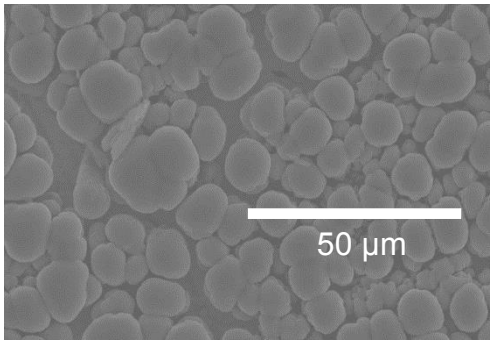

(b)

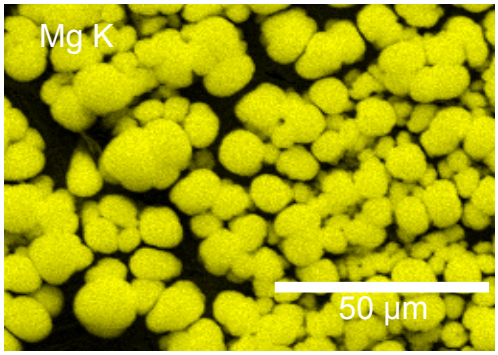

Figure 2-3. (a) SEM image and (b) EDX mapping of Mg *K* for Pt substrate after electrochemical measurements in 0.5 M $Mg(TFSA)_2$/triglyme.

(a)

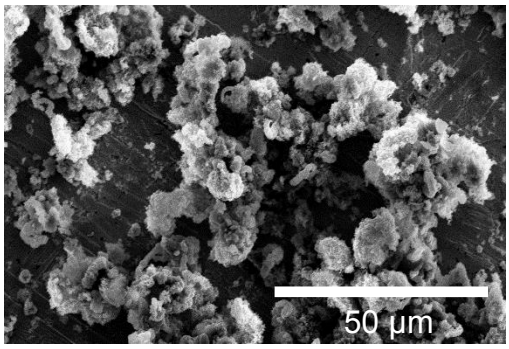

(b)

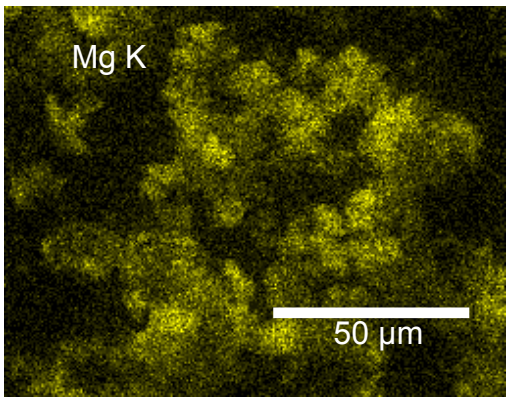

Figure 2-4. (a) SEM image and (b) EDX mapping of Mg *K* for Pt substrate after electrochemical measurements in 0.5 M $Mg(BH_4)_2$/THF.

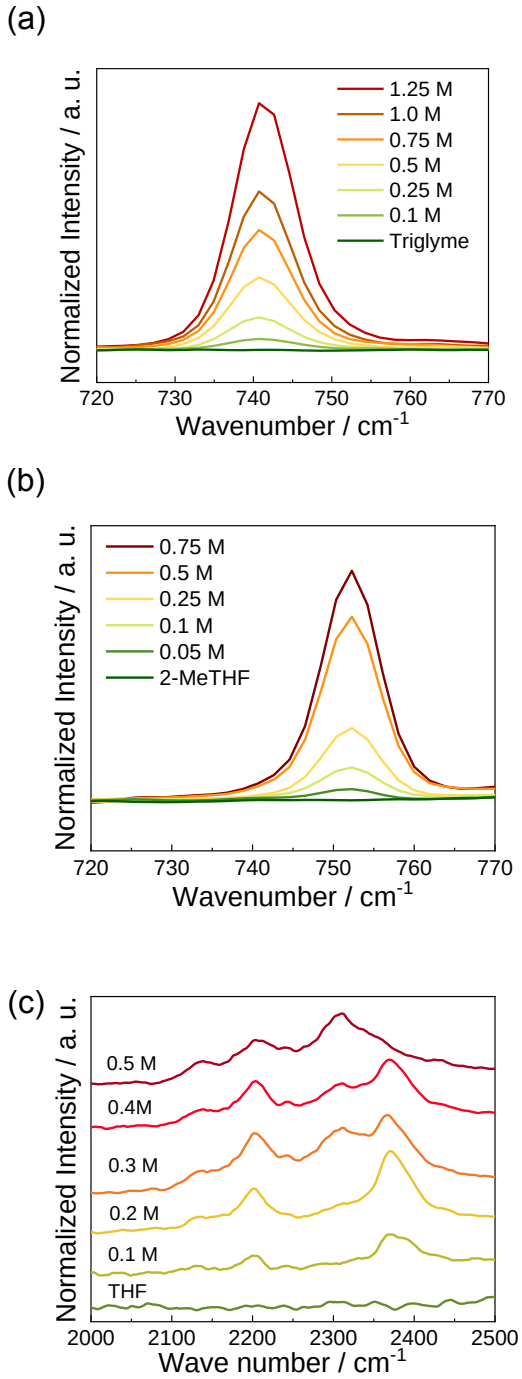

Figure 2-5. Raman spectra of (a) $Mg(TFSA)_2$/triglyme and (b) $Mg(TFSA)_2$/2-MeTHF with several concentrations in the region between 720 and 770 cm^{-1} (c) $Mg(BH_4)_2$/THF in several concentrations in the region between 2000 and 2500 cm^{-1}.

(a)

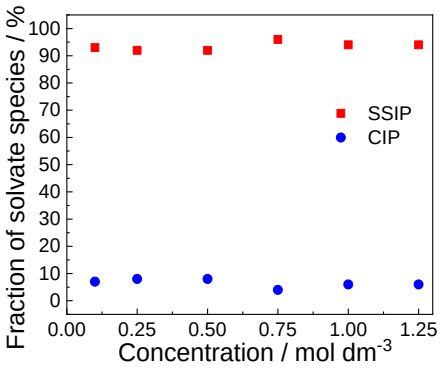

(b)

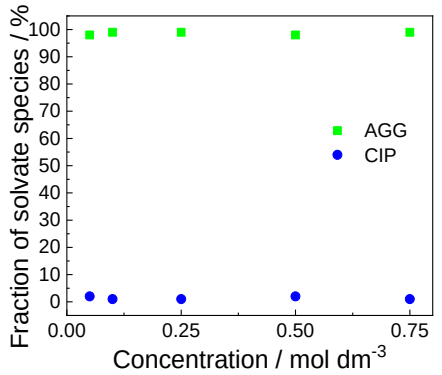

(c)

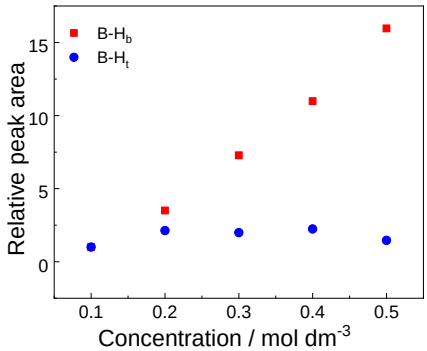

Figure 2-6. Fraction of solvated species of (a) $Mg(TFSA)_2$/triglyme and (b) $Mg(TFSA)_2$/2-MeTHF, SSIP = solvent-separated ion pairs; CIP = contact ion pairs; and AGG = aggregate. Relative peak area of (c) $Mg(BH_4)_2$/THF (b: bridging, t: terminal) with several concentrations.

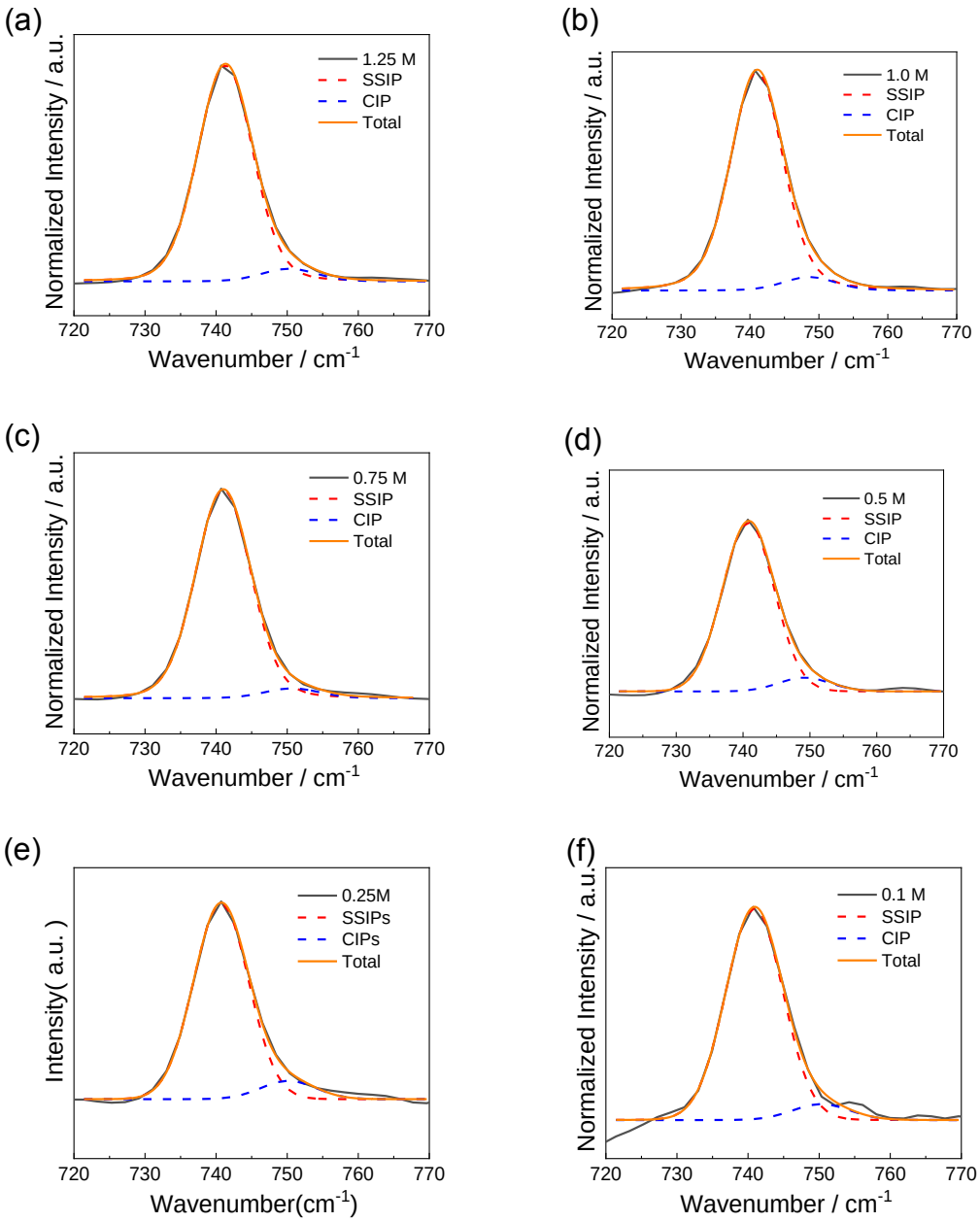

Figure 2-7. Raman spectra and Voigt function fitting results of $Mg(TFSA)_2$/triglyme in several concentrations (a) 1.25 M (b) 1.0 M (c) 0.75 M (d) 0.5 M (e) 0.25 M and (f) 0.1 M in the wave number between 720 and 770 cm^{-1}.

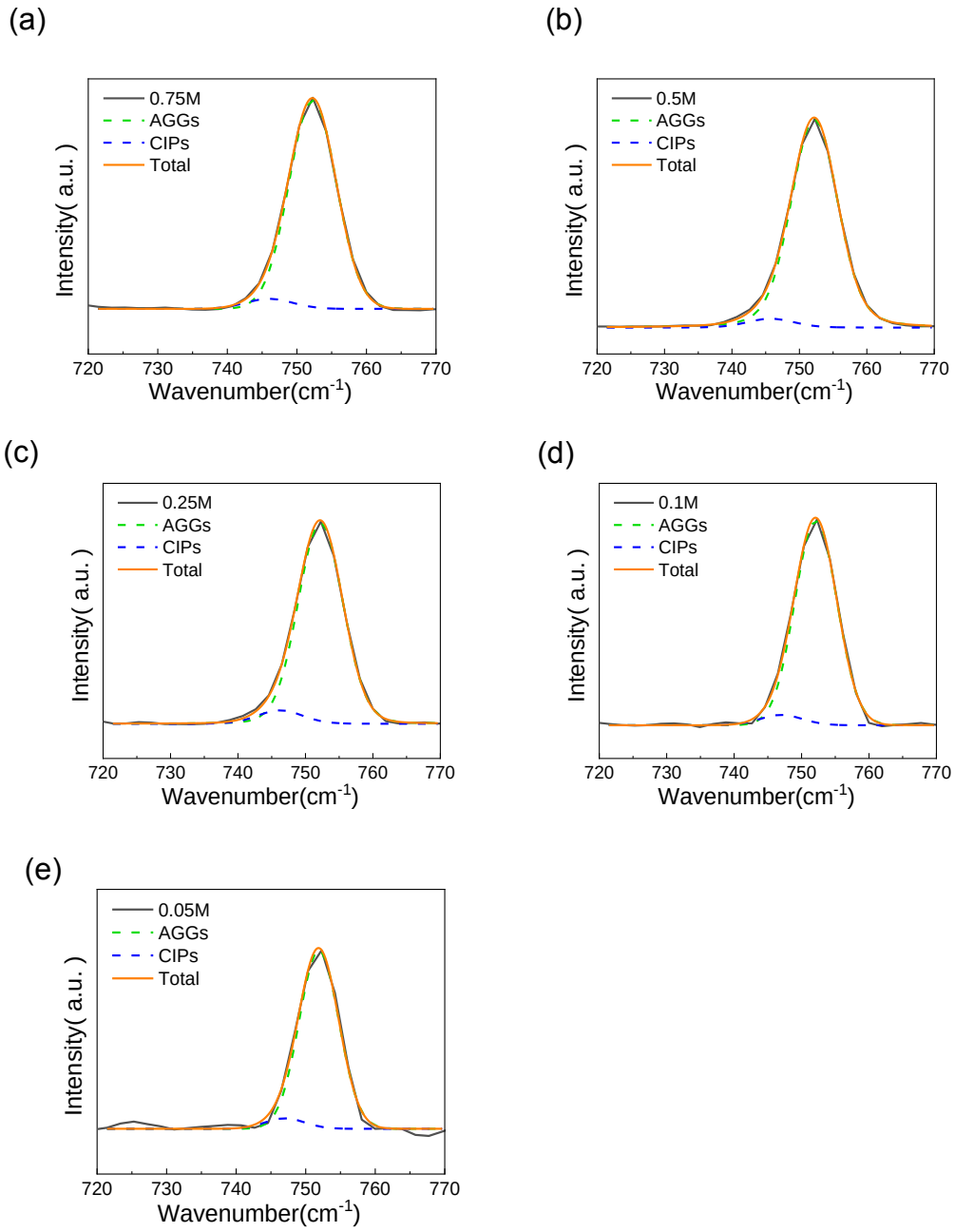

Figure 2-8. Raman spectra and Voigt function fitting results of $Mg(TFSA)_2$/2-MeTHF in several concentrations (a) 0.75 M (b) 0.5 M (c) 0.25 M (d) 0.1 M and (e) 0.05 M in the wave number between 720 and 770 cm^{-1}.

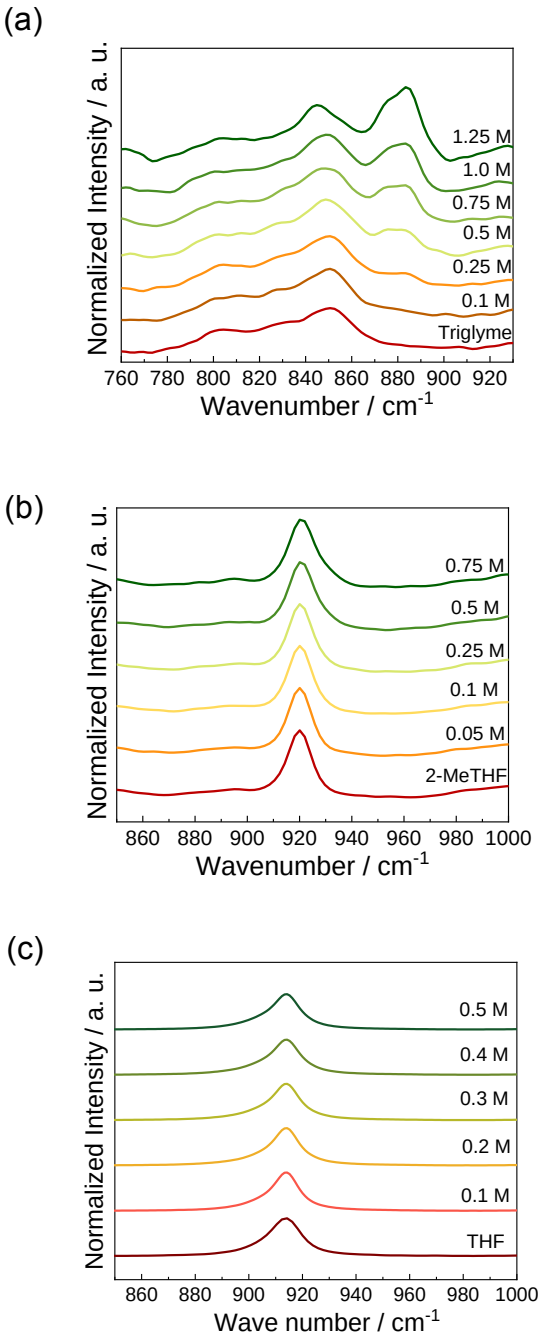

Figure 2-9. Raman spectra of (a) $Mg(TFSA)_2$/triglyme with several concentrations in the wave number between 760 and 930 cm^{-1} (b) $Mg(TFSA)_2$/2-MeTHF and (c) $Mg(BH_4)_2$/THF in the wave number between 850 and 1000 cm^{-1}.

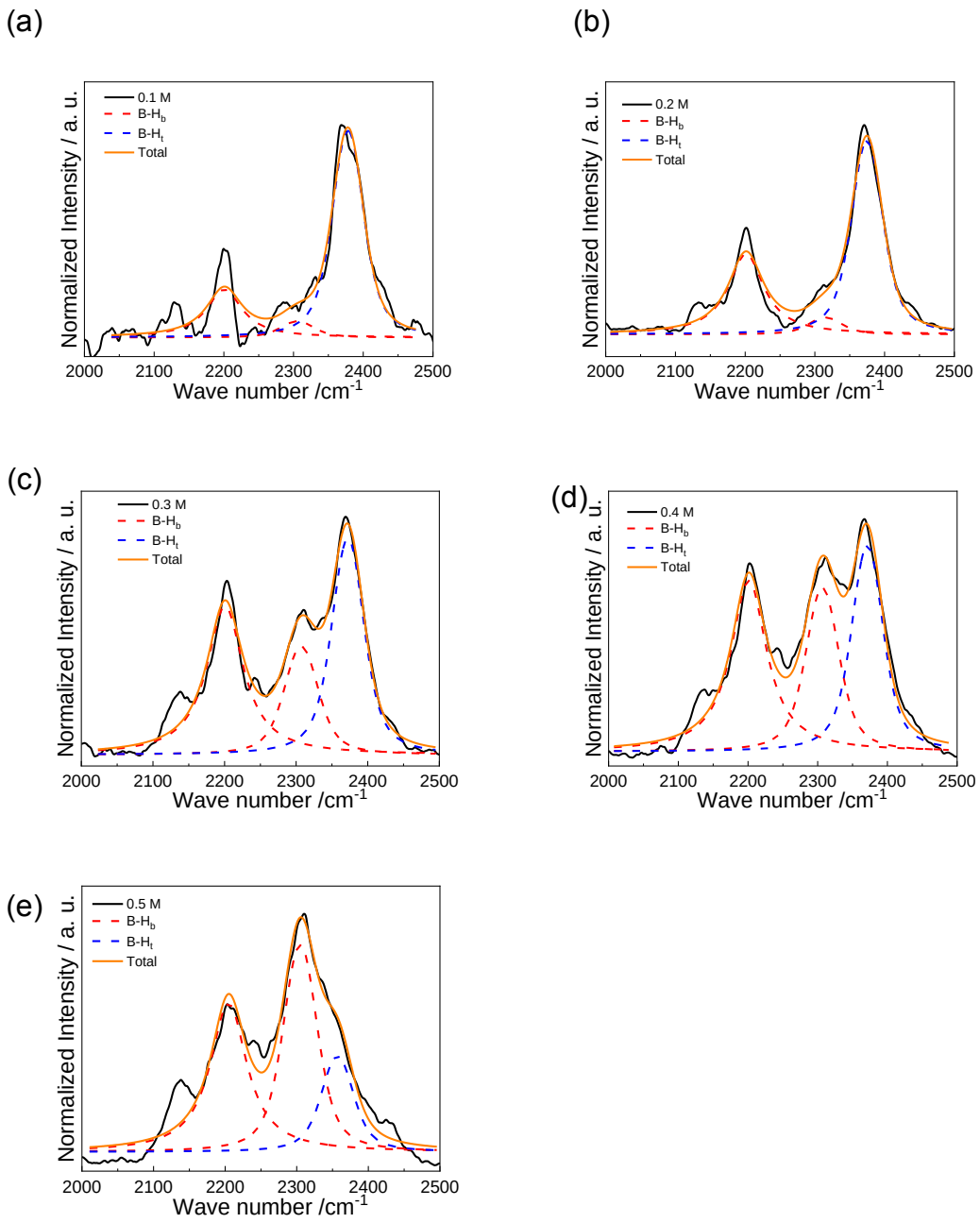

Figure 2-10. Raman spectra and Voigt function fitting results of $Mg(BH_4)_2$/THF in several concentrations (a) 0.1 M (b) 0.2 M (c) 0.3 M (d) 0.4 M and (e) 0.5 M in the region between 2000 and 2500 cm^{-1}

(a)

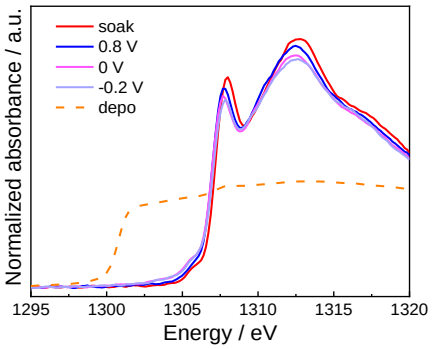

(b)

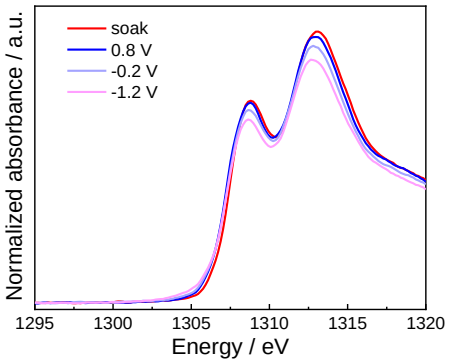

(c)

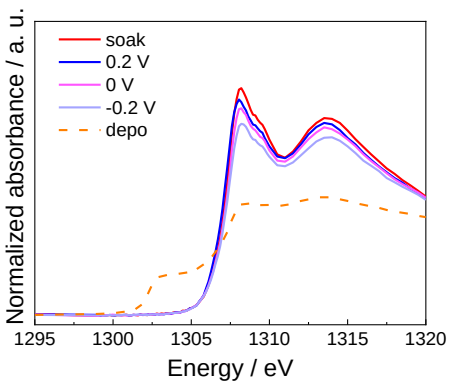

Figure 2-11. Mg *K*-edge XANES spectra obtained from the *operando* XAS measurements for the (a) 0.5 M $Mg(TFSA)_2$/triglyme, (b) 0.5 M $Mg(TFSA)_2$/2-MeTHF, and (c) 0.5 M $Mg(BH_4)_2$/THF electrolytes. The potential is expressed as vs. Mg^{2+}/Mg.

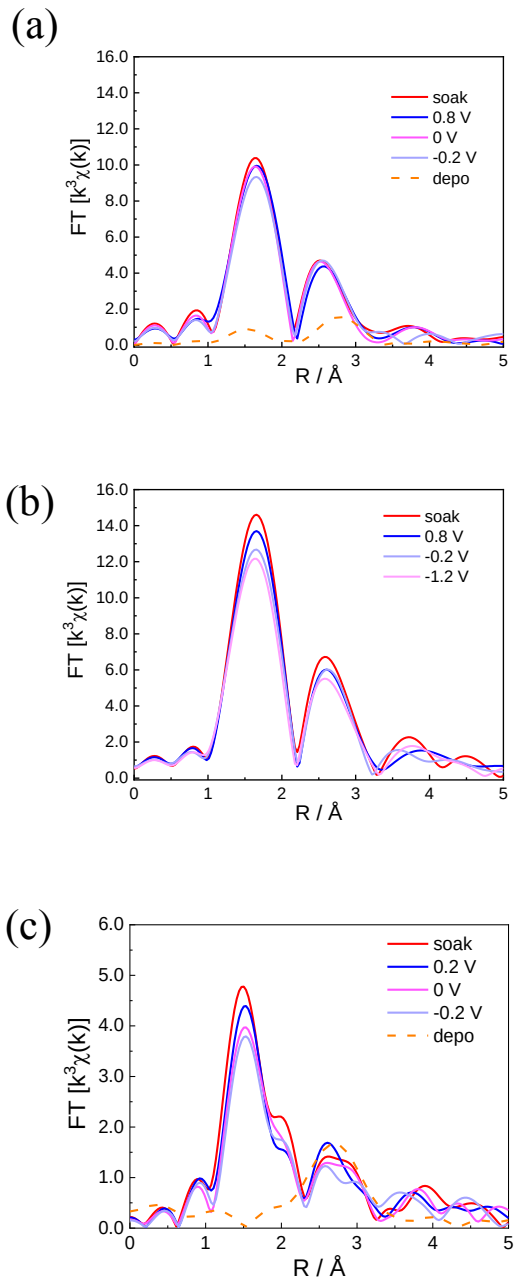

Figure 2-12. Mg *K*-edge Fourier-transformed EXAFS spectra obtained from the *operando* XAS measurements for the (a) 0.5 M $Mg(TFSA)_2$/triglyme, (b) 0.5 M $Mg(TFSA)_2$/2-MeTHF, and (c) 0.5 M $Mg(BH_4)_2$/THF electrolytes. The potential is expressed as vs. Mg^{2+}/Mg.

Table 2-1. Summary of the LUMO and HOMO energy levels for the free anion and coordinated electrolytes

Electrolytes	Free Anion		Coordinated Anion	
	HOMO / eV	LUMO / eV	HOMO / eV	LUMO / eV
$Mg(TFSA)_2$ / triglyme	-8.02	-0.35	-8.92	-1.86
$Mg(TFSA)_2$ / 2-MeTHF [24]	-8.01	-0.35	-9.35	-1.66
$Mg(BH_4)_2$ / THF	-6.74	0.37	-9.06	-1.05

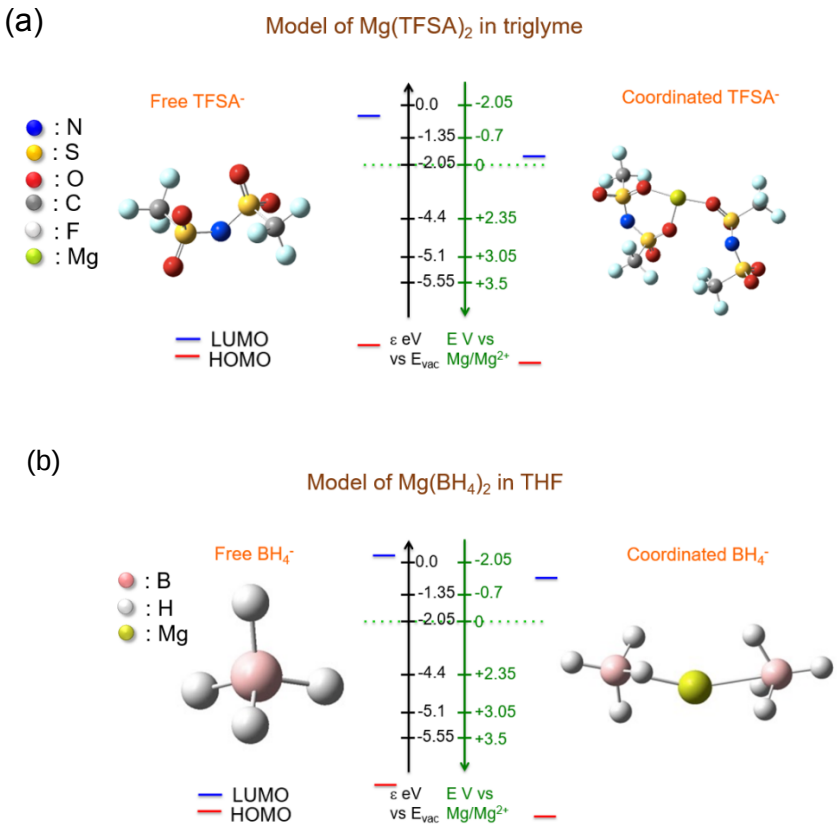

Figure 2-13. DFT cluster calculations in (a) free $TFSA^-$ and $TFSA^-$ coordinated with Mg^{2+} in $Mg(TFSA)_2$/triglyme, (b) free BH_4^- and BH_4^- coordinated with Mg^{2+} in $Mg(BH_4)_2$ /THF.

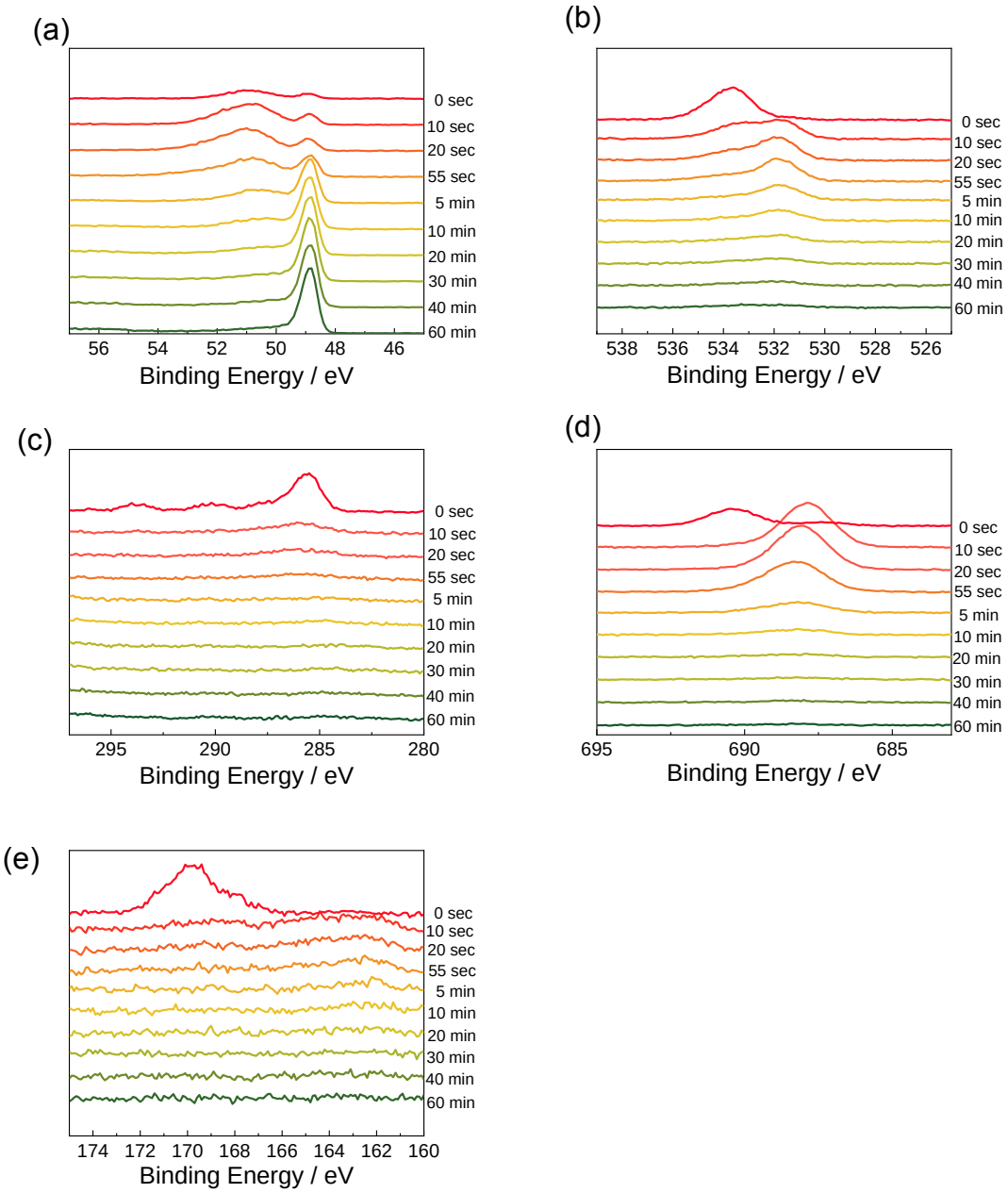

Figure 2-14. XPS spectra for the Mg metal immersed in the 0.5 M $Mg(TFSA)_2$/triglyme; (a) Mg 2p, (b) O 1s, (c) C 1s, (d) F 1s and (e) S 2p. The Ar ion beam sputtering times are marked at the right side of the graph.

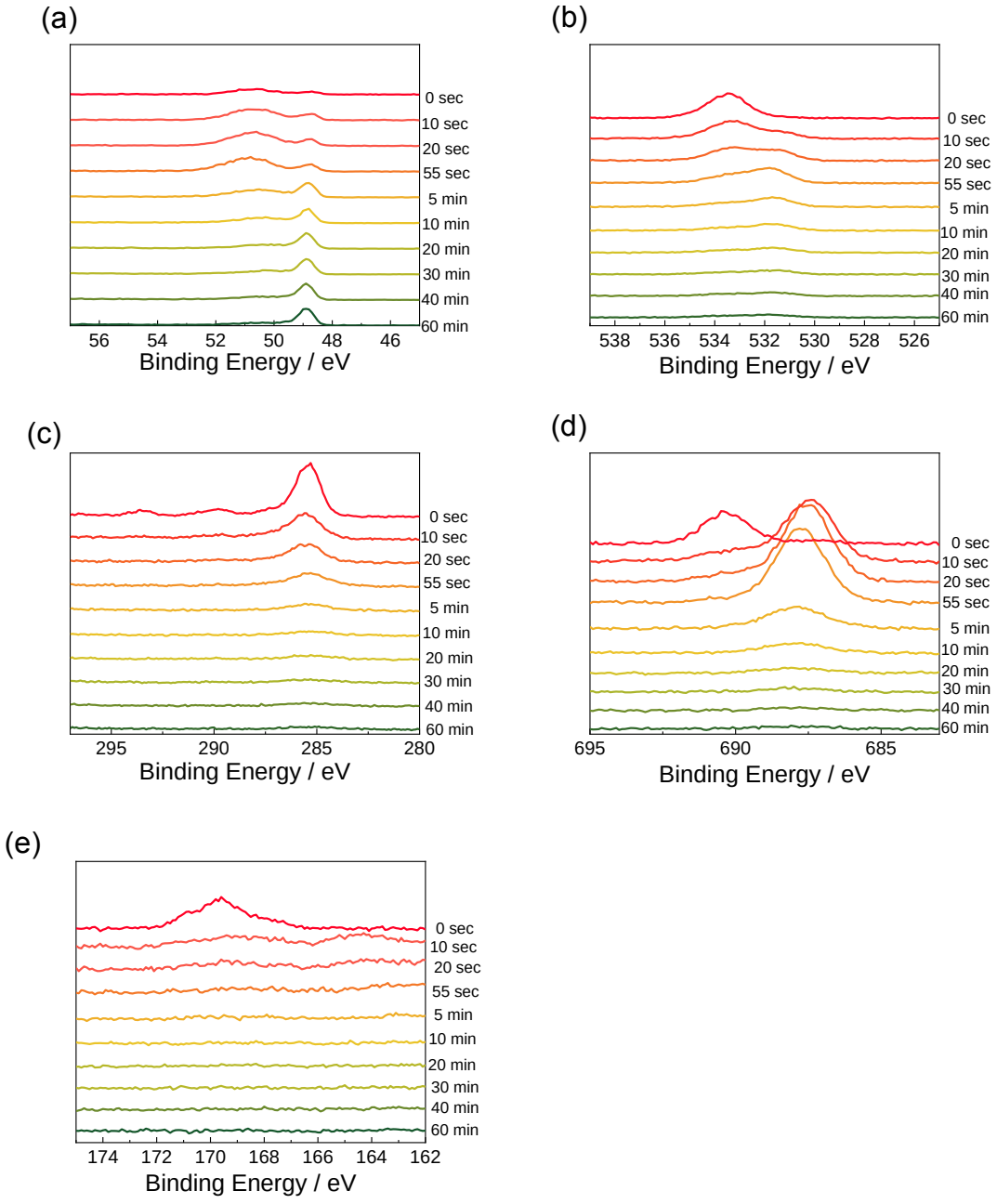

Figure 2-15. XPS spectra for the Mg metal immersed in the 0.5 M $Mg(TFSA)_2$/2-MeTHF; (a) Mg 2p, (b) O 1s, (c) C 1s, (d) F 1s and (e) S 2p. The Ar ion beam sputtering times are marked at the right side of the graph.

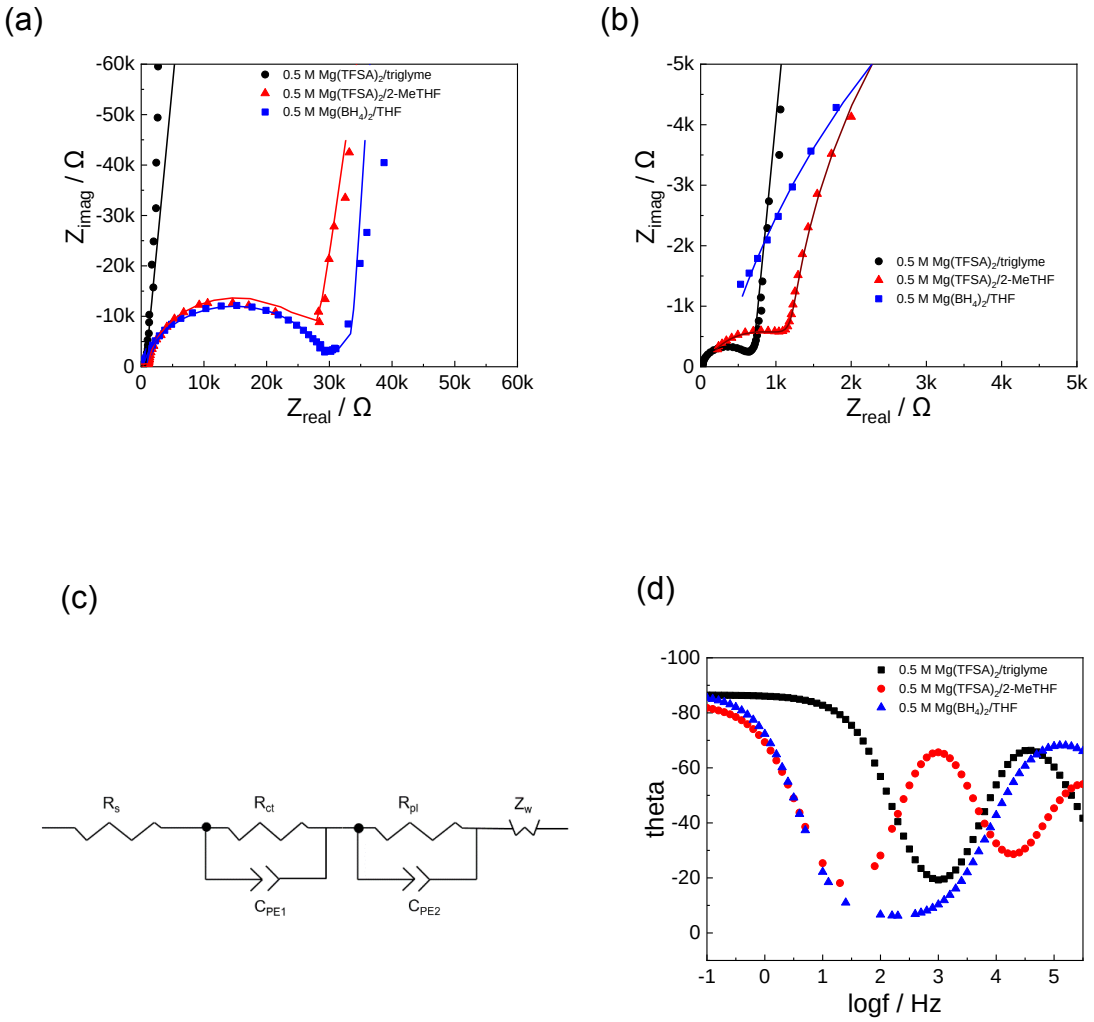

Figure 2-16. (a) Nyquist plots of Mg electrode immersed in 0.5 M $Mg(TFSA)_2$/triglyme, 0.5 M $Mg(TFSA)_2$/2-MeTHF and 0.5 M $Mg(BH_4)_2$/THF electrolytes. Fitted impedance spectra shown in solid line. (b) Enlarged figure of (a) between 0 and 5kΩ. (c) Equivalent circuit model, in which electrolyte solution resistance is R_s, charge transfer resistance is R_{ct}, constant phase element is C_{PE1}, passivation layer resistance is R_{pl}, constant phase element is C_{PE2} and the Warburg impedance is Z_w. (d) Bode phase shift plot that donates the capacitive responses.

Table 2-2. The fitted parameter results of Figure 2-16(a).

Electrolyte	0.5 M $Mg(TFSA)_2$/triglyme	0.5 M $Mg(TFSA)_2$/2-MeTHF	0.5 M $Mg(BH_4)_2$/THF
R_s / Ω	15.2	81.06	233.4
R_{ct} / Ω	642.4	1129	28012
CPE1	5.0×10^{-8}	8.7×10^{-9}	2.5×10^{-9}
p1	0.97	0.87	0.88
C / F	4.1×10^{-8}	2.0×10^{-9}	6.8×10^{-10}
Time constant / s	2.5×10^{-5}	3.2×10^{-6}	2.0×10^{-5}
R_{pl} / Ω	--	26366	--
CPE2	--	3.4×10^{-8}	--
p2	--	0.98	--
C / F	--	3.0×10^{-8}	--
Time constant / s	--	7.9×10^{-4}	--

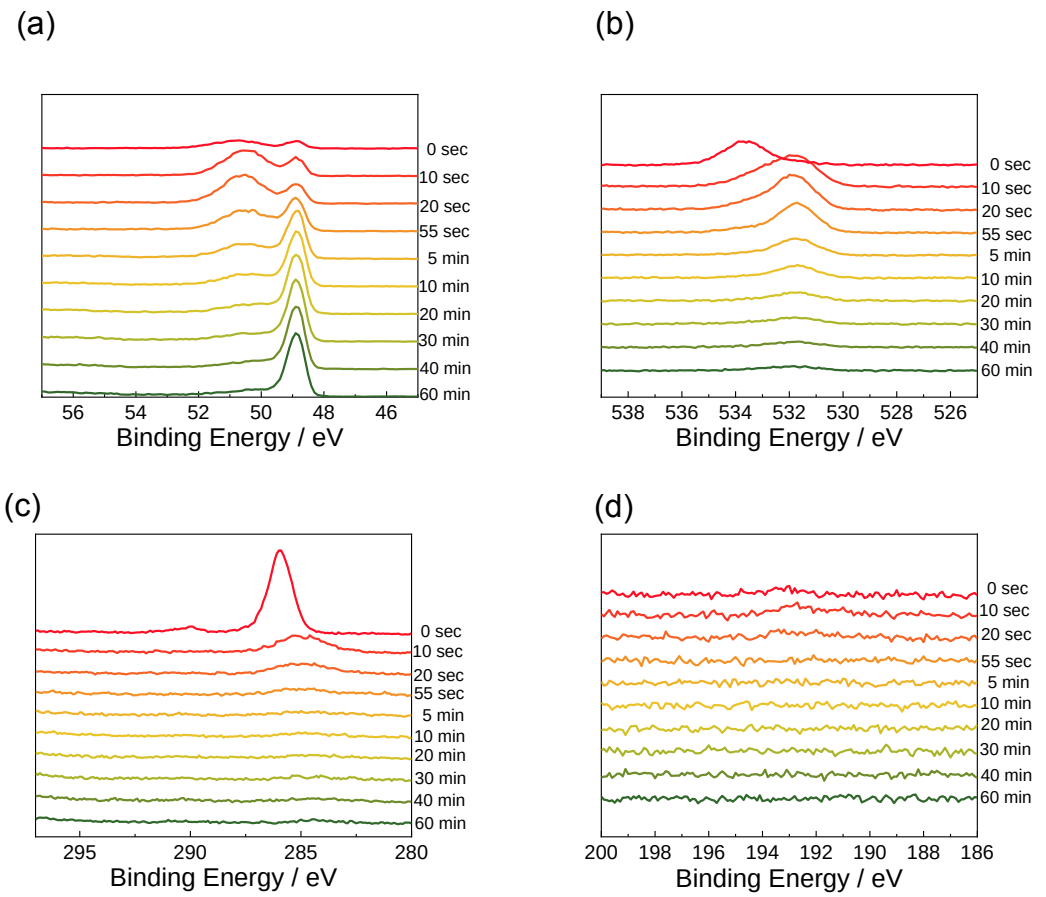

Figure 2-17. XPS spectra for the Mg metal immersed in the 0.5 M $Mg(BH_4)_2$/THF; (a) Mg 2p, (b) O 1s, (c) C 1s and (d) B 1s. The Ar ion beam sputtering times are marked at the right side of the graph.

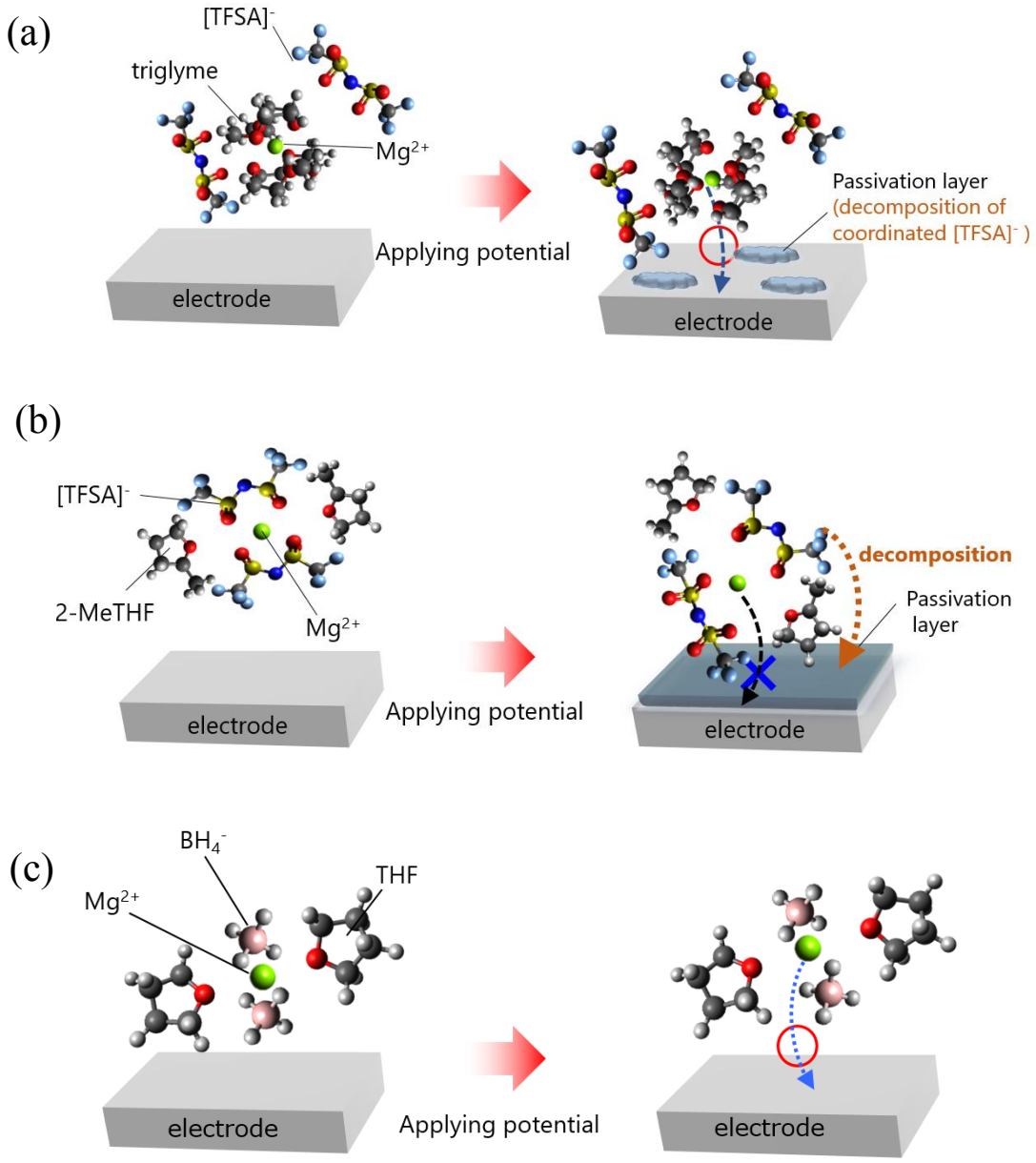

Figure 2-18. Schematic illustrations of the behavior of the magnesium ions at the anode/electrolyte interface in the (a) 0.5 M $Mg(TFSA)_2$/triglyme, (b) 0.5 M $Mg(TFSA)_2$/2-MeTHF, and (c) 0.5 M $Mg(BH_4)_2$/THF electrolytes.

Chapter 3. Effect of Interaction Among Magnesium Ions, Anion and Solvent on Kinetics of Magnesium Deposition Process

3-1. Introduction

With the rapid development of electric automobiles, rechargeable batteries have become increasingly necessary for providing higher energy density and power density than those currently provided by lithium-ion batteries. Magnesium rechargeable batteries are attractive, high-performance systems that use magnesium metal as the anode, which has a high theoretical volumetric capacity (3832 mAh/cm^3) and a relatively low reduction potential (−2.38 V vs. SHE). [1-9] Moreover, the safety and cost of employing magnesium make it a superior choice compared to lithium. [10,11] However, electrolytes that provide reversible magnesium deposition/dissolution reactions are limited, hindering potential applications of these rechargeable magnesium batteries. [12-17] In many organic solutions, which are typically used in lithium-ion batteries, the reversible, electrochemical magnesium deposition/dissolution process is difficult to achieve because passivation films form on the anode surface and inhibit the passage of magnesium ions. [18] Although magnesium organohaloaluminate-based electrolytes provide this reversible process, [5,7,19,20] they are hazardous, corrosive, and exhibit low anodic stability; thus, a breakthrough in the development of suitable electrolytes is necessary.

Recently, it has been reported that reversible Mg deposition/dissolution reactions can occur in non-Grignard and halide-free electrolytes based on “simple” Mg salts;

combination of $Mg(TFSA)_2$, [21-24] $Mg(BH_4)_2$, [25] and weakly coordinating anion, such as, $Mg(CB_{11}H_{12})_2$,[26] $Mg(CB_{11}H_{11}F)_2$,[27] $Mg[Al(HFIP)_4]_2$,[28] $Mg[B(HFIP)_4]_2$ (HFIP=-$OCH(CF_3)_2$)[29,30] and $Mg[B(O_2C_2(CF_3)_4)_2]_2$, [31] and strongly interacting solvents such as glyme. The coulombic efficiency and polarization of magnesium deposition/ dissolution reactions vary depending on the anion species and solvents involved. Recent studies, including those by our group, have suggested that the $[TFSA]^-$ coordinated to the magnesium ions in a $Mg(TFSA)_2$- based electrolyte system undergoes reduction decomposition, inhibiting the magnesium deposition.[32-34] Although deposition is not inhibited with the $Mg(BH_4)_2$/THF electrolyte, a small current density is observed due to the $[BH_4]^-$ coordination to the magnesium ions.[34] Since the coordination between the anion and magnesium ions causes anion decomposition and/or impedes magnesium deposition reactions, separating the magnesium ion from the anion is crucial for accelerating magnesium deposition.

The association between magnesium ions and anions is determined by the interactions among the magnesium ions, anions, and solvents. When a weakly coordinating anion is employed, a wider variety of solvents can be used, which is applicable to magnesium deposition because of the relatively low interaction between the anion and magnesium ion. However, only limited solvents have been studied for use in electrolytes. For reversible Mg deposition/dissolution ether-based solvents with good reducing properties are used. Among them, dimethyl ether (DME) has a relatively high donor number (DN) (24 kcal/mol)[35] and has been the solvent of choice for previous reported electrolytes. Glymes are also typical electrolyte solvents due to their strong solvation of metal cations and their good chemical stabilities. [36,37] The complex formation

constant value becomes larger with increasing number of the coordinating sites in a single ligand molecule. The entropy change caused by the formation of a complex with a multidentate ligand is smaller than that caused by the formation of a complex with the relevant monodentate ligand, resulting in a higher stabilization energy for the former. [38] The solvating energies of the glyme series are in the following order: monoglyme (G1) < diglyme (G2) < triglyme (G3) < tetraglyme (G4).[36] However, higher solvating energies correlate with larger desolvation energies of the metal cation to cause that the kinetics of charge transfer would be sluggish.[39] Thus, developing solvents with relatively low solvation energies is essential. Considering the interactions between magnesium ions, anions, and solvents, as well as the relatively low DN (18 kcal/mol)[40] of 2-MeTHF, we speculate that the solvent 2-MeTHF which could not be used in electrolyte such as $Mg(TFSA)_2$, [32,34] is possible to be used in weakly coordinating anion electrolytes.

In this study, $Mg[B(HFIP)_4]_2$ was chosen as a model magnesium salt, as it has a weakly coordinating anion, to demonstrate the potential for expanding the choice of electrolyte solvent and was compared with that of $Mg(TFSA)_2$. We carried out a comparative study of the electrochemical deposition processes of magnesium in $Mg[B(HFIP)_4]_2$-based and $Mg(TFSA)_2$-based electrolyte systems employing both triglyme and 2-MeTHF solvents. We mainly focused on the interactions among the magnesium ions, anions, and solvent during magnesium deposition and discussed the determining factor on the polarization behavior. The coordination structure of the magnesium ions in the bulk solution of each electrolyte was analyzed by Raman spectroscopy. Subsequently, the dynamic change in the electronic and local structures of the magnesium ions near the anode surface in each electrolyte was examined using the

operando soft X-ray absorption fine structure (SXAS) technique. The reductive stability and decomposition reaction of each anion in these electrolytes was determined by density functional theory (DFT) calculations and X-ray photoelectron spectroscopy (XPS) measurements.

3-2. Experimental

3.2.1. Material preparation

$Mg[B(HFIP)_4]_2$ was synthesized by the dehydrogenation reaction of $Mg(BH_4)_2$ with hexafluoro-2-propanol (hfip-H) in DME. [29] The 0.3 M $Mg[B(HFIP)_4]_2$/triglyme and 0.3 M $Mg[B(HFIP)_4]_2$/2-MeTHF electrolytes were prepared by mixing $Mg[B(HFIP)_4]_2$ with triglyme (KISHIDA CHEMICAL Co., Ltd. >99%) or 2-MeTHF (Merck, >98%), respectively, in an Ar-filled glove box. The 0.5 M $Mg(TFSA)_2$/triglyme and 0.5 M $Mg(TFSA)_2$/2-MeTHF electrolytes were similarly prepared by mixing $Mg(TFSA)_2$ (KISHIDA CHEMICAL Co., Ltd., >99.9%) with triglyme or 2-MeTHF, respectively, in an Ar-filled glove box. To decrease the water content, the $Mg(TFSA)_2$ salt was dried under vacuum at 180 °C for 48 h.

3.2.2. Electrochemical measurements

Cyclic voltammograms (CVs) were collected by three-electrode cells to examine the magnesium deposition/dissolution reactions in each electrolyte. A platinum plate was used as the working electrode and a magnesium rod (99.9%, Nilaco Co., Ltd.) as the counter electrode. Different reference electrodes were used for each electrolyte. For the $Mg(TFSA)_2$/triglyme or $Mg(TFSA)_2$/2-MeTHF electrolytes, a double-junction reference electrode equipped with a microporous glass membrane was employed. The inner part contained silver wire that was inserted into a 0.01 M solution of $AgNO_3$ in triglyme or 2-

MeTHF, and the outer part contained the electrolyte being analyzed. For $Mg[B(HFIP)_4]_2$/triglyme and $Mg[B(HFIP)_4]_2$/2-MeTHF, a magnesium plate was employed as the reference electrode. All the electrodes were polished in an Ar-filled glove box before use. Cyclic voltammetry was performed at 25 ℃ with a potential sweep rate of 10 mV/s. The potential range was −4.0–1.5 V vs. Ag^+/Ag (−1.5–4.0 V vs. Mg^{2+}/Mg) for $Mg(TFSA)_2$/triglyme and $Mg(TFSA)_2$/2-MeTHF and −1.5–3.5 V vs. Mg^{2+}/Mg for $Mg[B(HFIP)_4]_2$/triglyme and $Mg[B(HFIP)_4]_2$/2-MeTHF.

Electrochemical impedance spectroscopy (EIS) was carried out to analyze the differences in the interfacial resistance using a similar cell configuration as that used in the CV measurements. The alternating current (AC) frequency was scanned from 1 MHz to 10 mHz with an amplitude of 50 mV. All experiments, including the electrolyte preparation, cell construction, and electrochemical measurements, were carried out under a dry Ar atmosphere.

3.2.3. Characterization

X-ray diffraction (XRD) was performed using an Ultima Ⅳ diffractometer (Rigaku Co., Inc.) with a Cu Kα X-ray source. Scanning electron microscopy (SEM) images and energy-dispersive X-ray spectroscopy (EDX) spectra were recorded using an S-3400 N instrument (Hitachi HighTech Co.). After the potentiostatic deposition of magnesium metal, the electrochemical cells were disassembled and the obtained electrodes were washed with THF. Subsequently, these electrodes were dried in an Ar-filled glove box overnight. All measurements were performed without air exposure of the samples.

The Raman spectra were collected by a DXR3 Smart Raman spectrometer (Thermo Fisher Scientific) using a 532 nm diode-pumped solid-state laser at room temperature. All the electrolytes were sealed in glass vessels in an Ar-filled glove box and measured between 50 and 1800 cm^{-1} without air exposure.

XPS measurements were performed to analyze the surface structure of magnesium metal deposited galvanostatically on platinum substrate using the 0.3 M $Mg[B(HFIP)_4]_2$/triglyme and 0.3 M $Mg[B(HFIP)_4]_2$/2-MeTHF electrolytes. After the galvanostatic deposition, the electrodes were than rinsed with DME, dried under vacuum, and subsequently sealed in a transfer vessel in the glove box. XPS was performed using a VersaProbe II spectrometer (ULVAC-PHI, Inc.) with an Al Kα X-ray source. Depth profiles were taken by argon sputtering with the ion gun. The emission currents of 20 mA and acceleration voltage of 2 kV were applied. The etching time was 0–100 min for every 10 min.

The *operando* SXAS spectra for the Mg *K*-edge of the electrolytes were recorded by the partial fluorescence yield method at the beamline BL27SU in the SPring-8 synchrotron radiation facility in Hyogo, Japan. A custom-made, three-electrode cell with a Si_3N_4 window[32,34] was used for the *operando* XAS measurements. Pt with a thickness of 30 nm, was deposited as a working electrode onto a Si_3N_4 window with a 100 nm thickness (Norcada Inc.) by magnetron sputtering. The fluorescence X-ray generated from the electrolyte passing through the Si_3N_4 window was detected by a silicon drift detector (Techno X Co., Ltd.). The *operando* cell was assembled in an Ar-filled glove box and transferred into a vacuum chamber for the XAS measurements without air exposure. The *operando* XAS measurements were performed while maintaining the

potential of the working electrode at several values prior to the magnesium deposition. Afterward, the magnesium metal was deposited on the working electrode by applying a potential step method and additional XAS measurements were performed. Magnesium oxide powder was used as references for X-ray energy calibration. Fourier-transformed EXAFS with k^3-weight was calculated using the Athena software package.[41]

DFT calculations were carried out using the Gaussian16 Revision A.03 code to investigate the coordination effect on the electronic states. [42] We calculated the optimized geometries and the corresponding HOMO and LUMO energies of the free $[B(HFIP)_4]^-$ ion and $Mg[B(HFIP)_4]_2$ salt in the triglyme solvent using the polarized continuum model method with the parameters for the triglyme bulk solvent (dielectric constant ε=7.62).

3-3. Results and discussion

3.3.1. Behavior of the magnesium deposition/dissolution reactions

Considering the optimal conductivity of each electrolyte, the concentration of the $Mg[B(HFIP)_4]_2$ and $Mg(TFSA)_2$ were selected as 0.3 M and 0.5 M, respectively. Magnesium metal deposition/dissolution reactions were examined for the 0.5 M $Mg(TFSA)_2$/triglyme, 0.5 M $Mg(TFSA)_2$/2-MeTHF, 0.3 M $Mg[B(HFIP)_4]_2$/triglyme and 0.3 M $Mg[B(HFIP)_4]_2$/2-MeTHF by cyclic voltammetry. Figure 3-1a shows the obtained cyclic voltammograms (CVs) in 0.3 M $Mg[B(HFIP)_4]_2$/triglyme and 0.5 M $Mg(TFSA)_2$/triglyme. In both electrolytes, cathodic and anodic currents, which are attributed to magnesium metal deposition and dissolution reactions, were observed. In contrast to the 0.5 M $Mg(TFSA)_2$/triglyme electrolyte, 0.3 M $Mg[B(HFIP)_4]_2$/triglyme showed significantly lower overpotential and higher current density. CVs were also obtained for 0.5 M $Mg(TFSA)_2$/2-MeTHF and 0.3 M $Mg[B(HFIP)_4]_2$/2-MeTHF (Figure

3-1b), where the cathodic and anodic currents attributed to the magnesium deposition and dissolution reactions were not observed in the 0.5 M $Mg(TFSA)_2$/2-MeTHF electrolyte, as was previously reported.[32, 34] However, these currents were observed in the 0.3 M $Mg[B(HFIP)_4]_2$/2-MeTHF electrolyte under the same conditions. Although the cathodic and anodic current densities of 0.3 M $Mg[B(HFIP)_4]_2$/2-MeTHF were similar to those of 0.3 M $Mg[B(HFIP)_4]_2$/triglyme, the overpotential of the 0.3 M $Mg[B(HFIP)_4]_2$/2-MeTHF electrolyte was higher than that of the 0.3 M $Mg[B(HFIP)_4]_2$/triglyme electrolyte. The coulombic efficiencies of the magnesium metal deposition/dissolution reactions were 94% and 87% in 0.3 M $Mg[B(HFIP)_4]_2$/triglyme and 0.3 M $Mg[B(HFIP)_4]_2$/2-MeTHF, respectively. After the passage of the cathodic current in both electrolytes, the deposited product was characterized as magnesium metal by X-ray diffraction (XRD) (Figure 3-2) and scanning electron microscopy-energy dispersive X-ray spectroscopy (SEM-EDX) (Figures 3-3, 3-4). The morphology of the $Mg[B(HFIP)_4]_2$/2-MeTHF is smoother than that of the $Mg[B(HFIP)_4]_2$/triglyme in Figures 3-3 and 3-4. It has been reported that the deposited Li nuclei decrease in size and become more closely packed as the current density increased for a fixed amount of Li because of increase overpotential.[43] In the case of $Mg[B(HFIP)_4]_2$/2-MeTHF, because the overpotential is higher than that of $Mg[B(HFIP)_4]_2$/triglyme, resulting in a smaller nuclei size of $Mg[B(HFIP)_4]_2$/2-MeTHF than that of $Mg[B(HFIP)_4]_2$/triglyme.

3.3.2. Coordination structure of the magnesium ions in bulk solution

To examine the interactions between the magnesium ions, anions, and solvent molecules in the bulk solutions of those electrolytes, Raman spectra were collected. In bulk solution, magnesium ions compete with the solvent molecules to interact with the anions. If the interaction between the magnesium ion and anion is strong, magnesium ions

will coordinate with both the anion and solvent. In our previous report, Raman spectroscopy revealed that less than 10% of the $[TFSA]^-$ anions in the $Mg(TFSA)_2$/triglyme electrolyte coordinated with magnesium ions, while the remaining existed as solvent-separated ion pairs (SSIPs). The coordination state of $[TFSA]^-$ was also not dependent on the concentration. [34] In the $Mg(TFSA)_2$/2-MeTHF electrolyte, all the $[TFSA]^-$ anions existed as aggregates (AGGs) and the coordination state of $[TFSA]^-$ was not concentration dependent. [32, 34] Typically, Raman peaks corresponding to the CF_3 bending vibration of $[TFSA]^-$ are observed in the region between 710 and 730 cm^{-1} and reflect its interaction with the cation.[37, 44] Therefore, when we collected Raman spectra for the $Mg[B(HFIP)_4]_2$/triglyme and $Mg[B(HFIP)_4]_2$/2-MeTHF electrolytes in this region (Figure 3-5), we speculated that the peaks we observed were similarly attributable to the CF_3 bending vibration of $[B(HFIP)_4]^-$ and reflected its interaction with the cation. The peak top wavenumber of the CF_3 bending vibration for the $Mg[B(HFIP)_4]_2$/triglyme and $Mg[B(HFIP)_4]_2$/2-MeTHF electrolytes (Figure 3-6a) was determined under several concentrations by Voigt function fitting (Figures 3-7, 3-8). Compared to that of $Mg[B(HFIP)_4]_2$/triglyme, the CF_3 bending vibration band of $Mg[B(HFIP)_4]_2$/2-MeTHF appeared at a higher wavenumber. Regarding $[TFSA]^-$, shifts in its wavenumber to higher frequency occur if it is directly bound to the cation and forms a contact ion pair or AGG.[37] Therefore, since the $[B(HFIP)_4]^-$ wavenumber of the $Mg[B(HFIP)_4]_2$/2-MeTHF electrolyte was higher than that of the $Mg[B(HFIP)_4]_2$/triglyme electrolyte, we concluded that the $[B(HFIP)_4]^-$ ions were coordinated to the magnesium ions when the solvent was 2-MeTHF.

The Raman spectra for the $Mg(TFSA)_2$/triglyme and $Mg[B(HFIP)_4]_2$/triglyme electrolytes with various concentrations were collected for the region between 750 and

950 cm^{-1} (Figures 3-9 a, b). The Raman bands corresponding to the CH_2 rocking and C–O–C stretching vibrations of the glyme solvent appear between 800 and 900 cm^{-1};[44, 45] specifically, between 800 and 865 cm^{-1} when the solvent does not coordinate to metal ions and between 865 and 890 cm^{-1} when they do interact.[44] We observed the intensity of the band between 865 and 890 cm^{-1} to increase with increasing salt concentration, which indicated that the triglyme solvent in both electrolyte systems were well coordinated to magnesium ions. To estimate the coordination degree of magnesium ions with triglyme molecules, we focused on the bands near 865–890 cm^{-1} and performed a nonlinear least-squares curve-fitting analysis for the observed Raman spectra (Figures 3-10, 3-11). Using the integrated area of the coordinated triglyme, we compared the solvation degree of the two electrolyte systems. We employed Voigt function fitting to show the ratio of complexation between the magnesium ions and triglyme molecules with various concentrations of the $Mg(TFSA)_2$/triglyme and $Mg[B(HFIP)_4]_2$/triglyme electrolytes (Figure 3-6 b). The plots exhibited straight lines for both electrolytes systems, but the slope of the $Mg(TFSA)_2$/triglyme plot was smaller than that of the $Mg[B(HFIP)_4]_2$/triglyme plot. These results indicated that the triglyme molecules coordinated to magnesium ions stronger in the $Mg[B(HFIP)_4]_2$/triglyme electrolyte than in the $Mg(TFSA)_2$/triglyme electrolyte. Raman peaks around 800 cm^{-1} with increasing salt concentration probably corresponding to the B-O vibration of $[B(HFIP)_4]^-$.[46] Because it presents in Raman spectra of both $Mg[B(HFIP)_4]_2$ electrolytes (Figure 3-9 b,c), with increasing salt concentration, but not observed in $Mg[TFSA]_2$/triglyme electrolyte (Figure 3-9 a), indicating that it's not a solvent-derived peak.

Raman spectra in the region between 750 and 950 cm^{-1} were taken for the $Mg[B(HFIP)_4]_2$/2-MeTHF electrolyte at various concentrations (Figure 3-9 c), where the

peaks assigned to the C–C and C–O stretching modes of 2-MeTHF were observed at 920 cm^{-1}.[34,47,48] It has been reported that when THF coordinates to the cation a peak appears at a wavenumber 10 cm^{-1} lower than those indicative of the C–C and C–O stretching of the non-coordinated THF.[47, 48] This peak was not observed in the Raman spectra of the $Mg[B(HFIP)_4]_2$/2-MeTHF electrolyte, indicating that 2-MeTHF did not directly coordinate to magnesium ions. This result is consistent with the result of $Mg(TFSA)_2$/2-MeTHF, which we previously reported.[32,34] When the $Mg[B(HFIP)_4]_2$/2-MeTHF electrolyte concentration was increased, the new peak that had not been observed in the $Mg(TFSA)_2$/2-MeTHF electrolyte appeared between 865 and 890 cm^{-1}. Additionally, the $Mg[B(HFIP)_4]_2$ crystal unit consists of typical ion pairs, in which the magnesium ion is solvated by three DME molecules. [29] Based on these reports, we assigned the peak at 880 cm^{-1} to the CH_2 rocking and C–O–C stretching vibrations of the glyme molecules coordinated to magnesium ions. These results indicate that the magnesium ions in the $Mg[B(HFIP)_4]_2$/2-MeTHF electrolyte were coordinated to both residual DME and $[B(HFIP)_4]^-$ ions.

3.3.3. Electronic and local structure of the magnesium ions at the interface between the anode and the electrolyte under an applied potential

Operando SXAS measurements were performed for the 0.3 M $Mg[B(HFIP)_4]_2$/triglyme and 0.3 M $Mg[B(HFIP)_4]_2$/2-MeTHF electrolytes, and the X-ray absorption near edge structure (XANES) and Fourier-transformed extended X-ray absorption fine structure (EXAFS) of each electrolyte were evaluated (Figure 3-12).

The XANES spectra (Figure 3-12(a) and (c)) showed different peak intensity ratios at 0 V for the two electrolyte systems, indicating that the coordination environment of the two electrolytes was different. These results were also in agreement with the Raman

spectroscopy results. The XANES spectra of both electrolytes remained unchanged from 0 V to −0.4 V, which was slightly above the potential where magnesium deposition starts. The photon energy at the peak top for each spectrum remained constant over this same range, indicating that the valency of the magnesium ions did not change. However, once the magnesium deposition began the XANES spectra changed drastically.

In the Fourier-transformed EXAFS spectra (Figure 3-12(b) and (d)), two considerable peaks were observed around 1.6 Å and 2.6 Å. For both electrolytes, the distance between the magnesium ion and the first nearest neighbor atom did not change from 0 V to −0.4 V, which indicates that the valency of the magnesium ions did not change and agreed with the XANES results. The intensity of the peak at 1.6 Å in both spectra was nearly constant from 0 V to −0.4 V, indicating that the local structure of the magnesium ions near the negative electrode surface in both electrolytes did not change before magnesium deposition. These behaviors were different from those of $Mg(TFSA)_2$-based electrolytes.[34] In a previous study, we reported an increase in the local structure distortion around the magnesium ions in $Mg(TFSA)_2$-based electrolytes at the magnesium electrode/electrolyte interface during cathodic polarization.[34] Unlike those in the $Mg(TFSA)_2$-based electrolyte, the magnesium ions in $Mg[B(HFIP)_4]_2$-based electrolytes are highly coordinated with the solvent molecules but weakly interact with the anions. Therefore, ligand exchange is relatively inhibited by the applied potential and the local distortion around the magnesium ions in $Mg[B(HFIP)_4]_2$-based electrolytes at the magnesium electrode/electrolyte interface remains unchanged. From the result that the EXAFS oscillations are affected by the applied potential, [34] we also can confirm that the XAS detected the information of magnesium ions in the electrical double layer region.

3.3.4. Reductive stability of the anion

To understand the difference in magnesium deposition behavior for each electrolyte, DFT calculations and XPS were used to identify reductive stabilities of the different anions. DFT calculations were conducted for both Mg-coordinated and Mg-uncoordinated $[B(HFIP)_4]^-$ anions in the $Mg[B(HFIP)_4]_2$ electrolytes (Figure 3-13). The lowest unoccupied molecular orbital (LUMO) energy level of the coordinated $[B(HFIP)_4]^-$ anion was −1.37 eV (−0.6 V vs. Mg^{2+}/Mg), which was much lower than that of the uncoordinated $[B(HFIP)_4]^-$ anion (−0.78 eV; −1.3 V vs. Mg^{2+}/Mg). In $Mg[B(HFIP)_4]_2$ electrolyte system, uncoordinated $[B(HFIP)_4]^-$ anions (free $[B(HFIP)_4]^-$ anions) are more stable than coordinated $[B(HFIP)_4]^-$ anions, as the LUMO energy level of the uncoordinated $[B(HFIP)_4]^-$ anion was much higher than that of the coordinated $[B(HFIP)_4]^-$ anion. When the reductive stability compared with $Mg[TFSA]_2$ electrolyte system,[34] DFT results show that, coordinated $[B(HFIP)_4]^-$ anions are also stable than coordinated $[TFSA]^-$ anions under the potential of the magnesium deposition, even the LUMO energy of the $[B(HFIP)_4]^-$ decrease upon coordination to the magnesium ions. The magnesium deposition is not inhibited by the decomposition of the $[B(HFIP)_4]^-$. Therefore, the quasi-reversible magnesium deposition/dissolution reactions occurred in $Mg[B(HFIP)_4]_2$/2-MeTHF.

To clarify the decomposition of $[B(HFIP)_4]^-$ on the magnesium metal surface, we analyzed the magnesium metal after immersion into 0.3 M $Mg[B(HFIP)_4]_2$/triglyme and 0.3 M $Mg[B(HFIP)_4]_2$/2-MeTHF. Fluorine species, a reduction product of the $[TFSA]^-$ anions, were observed on the surface of the magnesium metal in the $Mg(TFSA)_2$-based electrolytes.[33,34,49] Furthermore, XPS measurements indicated that the reduction attributable to the $[B(HFIP)_4]^-$anion was negligible on the magnesium metal surface when compared to that of the anion in $Mg(TFSA)_2$-based electrolytes (Figures 3-14, 3-15d),

which consistent with the recent report. [50] These results indicate that the $[B(HFIP)_4]^-$ anion is more stable for the magnesium metal than the $[TFSA]^-$ anion.

To further examine the interfacial resistance of the Mg anode, electrochemical impedance spectroscopy (EIS) was performed, where Nyquist plots of the Mg electrode immersed in different electrolytes were developed (Figure 3-16 a) and fitting parameters were evaluated using an equivalent electrical circuit (Figure 3-16 c) (Table 3-1). The solution resistance (R_s) value changes for each three-electrode cell because the position of the reference electrode cannot be correctly fixed in the cell. The Nyquist and bode plots showed that only one semicircle appeared in both electrolytes around a high frequency (10^5 Hz), which was attributed to the charge transfer resistance (R_{ct}). [34,51,52] The R_{ct} of the 0.3 M $Mg[B(HFIP)_4]_2$/2-MeTHF electrolyte was comparable to that of the 0.3 M $Mg[B(HFIP)_4]_2$/triglyme electrolyte (Table 3-1). In our previous study, we reported that the Mg deposition was inhibited by the decomposition of $[TFSA]^-$ anions due to the high passivation layer resistance (R_{pl}).[34] Compared to those of the $Mg(TFSA)_2$-based electrolyte, there are negligible passivation layer resistance of anionic decomposition, and the R_{ct} of the $Mg[B(HFIP)_4]_2$-based electrolyte were significantly small. These results indicated that it was difficult for the $[B(HFIP)_4]^-$ anions to decompose, which was due to the high reduction stability of the anion; this was in agreement with the XPS and DFT calculation results. Furthermore, the R_{ct} of the 0.3 M $Mg[B(HFIP)_4]_2$/2-MeTHF electrolyte was larger than that of the 0.3 M $Mg[B(HFIP)_4]_2$/triglyme electrolyte, corresponded to the slow interfacial reaction kinetics for the deposition/dissolution reactions (Figure 3-1).

3.3.5. Discussion

Figure 3-17 schematically illustrates the behavior of the magnesium ions at the anode/electrolyte interface. Based on the previous reports, [33, 34] the $[TFSA]^-$ coordinated to the magnesium ions in $Mg(TFSA)_2$-based electrolytes experience reduction decomposition, and this inhibits the magnesium deposition. Compared with the $Mg(TFSA)_2$/triglyme electrolytes, the $Mg[B(HFIP)_4]_2$/triglyme electrolyte showed excellent Coulombic efficiency and small polarization for the magnesium deposition/dissolution reactions. This is because magnesium ions highly coordinated with the solvent, the interaction between Mg^{2+} and $[B(HFIP)_4]^-$ is relatively week, compare to $[TFSA]^-$ anion. *operando* SXAS revealed that the coordination structures of the magnesium ions at the interface in the $Mg[B(HFIP)_4]_2$ electrolyte remained unchanged under applied potential. Consequently, the magnesium deposition is not inhibited by the decomposition of $[B(HFIP)_4]^-$ due to the high reduction stability, resulting in higher coulombic efficiency and smaller polarization than $Mg(TFSA)_2$ electrolyte in magnesium deposition/dissolution reactions.

Compared with $Mg(TFSA)_2$/2-MeTHF electrolyte, although $[B(HFIP)_4]^-$ coordinate with the magnesium ions in $Mg[B(HFIP)_4]_2$/2-MeTHF, the quasi-reversible magnesium deposition/dissolution reactions still occurred under the same condition. This is because the coordinated $[B(HFIP)_4]^-$ anions are more stable than coordinated $[TFSA]^-$ anions under the potential of the magnesium deposition, even the LUMO energy of the $[B(HFIP)_4]^-$ decrease upon coordination to the magnesium ions. The magnesium deposition is not inhibited by the decomposition of the $[B(HFIP)_4]^-$. However, the interaction between magnesium ions and $[B(HFIP)_4]^-$ in the $Mg[B(HFIP)_4]_2$/2-MeTHF is stronger than $Mg[B(HFIP)_4]_2$/triglyme electrolyte. These coordinated $[B(HFIP)_4]^-$ would be reduced easily than free $[B(HFIP)]^-$. The lower Coulombic efficiency of the

magnesium deposition/dissolution in $Mg[B(HFIP)_4]_2$/2-MeTHF is due to the partial reductive decomposition of $[B(HFIP)_4]^-$ during the magnesium deposition process.

3-4. Conclusions

In this study, the effects of anion species and solvents on the coulombic efficiency and polarization of magnesium deposition/dissolution reactions were analyzed using $Mg[B(HFIP)_4]_2$/triglyme, $Mg[B(HFIP)_4]_2$/2-MeTHF, $Mg(TFSA)_2$/triglyme, and $Mg(TFSA)_2$/2-MeTHF electrolytes. When triglyme was the solvent, the cyclic voltammetry demonstrates that $Mg[B(HFIP)_4]_2$/triglyme shows significantly lower overpotential and high Coulomb efficiency for magnesium deposition/dissolution reactions than Mg $(TFSA)_2$/triglyme. When using 2-MeTHF solvent, magnesium deposition/dissolution reactions did not occur in $Mg[TFSA]_2$/2-MeTHF electrolyte. However, the reactions occurred in the $Mg[B(HFIP)_4]_2$/2-MeTHF electrolyte although the Coulombic efficiency was lower and overpotential was higher than $Mg[B(HFIP)_4]_2$/triglyme. Raman spectra showed that the magnesium ions largely coordinated to the solvent molecules in the $Mg[B(HFIP)_4]_2$/triglyme electrolyte, but coordinated to the $[B(HFIP)_4]^-$ in $Mg[B(HFIP)_4]_2$/2-MeTHF. *Operando* SXAS revealed that the local distortion around the magnesium ions remained unchanged at the magnesium electrode/electrolyte interface in the $Mg[B(HFIP)_4]_2$/triglyme and 2-MeTHF electrolytes. Our DFT, XPS, and EIS results indicated that $[B(HFIP)_4]^-$ decomposition in the $Mg[B(HFIP)_4]_2$/triglyme electrolyte was hard to occur due to the high reduction stability of uncoordinated $[B(HFIP)_4]^-$ anion, resulting in higher coulombic efficiency and smaller polarization. The opposite was observed for the $Mg[B(HFIP)_4]_2$/2-MeTHF electrolyte, where reduction decomposition easily occurred because the magnesium and $[B(HFIP)_4]^-$ interactions were stronger in the $Mg[B(HFIP)_4]_2$/2-MeTHF electrolyte than

those in the $Mg[B(HFIP)_4]_2$/triglyme electrolyte. This study demonstrates the importance of controlling the interactions between magnesium ions and anions, which can be done by selecting suitable anions and solvents. We believe that our findings can significantly promote developments of new electrolytes for magnesium rechargeable batteries.

References

1. D. Aurbach, Z. Lu, A. Schechter, Y. Gofer, H. Gizbar, R. Turgeman, Y. Cohen, M. Moshkovich and E. Levi, *Nature*, **2000**, 407, 724-727.

2. D. Aurbach, Y. Gofer, A. Schechter, O. Chusid, H. Gizbar, Y. Cohen, M. Moshkovich and R. Turgeman*, J. Power Sources,* **2001,** 97-8, 269-273.

3. T. D. Gregory, R. J. Hoffman and R. C. Winterton, *J. Electrochem. Soc*., **1990**, 137, 775-780.

4. P. Novak, R. Imhof and O. Haas, *Electrochim Acta*, **1999**, 45, 351-367.

5. D. Aurbach, H. Gizbar, A. Schechter, O. Chusid, H. E. Gottlieb, Y. Gofer and I. Goldberg, *J. Electrochem. Soc*., **2002,** 149, A115-A121.

6. J. O. Besenhard and M. Winter, *Chemphyschem,* **2002**, 3, 155-+.

7. D. Aurbach, A. Schechter, M. Moshkovich and Y. Cohen, *J. Electrochem. Soc*., **2001**, 148, A1004-A1014.

8. B. Dunn, H. Kamath and J. M. Tarascon, *Science,* **2011**, 334, 928-935.

9. H. D. Yoo, I. Shterenberg, Y. Gofer, G. Gershinsky, N. Pour and D. Aurbach, Energ *Environ Sci*, **2013**, 6, 2265-2279.

10. J. O. Besenhard and M. Winter*, Chemphyschem*, **2002**, 3, 155-159.

11. T. D. Gregory, R. J. Hoffman and R. C. Winterton, *J. Electrochem. Soc*., **1990,** 137, 775.

12. F. F. Liu, T. T. Wang, X. B. Liu and L. Z. Fan*, Adv. Energy Mater*., **2020**, 2000787.

13. J. Muldoon, C. B. Bucur and T. Gregory, *Angew. Chem*., **2017,** 56, 12064-12084.

14. X. Y. Zhao, Z. Zhao-Karger, M. Fichtner and X. D. Shen, *Angew. Chem.***, 2020**, 59, 5902-5949.

15. J. Z. Niu, Z. H. Zhang and D. Aurbach, *Adv. Energy Mater*., **2020**, 10, 2000697.

16. P. W. Wang and M. R. Buchmeiser*, Adv. Funct. Mater*., **2019**, 29, 1905248.

17. H. Zhang, X. Liu, H. Li, I. Hasa and S. Passerini, *Angew. Chem., Int. Ed*., **2020**, 59, 2-21.

18. Z. Lu, A. Schechter, M. Moshkovich and D. Aurbach*, J Electroanal Chem*, **1999**, 466, 203-217.

19. O. Mizrahi, N. Amir, E. Pollak, O. Chusid, V. Marks, H. Gottlieb, L. Larush, E. Zinigrad and D. Aurbach, *J. Electrochem. Soc*., **2008**, 155, A103-A109.

20. H. S. Kim, T. S. Arthur, G. D. Allred, J. Zajicek, J. G. Newman, A. E. Rodnyansky, A. G. Oliver, W. C. Boggess and J. Muldoon, *Nat. Commun.*, **2011**, 2, 1-6.

21. S.-Y. Ha, Y.-W. Lee, S. W. Woo, B. Koo, J.-S. Kim, J. Cho, K. T. Lee, N.-S. J. A. a. m. Choi and interfaces, *ACS Appl. Mater. Interfaces*, **2014,** 6, 4063-4073.

22. Y. Orikasa, T. Masese, Y. Koyama, T. Mori, M. Hattori, K. Yamamoto, T. Okado, Z.-D. Huang, T. Minato and C. Tassel, *Sci. Rep*., **2014**, 4, 5622.

23. T. Fukutsuka, K. Asaka, A. Inoo, R. Yasui, K. Miyazaki, T. Abe, K. Nishio and Y. Uchimoto, *Chem Lett*, **2014**, 43, 1788-1790.

24. I. T. Kim, K. Yamabuki, M. Morita, H. Tsutsumi and N. Yoshimoto, *J. Power Sources*, **2015**, 278, 340-343.

25. R. Mohtadi, M. Matsui, T. S. Arthur and S. J. Hwang, *Angew. Chem.,* **2012,** 51, 9780-9783.

26. O. Tutusaus, R. Mohtadi, T. S. Arthur, F. Mizuno, E. G. Nelson and Y. V. Sevryugina, *Angew. Chem*., **2015**, 54, 7900-7904.

27. N. T. Hahn, T. J. Seguin, K. C. Lau, C. Liao, B. J. Ingram, K. A. Persson and K. R. Zavadil, *J. Am. Chem. Soc.,* **2018**, 140, 11076-11084.

28. J. T. Herb, C. A. Nist-Lund and C. B. Arnold, *ACS Energy Lett*., **2016,** 1, 1227-1232.

29. Z. Zhao-Karger, M. E. G. Bardaji, O. Fuhr and M. Fichtner, *J. Mater. Chem. A*, **2017,** 5, 10815-10820.

30. Z. Zhao-Karger, R. Y. Liu, W. X. Dai, Z. Y. Li, T. Diemant, B. P. Vinayan, C. B. Minella, X. W. Yu, A. Manthiram, R. J. Behm, M. Ruben and M. Fichtner, *ACS Energy Lett*., **2018**, 3, 2005-2013.

31. J. Luo, Y. J. Bi, L. P. Zhang, X. Y. Zhang and T. B. L. Liu, *Angew. Chem.,* **2019**, 58, 6967-6971.

32. M. Hattori, K. Yamamoto, M. Matsui, K. Nakanishi, T. Mandai, A. Choudhary, Y. Tateyama, K. Sodeyama, T. Uchiyama and Y. Orikasa, *J. Phys. Chem. C*, **2018**, 122, 25204-25210.

33. R. Jay, A. W. Tomich, J. Zhang, Y. F. Zhao, A. De Gorostiza, V. Lavallo and J. C. Guo, *ACS Appl. Mater. Interfaces*, **2019,** 11, 11414-11420.

34. F. Tuerxun, K. Yamamoto, M. Hattori, T. Mandai, K. Nakanishi, A. Choudhary, Y. Tateyama, K. Sodeyama, A. Nakao, T. Uchiyama, M. Matsui, K. Tsuruta, Y. Tamenori, K. Kanamura and Y. Uchimoto, *ACS Appl. Mater. Interfaces*, **2020**, 12, 25775-25785.

35. Q. L. Zou and Y. C. Lu, *J. Phys. Chem. Lett*., **2016,** 7, 1518-1525.

36. S. Tsuzuki, T. Mandai, S. Suzuki, W. Shinoda, T. Nakamura, T. Morishita, K. Ueno, S. Seki, Y. Umebayashi, K. Dokko and M. Watanabe, *Phys. Chem. Chem. Phys*., **2017**, 19, 18262-18272.

37. C. Zhang, K. Ueno, A. Yamazaki, K. Yoshida, H. Moon, T. Mandai, Y. Umebayashi, K. Dokko and M. Watanabe, *J. Phys. Chem. B*, **2014,** 118, 5144-5153.

38. T. Kimura, K. Fujii, Y. Sato, M. Morita and N. Yoshimoto, *J. Phys. Chem. C*, **2015,** 119, 18911-18917.

39. N. N. Rajput, T. J. Seguin, B. M. Wood, X. H. Qu and K. A. Persson, *Topics Curr Chem*, **2018**, 376.

40. F. M. Kerton, Rsc Green *Chem Ser,* **2009**, 2, 1-226.

41. B. Ravel and M. Newville*, J. Synchrotron Radiat*., **2005**, 12, 537-541.

42. M. Frisch, G. Trucks, H. B. Schlegel, G. E. Scuseria, M. A. Robb, J. R. Cheeseman, G. Scalmani, V. Barone, B. Mennucci and G. Petersson, Inc., Wallingford CT, **2009**, 201.

43. A. Pei, G. Zheng, F. Shi, Y. Li and Y. Cui, *Nano Lett.,* **2017**, 17, 1132-1139.

44. D. Brouillette, D. E. Irish, N. J. Taylor, G. Perron, M. Odziemkowski and J. E. Desnoyers, *Phys. Chem. Chem. Phys*., **2002,** 4, 6063-6071.

45. Z. Zhang, Z. Cui, L. Qiao, J. Guan, H. Xu, X. Wang, P. Hu, H. Du, S. Li and X. Zhou, *Adv. Energy Mater.,* **2017**, 7, 1602055.

46. C. C. Alves, T. B. C. Campos and W. A. Alves, *Spectrochim Acta A*, **2012,** 97, 1085-1088.

47. R. L. Benevenuto and W. A. Alves, *J Raman Spectrosc,* **2008**, 39, 490-494.

48. H. Kuwata, M. Matsui and N. Imanishi, *J. Electrochem. Soc*., 2017, 164, A3229-A3236.

49. T. Mandai, *ACS Appl. Mater. Interfaces*, **2020**, DOI: 10.1021/acsami.0c09948.

50. S. J. Kang, H. Kim, S. Hwang, M. Jo, M. Jang, C. Park, S. T. Hong and H. Lee, *ACS Appl. Mater. Interfaces*, **2019,** 11, 517-524.

51. O. Tutusaus, R. Mohtadi, N. Singh, T. S. Arthur and F. Mizuno, *ACS Energy Lett***.,** **2017,** 2, 224-229.

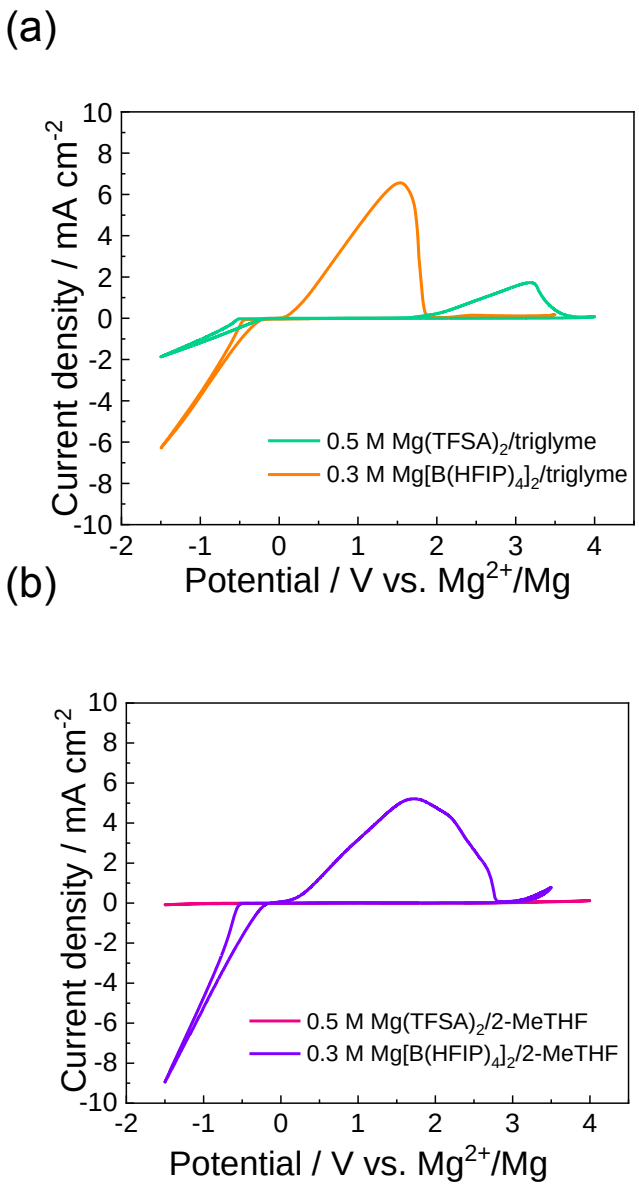

Figure 3-1. Cyclic voltammograms of (a) 0.3 M $Mg[B(HFIP)_4]_2$/triglyme and 0.5 M $Mg[TFSA]_2$/ triglyme (b) 0.3 M $Mg[B(HFIP)_4]_2$/2-MeTHF and 0.5 M $Mg(TFSA)_2$/2-MeTHF at a scanning rate of 10 mV/sec.

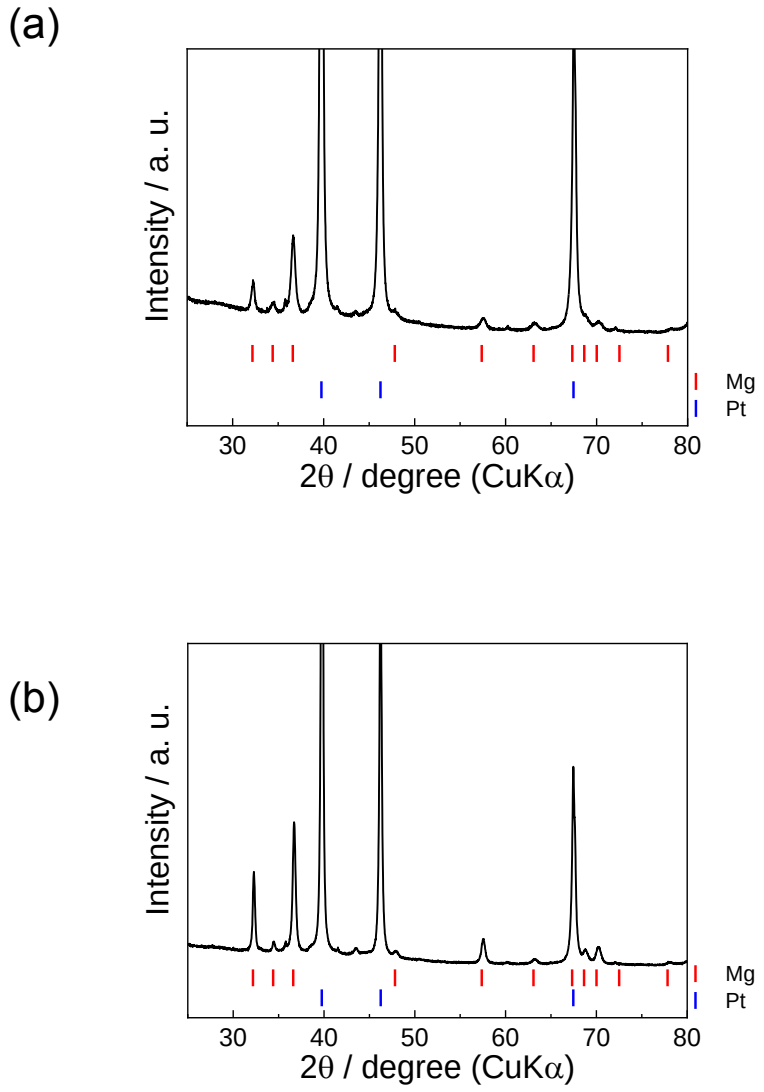

Figure 3-2. XRD patterns of electrodeposited of (a) 0.3 M $Mg[B(HFIP)_4]_2$/triglyme (b) 0.3 M $Mg[B(HFIP)_4]_2$/2-MeTHF on Pt substrate.

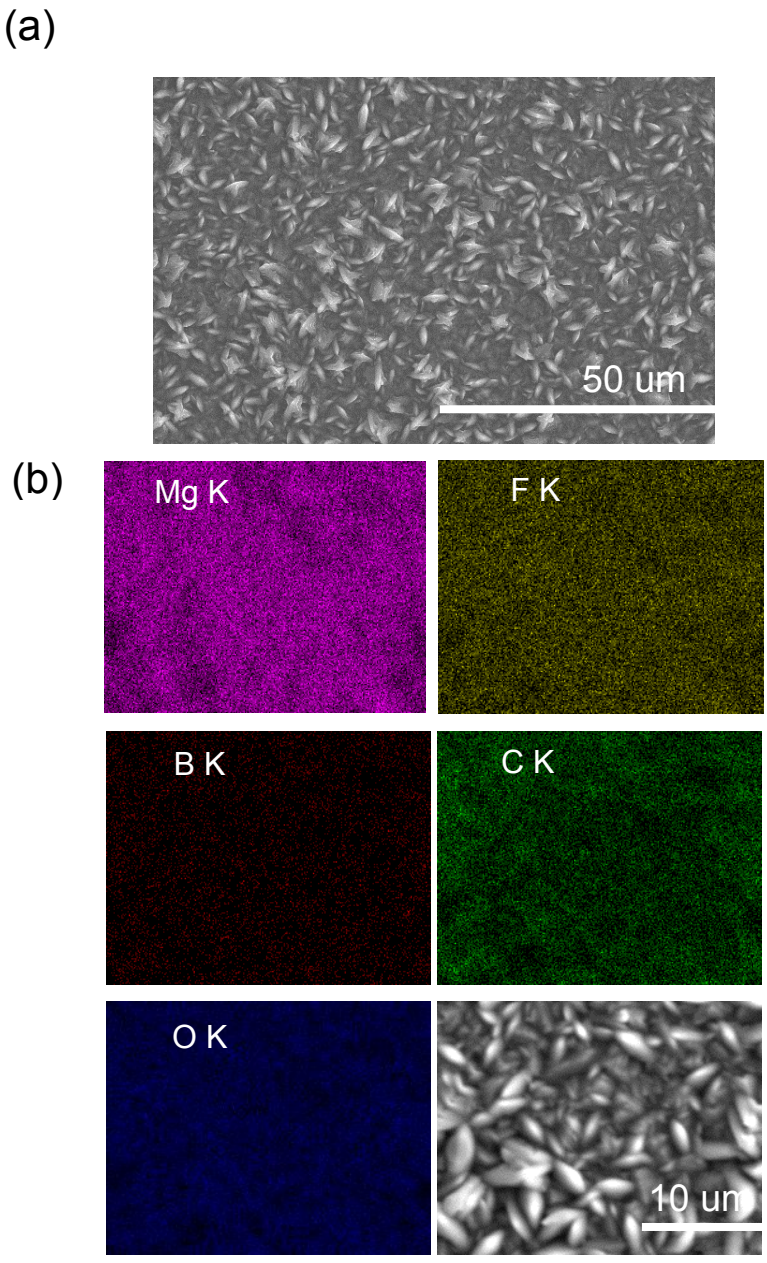

Figure 3-3. (a) SEM image, (b) EDX mapping and spectrum of Pt substrate after electrochemical measurements in 0.3 M $Mg[B(HFIP)_4]_2$/triglyme.

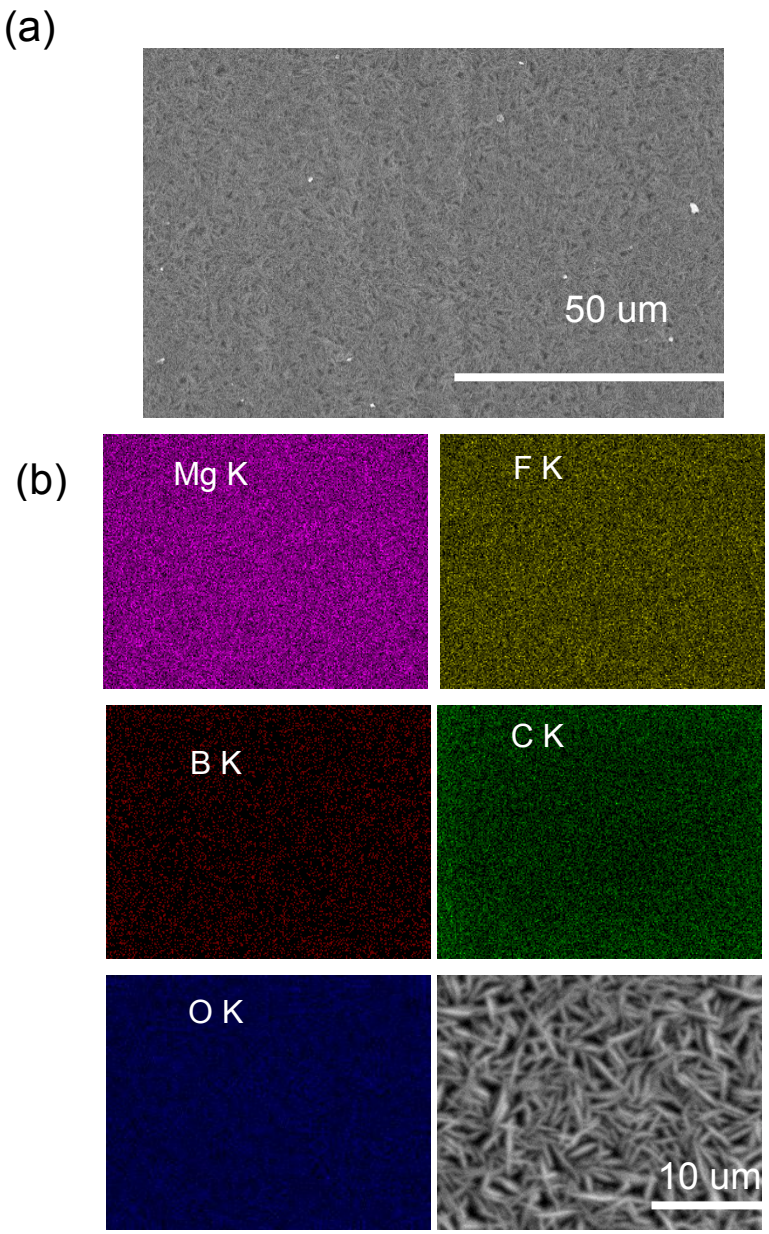

Figure 3-4. (a) SEM image, (b) EDX mapping and spectrum of Pt substrate after electrochemical measurements in 0.3 M $Mg[B(HFIP)_4]_2$/2-MeTHF.

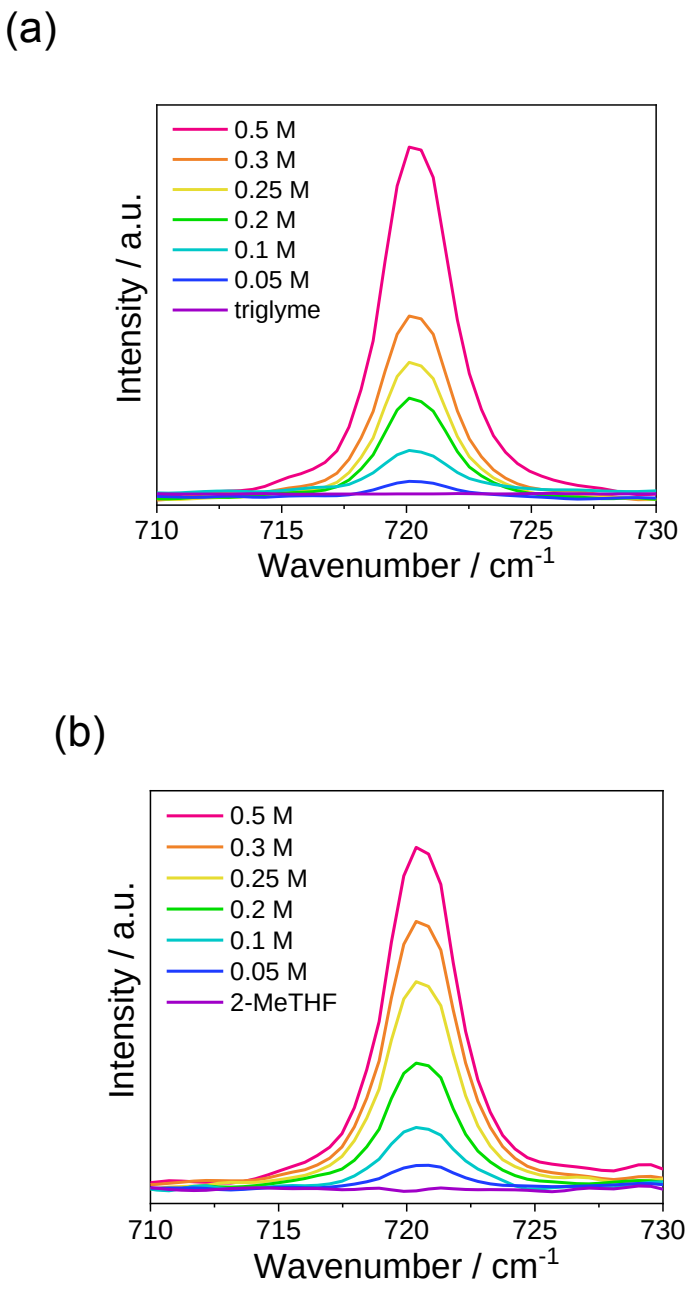

Figure 3-5. Raman spectra of (a) $Mg[B(HFIP)_4]_2$/triglyme and (b) $Mg[B(HFIP)_4]_2$/2-MeTHF with several concentrations in the region between 710 and 730 cm^{-1}

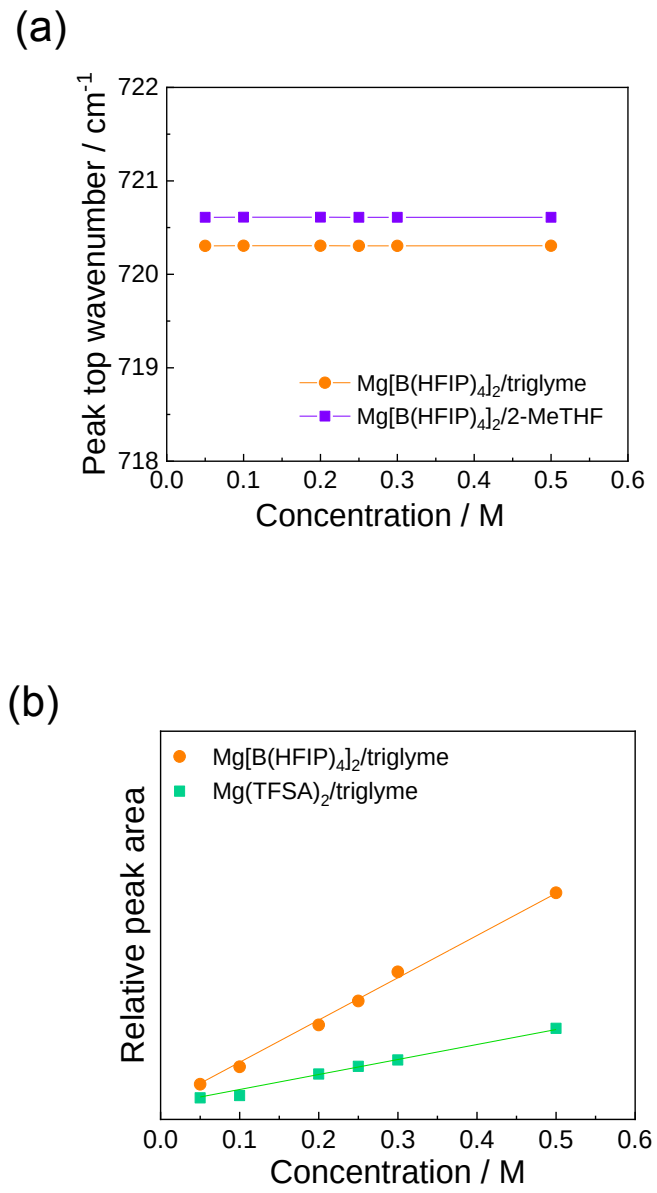

Figure 3-6. (a) Peak top wavenumber of $Mg[B(HFIP)_4]_2$/triglyme and $Mg[B(HFIP)_4]_2$/2-MeTHF plotted against concentration in the region between 710 and 730 cm^{-1}. (b) Relative peak area of $Mg[B(HFIP)_4]_2$/triglyme and $Mg[TFSA]_2$/ triglyme with several concentrations.

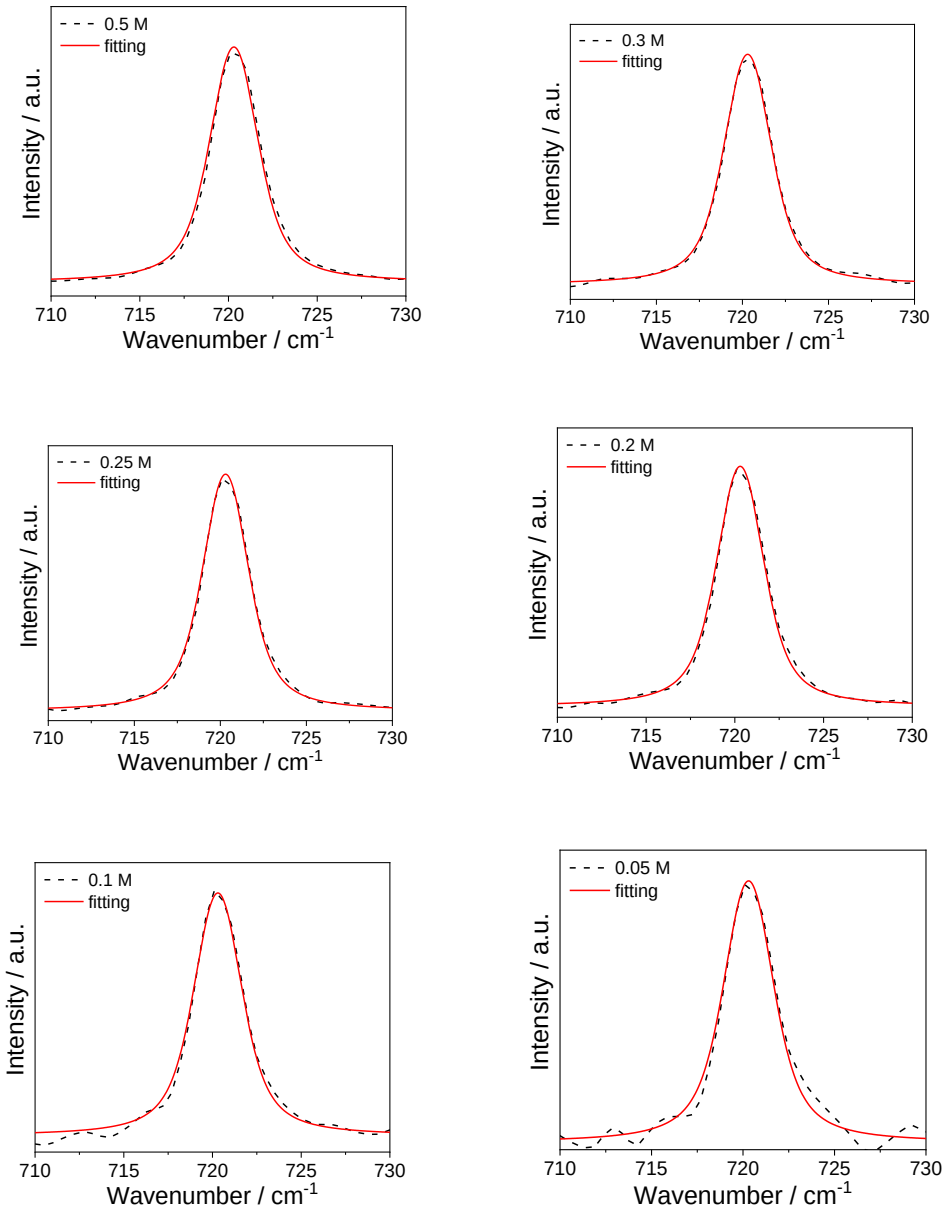

Figure 3-7. Raman spectra and voigt function fitting results of $Mg[B(HFIP)_4]_2$/triglyme in several concentrations in the wave number between 710 and 730 cm^{-1}.

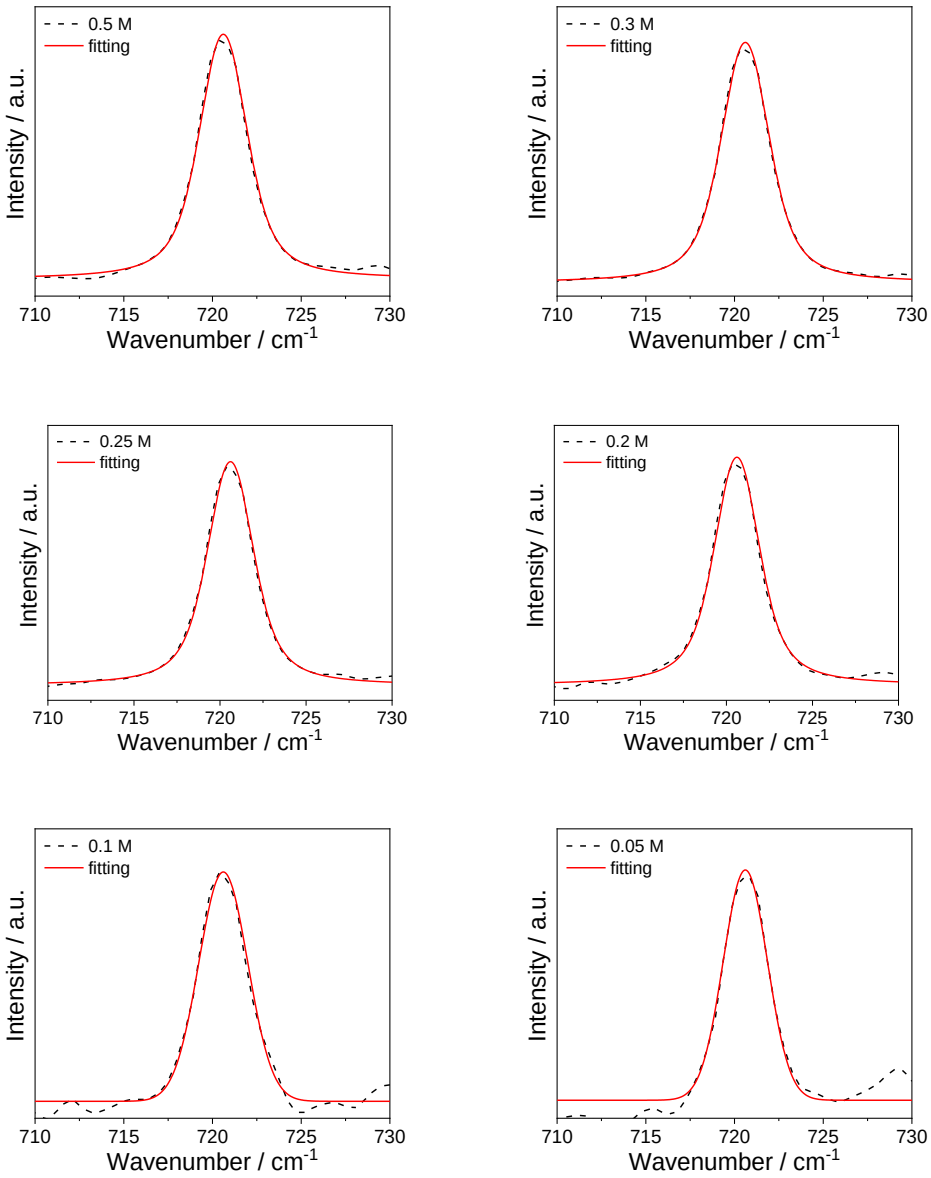

Figure 3-8. Raman spectra and Voigt function fitting results of $Mg[B(HFIP)_4]_2$/2-MeTHF in several concentrations in the wave number between 710 and 730 cm^{-1}.

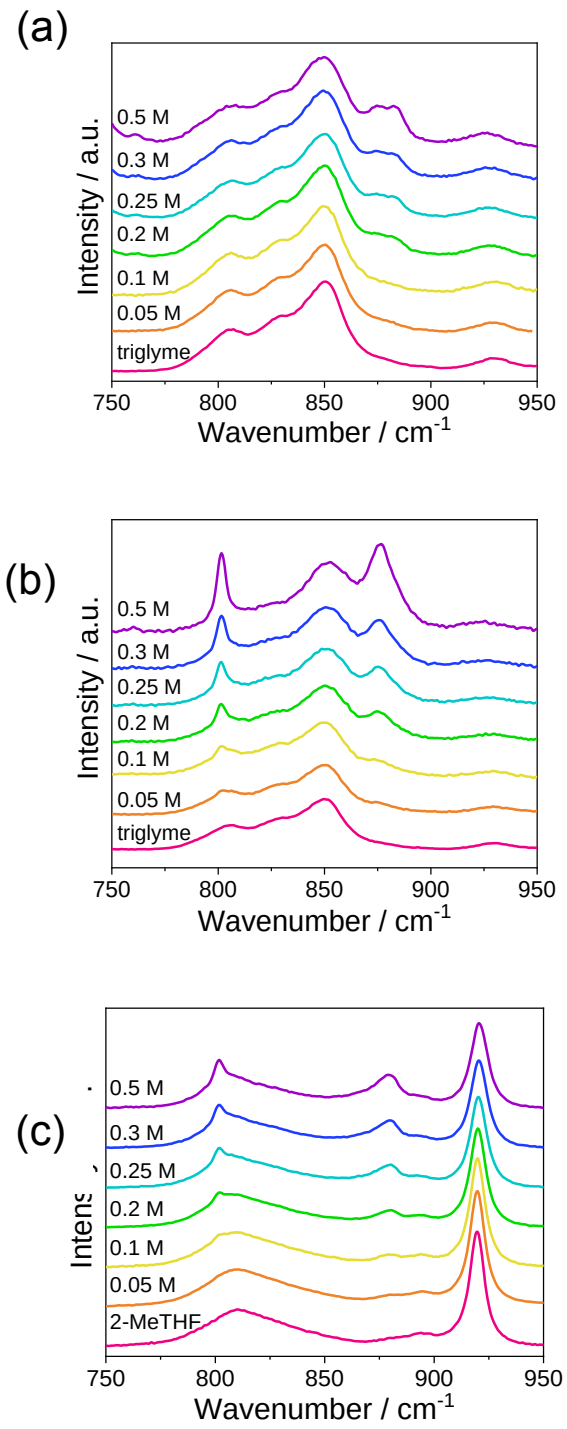

Figure 3-9. Raman spectra of (a) $Mg[TFSA]_2$/ triglyme (b) $Mg[B(HFIP)_4]_2$/triglyme and (c) $Mg[B(HFIP)_4]_2$/2-MeTHF in the wave number between 750 and 950 cm^{-1}.

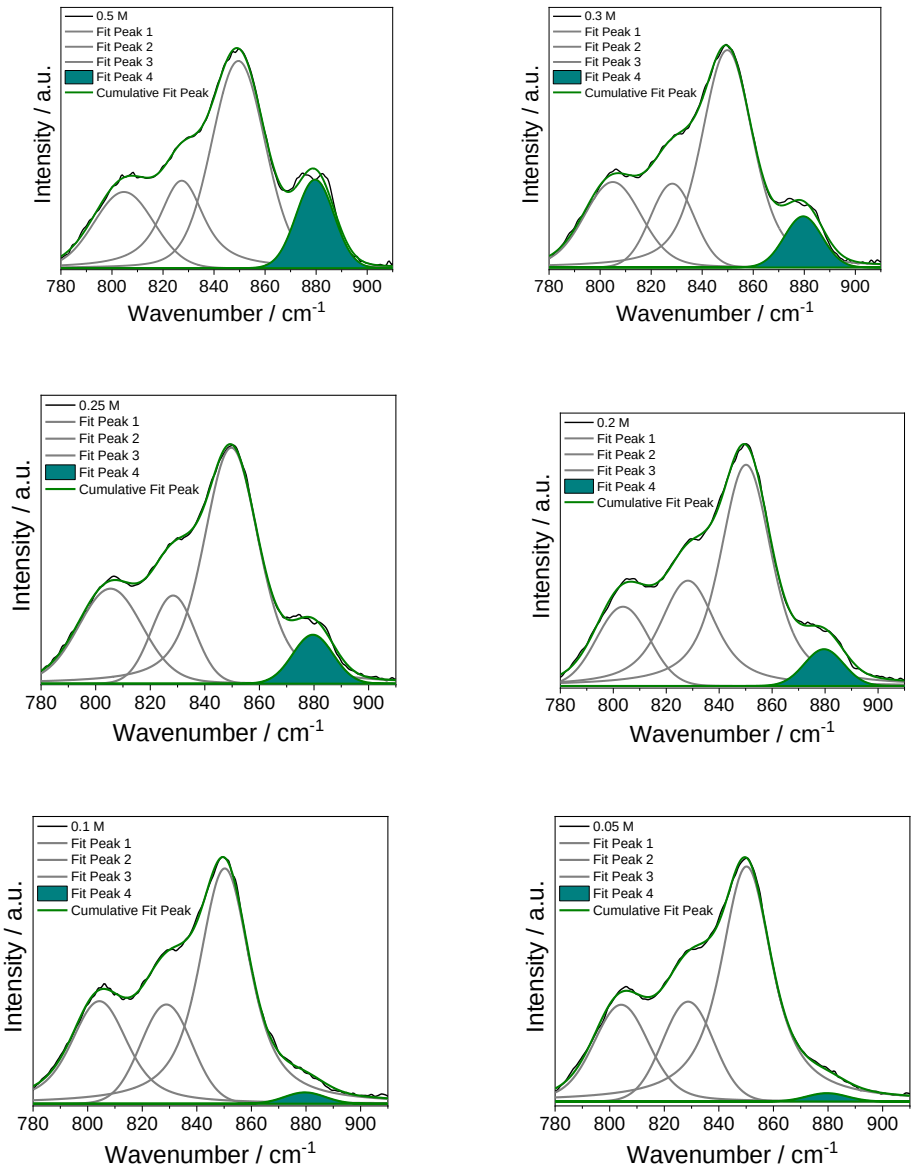

Figure 3-10. Raman spectra and Voigt function fitting results of $Mg(TFSA)_2$/triglyme in several concentrations in the wave number between 780 and 910 cm^{-1}.

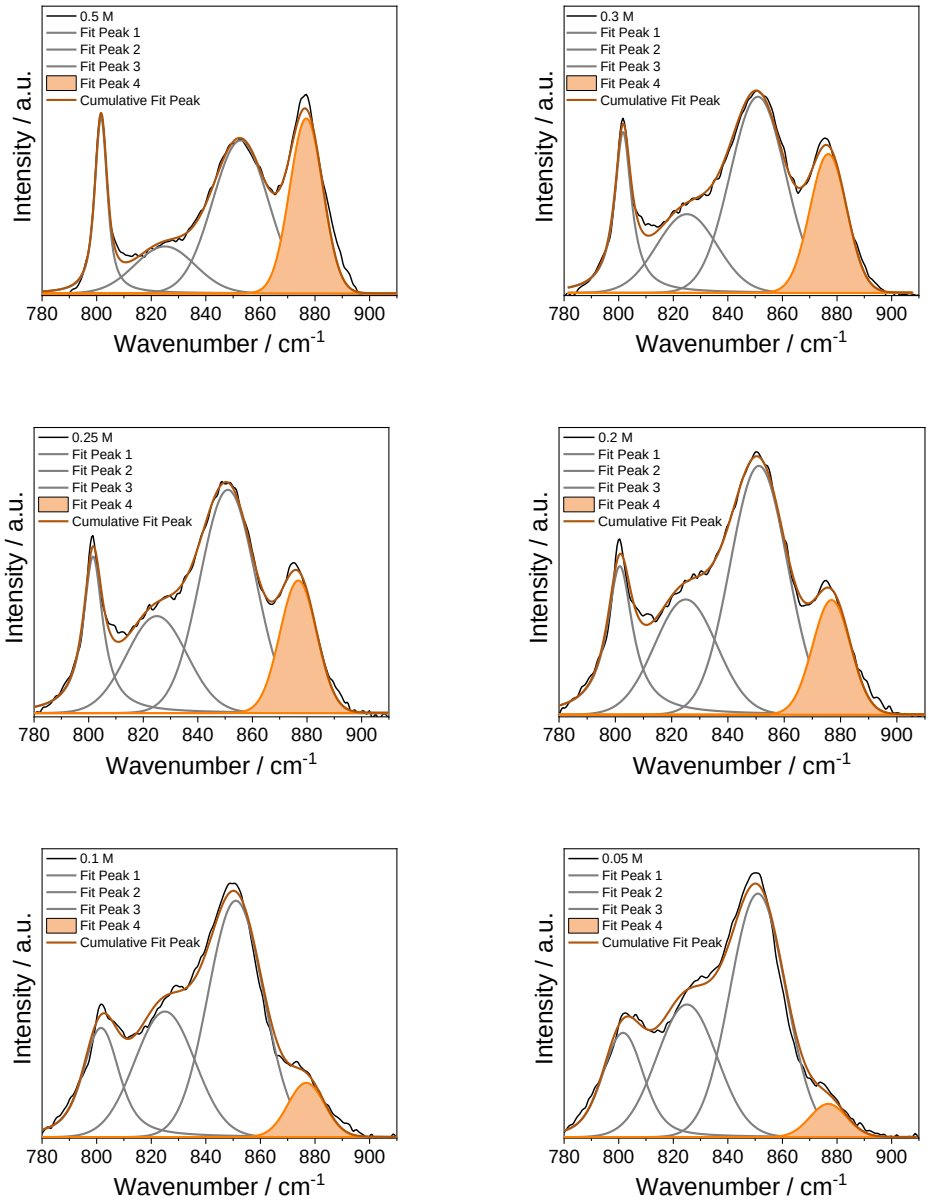

Figure 3-11. Raman spectra and Voigt function fitting results of $Mg[B(HFIP)_4]_2$/triglyme in several concentrations in the wave number between 780 and 910 cm^{-1}.

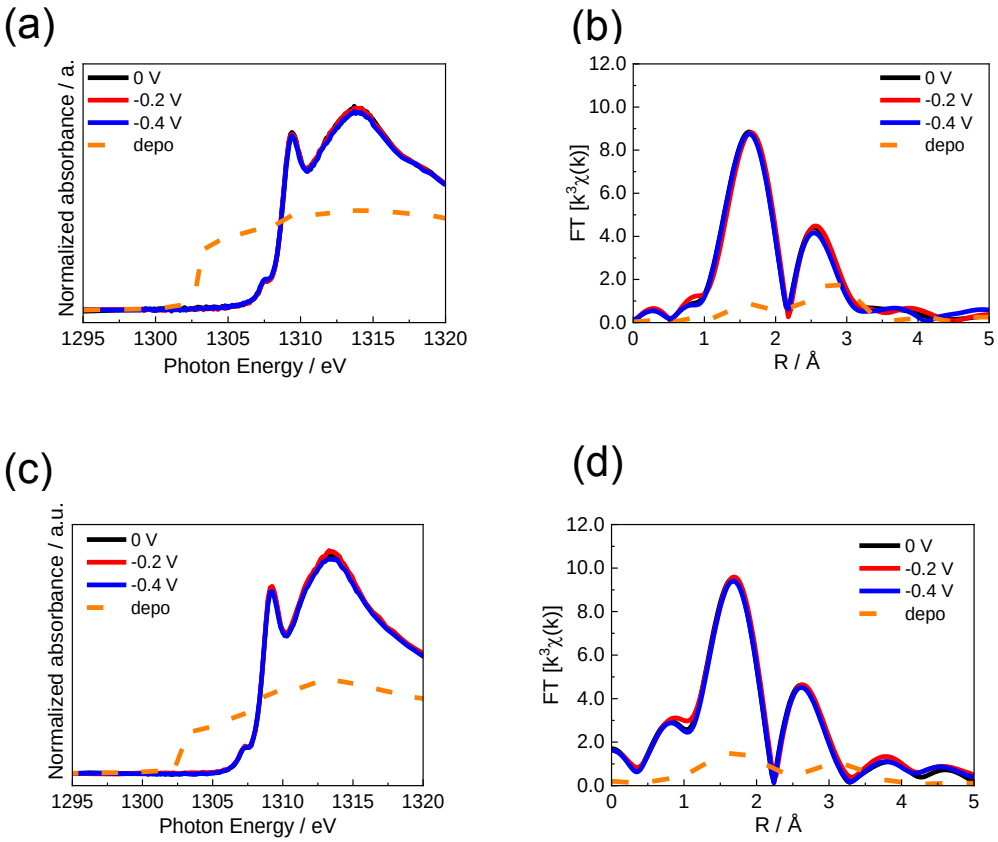

Figure 3-12. Mg *K*-edge (a) XANES spectra (b) Fourier-transformed EXAFS spectra obtained from *operando* XAS measurements 0.3 M $Mg[B(HFIP)_4]_2$/triglyme and (c) XANES spectra (d) Fourier-transformed EXAFS spectra obtained from *operando* XAS measurements 0.3 M $Mg[B(HFIP)_4]_2$/2-MeTHF.

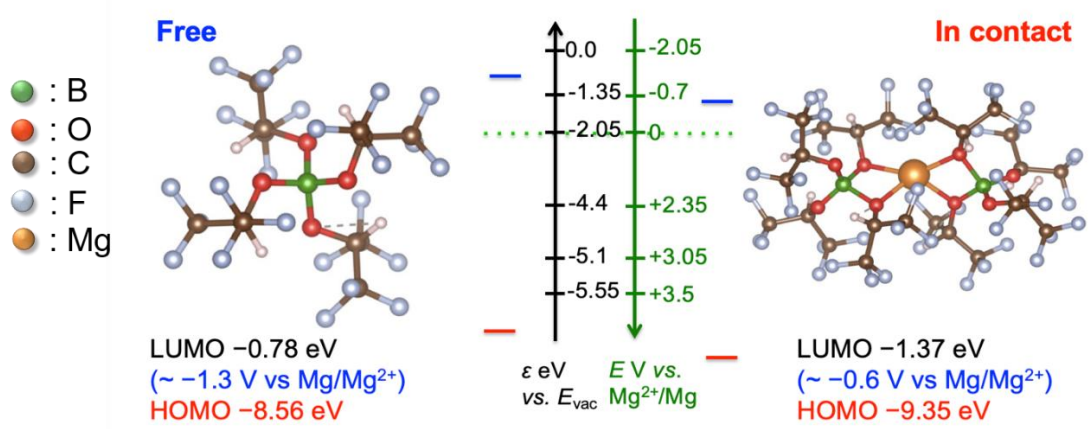

Figure 3-13. DFT cluster calculations of free $[B(HFIP)_4]^-$ and in contact $[B(HFIP)_4]^-$.

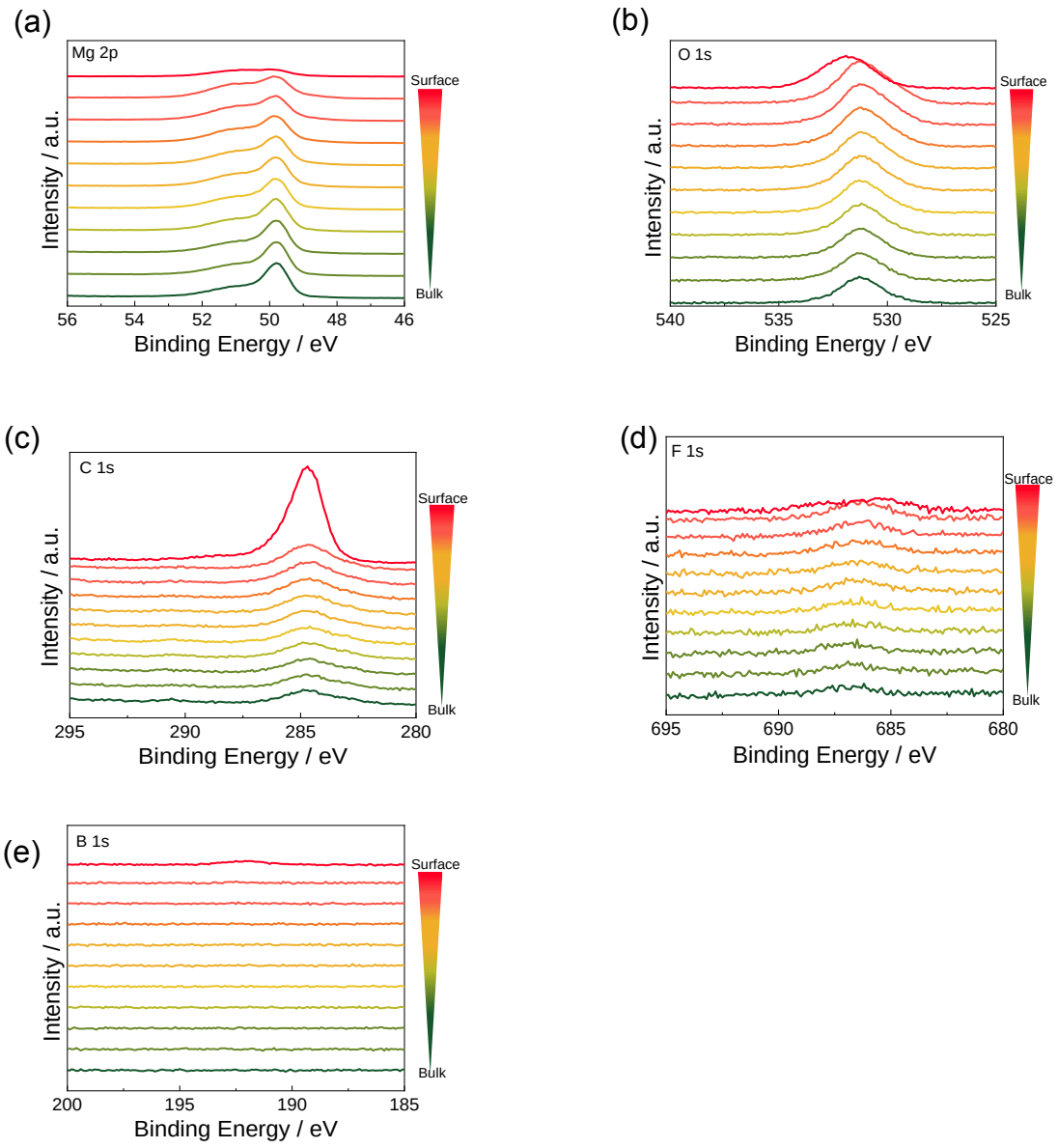

Figure 3-14. XPS spectra for the Mg metal immersed in the 0.3 M $Mg[B(HFIP)_4]_2$/triglyme; (a) Mg 2p, (b) O 1s, (c) C 1s, (d) F 1s and (e) B 1s. The Ar ion beam sputtering times are marked at the right side of the graph.

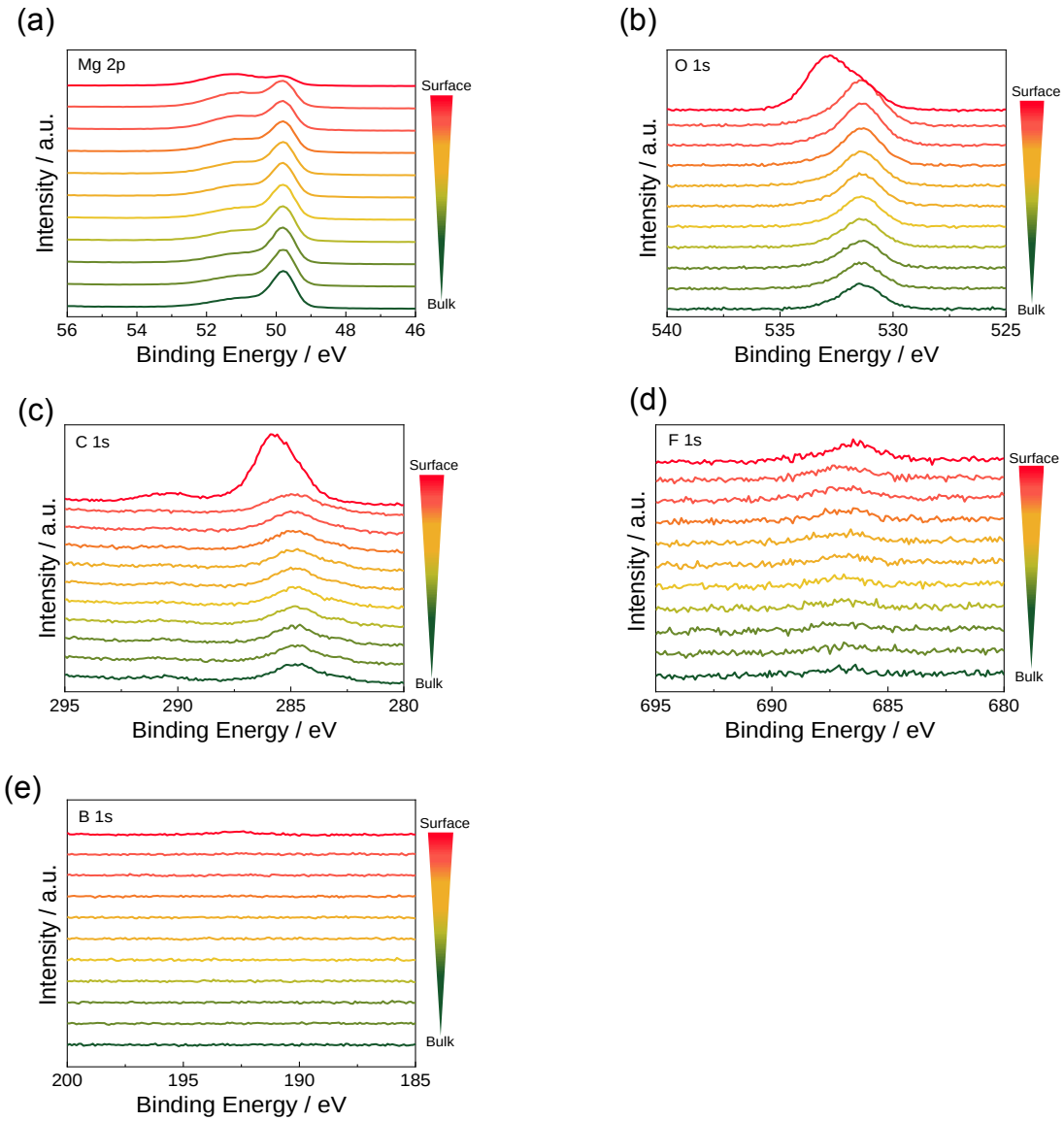

Figure 3-15. XPS spectra for the Mg metal immersed in the 0.3 M $Mg[B(HFIP)_4]_2$/2-MeTHF; (a) Mg 2p, (b) O 1s, (c) C 1s, (d) F 1s and (e) B 1s. The Ar ion beam sputtering times are marked at the right side of the graph.

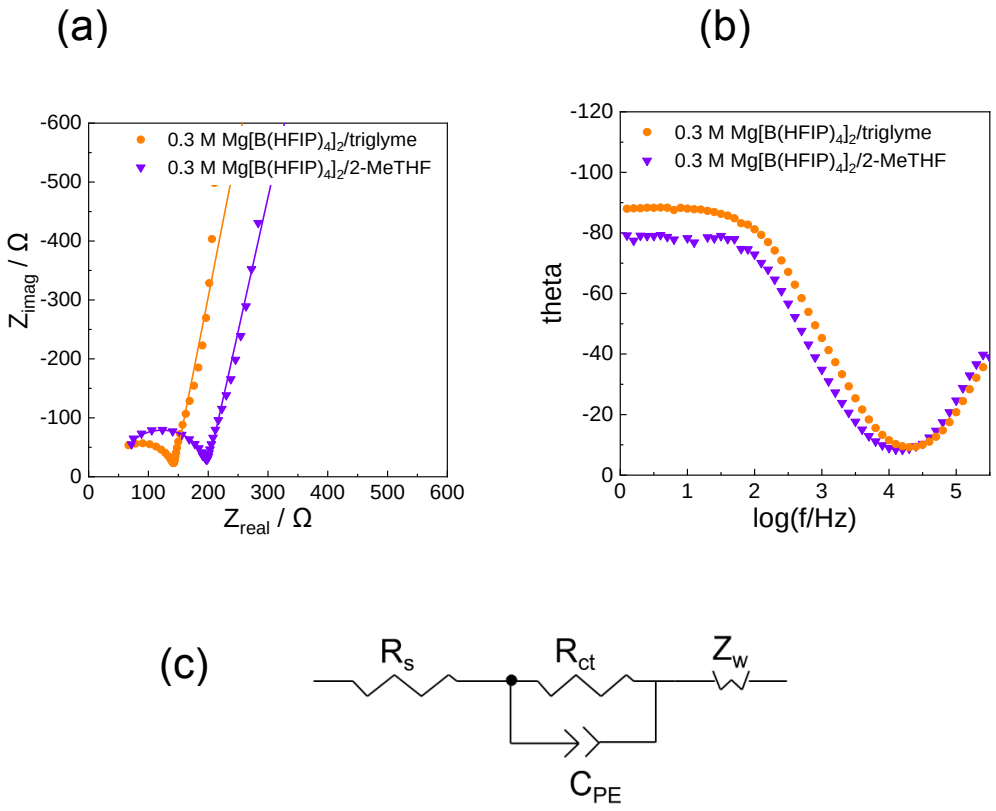

Figure 3-16. (a) Nyquist plots of Mg electrode immersed in 0.3 M $Mg[B(HFIP)_4]_2$/triglyme, and 0.3 M $Mg[B(HFIP)_4]_2$/2-MeTHF electrolytes. Fitted impedance spectra shown in solid line. (b) Bode phase shift plot that donates the capacitive responses. (c) Equivalent circuit model, in which electrolyte solution resistance is R_s, charge transfer resistance is R_{ct}, constant phase element is C_{PE} and the Warburg impedance is Z_w.

Table 3-1. The fitted parameter results of Figure 3-16.

Electrolyte	0.3 M $Mg[B(HFIP)_4]_2$/triglyme	0.3 M $Mg[B(HFIP)_4]_2$/2-MeTHF
R_s / Ω	22.3	45.3
R_{ct} / Ω	115.6	151.4
CPE	1.1×10^{-8}	5.3×10^{-9}
p	0.96	1.05
C / F	6.2×10^{-9}	1.0×10^{-8}
Time constant / s	7.9×10^{-7}	1.0×10^{-6}

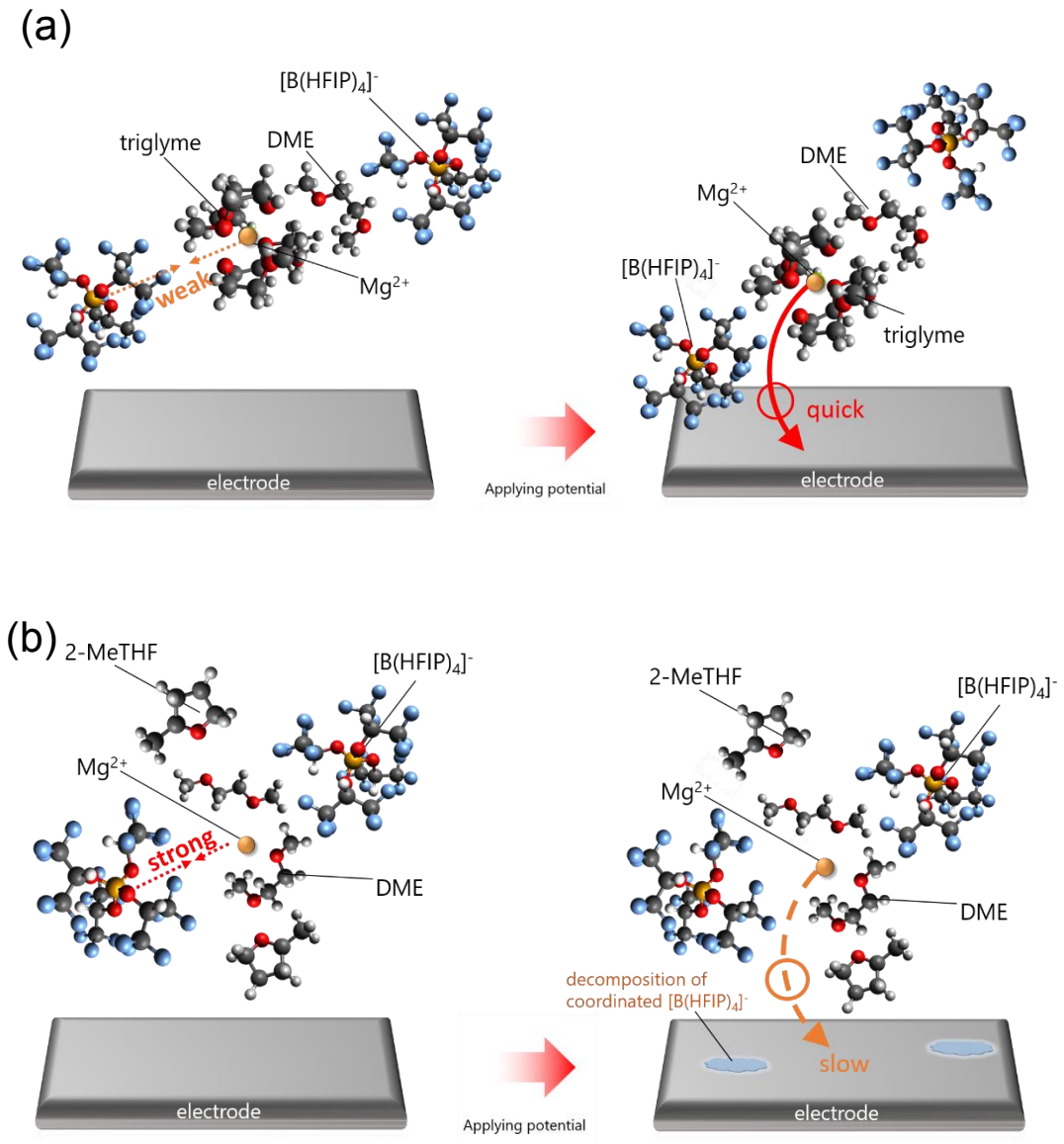

Figure 3-17. Schematic illustrations of the behavior of the magnesium ions at the anode/electrolyte interface in the (a) $Mg[B(HFIP)_4]_2$/triglyme electrolytes.

Chapter 4. Reaction Mechanism of Boron-Based Mg Electrolytes with Different Anion Sizes

4-1. Introduction

With the rapid development of electric vehicles, it will be necessary for rechargeable batteries to provide higher energy and power densities than the current lithium-ion batteries. Magnesium rechargeable batteries are expected as high energy density batteries, because the magnesium metal has a high theoretical volumetric capacity (3834 mAh/cm^3) and a relatively low reduction potential (-2.38 V *vs.* SHE). [1-9] Moreover, the safety and cost of magnesium make it a superior option to lithium. [10, 11] However, magnesium rechargeable batteries have many challenges that hinder practical applications.[12-17] The electrolyte containing an inorganic salt and carbonate solvent, which is normally used in lithium-ion batteries, cannot be used for the magnesium metal deposition because the passivation film formed on the anode surface inhibits the passage of magnesium ions.[18] Although magnesium organohaloaluminate-based electrolytes provide this reversible process, [5, 7, 19, 20] they are hazardous, corrosive, and exhibit low anodic stability; thus, a breakthrough in the development of suitable electrolytes is necessary.

The bivalent nature of the magnesium cation leads not only to a very high volume capacity, but also to strong electrostatic interactions with the anion as well as with the solvent. Thus, the dissolution of ions always competes with their binding, which usually manifests itself in poor salt solubility and/or poor ionic conductivity. [21] In fact, ion pairs and larger clusters have been found to form in many magnesium-based electrolytes, for

example, $Mg(TFSA)_2$,[22-25] $Mg(BH_4)_2$.[26] Thereby, the formation and size of the agglomerates strongly depends on the anion, the solvent and the electric field strength. [21] Such clusters can significantly affect the properties of the electrolyte: clusters can effectively shield the double charge of magnesium cations, thus reducing the charge density and the interaction between ion clusters; but at the same time, the cluster size is large, reducing its diffusivity. Reduces the ionic conductivity, sterically impedes the charge transfer on the electrode.

Recently, it has been reported that reversible Mg deposition/dissolution reactions can occur in boron based weakly coordinating anion, such as, $Mg(CB_{11}H_{12})_2$,[27] $Mg(CB_{11}H_{11}F)_2$, [28] $Mg[B(HFIP)_4]_2$ (HFIP=-$OCH(CF_3)_2$)[29, 30] and $Mg[B(O_2C_2(CF_3)_4)_2]_2$,[31] and strongly interacting solvents such as glyme. Each of these anion classes possesses rich substitutional chemistry that can be exploited to correlate anion structure with electrolyte function and stability, thereby enabling rational electrolyte design. The alkoxyborates anion is of particular interest because of its reported electrochemical stability and high coulombic efficiency. However, the behavior of magnesium ions at the interface between the negative electrode and the effects of formation and size of the agglomerates on Coulomb efficiency and polarization have not been clearly understood.

In this study, we choose the different size of boron based electrolytes (Figure4-1), to develop a better understanding of the influence of the cluster formation and size of ion clusters on the overall battery performance. Raman spectroscopy, density functional theory (DFT) calculations and electrochemical impedance spectroscopy (EIS) were done to analyze the coordination structure of the magnesium ions in the bulk solution and reductive stability of each anion in these electrolytes.

4-2. Experimental

4.2.1. Material preparation

$Mg[B(HFIP)_4]_2$, $Mg[B(PFTB)_4]_2$ and $Mg[B(TFE)_4]_2$ were synthesized by the dehydrogenation reaction of $Mg(BH_4)_2$ with hexafluoro-2-propanol, nonafluoro-tert-butyl alcohol and 2,2,2-trifluoroethanol in DME, respectively.[29] The 0.3 M $Mg[B(HFIP)_4]_2$/triglyme , 0.3 M $Mg[B(PFTB)_4]_2$/triglyme and 0.3 M $Mg[B(TFE)_4]_2$/ triglyme electrolytes were prepared by mixing $Mg[B(HFIP)_4]_2$, $Mg[B(PFTB)_4]_2$ and $Mg[B(TFE)_4]_2$ with triglyme (KISHIDA CHEMICAL Co., Ltd. >99%) respectively, in an Ar-filled glove box.

4.2.2. Electrochemical measurements

Cyclic voltammograms (CVs) were collected by three-electrode cells to examine the magnesium deposition/dissolution reactions in each electrolyte. A platinum plate was used as the working electrode and a magnesium plate (99.9%, Nilaco Co., Ltd.) as the counter electrode and the reference electrode. All the electrodes were polished in an Ar-filled glove box before use. Cyclic voltammetry was performed at 25 ℃ with a potential sweep rate of 10 mV/s. The potential range was −1.5–3.5 V vs. Mg^{2+}/Mg for each electrolyte.

Electrochemical impedance spectroscopy (EIS) was carried out to analyze the differences in the interfacial resistance using a similar cell configuration as that used in the CV measurements. The alternating current (AC) frequency was scanned from 1 MHz to 10 mHz with an amplitude of 50 mV. All experiments, including the electrolyte preparation, cell construction, and electrochemical measurements, were carried out under a dry Ar atmosphere.

4.2.3. Characterization

The Raman spectra were collected by a DXR3 Smart Raman spectrometer (Thermo Fisher Scientific) using a 532 nm diode-pumped solid-state laser at room temperature. All the electrolytes were sealed in glass vessels in an Ar-filled glove box and measured between 50 and 1800 cm^{-1} without air exposure.

DFT calculations were carried out using the Gaussian16 Revision A.03 code to investigate the coordination effect on the electronic states. [32] We calculated the optimized geometries and the corresponding HOMO and LUMO energies of the free anion and coordinated anion in the triglyme solvent using the polarized continuum model method with the parameters for the triglyme bulk solvent (dielectric constant Ɛ=7.62).

4-3. Results and discussion

4.3.1. Behavior of the magnesium deposition/dissolution reactions

Magnesium metal deposition/dissolution reactions were examined for the 0.3 M $Mg[B(HFIP)_4]_2$/triglyme, 0.3 M $Mg[B(PFTB)_4]_2$/triglyme and 0.3 M $Mg[B(TFE)_4]_2$/triglyme by cyclic voltammetry. Figure 4-2 shows the obtained voltammograms. Figure 4-2(b) shows an enlarged figure of the current density, near the potential that the magnesium deposition occurs, during the potential sweep in the negative direction (Figure 4-2(a)). In each electrolyte, cathodic and anodic currents, which are attributed to magnesium metal deposition and dissolution reactions, were observed. In contrast to the 0.3 M $Mg[B(PFTB)_4]_2$/triglyme and 0.3 M $Mg[B(TFE)_4]_2$/triglyme electrolyte, 0.3 M $Mg[B(HFIP)_4]_2$/triglyme showed significantly lower overpotential and higher current density. The coulombic efficiencies of the magnesium metal deposition/dissolution reactions were 94%, 82% and 20% in 0.3 M

$Mg[B(HFIP)_4]_2$/triglyme, 0.3 M $Mg[B(PFTB)_4]_2$/triglyme and 0.3 M $Mg[B(TFE)_4]_2$/triglyme, respectively.

4.3.2. Coordination structure of the magnesium ions in bulk solution

The coordination structure of the magnesium ions in each electrolyte is influenced by the cation-anion interactions. The magnesium ions compete with the solvents to interact with the anion; consequently, if the interaction between the magnesium ion and anion is strong, magnesium ions coordinate to the anion as well as the solvent. To examine the interactions between the anions and magnesium ions in the bulk solutions the Raman spectra of these electrolytes were collected. The Raman spectra for the $Mg[B(TFE)_4]_2$/triglyme and $Mg[B(HFIP)_4]_2$/triglyme electrolytes with various concentrations were collected for the region between 750 and 950 cm^{-1} (Figure 4-3). The Raman bands corresponding to the CH_2 rocking and C–O–C stretching vibrations of the glyme solvent appear between 800 and 900 cm^{-1}; [33, 34] specifically, between 800 and 865 cm^{-1} when the solvent does not coordinate to metal ions and between 865 and 890 cm^{-1} when they do interact. [34] We observed the intensity of the band between 865 and 890 cm^{-1} to increase with increasing salt concentration, which indicated that the triglyme solvent in both electrolyte systems were well coordinated to magnesium ions. To estimate the coordination degree of magnesium ions with triglyme molecules, we focused on the bands near 865–890 cm^{-1} and performed a nonlinear least-squares curve-fitting analysis for the observed Raman spectra (Figure4-5, 4-6).[34] Using the integrated area of the coordinated triglyme, we compared the solvation degree of the two electrolyte systems. We employed Voigt function fitting to show the ratio of complexation between the magnesium ions and triglyme molecules with various concentrations of the $Mg[B(TFE)_4]_2$/triglyme and $Mg[B(HFIP)_4]_2$/triglyme electrolytes (Figure 4-4). The plots exhibited straight lines for

both electrolytes systems, but the slope of the $Mg[B(TFE)_4]_2$/triglyme plot was smaller than that of the $Mg[B(HFIP)_4]_2$/triglyme plot. These results indicated that the triglyme molecules coordinated to magnesium ions stronger in the $Mg[B(HFIP)_4]_2$/triglyme electrolyte than in the $Mg[B(TFE)_4]_2$/triglyme electrolyte.

4.3.3. Reductive stability of the anion

To understand the difference in magnesium deposition behavior for each electrolyte, DFT calculations was used to identify reductive stabilities of the different anions. DFT calculations were conducted for both Mg-coordinated and Mg-uncoordinated anions. The lowest unoccupied molecular orbital (LUMO) energy level of $B(HFIP)_4]^-$ anion for both coordinated and uncoordinated states to the magnesium ions were calculated, and are shown in Figure 4-7. The LUMO energy level of the coordinated $[B(HFIP)_4]^-$ anion was −1.26 eV (−0.79 V vs. Mg^{2+}/Mg), which was much lower than that of the uncoordinated $[B(HFIP)_4]^-$ anion (−0.73 eV; −1.32 V vs. Mg^{2+}/Mg). In $Mg[B(HFIP)_4]_2$ electrolyte system, uncoordinated $[B(HFIP)_4]^-$ anions (free $[B(HFIP)_4]^-$ anions) are more stable than coordinated $[B(HFIP)_4]^-$ anions, as the LUMO energy level of the uncoordinated $[B(HFIP)_4]^-$ anion was much higher than that of the coordinated $[B(HFIP)_4]^-$ anion. The DFT calculation results of both coordinated and uncoordinated $[B(PFTB)_4]^-$ anions to the magnesium ions in the case of $Mg[B(PFTB)_4]_2$ /triglyme, are shown in figure 4-8. DFT results show that, uncoordinated $[B(PFTB)_4]^-$ anions are more stable than coordinated $[B(PFTB)_4]^-$ anions. $Mg[B(PFTB)_4]^+$ was decomposed to Mg(PFTB) and $B(PFTB)_3$ even during structure optimization. The DFT results of both coordinated and uncoordinated $[B(TFE)_4]^-$ anions are shown in Figure 4-9. The LUMO energy level of the uncoordinated $[B(TFE)_4]^-$ anion was −0.76 eV (−1.29 V vs. Mg^{2+}/Mg), which was much higher than that of the coordinated $[B(TFE)_4]^-$ anion (−1.35 eV; −0.7 V

vs. Mg^{2+}/Mg). These results indicate that the coordinated $[B(TFE)_4]^-$ anion undergoes reduction decomposition more easily than the uncoordinated one.

To further examine the interfacial resistance of the Mg anode, electrochemical impedance spectroscopy (EIS) was performed, where Nyquist plots of the Mg electrode immersed in different electrolytes were developed (Figure 4-10a) and fitting parameters were evaluated using an equivalent electrical circuit (Figure 4-10c) (Table 4-1). The solution resistance (R_s) value changes for each three-electrode cell because the position of the reference electrode cannot be correctly fixed in the cell. The Nyquist and bode plots showed that only one semicircle appeared in both electrolytes around a high frequency (10^5 Hz), which was attributed to the charge transfer resistance (R_{ct}).[35-37] The R_{ct} of the 0.3 M $Mg[B(PFTB)_4]_2$/triglyme and 0.3 M $Mg[B(TFE)_4]_2$/triglyme electrolyte was comparable to that of the 0.3 M $Mg[B(HFIP)_4]_2$/triglyme electrolyte (Table 4-1). In our previous study, we reported that the Mg deposition was inhibited by the decomposition of $[TFSA]^-$ anions due to the high passivation layer resistance (R_{pl}).[37] Compared to those of the $Mg(TFSA)_2$-based electrolyte, there are negligible passivation layer resistance of anionic decomposition, and the R_{ct} of the $Mg[B(HFIP)_4]_2$ electrolytes were significantly small. These results indicated that it was difficult for the $[B(HFIP)_4]^-$ anions to decompose, which was due to the high reduction stability of the anion; Furthermore, the R_{ct} of 0.3 M $Mg[B(PFTB)_4]_2$/triglyme and 0.3 M $Mg[B(TFE)_4]_2$/triglyme electrolytes were larger than that of the 0.3 M $Mg[B(HFIP)_4]_2$/triglyme electrolyte, corresponded to the slow interfacial reaction kinetics for the deposition/dissolution reactions (Figure 4-2).

4.3.5. Discussion

Figure 4-11 schematically illustrates the behavior of the magnesium ions at the anode/electrolyte interface. Compared with the 0.3 M $Mg[B(PFTB)_4]_2$/triglyme and 0.3

M $Mg[B(TFE)_4]_2$/triglyme electrolytes, the 0.3 M $Mg[B(HFIP)_4]_2$/triglyme electrolyte showed excellent Coulombic efficiency and small polarization for the magnesium deposition/dissolution reactions. This is because magnesium ions highly coordinated with the solvent, the interaction between Mg^{2+} and $[B(HFIP)_4]^-$ is relatively week, compare to $[B(TFE)_4]^-$ anions. Consequently, the magnesium deposition is not inhibited by the decomposition of $[B(HFIP)_4]^-$ due to the high reduction stability, resulting in higher coulombic efficiency and smaller polarization than 0.3 M $Mg[B(PFTB)_4]_2$/triglyme and 0.3 M $Mg[B(TFE)_4]_2$/triglyme electrolyte in magnesium deposition/dissolution reactions.

4-4. Conclusion

In this study, the behavior of magnesium ions at the interface between the negative electrode and the effects of formation and size of the agglomerates on Coulomb efficiency and polarization were analyzed using different size of boron based electrolyte $Mg[B(HFIP)_4]_2$/triglyme, $Mg[B(PFTB)_4]_2$/triglyme and $Mg[B(TFE)_4]_2$/triglyme. The cyclic voltammetry demonstrates that $Mg[B(HFIP)_4]_2$/triglyme shows significantly lower overpotential and high Coulomb efficiency for magnesium deposition/dissolution reactions than $Mg[B(PFTB)_4]_2$/triglyme and $Mg[B(TFE)_4]_2$/triglyme. Raman spectra showed that the magnesium ions largely coordinated to the solvent molecules in the $Mg[B(HFIP)_4]_2$/triglyme electrolyte. Our DFT and EIS results indicated that $[B(HFIP)_4]^-$ decomposition in the $Mg[B(HFIP)_4]_2$/triglyme electrolyte was hard to occur due to the high reduction stability of uncoordinated $[B(HFIP)_4]^-$ anion, resulting in higher coulombic efficiency and smaller polarization. The opposite was observed for the $Mg[B(PFTB)_4]_2$/triglyme and $Mg[B(TFE)_4]_2$/triglyme electrolytes, where reduction decomposition easily occurred because the magnesium and anions interactions were stronger than those in the $Mg[B(HFIP)_4]_2$/triglyme electrolyte. This study demonstrates

the importance of controlling the interactions between magnesium ions and anions, which can be done by selecting suitable size of anions. We believe that our findings can significantly promote developments of new electrolytes for magnesium rechargeable batteries.

References

1. D. Aurbach, Z. Lu, A. Schechter, Y. Gofer, H. Gizbar, R. Turgeman, Y. Cohen, M. Moshkovich and E. Levi, *Nature*, **2000**, 407, 724-727.
2. D. Aurbach, Y. Gofer, A. Schechter, O. Chusid, H. Gizbar, Y. Cohen, M. Moshkovich and R. Turgeman, *J. Power Sources*, **2001**, 97-8, 269-273.
3. T. D. Gregory, R. J. Hoffman and R. C. Winterton, *J. Electrochem. Soc.*, **1990**, 137, 775-780.
4. P. Novak, R. Imhof and O. Haas, *Electrochim Acta*, **1999**, 45, 351-367.
5. D. Aurbach, H. Gizbar, A. Schechter, O. Chusid, H. E. Gottlieb, Y. Gofer and I. Goldberg, *J. Electrochem. Soc.*, **2002**, 149, A115-A121.
6. J. O. Besenhard and M. Winter, *Chemphyschem*, **2002**, 3, 155-+.
7. D. Aurbach, A. Schechter, M. Moshkovich and Y. Cohen, *J. Electrochem. Soc.*, **2001**, 148, A1004-A1014.
8. B. Dunn, H. Kamath and J. M. Tarascon, *Science*, **2011**, 334, 928-935.
9. H. D. Yoo, I. Shterenberg, Y. Gofer, G. Gershinsky, N. Pour and D. Aurbach, *Energ Environ Sci*, **2013**, 6, 2265-2279.
10. J. O. Besenhard and M. Winter, *Chemphyschem*, **2002**, 3, 155-159.
11. T. D. Gregory, R. J. Hoffman and R. C. Winterton, *J. Electrochem. Soc.*, **1990**, 137, 775.
12. F. F. Liu, T. T. Wang, X. B. Liu and L. Z. Fan, *Adv. Energy Mater.*, **2020**, 2000787.
13. J. Muldoon, C. B. Bucur and T. Gregory, *Angew. Chem.*, **2017**, 56, 12064-12084.
14. X. Y. Zhao, Z. Zhao-Karger, M. Fichtner and X. D. Shen, *Angew. Chem.*, **2020**, 59, 5902-5949.

15. J. Z. Niu, Z. H. Zhang and D. Aurbach, *Adv. Energy Mater.*, **2020**, 10, 2000697.

16. P. W. Wang and M. R. Buchmeiser, *Adv. Funct. Mater.*, **2019**, 29, 1905248.

17. H. Zhang, X. Liu, H. Li, I. Hasa and S. Passerini, *Angew. Chem., Int. Ed.*, **2020**, 59, 2-21.

18. Z. Lu, A. Schechter, M. Moshkovich and D. Aurbach, *J Electroanal Chem*, **1999**, 466, 203-217.

19. O. Mizrahi, N. Amir, E. Pollak, O. Chusid, V. Marks, H. Gottlieb, L. Larush, E. Zinigrad and D. Aurbach, *J. Electrochem. Soc.*, **2008**, 155, A103-A109.

20. H. S. Kim, T. S. Arthur, G. D. Allred, J. Zajicek, J. G. Newman, A. E. Rodnyansky, A. G. Oliver, W. C. Boggess and J. Muldoon, *Nat. Commun.*, **2011**, 2, 1-6.

21. J. Drews, T. Danner, P. Jankowski, T. Vegge, J. M. G. Lastra, R. Liu, Z. Zhao‐Karger, M. Fichtner and A. Latz, *Chemsuschem*, **2020**, 13, 3599.

22. S.-Y. Ha, Y.-W. Lee, S. W. Woo, B. Koo, J.-S. Kim, J. Cho, K. T. Lee, N.-S. J. A. a. m. Choi and interfaces, *ACS Appl. Mater. Interfaces*, **2014**, 6, 4063-4073.

23. Y. Orikasa, T. Masese, Y. Koyama, T. Mori, M. Hattori, K. Yamamoto, T. Okado, Z.-D. Huang, T. Minato and C. Tassel, *Sci. Rep.*, **2014**, 4, 5622.

24. T. Fukutsuka, K. Asaka, A. Inoo, R. Yasui, K. Miyazaki, T. Abe, K. Nishio and Y. Uchimoto, *Chem Lett*, **2014**, 43, 1788-1790.

25. I. T. Kim, K. Yamabuki, M. Morita, H. Tsutsumi and N. Yoshimoto, *J. Power Sources*, **2015**, 278, 340-343.

26. R. Mohtadi, M. Matsui, T. S. Arthur and S. J. Hwang, *Angew. Chem.*, **2012**, 51, 9780-9783.

27. O. Tutusaus, R. Mohtadi, T. S. Arthur, F. Mizuno, E. G. Nelson and Y. V. Sevryugina, *Angew. Chem.*, **2015**, 54, 7900-7904.

28. N. T. Hahn, T. J. Seguin, K. C. Lau, C. Liao, B. J. Ingram, K. A. Persson and K. R. Zavadil, *J. Am. Chem. Soc.*, **2018**, 140, 11076-11084.

29. Z. Zhao-Karger, M. E. G. Bardaji, O. Fuhr and M. Fichtner, *J. Mater. Chem. A*, **2017**, 5, 10815-10820.

30. Z. Zhao-Karger, R. Y. Liu, W. X. Dai, Z. Y. Li, T. Diemant, B. P. Vinayan, C. B. Minella, X. W. Yu, A. Manthiram, R. J. Behm, M. Ruben and M. Fichtner, *ACS Energy Lett.*, **2018**, 3, 2005-2013.

31. J. Luo, Y. J. Bi, L. P. Zhang, X. Y. Zhang and T. B. L. Liu, *Angew. Chem.*, **2019**, 58, 6967-6971.

32. M. Frisch, G. Trucks, H. B. Schlegel, G. E. Scuseria, M. A. Robb, J. R. Cheeseman, G. Scalmani, B. Mennucci and G. Petersson, *Inc., Wallingford CT*, **2009**, 201.

33. D. Brouillette, D. E. Irish, N. J. Taylor, G. Perron, M. Odziemkowski and J. E. Desnoyers, *Phys. Chem. Chem. Phys.*, **2002**, 4, 6063-6071.

34. T. Kimura, K. Fujii, Y. Sato, M. Morita and N. Yoshimoto, *J. Phys. Chem. C*, **2015**, 119, 18911-18917.

35. S. J. Kang, H. Kim, S. Hwang, M. Jo, M. Jang, C. Park, S. T. Hong and H. Lee, *ACS Appl. Mater. Interfaces*, **2019**, 11, 517-524.

36. O. Tutusaus, R. Mohtadi, T. S. Arthur, *ACS Energy Lett.*, **2017**, 2, 224-229.

37. F. Tuerxun, K. Yamamoto, M. Hattori, T. Mandai, K. Nakanishi, A. Choudhary, Y. Tateyama, K. Sodeyama, A. Nakao, T. Uchiyama, M. Matsui, K. Tsuruta, Y. Tamenori, K. Kanamura and Y. Uchimoto, *ACS Appl. Mater. Interfaces*, **2020**, 12, 25775-25785.

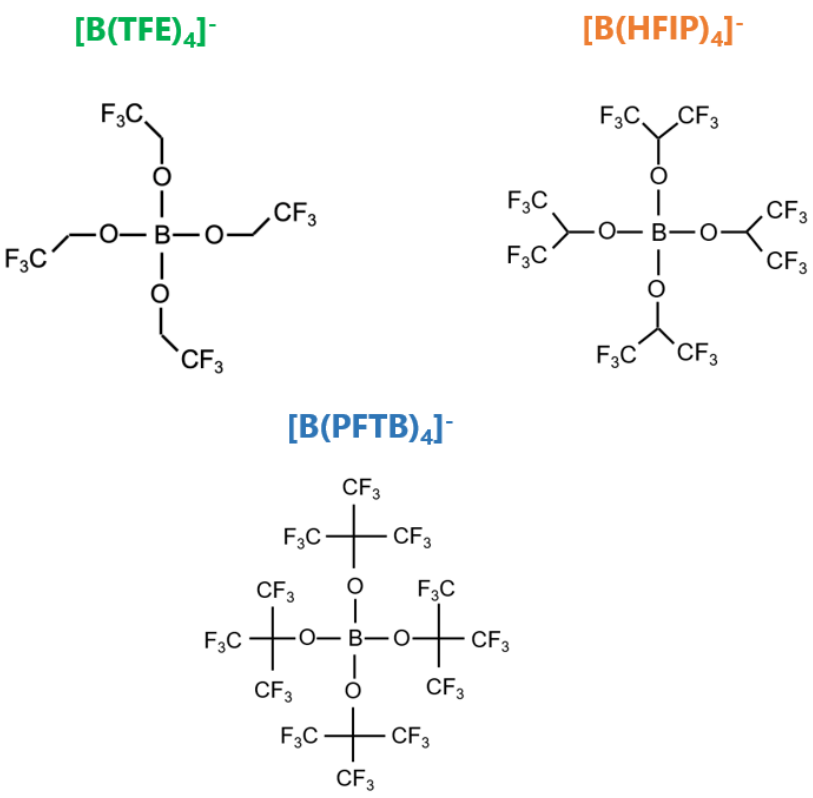

Figure 4-1. Boron-based Mg salts with different anion sizes

(a)

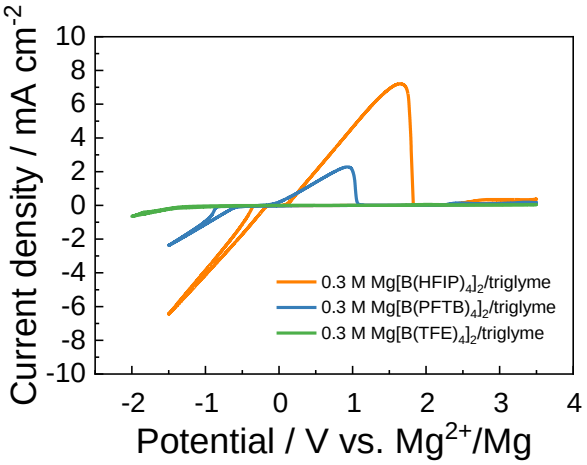

(b)

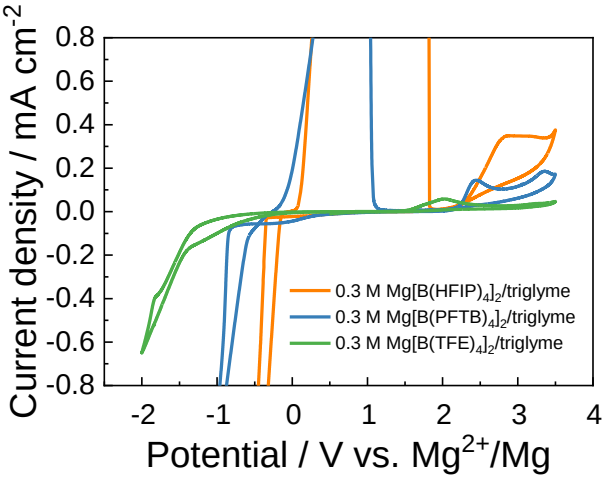

Figure 4-2. (a) Cyclic voltammograms of the 0.3 M $Mg[B(HFIP)_4]_2$/triglyme, 0.3 M $Mg[B(PFTB)_4]_2$/triglyme, and 0.3 M $Mg[B(TFE)_4]_2$/triglyme at a sweeping rate of 10 mV/s. (b) Enlarged figure of (a).

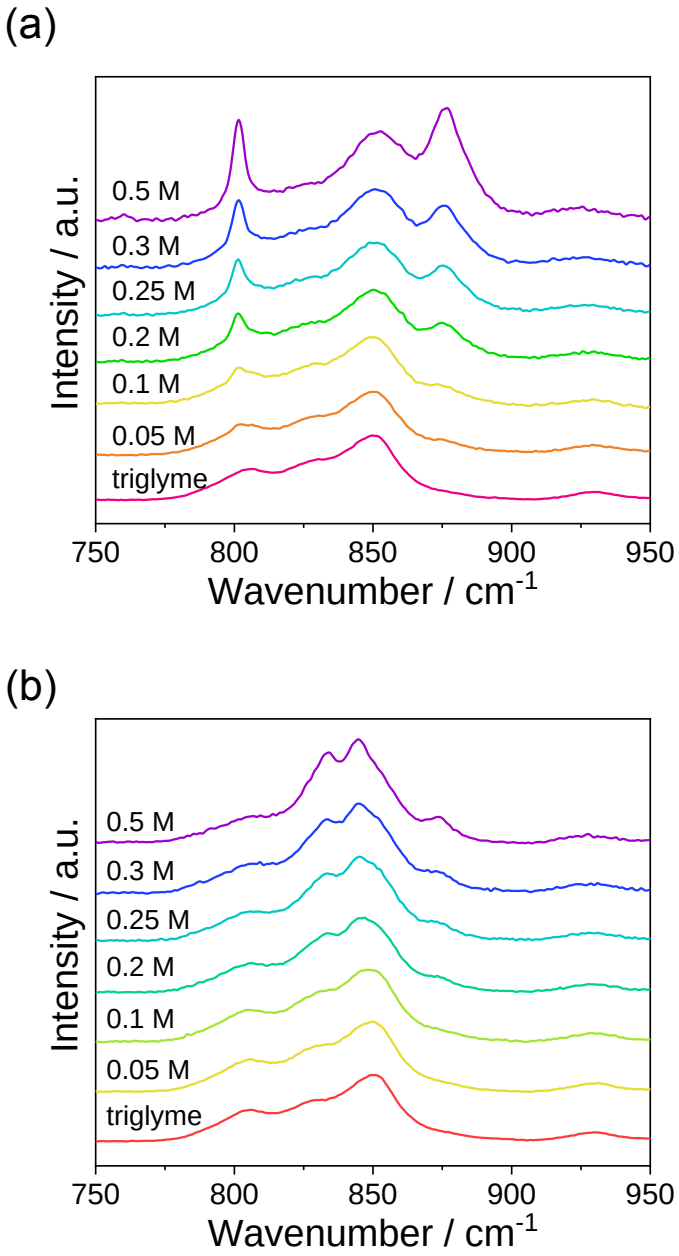

Figure 4-3. Raman spectra of (a) $Mg[B(HFIP)_4]_2$/triglyme and (b) $Mg[B(TFE)_4]_2$/triglyme with several concentrations in the region between 750 and 950 cm^{-1}

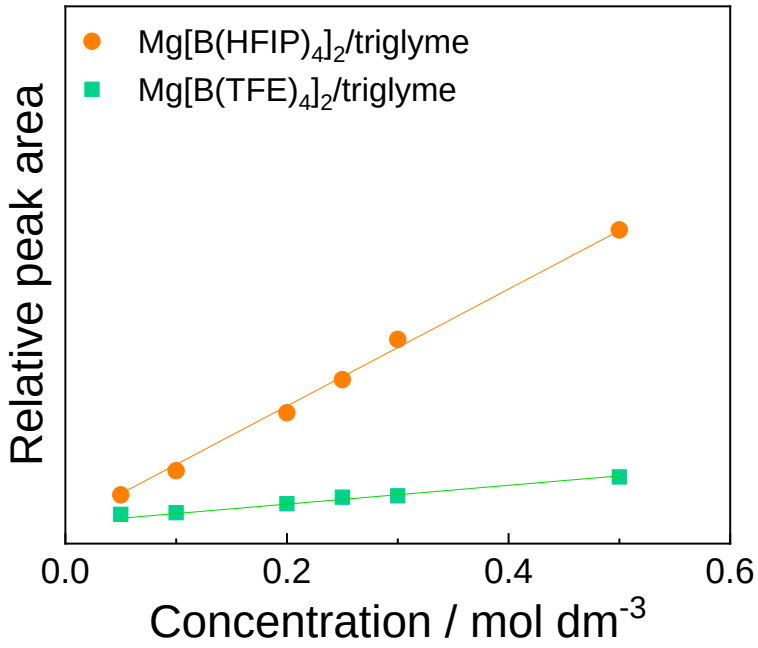

Figure 4-4. Relative peak area of $Mg[B(HFIP)_4]_2$/triglyme and $Mg[B(TFE)_4]_2$/triglyme with several concentrations.

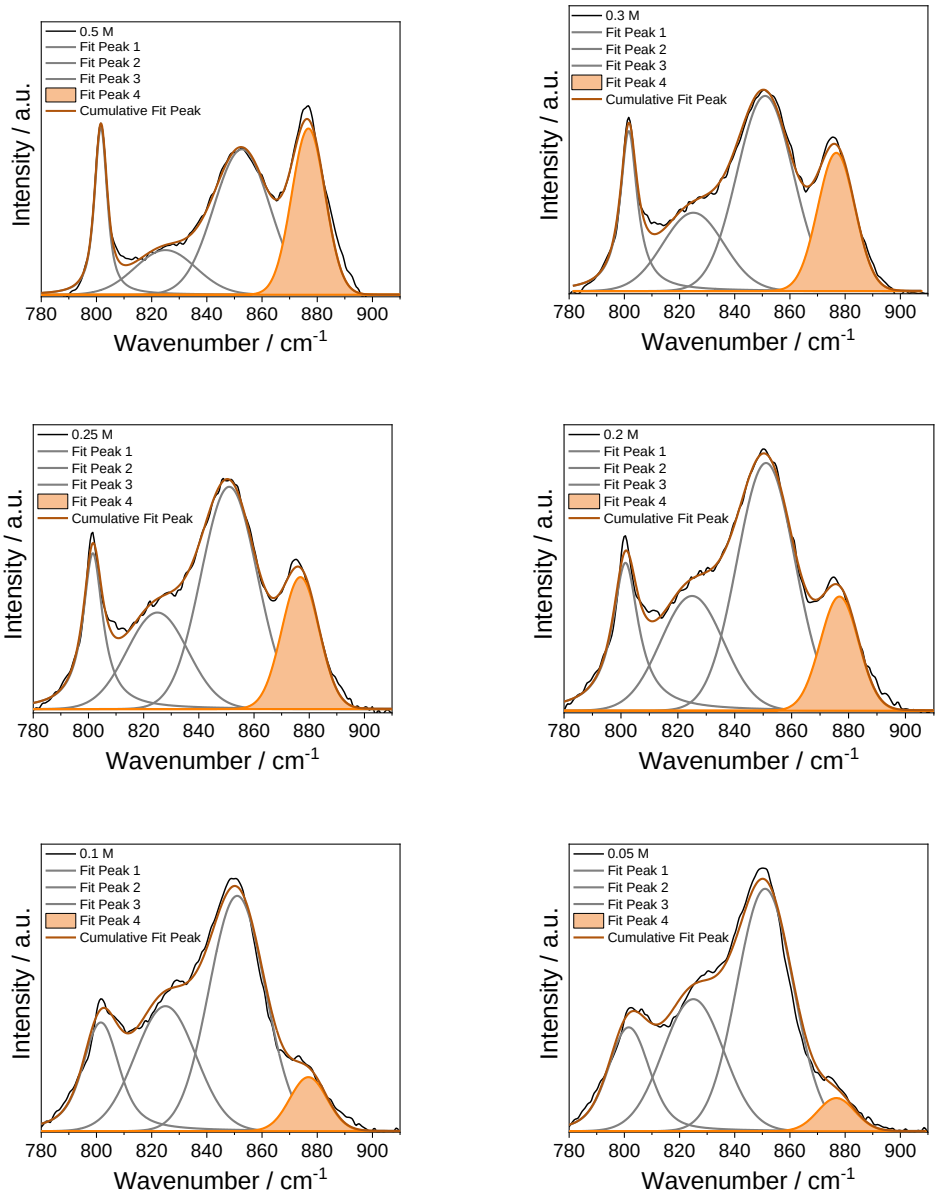

Figure 4-5. Raman spectra and Voigt function fitting results of $Mg[B(HFIP)_4]_2$/triglyme in several concentrations in the wave number between 780 and 910 cm^{-1}.

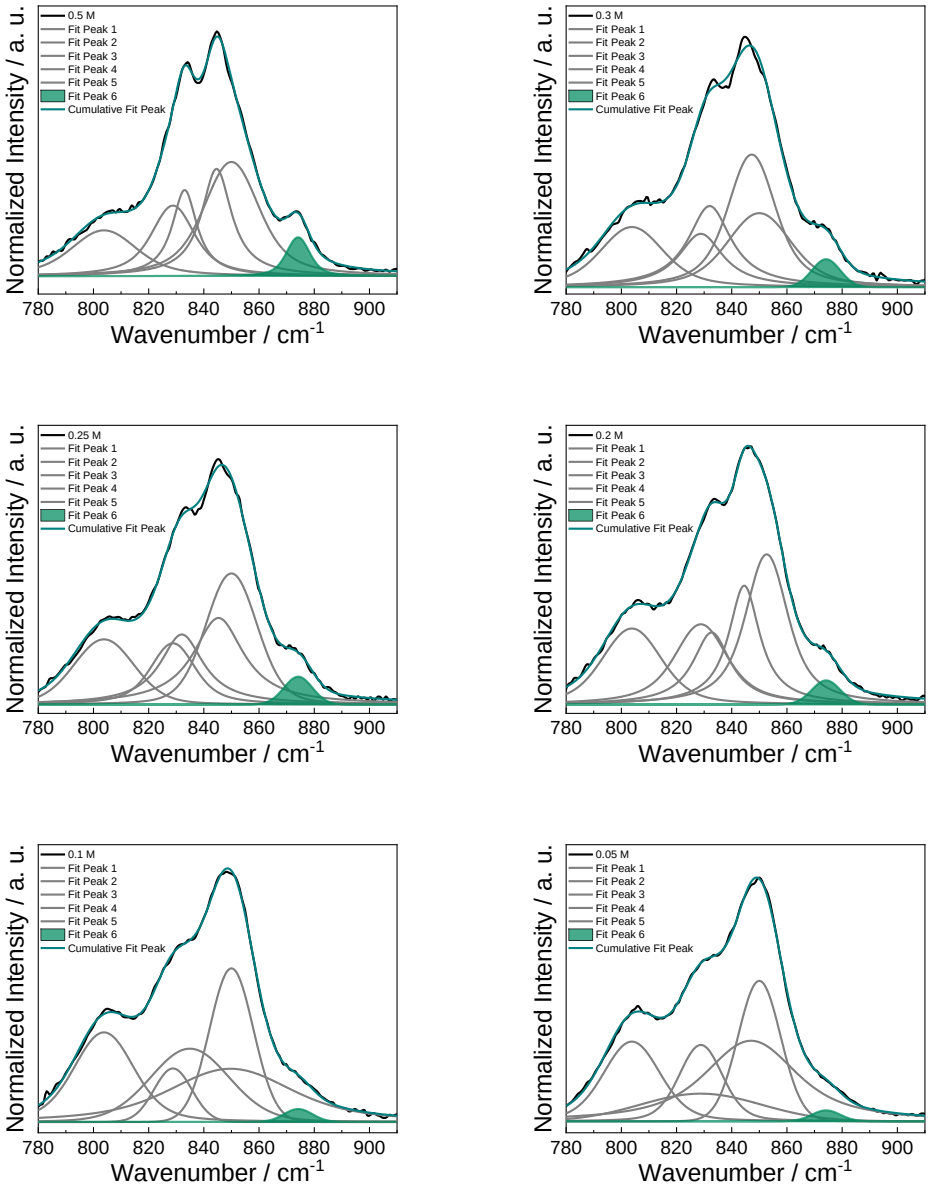

Figure 4-6. Raman spectra and Voigt function fitting results of $Mg[B(TFE)_4]_2$/triglyme in several concentrations in the wave number between 780 and 910 cm^{-1}.

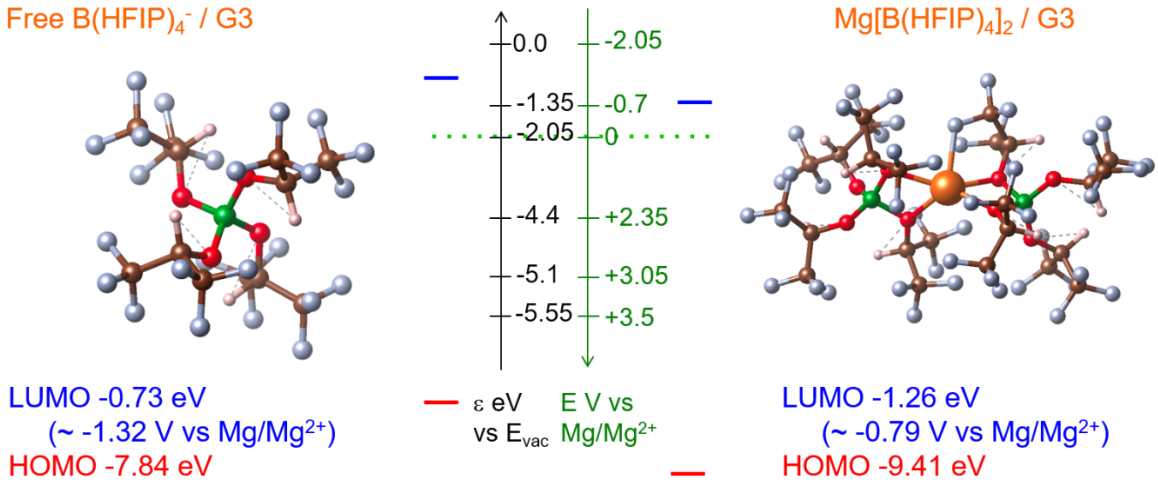

Figure 4-7. DFT cluster calculations of free $[B(HFIP)_4]^-$ and in contact $[B(HFIP)_4]^-$.

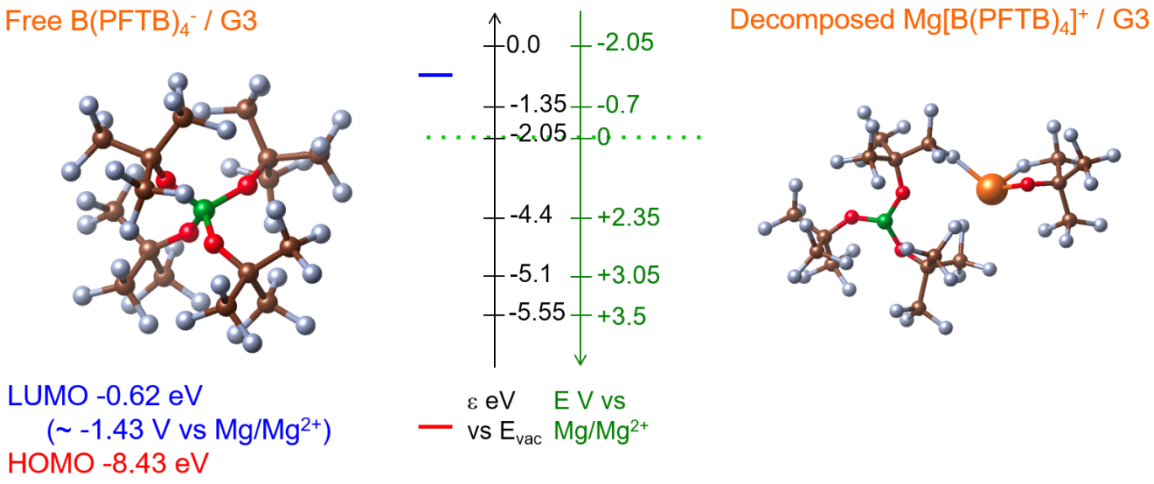

Figure 4-8. DFT cluster calculations of free $[B(PFTB)_4]^-$ and in contact $[B(PFTB)_4]^-$.

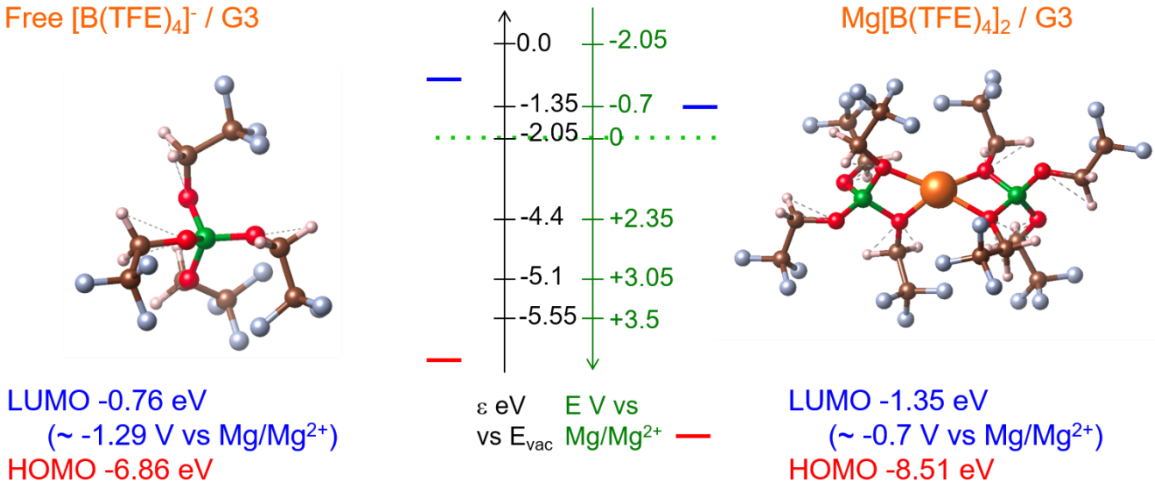

Figure 4-9. DFT cluster calculations of free $[B(TFE)_4]^-$ and in contact $[B(TFE)_4]^-$.

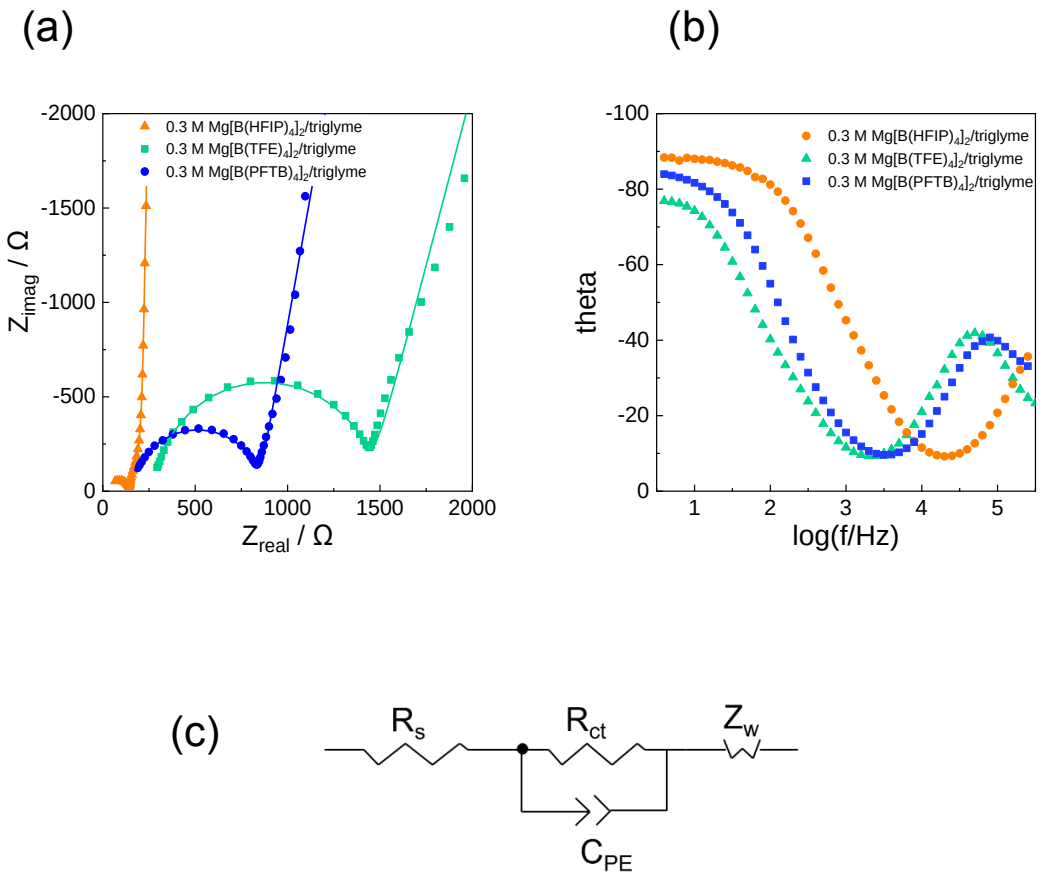

Figure 4-10. (a) Nyquist plots of Mg electrode immersed in 0.3 M $Mg[B(HFIP)_4]_2$/triglyme, 0.3 M $Mg[B(PFTB)_4]_2$/triglyme, and 0.3 M $Mg[B(TFE)_4]_2$/triglyme electrolytes. Fitted impedance spectra shown in solid line. (b) Bode phase shift plot that donates the capacitive responses. (c) Equivalent circuit model, in which electrolyte solution resistance is R_s, charge transfer resistance is R_{ct}, constant phase element is C_{PE} and the Warburg impedance is Z_w.

Table 4-1. The fitted parameter results of Figure 4-10.

Electrolyte	0.3 M $Mg[B(HFIP)_4]_2$/triglyme	0.3 M $Mg[B(PFTB)_4]_2$/triglyme	0.3 M $Mg[B(TFE)_4]_2$/triglyme
R_s / Ω	22.3	151.9	263.8
R_{ct} / Ω	115.6	653.8	1083
CPE2	1.1×10^{-8}	9.9×10^{-9}	7.0×10^{-9}
p2	0.96	0.96	0.99

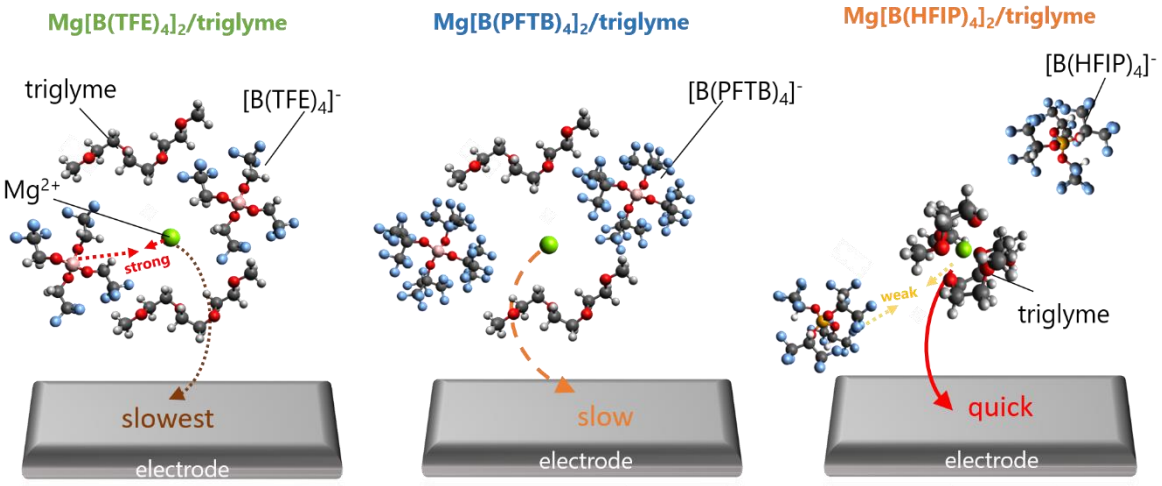

Figure 4-11. Schematic illustrations of the behavior of the magnesium ions at the anode/electrolyte interface in the $Mg[B(HFIP)_4]_2$/triglyme, $Mg[B(PFTB)_4]_2$/triglyme, and $Mg[B(TFE)_4]_2$/triglyme electrolytes.

Chapter 5. Phase Transition Behavior of $MgMn_2O_4$ Spinel Oxide Cathode During Magnesium Ion Insertion

5-1. Introduction

The development of energy storage devices is important for the realization of a sustainable society, and there is an urgent need to develop storage batteries that outperform the rechargeable lithium-ion batteries that are currently in practical use.[1,2] Rechargeable batteries with a magnesium metal anode are attracting attention as the next generation of rechargeable batteries due to the high theoretical capacity of magnesium metal anodes (2205 mAh/g, 3832 mAh/cm^3) and the abundance of resources and because magnesium metal anodes are highly safe.[3-6] However, the magnesium metal anode secondary batteries have major challenges that need to be addressed before they can be commercialized, one of which is the development of a cathode material that can reversibly insert and extract divalent magnesium ions.

Magnesium ions, which are divalent, are more difficult to insert into and extract from a host than are lithium ions, which are monovalent, owing to their strong interactions with anions.[7] Sulfide-based cathode materials, such as Chevrel[7-9] and thiospinel,[10-12] are capable of reversible insertion and extraction of magnesium ions, but their low capacity and potential make them difficult to construct high energy density batteries. Therefore, oxide materials such as V_2O_5, [13-15] MnO_2, [16,17] polyanions,[18-21] layered rock-salt, [22,23] and spinels[24-32] have been developed toward achieving higher charge-discharge potentials and capacities than those of sulfide-based cathode materials.

Among the oxides, spinel oxides have relatively high potential and capacity.[24-32] They are currently difficult to use in Me^{3+}/Me^{4+} redox, owing to their high potential and large polarization and because of the effects of electrolyte decomposition. [25-27,30-32] On the other hand, Okamoto et al. found that magnesium ions can be inserted into and extracted from spinel oxides at relatively low potentials using Me^{2+}/Me^{3+} redox, [30,31] similar to the insertion of lithium ions into $LiMn_2O_4$.[33] In Me^{2+}/Me^{3+} redox,[30,31]a transition from the spinel phase to the rock-salt phase occurs when a magnesium ion is inserted into the 16c empty site of the spinel structure, as the cation at the 8a site is transferred to the other 16c empty site. It has been investigated in detail that the phase transition behavior of $LiMn_2O_4$ spinel oxides, which is the cathode material for lithium-ion secondary batteries, undergoes typical two-phase reaction between $LiMn_2O_4$ spinel oxides and $Li_2Mn_2O_4$ rock-salt oxides.[33] However, detailed crystal structure analysis of magnesium insertion into spinel oxides has not been performed, and details of the mechanism of the transition from a spinel layer to a rock-salt layer have not been clarified. In this study, we investigated the crystal structural changes and valance changes in $MgMn_2O_4$ during Mg^{2+} insertion using X-ray diffraction (XRD) and X-ray absorption spectroscopy (XAS) in order to elucidate the mechanism of the phase transition from spinel to rock-salt.

5-2. Experimental

5.2.1. Synthesis of $MgMn_2O_4$

$MgMn_2O_4$ was prepared using a previously reported propylene-oxide-driven sol-gel method.[27] Stoichiometric amounts of magnesium and manganese chlorides were dissolved in ethanol with citric acid. Then, propylene oxide was added to the solution to

produce organic-metal complex gels. The wet gels were washed with ethanol and acetone to remove byproducts, and then the liquids in the pores were sequentially replaced with acetone and cyclohexane. After preparing for xerogel through freeze drying for the rinsed sample with liquid nitrogen, and then $MgMn_2O_4$ was obtained by calcining the xerogel at 300°C for 5 h in air.

5.2.2. Electrochemical measurements

Galvanostatic discharge/charge measurements were carried out using two-electrode cells. The composite electrodes were prepared by mixing 80 wt% $MgMn_2O_4$, 10 wt% acetylene black, and 10 wt% poly(vinylidene fluoride) in *N*-methylpyrrolidone solvent, and the resultant mixture was pasted on aluminum foil. The composite electrodes were used as the positive electrode, while a Mg-Al-Zn alloy (AZ31) with a Mg:Al:Zn atomic ratio of 96:3:1 was used as the negative electrode. 0.3 M Magnesium tetrakis(hexafluoroisopropyloxy)borate ($Mg[B(HFIP)_4]_2$)/triglyme, in which $Mg[B(HFIP)_4]_2$ was prepared by previously reported method,[34] used as electrolyte solution filled in separator. The charging capacity was fixed at 135 mAh/g instead of setting the upper limit potential during charging, as the decomposition of the electrolyte starts at 3.0 V or higher as shown in Figure 5-1. Galvanostatic discharge and charge measurements were performed at a rate of C/20 (1 C = 270 mA/g) with a capacity limit of 135 mAh/g at 50 °C, which is similar condition in the previously report.[27] Open-circuit-voltage (OCV) measurements were performed using a three-electrode cell; the composite electrode was used as the working electrode and AZ31 was used as the counter and reference electrodes, while 0.3 M $Mg[B(HFIP)_4]_2$/triglyme was used as the electrolyte. The OCV curve for the discharge process was obtained for the $MgMn_2O_4$ electrode by

repeating the electrochemical process consisting of current pulses at C/20 for 4 h and relaxation for 20 h.

5.2.3. Characterization

Synchrotron XRD measurements of the samples before and after the electrochemical measurements were performed at the BL5S2 beamline in Aichi Synchrotron Radiation Center, Aichi Science & Technology Foundation, Aichi, Japan. The wavelength was 0.62025 Å, which was calibrated using CeO_2. Rietveld refinement was carried out using the program JANA2006 (Windows version, copyright 2008)[35] with a pseudo-Voigt profile function. For the synchrotron XRD measurements, the samples were inserted into glass capillaries, which were then sealed with resin in an argon-filled glove box to prevent air exposure. The atomic ratio of the as-prepared $MgMn_2O_4$ powder was determined using inductively coupled plasma optical emission spectroscopy (ICP-OES) at the industrial research center of Shiga prefecture, Japan. The particle size of the as-prepared $MgMn_2O_4$ powder was determined using transmission electron microscopy (TEM, FEI Tecnai F20 or FEI Tecnai Osiris).

XAS measurements of the samples before and after the electrochemical measurements were performed in the energy region of the Mn *K*-edge in transmission mode at the BL11S2 beamline of the Aichi Synchrotron Radiation Center, Aichi Science & Technology Foundation, Aichi, Japan. For the XAS measurements, the samples that had undergone electrochemical measurements were sealed in an argon-filled glove box to prevent air exposure.

5-3. Results and discussion

The crystal structure of the spinel cathode was examined using XRD and the results are shown in Figure 5-2. Rietveld analysis of the obtained XRD pattern revealed

that the spinel cathode consisted of 86% spinel phase with an $I4_1/amd$ space group and 14% rock-salt phase with an $Fm\text{-}3m$ space group (Table 5-1). The X-ray absorption near edge structure (XANES) of the Mn *K*-edge of the cathode showed that the energy at a normalized intensity of 0.5 was lower than that of Mn_2O_3 (Figure 5-3). This indicates that the valence of Mn in the cathode was reduced compared to stoichiometric $MgMn_2O_4$. The ICP-OES measurements showed that the Mg/Mn ratio was 0.52, indicating that the cathode contained an excess amount of Mg and composition is $Mg_{1.04}Mn_2O_4$. These results suggest that the rock-salt phase was formed owing to the excess of Mg over the stoichiometric composition during synthesis. In order to determine the particle size of the $Mg_{1.04}Mn_2O_4$ oxides, TEM images of the samples were obtained (Figures 5-2 b). The average particle size of the as-prepared $Mg_{1.04}Mn_2O_4$ was approximately 10 nm, which was consistent with a previous report.[27]

The first discharge–charge curves of the synthesized $Mg_{1.04}Mn_2O_4$ is shown in Figure 5-4 a and the OCV plot for the first discharge is shown in Figure 5-4 b. A reversible charge / discharge behavior with large polarization can be seen in Figure 5-4 a, which is similar to previous report. [27] The OCV plot showed that the potential decreased gradually with Mg^{2+} insertion, unlike the charge–discharge behavior of $LiFePO_4$.[36, 37] This indicates that Mg^{2+} insertion into $Mg_{1.04}Mn_2O_4$ does not proceed via a typical two-phase reaction as does Li^+ insertion/extraction for $LiFePO_4$. [36, 37] When x ($Mg_{1.04+x}Mn_2O_4$) is 0.2 or less, the polarization is small, and when x is 0.2 or more, the polarization is large.

The XAS spectra of the Mn *K*-edge for $Mg_{1.04}Mn_2O_4$ after Mg^{2+} insertion was obtained in order to examine the charge compensation of the Mn in $Mg_{1.04+x}Mn_2O_4$ (Figure 5-5). The XANES shifted toward lower energy upon Mg^{2+} insertion (Figure 5-5 a). It can be seen that the oxidation number of Mn in the synthesized $MgMn_2O_4$ was

shifted to the lower energy side than the oxidation number of Mn(Ⅲ) in Mn_2O_3, and was further reduced. This is consistent with the XRD and ICP-OES results. The energy at a normalized intensity of 0.5 ($E_{0.5}$) decreased with Mg^{2+} insertion to the energy range between those of Mn_2O_3 and MnO (Figure 5-5 b), indicating that some of the Mn ions in $Mg_{1.04+x}Mn_2O_4$ were reduced from Mn^{3+} to Mn^{2+}. The XANES spectrum of $Mg_{1.04}Mn_2O_4$ during Mg^{2+} insertion did not show the isosbestic points that were observed for $LiFePO_4$[38] (Figure 5-5 a inset), indicating that Mg^{2+} insertion into $Mg_{1.04}Mn_2O_4$ does not proceed via a typical two-phase reaction as $LiFePO_4$ does. These XAS results were in agreement with the OCV measurement results.

Changes in the crystal structure of $Mg_{1.04}Mn_2O_4$ during Mg^{2+} insertion were examined using synchrotron XRD measurements. In the XRD patterns (Figure 5-6 a), $Mg_{1.04}Mn_2O_4$ before discharge gave peaks attributed to spinel phase with an $I4_1/amd$ space group and a small amount of rock-salt phase with an $Fm\text{-}3m$ space group. After the insertion of more than 0.2 mol of Mg^{2+}, the intensity of the spinel-derived peaks decreased with further Mg^{2+} insertion, while the intensity of the rock-salt-derived peaks increased. Rietveld analysis was used on the obtained XRD patterns to estimate the change in the phase fraction between the spinel and rock-salt phases with the insertion of Mg^{2+}. The results of Rietveld refinement are shown in Figures 5-7 – 5-11 and Tables 5-2 – 5-6. Before Mg^{2+} insertion, the spinel phase fraction was 86% and the rock-salt phase fraction was 14%, and the phase fractions were constant with the insertion of up to 0.2 mol of Mg^{2+} (Figure 5-6 b). However, when the amount of Mg^{2+} inserted exceeded 0.2 mol, the spinel phase fraction decreased with further Mg^{2+} insertion, while the rock-salt phase fraction increased, and the spinel and rock-salt phase fractions after the insertion of 0.5 mol of Mg^{2+} were 34% and 66%, respectively.

The changes in the lattice parameters of the spinel and rock-salt phases with Mg^{2+} insertion are shown in Figure 5-12. For the spinel phase, lattice constants a and b remained unchanged even after Mg^{2+} insertion (Figure 5-12 a). Lattice constant c increased with the insertion of up to 0.4 mol of Mg^{2+} and then remained unchanged with further Mg^{2+} insertion (Figure 5-12 a). For the rock-salt phase, the lattice constant increased with the insertion of up to 0.4 mol of Mg^{2+} and then remained unchanged with further Mg^{2+} insertion (Figure 5-12 b). The ratio of volume changes was calculated using the following equation:

$$\Delta V(\%) = \frac{Vrocksalt_x - Vspinel_x}{Vspinel_x} * 100$$

where $V_{rocksalt}$ and V_{spinel} are the lattice volumes normalized by the number of Mn atoms in a single lattice. The ratio of volume changes increased with the insertion of up to 0.4 mol of Mg^{2+} and remained unchanged with further Mg^{2+} insertion (Figure 5-12 c). However, the ratio of volume change at each amount of Mg was smaller than the ratio of volume changes for the conversion of $MgMn_2O_4$ to $Mg_2Mn_2O_4$ for stoichiometric composition.

In the early stage of Mg^{2+} insertion into $Mg_{1.04+x}Mn_2O_4$ ($0 < x < 0.2$), the ratio between the spinel and rock-salt phases remained unchanged (Figure 5-6 b), while the lattice constant of each phase increased (Figures 5-12 a and b). The expansion of lattice constant c for the spinel phase (Figure 5-12 a) indicates that Mg^{2+} insertion into $Mg_{1.04}Mn_2O_4$ proceeds via a solid-solution reaction ($Mg_{1+\alpha}Mn_2O_4$) and the lattice expansion was attributed to the reduction of Mn ions in the spinel phase. In contrast, the increase of the lattice constant for the rock-salt phase indicates that the rock-salt phase in the pristine state had Mg vacancies ($Mg_{2-\beta}Mn_2O_4$) and the reduction of Mn with Mg^{2+}

insertion into the $Mg_{2-\beta}Mn_2O_4$ rock-salt phase increased the lattice constant. In the middle stage of Mg^{2+} insertion ($0.2 < x < 0.4$), the amount of the spinel phase decreased while lattice constant c increased; conversely, the amount of the rock-salt phase increased while the lattice constant increased (Figure 5-6 b and Figures 5-12 a and b). This indicates that the phase transition from the $Mg_{1+\alpha}Mn_2O_4$ spinel phase to the $Mg_{2-\beta}Mn_2O_4$ rock-salt phase occurs with Mg^{2+} insertion into each phase. In the last stage ($0.4 < x < 0.5$), the amount of the spinel phase decreased and that of the rock-salt phase increased while the lattice constant of each phase remained unchanged (Figure 5-6 b and Figures 5-12 a and b). This indicates that the $Mg_{1+\alpha}Mn_2O_4$ spinel and $Mg_{2-\beta}Mn_2O_4$ rock-salt phases reached a solid solution limit and that Mg^{2+} insertion proceeded via a two-phase coexistence reaction between the two phases. The Mg contents in the $Mg_{1+\alpha}Mn_2O_4$ spinel and $Mg_{2-\beta}Mn_2O_4$ rock-salt phases in the two-phase coexistence region were estimated to be 1.4 ($Mg_{1.4}Mn_2O_4$ spinel) and ($Mg_{1.6}Mn_2O_4$ rock-salt) based on Rietveld analysis, respectively. The XRD results show that Mg^{2+} insertion into $MgMn_2O_4$ does not proceed via a typical two-phase reaction as $LiFePO_4$ does, which is in agreement with the results of OCV measurements and XAS.

The phase transition mechanism of Mg^{2+} insertion into $Mg_{1.04}Mn_2O_4$ is shown in Figure 5-13. Since polarization during Mg^{2+} insertion increases as the phase proportion between the $Mg_{1+\alpha}Mn_2O_4$ spinel and $Mg_{2-\beta}Mn_2O_4$ rock-salt phases changes (Figures 5-4b and 5-6b), [39] suppression of the phase transition from the spinel phase to the rock-salt phase to reduce this polarization is important. The phase transition from spinel to rock-salt is caused by the transfer of Mg^{2+} from an 8a site to a 16c site after the insertion of Mg into an empty 16c site of the spinel phase. Therefore, the substitution of Mg in spinel

$MgMn_2O_4$ with elements that prefer tetrahedral sites, such as zinc,[39] could suppress the polarization caused by the phase transition.

5-4. Conclusions

The mechanism for the phase transition during Mg^{2+} insertion into a spinel $MgMn_2O_4$ cathode for rechargeable magnesium batteries was clarified using OCV measurements, XAS, and XRD in this study. Mg^{2+} insertion into $Mg_{1.04}Mn_2O_4$ does not occur through a simple two-phase reaction between the $MgMn_2O_4$ spinel phase and $Mg_2Mn_2O_4$ rock-salt phase. In the early stage of Mg^{2+} insertion, Mg^{2+} is inserted into the spinel ($Mg_{1+\alpha}Mn_2O_4$) phase and rock-salt ($Mg_{2-\beta}Mn_2O_4$) phase, which are both found in pristine samples. In the middle stage, Mg^{2+} is inserted into the $Mg_{1+\alpha}Mn_2O_4$ spinel phase and the $Mg_{2-\beta}Mn_2O_4$ rock-salt phase with a phase transition from the spinel phase to the rock-salt phase. In the last stage of Mg^{2+} insertion process, Mg^{2+} insertion proceeds via a two-phase coexistence reaction between $Mg_{1.4}Mn_2O_4$ spinel and $Mg_{1.6}Mn_2O_4$ rock-salt phases without changes in the Mg content in either phase. As the phase transition from the spinel phase to the rock-salt phase increases the polarization in the Mg^{2+} insertion process, suppression of this phase transition is important in designing a spinel oxide cathode with a high rate performance.

References

1. J. M. Tarascon and M. Armand, *Nature*, **2001**, 414, 359-367.
2. A. Yoshino, *Angew. Chem., Int. Ed.*, **2012**, 51, 5798-5800.
3. D. Aurbach, Y. Cohen and M. Moshkovich, *ECS Solid State Lett.*, **2001**, 4, A113.
4. D. Aurbach, Z. Lu, A. Schechter, Y. Gofer, H. Gizbar, R. Turgeman, Y. Cohen, M. Moshkovich and E. Levi, *Nature*, **2000**, 407, 724-727.
5. J. O. Besenhard and M. Winter, *ChemPhysChem*, **2002**, 3, 155-159.
6. M. Matsui, *J. Power Sources*, **2011**, 196, 7048-7055.
7. E. Levi, M. Levi, O. Chasid and D. Aurbach, *J. Electroceramics*, **2009**, 22, 13-19.
8. D. Aurbach, G. S. Suresh, E. Levi, A. Mitelman, O. Mizrahi, O. Chusid and M. Brunelli, *Adv. Mater.*, **2007**, 19, 4260-4267.
9. E. Levi and D. Aurbach, *Chem. Mater.*, **2010**, 22, 3678-3692.
10. Y. Liang, R. Feng, S. Yang, H. Ma, J. Liang and J. Chen, *Adv. Mater.*, **2011**, 23, 640-643.
11. X. Sun, P. Bonnick, V. Duffort, M. Liu, Z. Rong, K. A. Persson, G. Ceder and L. F. Nazar, *Energy Environ. Sci.*, **2016**, 9, 2273-2277.
12. Z.-L. Tao, L.-N. Xu, X.-L. Gou, J. Chen and H.-T. Yuan, *Chem. Commun.*, **2004**, 2080-2081.
13. Q. Fu, A. Sarapulova, V. Trouillet, L. Zhu, F. Fauth, S. Mangold, E. Welter, S. Indris, M. Knapp and S. Dsoke, *J. Am. Chem. Soc.*, **2019**, 141, 2305-2315.
14. D. Imamura, M. Miyayama, M. Hibino and T. Kudo, *J. Electrochem. Soc.*, **2003**, 150, A753.

15. D. Le, S. Passerini, F. Coustier, J. Guo, T. Soderstrom, B. Owens and W. H. Smyrl, *Chem. Mater.*, **1998**, 10, 682-684.

16. C. Ling, R. Zhang and F. Mizuno, *ACS Appl. Mater. Interfaces*, **2016**, 8, 4508-4515.

17. R. Zhang, X. Yu, K.-W. Nam, C. Ling, T. S. Arthur, W. Song, A. M. Knapp, S. N. Ehrlich, X.-Q. Yang and M. Matsui, *Electrochem. commun*, **2012**, 23, 110-113.

18. Z.-D. Huang, T. Masese, Y. Orikasa, T. Mori, T. Minato, C. Tassel, Y. Kobayashi, H. Kageyama and Y. Uchimoto, *J. Mater. Chem. A*, **2014**, 2, 11578-11582.

19. Y. Orikasa, K. Kisu, E. Iwama, W. Naoi, Y. Yamaguchi, Y. Yamaguchi, N. Okita, K. Ohara, T. Munesada and M. Hattori, *Chem. Mater.*, **2020**, 32, 1011-1021.

20. Y. Orikasa, T. Masese, Y. Koyama, T. Mori, M. Hattori, K. Yamamoto, T. Okado, Z.-D. Huang, T. Minato and C. Tassel, *Sci. Rep.*, **2014**, 4, 5622.

21. A. Watanabe, K. Yamamoto, Y. Orikasa, T. Masese, T. Mori, T. Uchiyama, T. Matsunaga and Y. Uchimoto, *Solid State Ionics*, **2020**, 349, 115311.

22. N. Ishida, Y. Nakamura, T. Mandai, N. Kitamura and Y. Idemoto, *Solid State Ionics*, **2020**, 354, 115413.

23. N. Ishida, N. Yamazaki, T. Mandai, N. Kitamura and Y. Idemoto, *J. Electrochem. Soc.*, **2020**.

24. R. D. Bayliss, B. Key, G. Sai Gautam, P. Canepa, B. J. Kwon, S. H. Lapidus, F. Dogan, A. A. Adil, P. J. Baker, *Chem. Mater.*, **2019**, 32, 663-670.

25. T. Hatakeyama, N. L. Okamoto, K. Shimokawa, H. Li, A. Nakao, Y. Uchimoto, H. Tanimura, T. Kawaguchi and T. Ichitsubo, *Phys. Chem. Chem. Phys.*, **2019**, 21, 23749-23757.

26. L. Hu, J. R. Jokisaari, B. J. Kwon, L. Yin, S. Kim, H. Park, S. H. Lapidus, R. F. Klie, B. Key and P. Zapol, *ACS Energy Lett.*, **2020**, 5, 2721-2727.

27. K. Ishii, S. Doi, R. Ise, T. Mandai, Y. Oaki, S. Yagi and H. Imai, *J. Alloys Compd*, **2020**, 816, 152556.

28. B. J. Kwon, K.-C. Lau, H. Park, Y. A. Wu, K. L. Hawthorne, H. Li, S. Kim, I. L. Bolotin, T. T. Fister and P. Zapol, *Chem. Mater.*, **2019**, 32, 1162-1171.

29. B. J. Kwon, L. Yin, H. Park, P. Parajuli, K. Kumar, S. Kim, M. Yang, M. Murphy, P. Zapol and C. Liao, *Chem. Mater.*, **2020**, 32, 6577-6587.

30. S. Okamoto, T. Ichitsubo, T. Kawaguchi, Y. Kumagai, F. Oba, S. Yagi, K. Shimokawa, N. Goto, T. Doi and E. Matsubara, *Adv. Sci.*, **2015**, 2, 1500072.

31. K. Shimokawa, T. Atsumi, M. Harada, R. E. Ward, M. Nakayama, Y. Kumagai, F. Oba, N. L. Okamoto, K. Kanamura and T. Ichitsubo, *J. Mater. Chem. A*, **2019**, 7, 12225-12235.

32. S. Doi, R. Ise, T. Mandai, Y. Oaki, S. Yagi and H. Imai, *Langmuir*, **2020**, 36, 8537-8542.

33. T. Ohzuku, M. Kitagawa and T. Hirai, *J. Electrochem. Soc.*, **1990**, 137, 769.

34. Z. Zhao-Karger, M. E. G. Bardaji, O. Fuhr and M. Fichtner, *J. Mater. Chem. A*, **2017**, 5, 10815-10820.

35. V. Petříček, M. Dušek and L. Palatinus, *Z. Kristallogr. Cryst. Mater.*, **2014**, 229, 345-352.

36. T. Sasaki, Y. Ukyo and P. Novák, *Nat. Mater.*, **2013**, 12, 569-575.

37. Y. Zhu and C. Wang, *J. Phys. Chem. C*, **2010**, 114, 2830-2841.

38. Y. Orikasa, T. Maeda, Y. Koyama, H. Murayama, K. Fukuda, H. Tanida, H. Arai, E. Matsubara, Y. Uchimoto and Z. Ogumi, *Chem. Mater.*, **2013**, 25, 1032-1039.

39. A. Navrotsky and O. Kleppa, *Polyhedron*, **1967**, 29, 2701-2714.

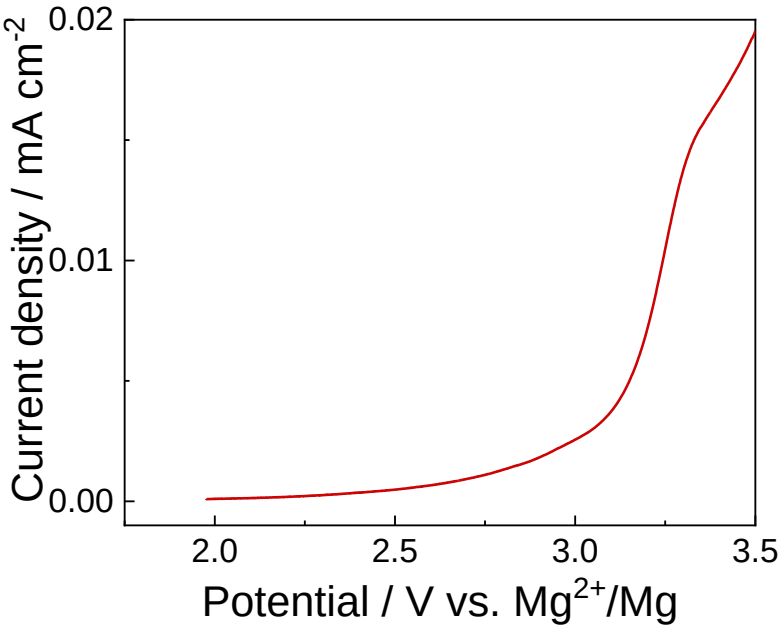

Figure 5-1. Linear sweep voltammetry. Three-electrode cells using Pt working electrode, Mg metal counter electrode, and reference electrodes were used. Electrolyte was 0.3 M Magnesium tetrakis(hexafluoroisopropyloxy)borate ($Mg[B(HFIP)_4]_2$) in triglyme. Potential sweeping rate was 10 mV s^{-1}, and measurement temperature was 50°C.

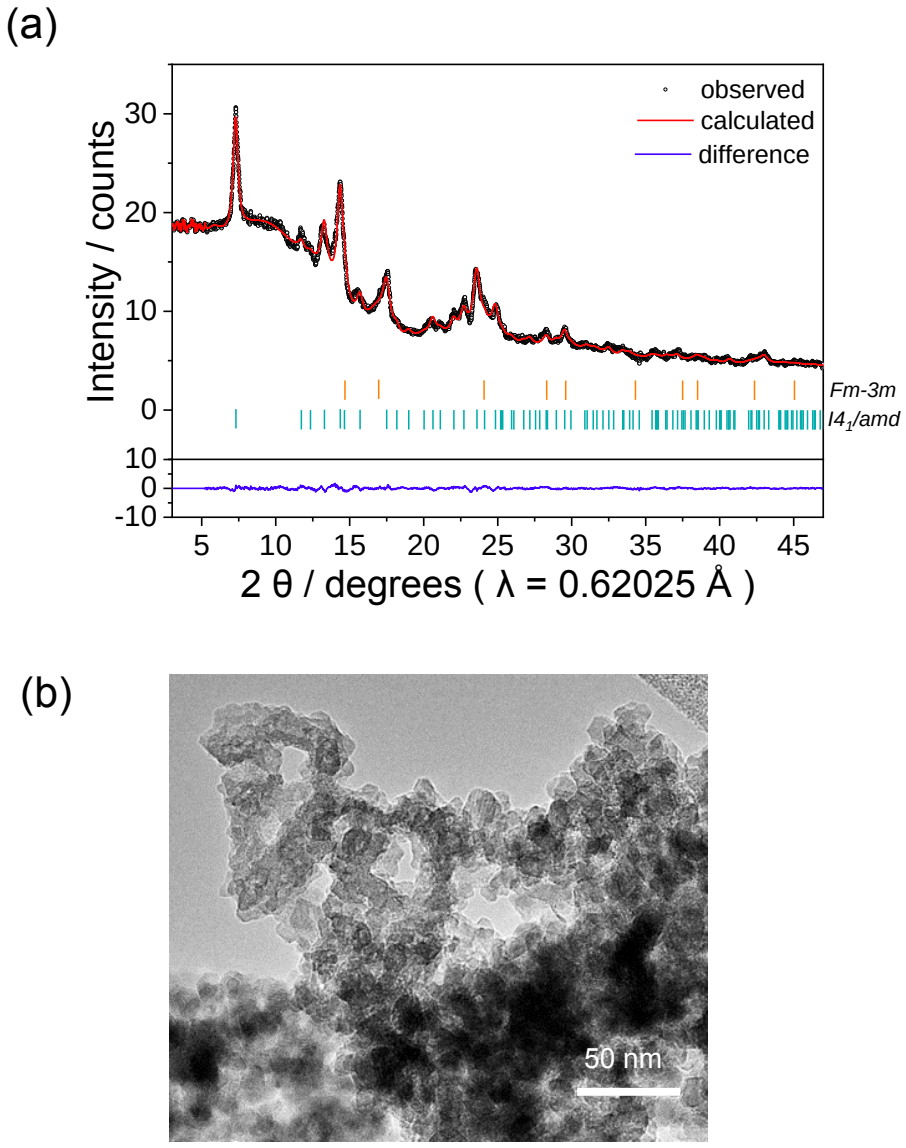

Figure 5-2. Characterization of $MgMn_2O_4$ cathode: (a) XRD pattern and Rietveld analytical fitting profile of the $Mg_{1.04}Mn_2O_4$ cathode sample and (b) TEM image of the $Mg_{1.04}Mn_2O_4$ powder.

Table 5-1. The crystal structure parameters obtained from Rietveld analysis of the $Mg_{1.04}Mn_2O_4$ cathode.

Sample :					$Mg_{1.04}Mn_2O_4$				R_{wp} = 3.14 %
Phase	Space group	Atom	site	x	y	z	Occu-pancy	Lattice parameter /Å	Phase amounts in mass
spinel	*I4₁/amd*	Mg11	4b	0	0	0.5	1	a 5.766(2)	0.859(18)
		Mn12	8c	0	-0.25	0.125	1	b 5.766(2)	
		O11	16h	0	0.252	0.364	1	c 9.082(3)	
rocksalt	*Fm-3m*	Mg21	4a	0	0	0	0.3	a 4.206(4)	0.141(19)
		Mn21	4a	0	0	0	0.5	b 4.206(4)	
		O21	4b	0.5	0.5	0.5	1	c 4.206(4)	

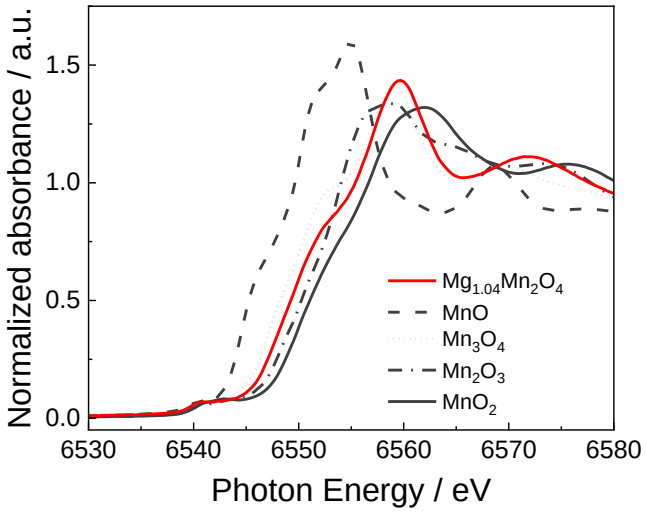

Figure 5-3. XANES for Mn *K*-edge of the $Mg_{1.04}Mn_2O_4$ cathode

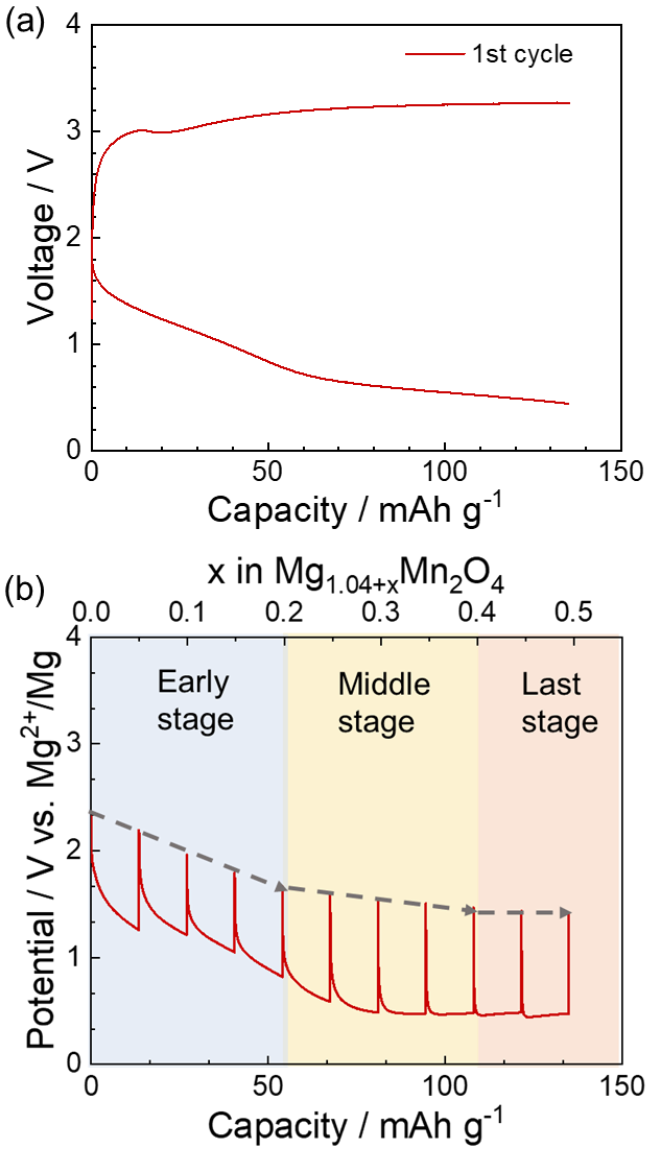

Figure 5-4. (a) Constant-current discharge–charge curves with a capacity limit of 135 mAh/g at 50 °C. (b) GITT profile of $Mg_{1.04}Mn_2O_4$. The grey arrows indicate the OCP change.

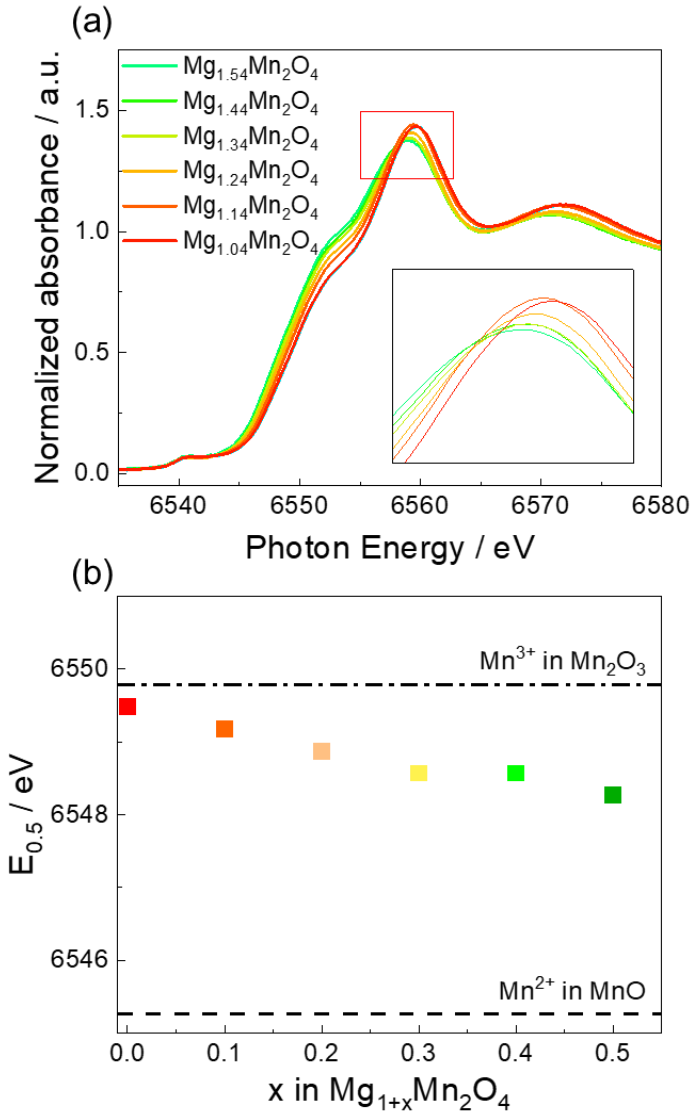

Figure 5-5. (a) Mn *K*-edge XANES of $Mg_{1.04}Mn_2O_4$ before and after Mg^{2+} insertion and (b) energy at a normalized intensity of 0.5 in the XANES.

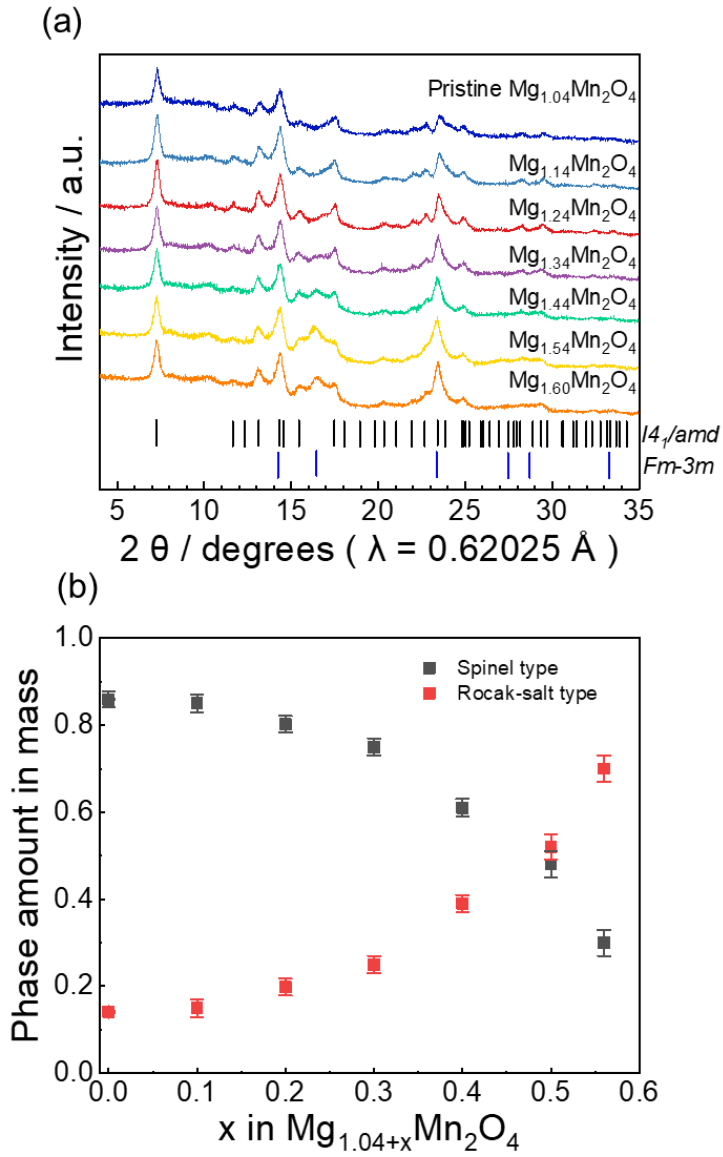

Figure 5-6. (a) XRD patterns of $Mg_{1.04+x}Mn_2O_4$ ($0 \leq x \leq 0.5$) before and after Mg^{2+} insertion. Black index shows diffraction pattern of spinel-type $MgMn_2O_4$ with tetragonal symmetry ($I4_1/amd$) while blue index shows diffraction pattern of rock-salt-type $Mg_2Mn_2O_4$ with cubic symmetry (Fm-$3m$). (b) Ratio between spinel and rock-salt phases estimated through Rietveld analysis.

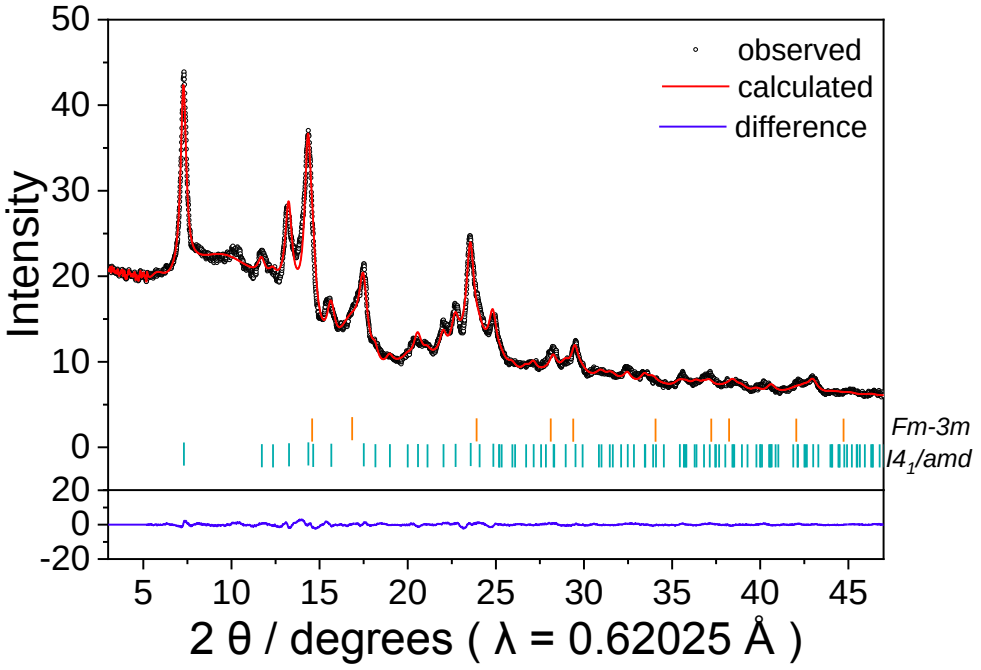

Figure 5-7. XRD pattern and Rietveld analytical fitting profile of the $Mg_{1.14}Mn_2O_4$ cathode sample.

Table 5-2. The crystal structure parameters obtained from Rietveld analysis of the $Mg_{1.14}Mn_2O_4$ cathode sample.

Sample :			$Mg_{1.14}Mn_2O_4$							R_{wp} = 3.83 %
Phase	Space group	Atom	site	x	y	z	Occu-pancy	Lattice parameter /Å		Phase amounts in mass
spinel	*I4₁/amd*	Mg11	4b	0	0	0.5	1	a	5.764(2)	0.85(2)
		Mg12	8d	0	-0.25	0.625	0.05	b	5.764(2)	
		Mn12	8c	0	-0.25	0.125	1	c	9.101(4)	
		O11	16h	0	0.252	0.367	1			
rocksalt	*Fm-3m*	Mg21	4a	0	0	0	0.325	a	4.235(4)	0.15(2)
		Mn21	4a	0	0	0	0.5	b	4.235(4)	
		O21	4b	0.5	0.5	0.5	1	c	4.235(4)	

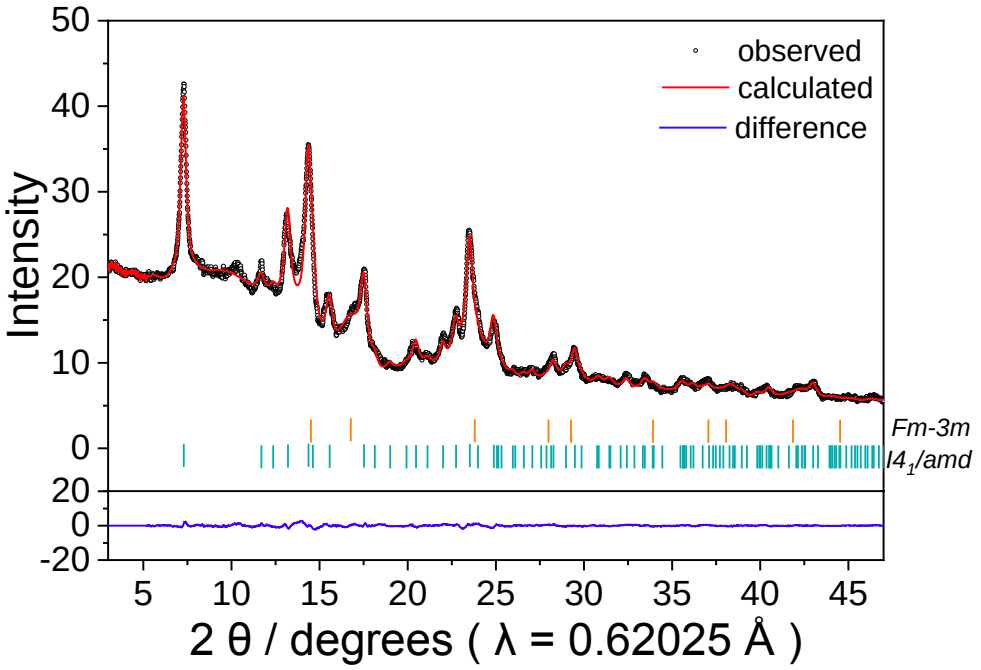

Figure 5-8. XRD pattern and Rietveld analytical fitting profile of the $Mg_{1.24}Mn_2O_4$ cathode sample.

Table 5-3. The crystal structure parameters obtained from Rietveld analysis of the $Mg_{1.24}Mn_2O_4$ cathode sample.

Sample :		$Mg_{1.24}Mn_2O_4$						R_{wp} = 3.62 %		
Phase	Space group	Atom	site	x	y	z	Occu-pancy	Lattice parameter /Å		Phase amounts in mass
spinel	*I4₁/amd*	Mg11	4b	0	0	0.5	1	a	5.758(2)	0.802(19)
		Mg12	8d	0	-0.25	0.625	0.1	b	5.758(2)	
		Mn12	8c	0	-0.25	0.125	1	c	9.158(3)	
		O11	16h	0	0.258	0.369	1			
rocksalt	*Fm-3m*	Mg21	4a	0	0	0	0.35	a	4.253(3)	0.198(19)
		Mn21	4a	0	0	0	0.5	b	4.253(3)	
		O21	4b	0.5	0.5	0.5	1	c	4.253(3)	

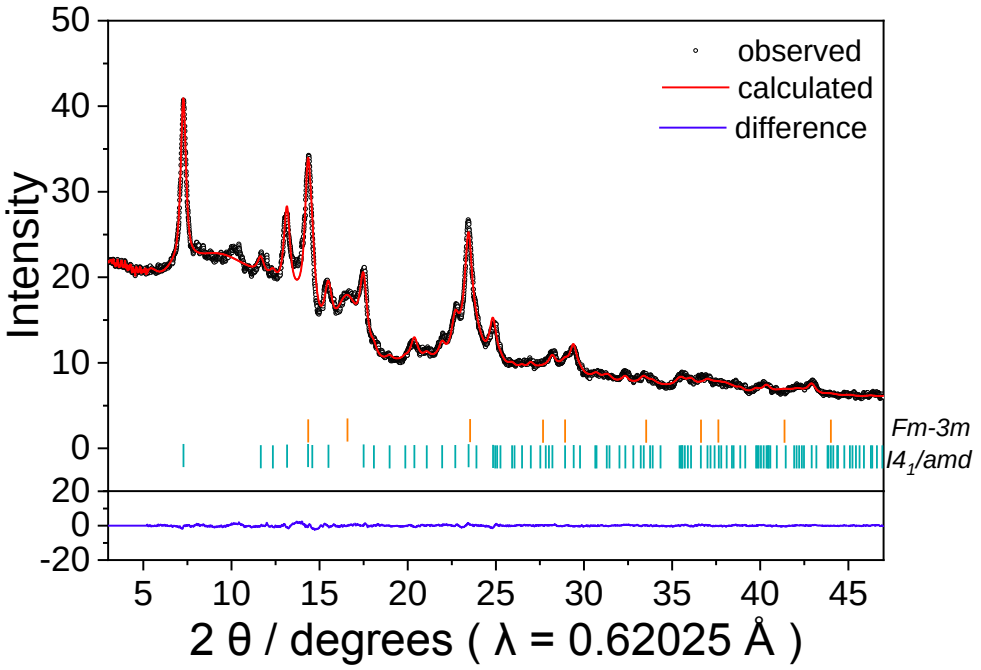

Figure 5-9. XRD pattern and Rietveld analytical fitting profile of the $Mg_{1.34}Mn_2O_4$ cathode sample.

Table 5-4. The crystal structure parameters obtained from Rietveld analysis of the $Mg_{1.34}Mn_2O_4$ cathode sample.

Sample :		$Mg_{1.34}Mn_2O_4$						R_{wp} = 3.17 %		
Phase	Space group	Atom	site	x	y	z	Occu-pancy	Lattice parameter /Å		Phase amounts in mass
spinel	*I4₁/amd*	Mg11	4b	0	0	0.5	1	a	5.767(2)	0.75(2)
		Mg12	8d	0	-0.25	0.625	0.15	b	5.767(2)	
		Mn12	8c	0	-0.25	0.125	1	c	9.200(3)	
		O11	16h	0	0.263	0.369	1			
rocksalt	*Fm-3m*	Mg21	4a	0	0	0	0.375	a	4.301(2)	0.25(2)
		Mn21	4a	0	0	0	0.5	b	4.301(2)	
		O21	4b	0.5	0.5	0.5	1	c	4.301(2)	

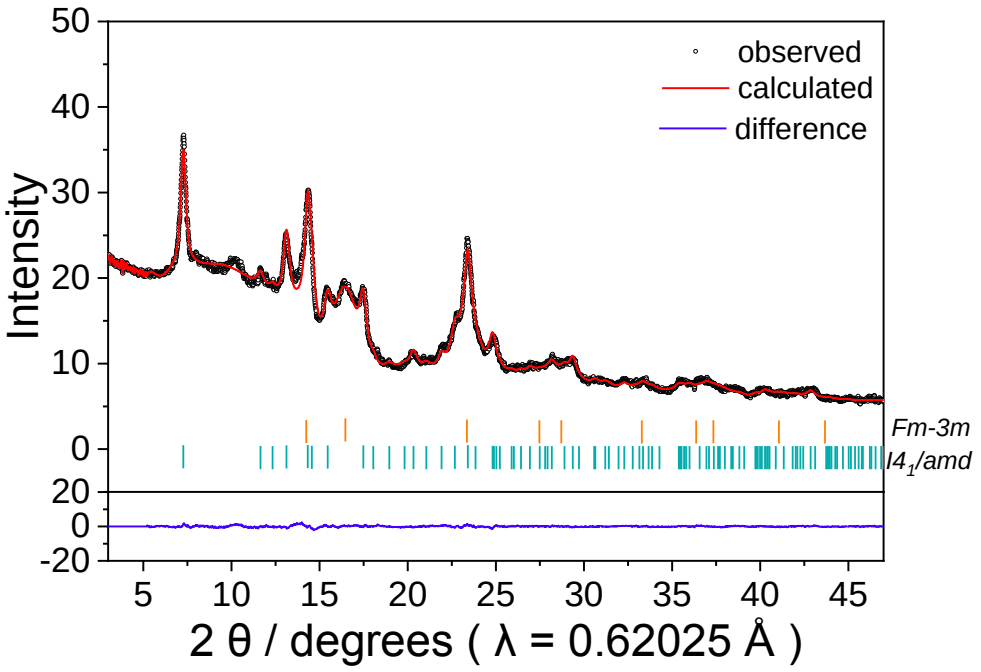

Figure 5-10. XRD pattern and Rietveld analytical fitting profile of the $Mg_{1.44}Mn_2O_4$ cathode sample.

Table 5-5. The crystal structure parameters obtained from Rietveld analysis of the $Mg_{1.44}Mn_2O_4$ cathode sample.

Sample :		$Mg_{1.44}Mn_2O_4$						R_{wp} = 2.96 %		
Phase	Space group	Atom	site	x	y	z	Occu-pancy	Lattice parameter /Å		Phase amounts in mass
spinel	*I4₁/amd*	Mg11	4b	0	0	0.5	1	a	5.773(2)	0.61(2)
		Mg12	8d	0	-0.25	0.625	0.2	b	5.773(2)	
		Mn12	8c	0	-0.25	0.125	1	c	9.224(3)	
		O11	16h	0	0.259	0.372	1			
rocksalt	*Fm-3m*	Mg21	4a	0	0	0	0.4	a	4.332(2)	0.39(2)
		Mn21	4a	0	0	0	0.5	b	4.332(2)	
		O21	4b	0.5	0.5	0.5	1	c	4.332(2)	

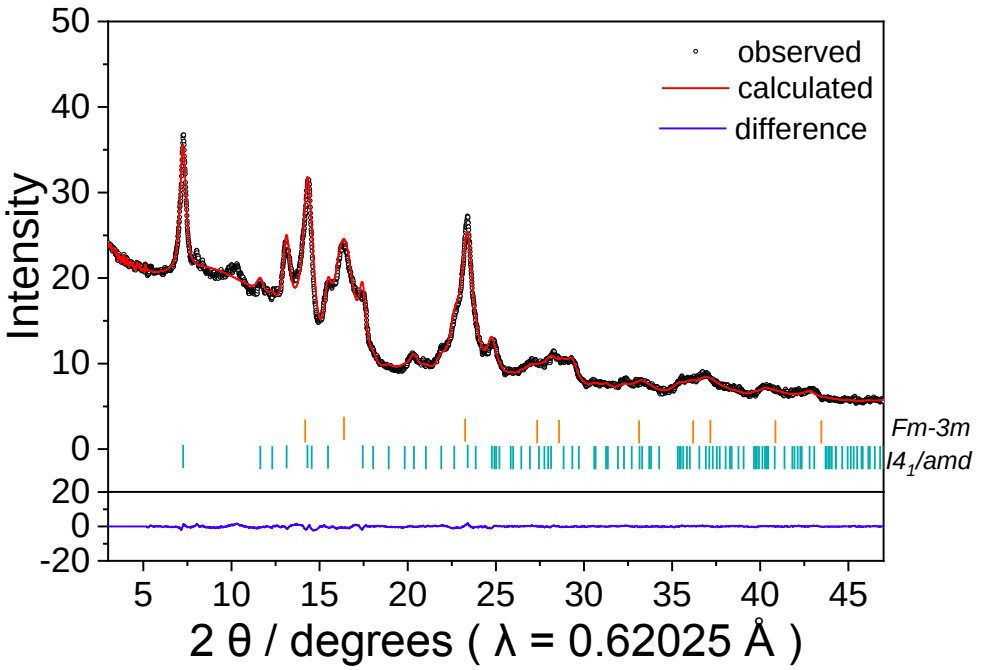

Figure 5-11. XRD pattern and Rietveld analytical fitting profile of the $Mg_{1.54}Mn_2O_4$ cathode sample.

Table 5-6. The crystal structure parameters obtained from Rietveld analysis of the $Mg_{1.54}Mn_2O_4$ cathode sample.

Sample :		$Mg_{1.54}Mn_2O_4$						R_{wp} = 3.23 %		
Phase	Space group	Atom	site	x	y	z	Occu-pancy	Lattice parameter /Å		Phase amounts in mass
spinel	*I4₁/amd*	Mg11	4b	0	0	0.5	1	a	5.775(2)	0.48(3)
		Mg12	8d	0	-0.25	0.625	0.2	b	5.775(2)	
		Mn12	8c	0	-0.25	0.125	1	c	9.218(4)	
		O11	16h	0	0.259	0.375	1			
rocksalt	*Fm-3m*	Mg21	4a	0	0	0	0.4	a	4.342(2)	0.52(3)
		Mn21	4a	0	0	0	0.5	b	4.342(2)	
		O21	4b	0.5	0.5	0.5	1	c	4.342(2)	

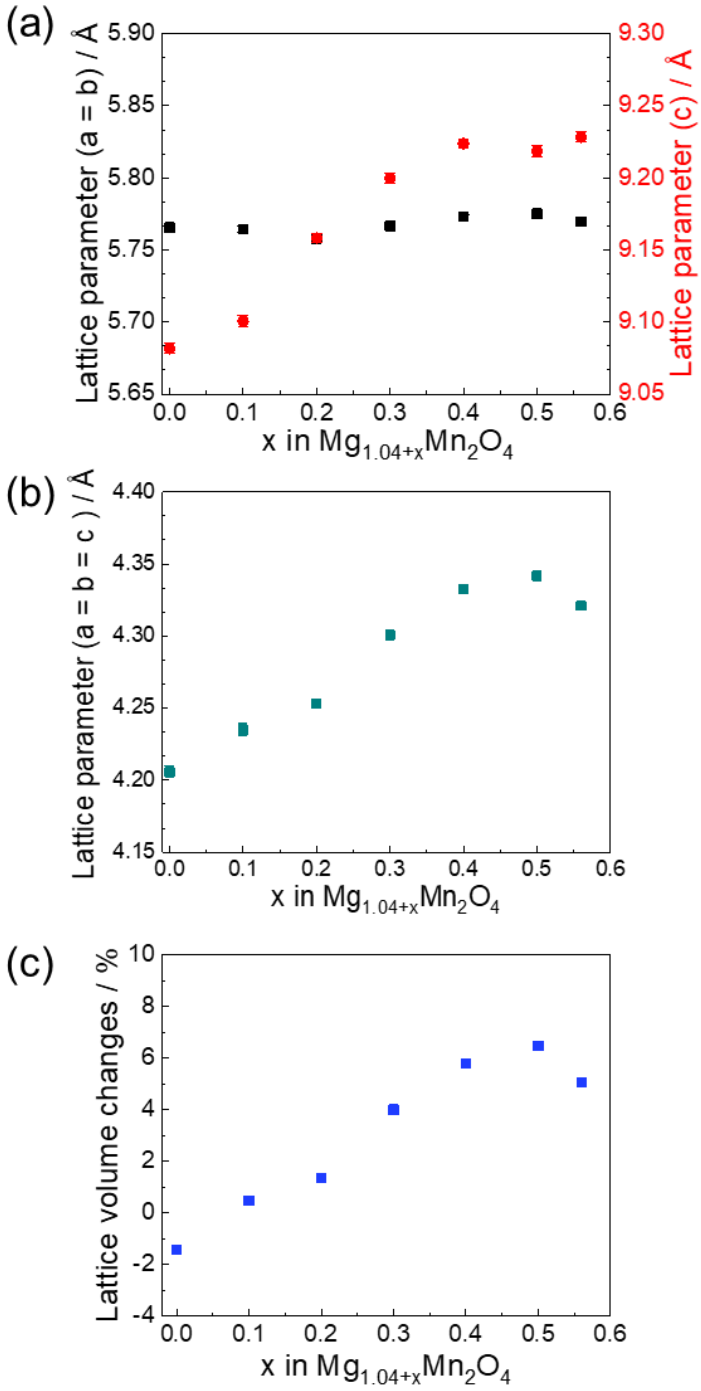

Figure 5-12. Lattice constants of (a) tetragonal spinel-type and (b) cubic rock-salt-type samples. (c) Ratios of volume changes of $Mg_{1.04+x}Mn_2O_4$ ($0 \leq x \leq 0.56$) before and after Mg^{2+} insertion.

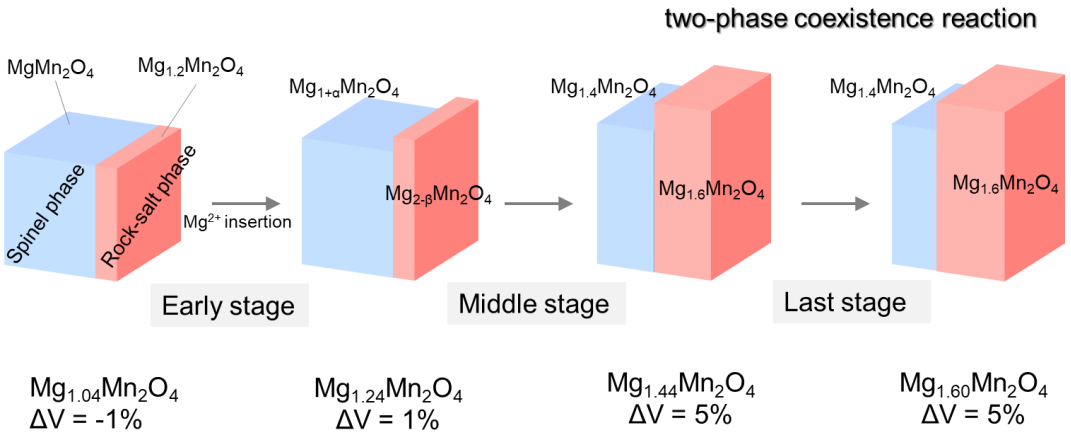

Figure 5-13. Schematic illustration of the volume changes and phase transition model for the transition from spinel phase to rock-salt phase upon magnesium ion insertion.

Chapter 6. Reaction Mechanism of Electrochemical Insertion of Magnesium Ions in $ZnMn_2O_4$ Spinel Oxide Cathode

6-1. Introduction

To achieve a sustainable society of the future, there is a growing demand for large batteries for electric vehicles and stationary energy storage systems.[1,2] Magnesium rechargeable batteries are candidates for next-generation battery systems because low-cost magnesium metal anodes provide high energy density and stability without the formation of dendritic structures such as those resulting from lithium deposition.[3-6] However, compared to the monovalent lithium ion, the divalent magnesium ion has a stronger interaction, which making it more difficult to insert into or extract from the host materials. One of the major challenges in the development of magnesium rechargeable batteries is the limited availability of alternative cathode materials.

In recent years, various cathode materials such as Chevrel[7-9] and thiospinel,[10-12] which are capable of reversible insertion and extraction of magnesium ions have been reported. But their low capacity and low potential make them difficult to construct high energy density batteries. As a strategy to improve electrochemical properties, intercalation materials with high theoretical voltage and capacity were focused on. In terms of higher voltage and capacity, oxides are attractive as cathode materials for magnesium rechargeable batteries. Therefore, oxide materials such as V_2O_5,[13-15] MnO_2,[16, 17] polyanions,[18-21] layered rock-salt,[22, 23] and spinels[24-32] have been developed toward

achieving higher charge-discharge potentials and capacities than those of sulfide-based cathode materials.

Among the oxides, 3d transition metal oxides with a spinel structure are the most promising because of their relatively high potential and capacity. [24-32] Recent studies, including those by our group, have suggested that the phase transition from the spinel phase to the rock-salt phase increases the polarization in the Mg^{2+} insertion process, suppression of the phase transition from the spinel phase to the rock-salt phase to reduce this polarization is important. The phase transition from spinel to rock-salt is caused by the transfer of Mg^{2+} from an 8a site to a 16c site after the insertion of Mg into an empty 16c site of the spinel phase. Therefore, the substitution of Mg in spinel $MgMn_2O_4$ with elements that prefer tetrahedral sites, such as zinc, could suppress the polarization caused by the phase transition. Recently, Ichitsubo's group focusing on the feature that Zn prefers a tetrahedral configuration in spinel oxides, they demonstrate theoretically and experimentally that Zn-based spinel oxides exhibit a markedly improved reversibility in the spinel–rocksalt transition.[31] However, there is a lack of information on the reaction mechanism for the insertion of magnesium ions into the Zn-based spinel oxides.

To investigate the magnesium ion insertion mechanism, Zn-based spinel oxide $ZnMn_2O_4$ is chosen here as a host structure. In this study, we carried out a comparative study of the magnesium insertion mechanism in $MgMn_2O_4$ and $ZnMn_2O_4$ spinel oxides. we investigated the crystal and local structural changes in $ZnMn_2O_4$ during Mg^{2+} insertion

using X-ray diffraction (XRD) and X-ray absorption spectroscopy (XAS) in order to elucidate the mechanism of the phase transition from spinel to rock-salt.

6-2. Experimental

6.2.1. Synthesis of $ZnMn_2O_4$

Nanocrystalline $ZnMn_2O_4$ was prepared using a previously reported inverse coprecipitation method. [31, 33] An aqueous solution of metallic nitrate salts was added dropwise to a solution of Na_2CO_3 at 70 ℃ to obtain a precursor. The obtained precursor was ball-milled after vacuum drying, and then calcined in air at 350 ℃ for two hours.

6.2.2. Electrochemical measurements

Galvanostatic discharge/charge measurements were carried out using two-electrode cells. The composite electrodes were prepared by mixing 80 wt% $ZnMn_2O_4$, 10 wt% acetylene black, and 10 wt% poly(vinylidene fluoride) in *N*-methylpyrrolidone solvent, and the resultant mixture was pasted on aluminum foil. The composite electrodes were used as the positive electrode, while a Mg-Al-Zn alloy (AZ31) with a Mg:Al:Zn atomic ratio of 96:3:1 was used as the negative electrode. 0.3 M Magnesium tetrakis(hexafluoroisopropyloxy)borate ($Mg[B(HFIP)_4]_2$)/triglyme, in which $Mg[B(HFIP)_4]_2$ was prepared by previously reported method,[34] used as electrolyte solution filled in separator. The charging capacity was fixed at 112 mAh/g instead of setting the upper limit potential during charging, as the decomposition of the electrolyte starts at 3.0V or higher as shown in Figure 6-1. Open-circuit-potential (OCP) measurements were performed using a three-electrode cell; the composite electrode was used as the working electrode and AZ31 was used as the counter and reference electrodes,

while 0.3 M $Mg[B(HFIP)_4]_2$/triglyme was used as the electrolyte. The OCP curve for the discharge process was obtained for the $ZnMn_2O_4$ electrode by repeating the electrochemical process consisting of current pulses at C/30 for 1 h and relaxation for 12 h.

6.2.3. Characterization

Synchrotron XRD measurements of the samples before and after the electrochemical measurements were performed at the BL02B2 beamline in SPring-8, Japan. The wavelength was 0.6193 Å, which was calibrated using CeO_2. Rietveld refinement was carried out using the program JANA2006 (Windows version, copyright 2008)[35] with a pseudo-Voigt profile function. For the synchrotron XRD measurements, the samples were inserted into glass capillaries, which were then sealed with resin in an argon-filled glove box to prevent air exposure. The particle size of the as-prepared $ZnMn_2O_4$ powder was determined using transmission electron microscopy (TEM, FEI Tecnai F20 or FEI Tecnai Osiris).

XAS measurements of the samples before and after the electrochemical measurements were performed in the energy region of the Mn *K*-edge in transmission mode at beam lines BL01B1 and BL14B2 of the SPring-8 synchrotron radiation facility in Hyogo, Japan. For the XAS measurements, the samples that had undergone electrochemical measurements were sealed in an argon-filled glove box to prevent air exposure.

6-3. Results and discussion

The crystal structure of the spinel cathode was examined using XRD and the results are shown in Figure 6-2a. The XRD pattern was indexed to the $I4_1/amd$ space

group. There are no detectable peaks attributed to impurities in the sample. In order to investigate the particle size of the $ZnMn_2O_4$, a TEM image of the sample was captured (Figure 6-2b). The average particle size of the as-prepared $ZnMn_2O_4$ was about 10 nm. From the transmission electron image and electron diffraction pattern of $ZnMn_2O_4$ (Figure 6-3), we also can confirm that the as-prepared powder sample was indexed to the spinel phase. The X-ray absorption near edge structure (XANES) of the Mn *K*-edge of the cathode showed that the energy at a normalized intensity of 0.5 was in good agreement with Mn_2O_3 (Figure 6-4). This indicates that the valence of Mn in the cathode was not reduced compared to stoichiometric $ZnMn_2O_4$ which is comparable with $MgMn_2O_4$. As the cathode $MgMn_2O_4$ contained an excess amount of Mg and composition is $Mg_{1.04}Mn_2O_4$.

The first discharge–charge curves of the synthesized $ZnMn_2O_4$ are shown in Figure 6-5. As shown in Figure 6-5a, reversible charge / discharge behavior can be occurred in $ZnMn_2O_4$. In contrast to the $MgMn_2O_4$ cathode, $ZnMn_2O_4$ showed significantly small polarization. We performed cyclability test for $ZnMn_2O_4$ cathode in the 0.3 M ($Mg[B(HFIP)_4]_2$)/triglyme electrolyte under the capacity limiting condition of 112 mAh/g. (Figure 6-6) The charge capacity remained unchanged during 5 cycles, whereas the discharge capacity drastically decreased after first cycle and gradually decreased in the subsequent cycles. The unchanged charge capacity is attributed to the oxidation of the electrolyte because the anodic current appears around 2.5 V by using platinum electrode. The oxidation of the electrolyte inhibits the magnesium extraction reaction of the cathode, resulting in the discharge capacity fading after first cycling. Therefore, in this study, we focus on the Mg insertion reaction instead of Mg extraction reaction, because it is hard to evaluate the charging capacity and Mg composition of the

$ZnMn_2O_4$ cathode due to the effects of the electrolyte decomposition. The OCP plot showed that the potential decreased gradually with Mg^{2+} insertion, unlike the charge–discharge behavior of $LiFePO_4$.[33,34] This indicates that Mg^{2+} insertion into $ZnMn_2O_4$ does not proceed via a typical two-phase reaction as does Li^+ insertion/extraction for $LiFePO_4$.[33,34] When x ($Mg_xZnMn_2O_4$) is 0.4 or less, the polarization is small, and when x is 0.4 or more, the polarization is large.

The XAS spectra of the Mn *K*-edge for $ZnMn_2O_4$ after Mg^{2+} insertion was obtained in order to examine the charge compensation of the Mn in $Mg_xZnMn_2O_4$ (Figure 6-6). The obtained XANES spectra shifted toward the lower energy region with increasing amounts of inserted Mg^{2+}. (Figure 6-7a). This shift to lower energy means that the Mn ions in $ZnMn_2O_4$ are reduced. The energy at a normalized intensity of 0.5 ($E_{0.5}$) decreased with Mg^{2+} insertion to the energy range between those of Mn_2O_3 and Mn_3O_4 (Figure 6-7b), indicating that some of the Mn ions in $ZnMn_2O_4$ were reduced from Mn^{3+} to Mn^{2+}.

Changes in the crystal structure of $ZnMn_2O_4$ during Mg^{2+} insertion were examined using synchrotron XRD measurements. In the XRD patterns (Figure 6-8), $ZnMn_2O_4$ before discharge gave peaks attributed to spinel phase with an $I4_1/amd$ space group. As shown in Figure 6-8, a rocksalt phase is formed after discharge process. After the insertion of more than 0.4 mol of Mg^{2+}, the intensity of the spinel-derived peaks decreased with further Mg^{2+} insertion, while the intensity of the rock-salt-derived peaks increased. This indicates that the phase transition from the spinel phase to the rock-salt phase occurs with Mg^{2+} insertion into each phase. Although Zn prefers tetrahedral coordination, it was reported that a metastable cubic rocksalt structure can be formed due to coexistence with Mg.[31] The XRD results show that Mg^{2+} insertion into $ZnMn_2O_4$ does

not proceed via a typical two-phase reaction as $LiFePO_4$ does, which is in agreement with the results of OCP measurements and XAS.

The phase transition mechanism of Mg^{2+} insertion into $ZnMn_2O_4$ is shown in Figure 6-9. In the beginning stage of Mg^{2+} insertion into $Mg_xZnMn_2O_4$ ($0 < x < 0.4$), Mg^{2+} insertion into $ZnMn_2O_4$ spinel phase proceeds via a solid-solution reaction with the reduction of Mn ions in the spinel phase. When the x up to 0.4, the phase transition from the spinel phase to the rock-salt phase occurs with Mg^{2+} insertion into each phase.

6-4. Conclusions

The mechanism for the phase transition during Mg^{2+} insertion into a spinel $ZnMn_2O_4$ cathode, which is considered to be more stable at tetrahedral sites and less prone to the spinel-to-rock salt phase transition was clarified using XAS and XRD in this study. From the electrochemical measurements, it was confirmed that the polarization during Mg^{2+} insertion of $ZnMn_2O_4$ was smaller than that of $MgMn_2O_4$. Mg^{2+} insertion into $ZnMn_2O_4$ does not occur through a simple two-phase reaction between the spinel phase and rock-salt phase. The XRD results showed that, unlike the $MgMn_2O_4$ cathode material, the Mg^{2+} insertion into $ZnMn_2O_4$ proceeded in a single phase from the initial state, and the phase transition between the spinel and rock salt phases occurred after the Mg^{2+} insertion amount reached 0.4 mol. Since polarization during Mg^{2+} insertion increases as the phase proportion between the spinel and rock-salt phases changes, suppression of the phase transition from the spinel phase to the rock-salt phase to reduce this polarization is important. From the above results, we can confirm that the polarization due to the phase transition was suppressed by substituting elements in the tetrahedral sites in the spinel oxide.

References

1. J. M. Tarascon and M. Armand, *Nature*, **2001**, 414, 359-367.
2. A. Yoshino, *Angew. Chem., Int. Ed.*, **2012**, 51, 5798-5800.
3. D. Aurbach, Y. Cohen and M. Moshkovich, *ECS Solid State Lett.*, **2001**, 4, A113.
4. D. Aurbach, Z. Lu, A. Schechter, Y. Gofer, H. Gizbar, R. Turgeman, Y. Cohen, M. Moshkovich and E. Levi, *Nature*, **2000**, 407, 724-727.
5. J. O. Besenhard and M. Winter, *ChemPhysChem*, **2002**, 3, 155-159.
6. M. Matsui, *J. Power Sources*, **2011**, 196, 7048-7055.
7. E. Levi, M. Levi, O. Chasid and D. Aurbach, *J. Electroceramics*, **2009**, 22, 13-19.
8. D. Aurbach, G. S. Suresh, E. Levi, A. Mitelman, O. Mizrahi, O. Chusid and M. Brunelli, *Adv. Mater.*, **2007**, 19, 4260-4267.
9. E. Levi and D. Aurbach, *Chem. Mater.*, **2010**, 22, 3678-3692.
10. Y. Liang, R. Feng, S. Yang, H. Ma, J. Liang and J. Chen, *Adv. Mater.*, **2011**, 23, 640-643.
11. X. Sun, P. Bonnick, V. Duffort, M. Liu, Z. Rong, K. A. Persson, G. Ceder and L. F. Nazar, *Energy Environ. Sci.*, **2016**, 9, 2273-2277.
12. Z.-L. Tao, L.-N. Xu, X.-L. Gou, J. Chen and H.-T. Yuan, *Chem. Commun.*, **2004**, 2080-2081.
13. Q. Fu, A. Sarapulova, V. Trouillet, L. Zhu, F. Fauth, S. Mangold, E. Welter, S. Indris, M. Knapp and S. Dsoke, *J. Am. Chem. Soc.*, **2019**, 141, 2305-2315.
14. D. Imamura, M. Miyayama, M. Hibino and T. Kudo, *J. Electrochem. Soc.*, **2003**, 150, A753.
15. D. Le, S. Passerini, F. Coustier, J. Guo, T. Soderstrom, B. Owens and W. H. Smyrl, *Chem. Mater.*, **1998**, 10, 682-684.

16. C. Ling, R. Zhang and F. Mizuno, *ACS Appl. Mater. Interfaces*, **2016**, 8, 4508-4515.
17. R. Zhang, X. Yu, K.-W. Nam, C. Ling, T. S. Arthur, W. Song, A. M. Knapp, S. N. Ehrlich, X.-Q. Yang and M. Matsui, *Electrochem. commun*, **2012**, 23, 110-113.
18. Z.-D. Huang, T. Masese, Y. Orikasa, T. Mori, T. Minato, C. Tassel, Y. Kobayashi, H. Kageyama and Y. Uchimoto, *J. Mater. Chem. A*, **2014**, 2, 11578-11582.
19. Y. Orikasa, K. Kisu, E. Iwama, W. Naoi, Y. Yamaguchi, Y. Yamaguchi, N. Okita, K. Ohara, T. Munesada and M. Hattori, *Chem. Mater.*, **2020**, 32, 1011-1021.
20. Y. Orikasa, T. Masese, Y. Koyama, T. Mori, M. Hattori, K. Yamamoto, T. Okado, Z.-D. Huang, T. Minato and C. Tassel, *Sci. Rep.*, **2014**, 4, 5622.
21. A. Watanabe, K. Yamamoto, Y. Orikasa, T. Masese, T. Mori, T. Uchiyama, T. Matsunaga and Y. Uchimoto, *Solid State Ionics*, **2020**, 349, 115311.
22. N. Ishida, Y. Nakamura, T. Mandai, N. Kitamura and Y. Idemoto, *Solid State Ionics*, **2020**, 354, 115413.
23. N. Ishida, N. Yamazaki, T. Mandai, N. Kitamura and Y. Idemoto, *J. Electrochem. Soc.*, **2020**.
24. R. D. Bayliss, B. Key, G. Sai Gautam, P. Canepa, B. J. Kwon, S. H. Lapidus, F. Dogan, A. A. Adil, A. S. Lipton and P. J. Baker, *Chem. Mater.*, **2019**, 32, 663-670.
25. T. Hatakeyama, N. L. Okamoto, K. Shimokawa, H. Li, A. Nakao, Y. Uchimoto, H. Tanimura, T. Kawaguchi and T. Ichitsubo, *Phys. Chem. Chem. Phys.*, **2019**, 21, 23749-23757.
26. L. Hu, J. R. Jokisaari, B. J. Kwon, L. Yin, S. Kim, H. Park, S. H. Lapidus, R. F. Klie, B. Key and P. Zapol, *ACS Energy Lett.*, **2020**, 5, 2721-2727.

27. K. Ishii, S. Doi, R. Ise, T. Mandai, Y. Oaki, S. Yagi and H. Imai, *J. Alloys Compd*, **2020**, 816, 152556.

28. B. J. Kwon, K.-C. Lau, H. Park, Y. A. Wu, K. L. Hawthorne, H. Li, S. Kim, I. L. Bolotin, T. T. Fister and P. Zapol, *Chem. Mater.*, **2019**, 32, 1162-1171.

29. B. J. Kwon, L. Yin, H. Park, P. Parajuli, K. Kumar, S. Kim, M. Yang, M. Murphy, P. Zapol and C. Liao, *Chem. Mater.*, **2020**, 32, 6577-6587.

30. S. Okamoto, T. Ichitsubo, T. Kawaguchi, Y. Kumagai, F. Oba, S. Yagi, K. Shimokawa, N. Goto, T. Doi and E. Matsubara, *Adv. Sci.*, **2015**, 2, 1500072.

31. K. Shimokawa, T. Atsumi, M. Harada, R. E. Ward, M. Nakayama, Y. Kumagai, F. Oba, N. L. Okamoto, K. Kanamura and T. Ichitsubo, *J. Mater. Chem. A*, **2019**, 7, 12225-12235.

32. S. Doi, R. Ise, T. Mandai, Y. Oaki, S. Yagi and H. Imai, *Langmuir*, **2020**, 36, 8537-8542.

33. S. Yagi, Y. Ichikawa, I. Yamada, T. Doi, T. Ichitsubo and E. Matsubara, *Jpn. J. Appl. Phys.*, **2013**, 52, 025501.

34. Z. Zhao-Karger, M. E. G. Bardaji, O. Fuhr and M. Fichtner, *J. Mater. Chem. A*, **2017**, 5, 10815-10820.

35. V. Petříček, M. Dušek and L. Palatinus, *Z. Kristallogr. Cryst. Mater.*, **2014**, 229, 345-352.

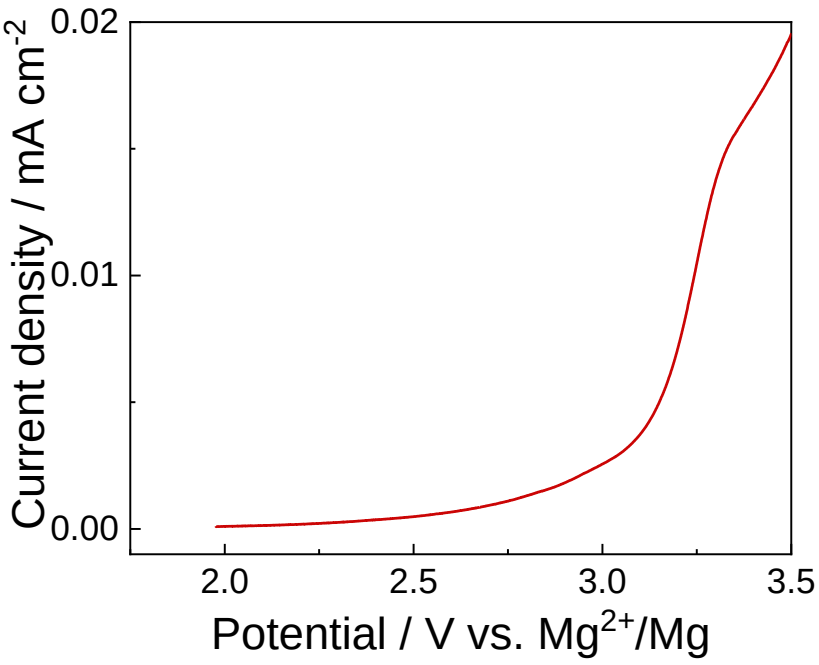

Figure 6-1. Linear sweep voltammetry. Three-electrode cells using Pt working electrode, Mg metal counter electrode, and reference electrodes were used. Electrolyte was 0.3 M Magnesium tetrakis(hexafluoroisopropyloxy)borate ($Mg[B(HFIP)_4]_2$) in triglyme. Potential sweeping rate was 10 mV s^{-1}, and measurement temperature was 50°C

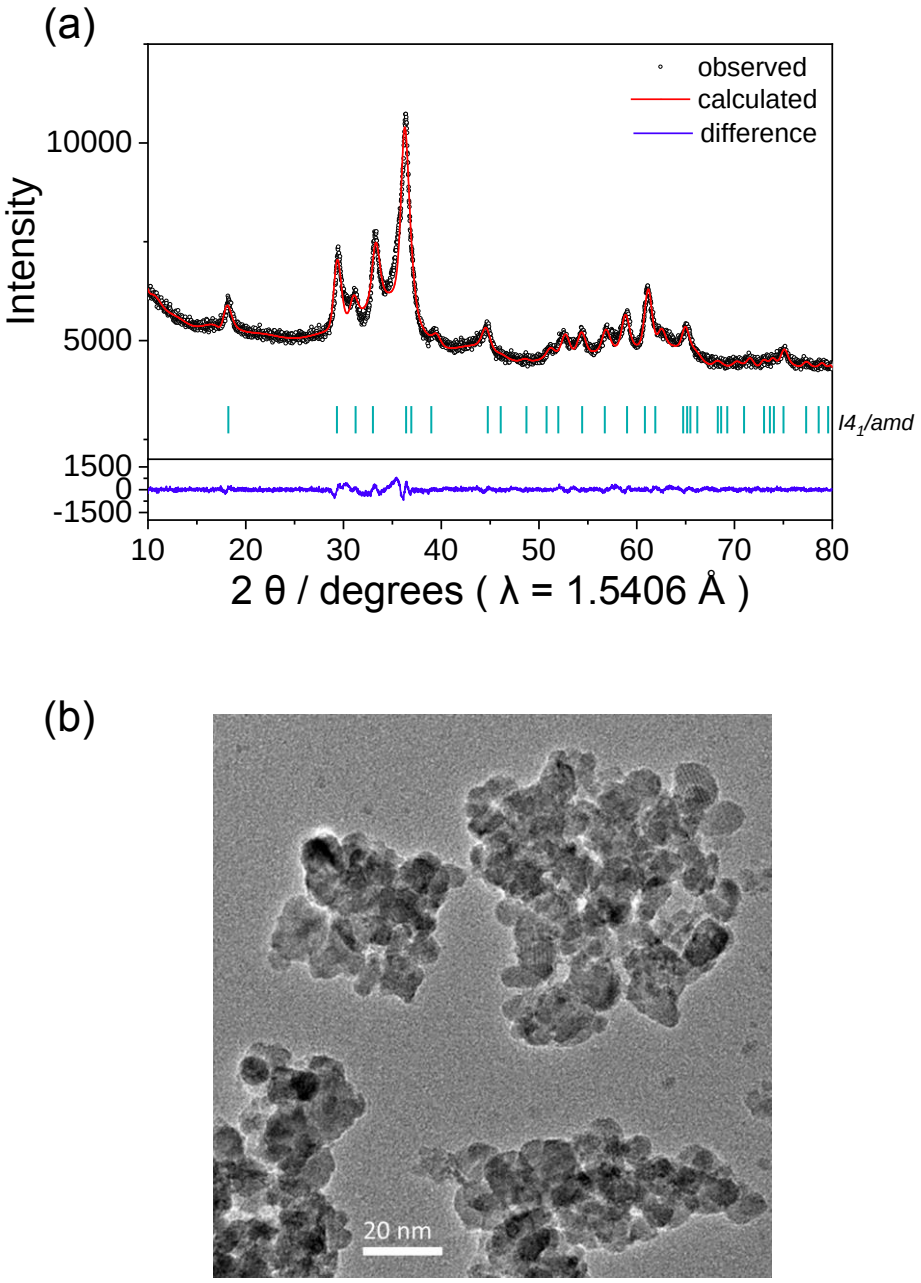

Figure 6-2. Characterization of $ZnMn_2O_4$ cathode: (a) XRD pattern and Rietveld analytical fitting profile of the $ZnMn_2O_4$ cathode sample and (b) TEM image of the $ZnMn_2O_4$ powder.

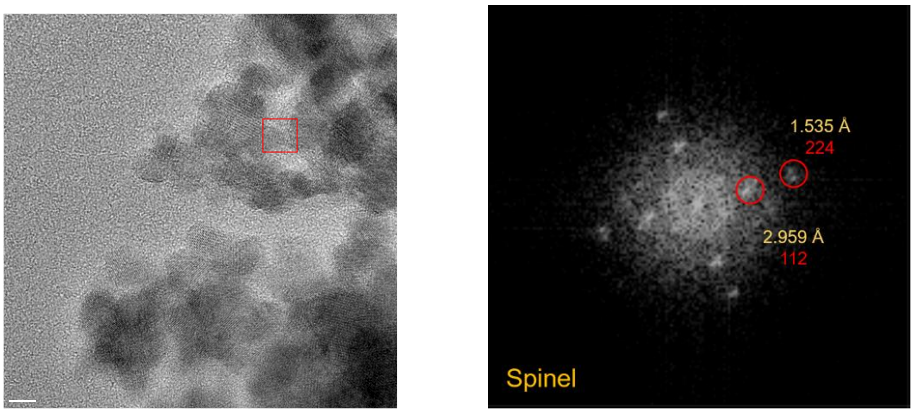

Figure 6-3. Transmission electron image and electron diffraction pattern of $ZnMn_2O_4$.

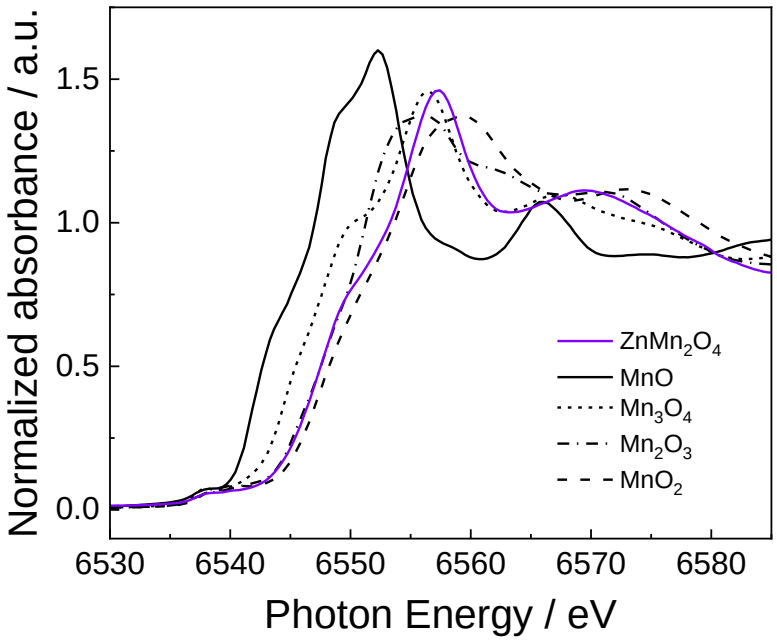

Figure 6-4. XANES for Mn *K*-edge of the $ZnMn_2O_4$ cathode.

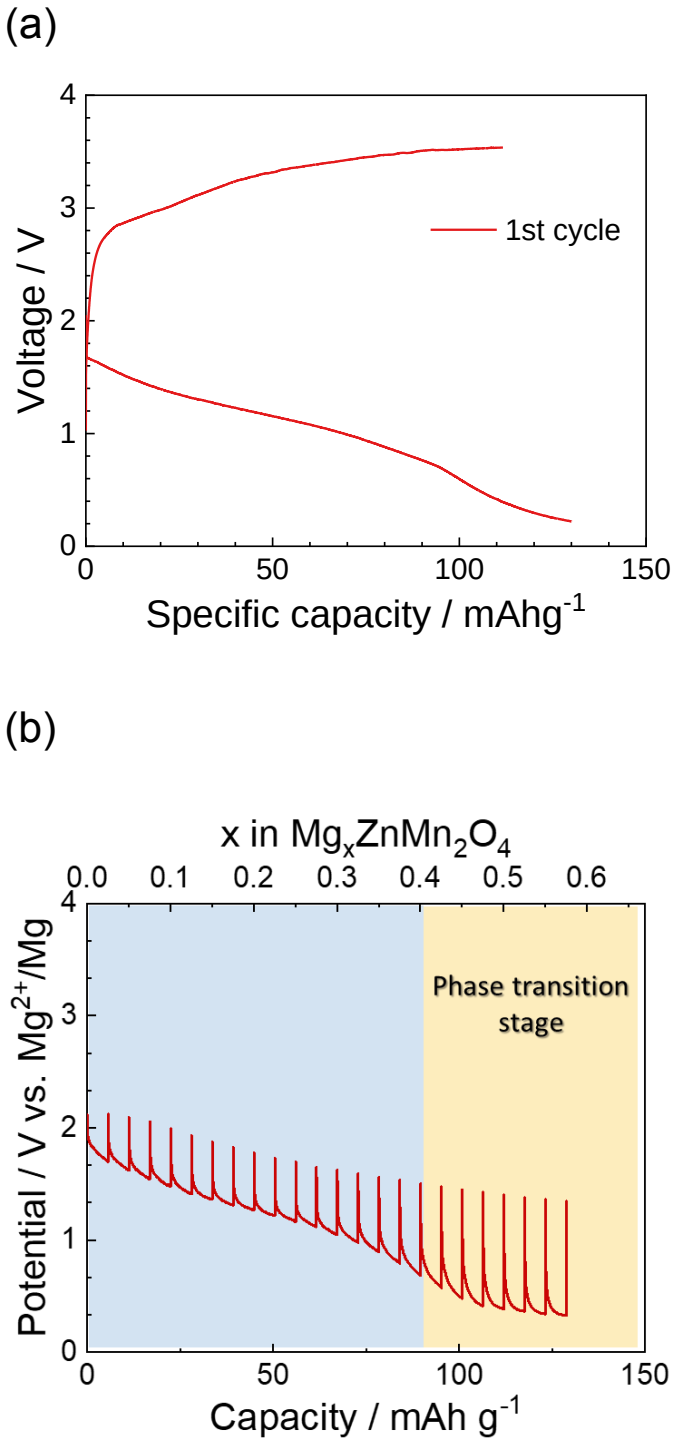

Figure 6-5. (a) Constant-current discharge–charge curves of $ZnMn_2O_4$ at 50 °C. (b) GITT profile of $ZnMn_2O_4$.

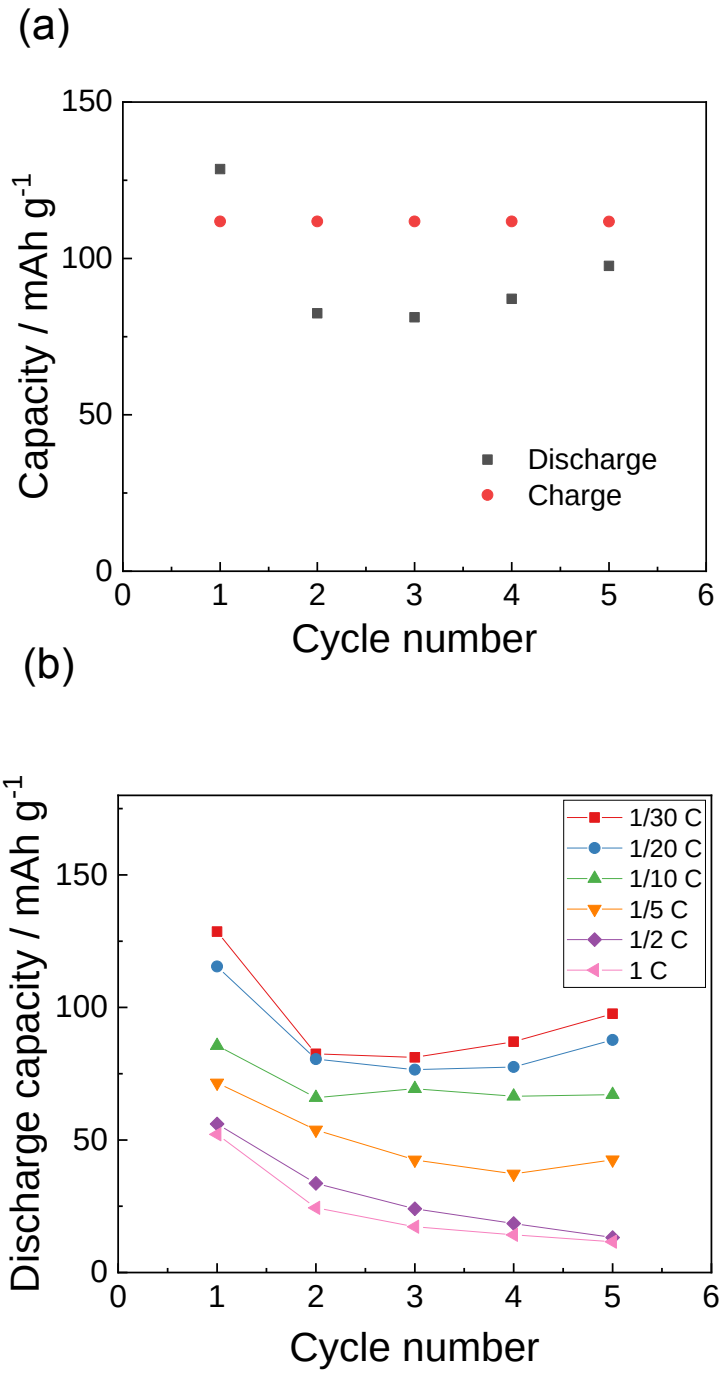

Figure 6-6. Cycling performance of the $ZnMn_2O_4$ electrode derived from $Mg[B(HFIP)_4]_2$/triglyme electrolyte at (a) 1/30 C and (b) different rates.

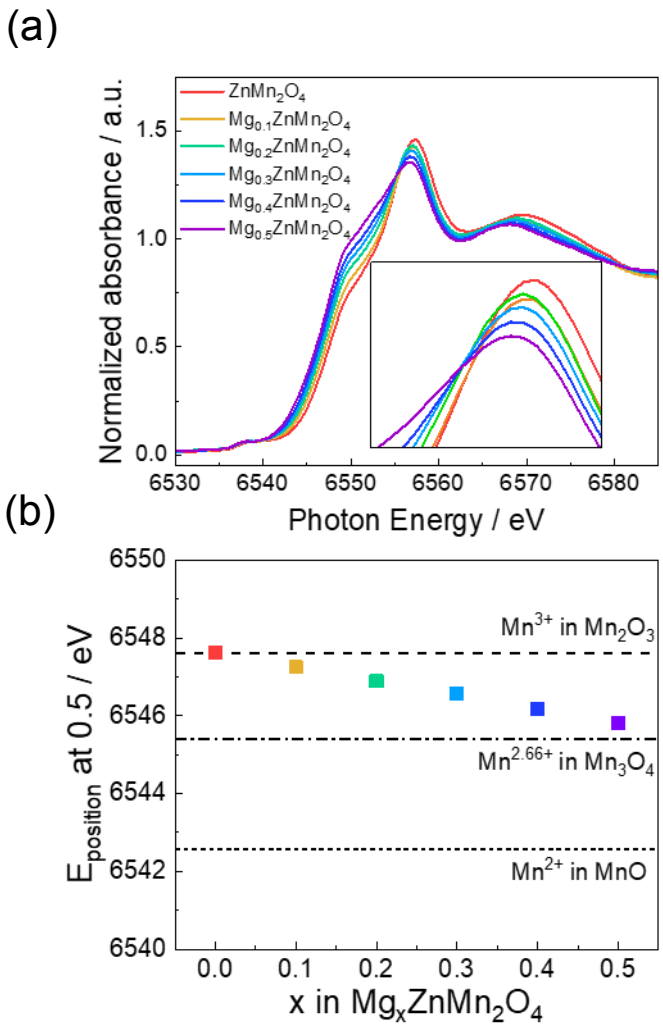

Figure 6-7. (a) Mn *K*-edge XANES of $ZnMn_2O_4$ before and after Mg^{2+} insertion and (b) energy at a normalized intensity of 0.5 in the XANES.

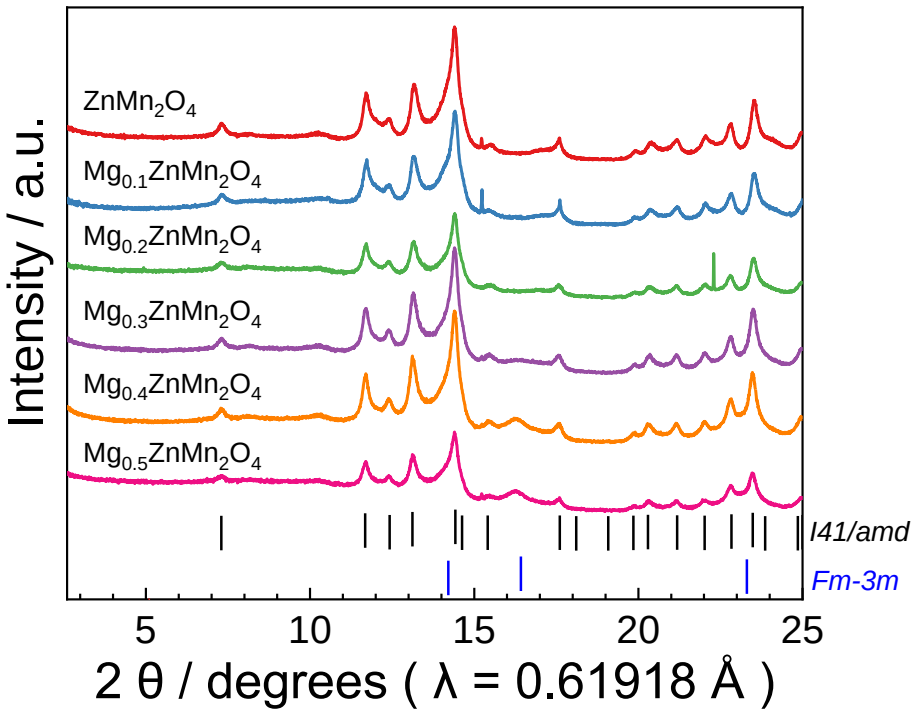

Figure 6-8. XRD patterns of $Mg_xZnMn_2O_4$ ($0 \leq x \leq 0.5$) before and after Mg^{2+} insertion. Black index shows diffraction pattern of spinel-type $ZnMn_2O_4$ with tetragonal symmetry ($I4_1/amd$) while blue index shows diffraction pattern of rock-salt-type $MgZnMn_2O_4$ with cubic symmetry (Fm-3m).

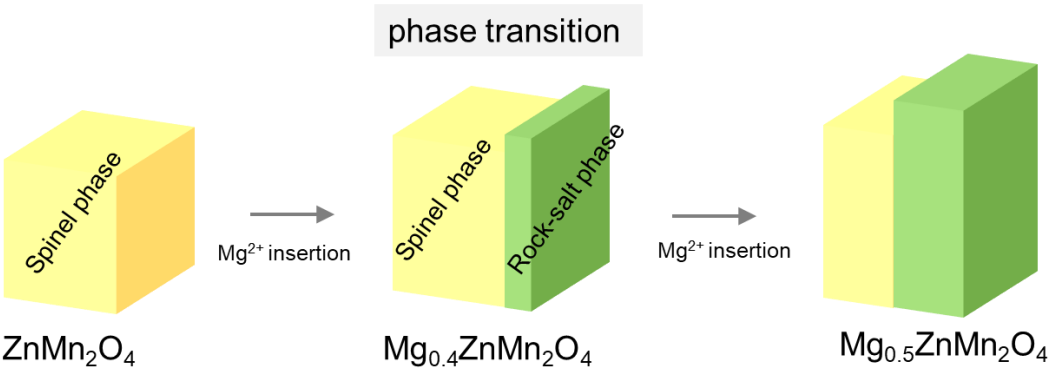

Figure 6-9. Schematic illustration of the volume changes and phase transition model for the transition from spinel phase to rock-salt phase upon magnesium ion insertion.

Chapter 7. General Conclusion

Rechargeable magnesium batteries, which have attracted tremendous attention in large-scale energy-storage applications beyond LIBs, have many advantages such as high volumetric capacity, low cost, environmental friendliness and high abundance of magnesium. However, the combination of electrolytes and cathode being studied is limited. A clear understanding of the reaction mechanism will provide useful information for designing new electrolyte and cathode materials for practical magnesium rechargeable batteries. In this study, we combined the *operando* soft X-ray absorption spectroscopy, Raman spectroscopy, electrochemical impedance spectroscopy (EIS), X-ray photoelectron spectroscopy (XPS), and DFT calculation to elucidate the reaction mechanism at the anode/electrolyte interface for different types of electrolyte systems. Furthermore, we investigated the crystal and local structural changes in spinel oxides during Mg^{2+} insertion using X-ray diffraction (XRD) and X-ray absorption spectroscopy (XAS) in order to elucidate the mechanism of the phase transition from spinel to rock-salt.

In chapter 1, the necessity of magnesium rechargeable batteries was described. We mainly reported the past magnesium rechargeable battery electrolytes and cathode. The importance of understanding the anode reaction mechanism in magnesium rechargeable batteries was presented, especially focusing on the interface between electrolytes and cathodes were reviewed.

In chapter 2, the coordination structures of the magnesium ions in the bulk solution and at the anode/electrolyte interface of three magnesium electrolytes were analyzed in this study. In the 0.5 M $Mg(TFSA)_2$/triglyme electrolyte, quasi-reversible magnesium deposition/dissolution reactions occurred, whereas no magnesium deposition reaction occurred in the 0.5 M $Mg(TFSA)_2$/2-MeTHF electrolyte. In the 0.5 M $Mg(BH_4)_2$/THF electrolyte, although the current density was relatively low, reversible magnesium deposition/dissolution reactions occurred. *Operando* XAS measurements showed that the valency of the magnesium ions did not change, and the local structure distortion around the magnesium ions increased in all the electrolytes at the magnesium electrode/electrolyte interface during the cathodic polarization. We conclude that suppressing the reduction decomposition of the anion is crucial for achieving successful magnesium deposition; furthermore, separating the magnesium ion from the anion is important for accelerating the magnesium deposition.

In chapter 3, the effects of anion species and solvents on the coulombic efficiency and polarization of magnesium deposition/dissolution reactions, the anode/electrolyte interfacial behavior of magnesium tetrakis(hexafluoroisopropyloxy) borate ($Mg[B(HFIP)_4]_2$) and magnesium bis(trifluoromethanesulfonyl)amide ($Mg(TFSA)_2$) was investigated and compared in triglyme and 2-methlytetrahydrofuran (2-MeTHF). When using triglyme, which has strong interaction with magnesium ion, decomposition of $[B(HFIP)_4]^-$ in $Mg[B(HFIP)_4]_2$/triglyme was hard to occur due to the high reduction stability of uncoordinated $[B(HFIP)_4]^-$ anion, resulting in significantly higher coulombic

efficiency and smaller polarization than $Mg(TFSA)_2$/triglyme. When 2-MeTHF was used as the solvent, magnesium deposition/dissolution reactions occurred in the $Mg[B(HFIP)_4]_2$/2-MeTHF electrolyte but not in the $Mg[TFSA]_2$/2-MeTHF electrolyte. This is because the coordinated $[B(HFIP)_4]^-$ anion in $Mg[B(HFIP)_4]_2$/2-MeTHF is stable at the magnesium deposition potential. However, the reductive stability of the coordinated $[B(HFIP)_4]^-$ anion is inferior to that of the uncoordinated $[B(HFIP)_4]^-$ anion, resulting in the $Mg[B(HFIP)_4]_2$/2-MeTHF coulombic efficiency being lower than that of $Mg[B(HFIP)_4]_2$/triglyme. Our results indicate that solvents that could not be used with $Mg(TFSA)_2$ are suitable in weakly coordinating anion electrolytes, such as $Mg[B(HFIP)_4]_2$.

In chapter 4, the effects of boron-based Mg electrolytes with different anion sizes on the Coulombic efficiency and polarization of magnesium deposition/dissolution reactions were investigated. The coordination structure of the magnesium ions in the bulk solution of each electrolyte was analyzed by Raman spectroscopy. The reductive stability and decomposition reaction of each anion in these electrolytes was determined by DFT calculations and EIS.

In chapter 5, we investigated the reaction mechanism of magnesium ion insertion for magnesium spinel oxides, $MgMn_2O_4$, by electrochemical measurements, X-ray absorption spectroscopy (XAS), and synchrotron X-ray diffraction (XRD) with Rietveld analysis. Open-circuit-voltage and XAS measurements showed that Mg^{2+} insertion into $MgMn_2O_4$ does not proceed via a simple two-phase coexistence reaction between the

spinel and rock-salt phases. Synchrotron XRD measurements showed that Mg^{2+} insertion into $MgMn_2O_4$ involves crystal structural changes in three stages. In the early stage of the Mg^{2+} insertion process, Mg^{2+} is inserted into the spinel ($Mg_{1+\alpha}Mn_2O_4$) phase and rock-salt ($Mg_{2-\beta}Mn_2O_4$) phases, which are included in the pristine samples, without significant volume changes. In the middle stage of the Mg^{2+} insertion process, Mg^{2+} is inserted into the $Mg_{1+\alpha}Mn_2O_4$ spinel phase and the $Mg_{2-\beta}Mn_2O_4$ rock-salt phases with a large volume change. In the last stage of Mg^{2+} insertion process, Mg^{2+} insertion proceeds via a two-phase coexistence reaction between $Mg_{1.4}Mn_2O_4$ spinel and $Mg_{1.6}Mn_2O_4$ rock-salt phases without Mg content changes in either phase. The phase transition from the $Mg_{1+\alpha}Mn_2O_4$ spinel phase to the $Mg_{2-\beta}Mn_2O_4$ rock-salt phase with a large volume change resulted in significant polarization during the Mg^{2+} insertion process.

In chapter 6, we investigated the mechanism of magnesium-ion insertion into $ZnMn_2O_4$ spinel oxides by electrochemical measurements, XAS, and synchrotron XRD with Rietveld analysis. The polarization during Mg^{2+} insertion of $ZnMn_2O_4$ was smaller than that of $MgMn_2O_4$. Mg^{2+} insertion into $ZnMn_2O_4$ does not occur through a simple two-phase reaction between the spinel phase and rock-salt phase. Unlike the $MgMn_2O_4$ cathode material, the Mg^{2+} insertion into $ZnMn_2O_4$ proceeded in a single phase from the initial state, and the phase transition between the spinel and rock salt phases occurred after the Mg^{2+} insertion amount reached 0.4 mol. The polarization due to the phase transition was suppressed by substituting elements in the tetrahedral sites in the spinel oxide.

Acknowledgment

I would like to express my deep gratitude to all those who have helped and cared for me. Firstly, I would like to express my sincere gratitude to my supervisor, Prof. Yoshiharu Uchimoto, whose innovative academic thinking, rigorous attitude and profound knowledge left a deep impression on me. He has walked me through all the stages of the writing of this thesis. Without his support and illuminating instruction, this thesis would not have been achievable.

I would like to appreciate to Dr. Kentaro Yamamoto who has been guiding me carefully, teaching me how to analyze and solve problems that arise in my experiments, and correcting my shortcomings and mistakes.

I am also grateful to Dr. Toshihiko Mandai, Dr. Koji Nakanishi and Prof. Toshiyuki Matsunaga for their helps on synthesis of electrolyte, measuring and analyzing XAS and XRD.

I would also like to thank all the members of Prof. Uchimoto's laboratory, who have instructed and helped me a lot.

Last, my thanks would go to my beloved family for their loving considerations and great confidence in me all through these years.

Tuerxun Feilure

Kyoto, JAPAN

※　著作権等

Determining Factor on Polarization Behavior of Magnesium Deposition for Magnesium Battery Anode
Tuerxun, Feilure; Yamamoto, Kentaro; Hattori, Masashi; Mandai, Toshihiko; Nakanishi, Koji; Choudhary, Ashu; Tateyama, Yoshitaka; Sodeyama, Keitaro; Nakao, Aiko; Uchiyama, Tomoki; Matsui, Masaki; Tsuruta, Kazuki; Tamenori, Yusuke; Kanamura, Kiyoshi; Uchimoto, Yoshiharu
ACS Applied Materials & Interfaces, 2020, 12, 23, 25775 – 25785
DOI: 10.1021/acsami.0c03696

Effect of Interaction among Magnesium Ions, Anion and Solvent on Kinetics of Magnesium Deposition Process
Tuerxun, Feilure; Yamamoto, Kentaro; Mandai, Toshihiko; Tateyama, Yoshitaka; Nakanishi, Koji; Uchiyama, Tomoki; Watanabe, Toshiki; Tamenori, Yusuke; Kanamura, Kiyoshi; Uchimoto, Yoshiharu
J. Phys. Chem. C, 2020, 124, 52, 28510 – 28519
DOI: 10.1021/acs.jpcc.0c08268

Phase transition behavior of MgMn2O4 spinel oxide cathode during magnesium ion insertion
Feilure Tuerxun, Saeko Otani, Kentaro Yamamoto, Toshiyuki Matsunaga, Hiroaki Imai, Toshihiko Mandai, Toshiki Watanabe, Tomoki Uchiyama, Kiyoshi Kanamura, Yoshiharu Uchimoto
Chem. Mater., 2021, 33, 3, 1006 – 1012
DOI: 10.1021/acs.chemmater.0c04194